Investigation of Soil-Structure Interaction for Deep Excavations



Peter Hensman
Linacre College
University of Oxford

A thesis submitted for the degree of
MSc by Research in Engineering Science

Michaelmas 2023

Abstract

Investigation of Soil-Structure Interaction for Deep Excavations

Peter J. Hensman
Linacre College, University of Oxford
A thesis submitted for the degree of *MSc by Research in Engineering Science*
Michaelmas 2023

Deep excavations are widely adopted in infrastructure projects for the construction of underground storage, deep foundations, basements, and launch and reception pits for tunnel boring machines for the transport, water and wastewater, energy, and commercial and industrial building sectors. Deep excavations typically comprise an *in situ* concrete or driven steel earth retaining wall braced with support structures including steel frames and ground anchorages. Rapid population growth in urban areas is driving the increasing depth and complexity of deep excavations, which is increasing the likelihood and severity of risks associated with ground deformations. Therefore, it is important that understanding of the performance of these structures, and the predictive tools used in their design, are improved through more sophisticated approaches, including complex three-dimensional (3D) numerical analyses and real-time monitoring systems.

This thesis explores the performance of a modern 'combi-wall' supported deep excavation, and its interaction with the neighbouring soil and internal support structures, using a combination of field monitoring and numerical analysis. The field monitoring scheme involved instrumenting a 12 m deep excavation in soft clays and peats for a deep underground waste storage bunker for the PROTOS Energy-from-Waste Facility in Chester, UK. The deep excavation was supported by a complex 'combi-wall' cofferdam, a reinforced concrete (RC) capping beam, and two levels of internal bracing, and its performance was assessed through measured wall deflections, bracing member loads, and site and bunker water levels. The permanent bunker RC structure was constructed within the excavation and was instrumented to monitor temperatures and strains using strain gauges and novel fibre optic monitoring systems. The monitoring scheme provided the site team with real-time feedback to inform construction decisions and promote a proactive approach to risk mitigation. The monitored data provide new insights into the behaviour of a combi-wall supported deep excavation in UK soft soils, for which little high quality field data exists in published literature.

The field monitoring program is complemented by numerical analyses to evaluate the capability of numerical models to capture observed behaviour in the field. The numerical predictions are compared to both the field measurements and simplified limit equilibrium predictions, which are often largely overconservative despite being typically adopted in industry. Also, a probabilistic analysis is performed to analyse uncertainty in the model soil input parameters. The results can provide confidence in the use of numerical models for the design of future deep excavation structures, leading to cost and carbon savings through a reduction in required material quantities.

Acknowledgements

First and foremost, I would like to thank my supervisors Brian Sheil and Byron Byrne for their continued support throughout this project. Their patient supervision and guidance were incredibly useful and I am extremely grateful to have had them as my supervisors. I would also like to thank Zhandos Orazalin for his support with the field monitoring work and for the development of the online dashboard.

This research would not have been possible without the support of Ward & Burke Construction. The technical guidance provided by numerous individuals within Ward & Burke contributed to the delivery of this research, and I would like to thank all those involved. Particular thanks must go to the site team at PROTOS energy recovery facility for their assistance with the field monitoring work. I would also like to thank Ronan Royston for guiding me through my early career with Ward & Burke, and for suggesting I pursue research opportunities. Finally I would like to thank Michael Ward, Padraig Burke and Alan Bruton for providing me with the opportunity to pursue this project, and for the continuous support and stimulating conversation throughout the research.

I have thoroughly enjoyed working alongside academics and students in the department, and I must thank those in Room 11 and the FOCUS research group for their friendship and support during my time at Oxford. I must also thank Clive Baker for the support in the lab, Harvey Burd and Vincenzo Nardelli for the guidance and advice they provided at the transfer stage of the research, and Harvey Burd and Mike Long for reviewing the research and conducting a stimulating and enjoyable viva examination.

I would like to thank my parents, brothers, grandparents, and wider family and friends for their encouragement and support in getting me to this position. Finally, I must thank my partner Kelsey for her unwavering love and support throughout.

Preface

For this research, I was responsible for the planning, installation and maintenance of the instrumentation employed for the field monitoring scheme at PROTOS energy-from-waste facility in Chester, UK. Ward and Burke Construction Ltd. were delivering this project. I was working for Ward and Burke as a design engineer and site construction supervisor. I was based on the site full-time from April 2021 until March 2022. During this time I was also responsible for temporary works designs across the project, including that of the bunker excavation. I was also a site engineer and construction supervisor for the bunker excavation and permanent works construction period. The design of the bunker reinforced concrete base and wall permanent works was the responsibility of the design consultant Sargent & Lundy.

From April 2022 until early 2023, I worked on processing and analysing the field monitoring data, and was responsible for developing the numerical modelling scheme described in Chapters 5 and 6 of this thesis.

A section of the field monitoring work presented in Chapters 3 and 4 of this thesis has been published in the peer-reviewed geotechnics journal Géotechnique (Hensman et al. (2023)). As the lead author of this publication I was responsible for collecting the field monitoring data, processing, presenting and analysing the data, developing the manuscript, and revising the manuscript based on peer-reviewed feedback. Brian Sheil provided guidance throughout the project and offered substantial feedback on the manuscript drafts. Zhandos Orazalin developed an online dashboard used to display the monitoring data in real-time to site personnel.

A different section of the field monitoring work was published in the proceedings of the 5th International Conference on Geotechnics for Sustainable Infrastructure Development (Hensman and Sheil (2023)). I presented the research at the conference held in Hanoi, Vietnam in December 2023.

Contents

1 Research introduction and objectives **1**
- 1.1 Introduction . . . 1
- 1.2 Research objectives . . . 4
- 1.3 Thesis outline . . . 5
- 1.4 Industry collaboration . . . 7

2 Literature review **8**
- 2.1 Introduction . . . 8
- 2.2 Typical excavation construction sequences . . . 8
  - 2.2.1 Cantilever wall . . . 8
  - 2.2.2 Top-down sequence . . . 8
  - 2.2.3 Bottom-up sequence . . . 9
- 2.3 Excavation retaining wall types . . . 10
  - 2.3.1 Contiguous piles . . . 10
  - 2.3.2 Secant piles . . . 10
  - 2.3.3 Diaphragm walls . . . 10
  - 2.3.4 Reinforced concrete caissons . . . 11
  - 2.3.5 Segmental caisson shafts . . . 11
  - 2.3.6 Driven steel cofferdams . . . 11
- 2.4 Simplified theoretical methods . . . 13
  - 2.4.1 Limit equilibrium methods . . . 13
  - 2.4.2 Subgrade reaction and pseudo finite element methods . . . 16
- 2.5 Empirical methods . . . 16
- 2.6 Numerical methods . . . 18
  - 2.6.1 Constitutive soil models . . . 20
  - 2.6.2 Application to deep excavations . . . 28
  - 2.6.3 Probabilistic uncertainty analyses . . . 29
- 2.7 Field case histories . . . 32
  - 2.7.1 Wall deformations . . . 33
  - 2.7.2 Prop loads . . . 35
- 2.8 Fibre optic monitoring . . . 37
- 2.9 Summary and gaps in knowledge . . . 40

3 Field testing and instrumentation setup **41**
- 3.1 Introduction . . . 41
- 3.2 Project description . . . 41
  - 3.2.1 Project overview . . . 41
  - 3.2.2 Ground conditions . . . 42
  - 3.2.3 Construction sequence . . . 47
- 3.3 Instrumentation plan . . . 55
  - 3.3.1 Inclinometers . . . 57
  - 3.3.2 Weldable VW strain gauges . . . 58
  - 3.3.3 Embedment type VW strain gauges . . . 61
  - 3.3.4 Fibre optics . . . 63
  - 3.3.5 Piezometers . . . 67
- 3.4 Lessons learnt and areas for improvement . . . 69

4 Field monitoring results **71**

4.1 Introduction . . . 71
4.2 Wall deflections . . . 71
4.2.1 Initial cantilever deflection . . . 71
4.2.2 Maximum wall deflection time series . . . 72
4.2.3 Deflected wall shape during excavation . . . 73
4.2.4 Deflected wall shape during bunker construction . . . 74
4.2.5 Comparison to case histories and empirical methods . . . 77
4.3 Prop axial loads and bending moments . . . 80
4.3.1 Raw measurements . . . 80
4.3.2 Temperature compensation method . . . 82
4.3.3 Comparison to case histories . . . 87
4.4 Bunker base structural response . . . 88
4.4.1 Base temperature response . . . 88
4.4.2 Base strains . . . 90
4.4.3 Axial load and bending moment time series . . . 91
4.4.4 Axial load and bending moment profiles . . . 92
4.5 Bunker wall structural response . . . 93
4.5.1 Wall temperature response . . . 93
4.5.2 Wall bending moments . . . 95
4.6 Water levels . . . 97
4.7 Summary of key findings . . . 98

5 Numerical model development 101
5.1 Introduction . . . 101
5.2 Constitutive soil modelling . . . 101
5.2.1 Field soil sampling . . . 103
5.2.2 Laboratory elemental testing . . . 104
5.2.3 Mohr-Coulomb Model parameter determination . . . 107
5.2.4 Hardening Soil Model parameter determination . . . 112
5.2.5 Hardening Soil with Small-Strain Stiffness Model parameter determination 113
5.2.6 Model calibration . . . 115
5.3 2D numerical model development . . . 119
5.3.1 Structural models . . . 119
5.3.2 Construction sequence . . . 122
5.3.3 Mesh refinement . . . 124
5.4 3D numerical model development . . . 126
5.4.1 Structural models . . . 127
5.4.2 Construction sequence . . . 129
5.4.3 Mesh refinement . . . 130
5.5 Lessons learnt and areas for improvement . . . 132

6 Numerical modelling results 135
6.1 Introduction . . . 135
6.2 2D model results . . . 135
6.2.1 Wall deflections . . . 135
6.2.2 Prop loads . . . 137
6.2.3 Comparison to limit equilibrium methods . . . 138
6.3 3D model results . . . 141
6.3.1 Wall deflections . . . 142
6.3.2 Prop loads . . . 145

6.3.3 Comparison to limit equilibrium methods . . . 147
6.4 Probabilistic uncertainty analysis . . . 148
6.4.1 Sensitivity study . . . 149
6.4.2 Soil input parameter distributions . . . 151
6.4.3 Results and discussion . . . 152
6.5 Summary of key findings . . . 156

7 Conclusions **158**
7.1 Introduction . . . 158
7.2 Key contributions . . . 158
7.3 Recommendations for future research . . . 162
7.4 Concluding remarks . . . 163

Bibliography **164**

Nomenclature

Abbreviations

2D	2-dimensional
3D	3-dimensional
3-SKH	Three surface of kinematic hardening
AOD	Above ordnance datum
BGL	Below ground level
BU	Bottom-up
CB	Corner brace
CD	Consolidated drained
CFA	Continuous flight augering
CPT	Cone penetrometer test
CRS	Constant rate of strain
CSD	Contiguous piles, secant piles and diaphragm walls
CU	Consolidated undrained
DFOS	Distributed fibre optic detection
EFW	Energy-from-waste
FBG	Fibre optic Bragg grating
FD	Finite difference
FE	Finite element
FO	Fibre optic
GGBS	Ground granulated blast-furnace slag
GI	Ground investigation
GM	Ground model
GT	Glacial till
GT-C	Glacial till clays
GT-S	Glacial till sands
HS	Hardening Soil
HSS	Hardening Soil with small strain stiffness
IC	Inclinometer
LE	Limit equilibrium

MC	Mohr-Coulomb
MG	Made ground
P	Peat
PI	Piezometer
PSR	Plane strain ratio
RC	Reinforced concrete
SCPT	Seismic cone penetrometer test
SI	Site investigation
SS	Sheet and soldier piles
TD	Top-down
TF	Tidal flats deposits
TP	Tube prop
UB	Universal beam
UC	Universal column
UU	Unconsolidated undrained
VW	Vibrating wire
WIP	Wished-in-place
WM	Wall model

Material and soil parameters

α_c	Concrete coefficient of thermal expansion
α_g	Gauge coefficient of thermal expansion
α_s	Structure coefficient of thermal expansion
β_{cc}	Time dependent concrete coefficient
$\gamma_{0.7}$	Characteristic shear strain level
γ_{bulk}	Soil bulk unit weight
γ_N	Numerical 3D unit weight
γ_s	Shear strain
γ_w	Unit weight of water
γ_{wall}	Wall unit weight
ν	Poisson's ratio
ν_{ur}	Unload-reload poisson's ratio

ϕ	Angle of friction
ϕ'	Effective angle of friction
ψ	Dilatancy angle
ρ	Density
ζ	Thermal-optic coefficient
c	Cohesion
c'	Effective cohesion
c_u	Undrained shear strength at formation level
c_{ub}	Undrained shear strength below formation level
c_{uh}	Undrained shear strength above formation level
E	Elastic modulus
E_{50}	Secant stiffness
E_{50}^u	Undrained secant modulus
E_{cm}	Concrete E at age of 28 days
E_i	Initial stiffness
E_{oed}	Oedometric stiffness
E_{ur}	Unload-reload stiffness
EI	Bending stiffness
f_{cm}	Concrete mean compressive strength at 28 days
FF	Thermal degree of restraint
G_0	Initial shear modulus
G_s	Secant shear modulus
I	Second moment of area
I_c	Soil behaviour type index
I_{sys}	Wall system second moment of area
I_x	Second moment of area about x plane
I_y	Second moment of area about y plane
K_0	At-rest lateral earth pressure coefficient
k_1	Compressibility dependent soil constant
K_a	Active earth pressure coefficient
K_p	Passive earth pressure coefficient
m	Power for stiffness stress dependency

m'	Grain size power law parameter
N_c	Bearing capacity factor
OCR	Overconsolidation ratio
P_o	Fibre optic photo-elastic coefficient
R_{fa}	Failure ratio
R_{inter}	Interface strength reduction factor
s	Cement coefficient
S_1	Fibre optic temperature coefficient
s_u	Undrained shear strength
w	Water content
Z	Elastic modulus

Geometric parameters

$\delta_{h,c}$	Wall displacement at cantilever stage
$\delta_{h,max}$	Maximum wall displacement
δ_h	Wall displacement
$\delta_{y,heave}$	Vertical heave displacement
λ	Wavelength
λ_B	Bragg wavelength
Ψ	Curvature
A	Cross-sectional area
A_{sys}	Wall system cross-sectional area
A_T	Tributary area
A_w	3D wall cross-sectional area
B	Excavation width
B_1	Basal heave failure mechanism width
b_{sys}	Wall system width
d	Wall depth
E_w	3D wall elastic modulus
H	Excavation depth
h	Thickness
h_c	Cantilever stage depth

L	Excavation length
$L_{spacing}$	Anchor spacing
L_t	Tributary length
OD	External diameter
s	Support spacing
t	Wall thickness
z	Depth
z_{ex}	Average excavation depth
z_{prop}	Prop depth

Force, stress and general parameters

α	Relative sensitivity
Δp	Change in percentage
η_s	Sensitivity ratio
η_{ss}	Sensitivity score
μ	Mean
σ	Standard deviation
σ'	Effective stress
σ'_1	Axial confining pressure
σ'_3	Radial confining pressure
σ'_a	Average effective axial stress
σ_{atm}	Atmospheric pressure
σ_{v0}	Overburden pressure
σ'_{v0}	Effective overburden pressure
ε	Strain
$\mu\varepsilon$	Microstrain
$\mu\varepsilon_{mech}$	Mechanically applied microstrain
ε^e	Elastic strain
ε^p	Plastic strain
ε_a	Axial strain
ε_r	Radial strain
C	Basal heave plane strain ratio factor

C_B	Batch calibration factor
C_G	Gauge calibration factor
COV	Coefficient of variation
DPL	Maximum distributed prop load
f	Frequency
F	Axial load
f'	Thermal relationship gradient
$f(x)$	Model output
$F_{adjusted}$	Thermally adjusted axial load
f_s	CPT sleeve friction
f_t	Thermally induced load assuming rigid end restraint
FOS_{BH}	Factor of safety against basal heave
k	Permeability
M	Bending moment
n	Number of simulations
N'	Axial load per unit length
N_{kt}	Empirical cone factor
N_{max}	Maximum compressive frame anchor load
p'	Mean effective stress
p_e	Probability of exceedance
p_{ref}	Reference stress for stiffnesses
q	Deviatoric stress
Q	Flow rate
q_f	Deviatoric stress at failure
q_i	Deviator stress at start of shearing
q_t	Corrected CPT cone resistance
R_f	Friction ratio
S	Dimensionless system stiffness factor
T	Temperature
t	Time
u	Pore pressure
V_s	Shear wave velocity

1 | Research introduction and objectives

1.1 Introduction

Rapid population growth in dense urban environments means that exploitation of underground spaces is often the only sustainable solution for the delivery of new infrastructure. Underground infrastructure projects often require the construction of deep excavations and shafts, which are commonly employed within the transport, water and wastewater (see Figure 1.1), energy, and commercial building sectors. Deep excavations constitute a significant part of the largest construction projects occurring in the UK at the moment, including HS2, Thames Tideway and Crossrail, which are estimated to be worth 98 billion, 4.5 billion, and 18.8 billion pounds respectively.

The structural performance of deep excavations depends on several factors, including ground conditions, construction method, and the wall type selected and their design involves numerous considerations as shown in Figure 1.2. The excavation process inevitably affects the stress state of the ground and can cause significant settlements and wall deflections. An inability to effectively predict, monitor and control these ground movements can lead to significant and costly consequences, ranging from minor damage to adjacent infrastructure to complete excavation collapse. The increasing depth and complexity of deep excavations, and their construction in dense urban environments, is providing design and construction challenges to the industry. Therefore, it is important that understanding of the performance of these structures, and the predictive tools used in their design, are improved through more sophisticated approaches, including complex three-dimensional (3D) numerical analyses and real-time monitoring systems.

Empirical methods remain an integral aspect of design and rely on analysis of monitored case history data to verify and refine design assumptions and methods. However, extrapolation of such methods to new ground conditions (i.e. outside of their calibration space) and



Figure 1.1: Example of deep excavations and shafts constructed as part of Blanchardstown Regional Drainage Scheme in Dublin. (Ward and Burke Construction).

different construction sequences incorporates considerable risk into the design and construction processes. Additionally, it is challenging to obtain consistent results using empirical relationships due to the inevitable variability between individual case histories, arising from variations in ground conditions and general workmanship. Empirical methods are developed to represent only the scenarios in their calibration meaning extrapolation to new scenarios is unvalidated. Therefore, it is essential to continue to enhance the database on which these empirical methods are based, particularly for cases involving complex components or challenging ground conditions.

Traditionally in industry, deep excavations have been designed using simplified limit equilibrium and pseudo finite element (FE) methods (e.g. Winkler spring approach). However, these methods are limited in that they are based on several broad simplifying assumptions and often do not provide information about ground movements and behaviour under working conditions, which are critical design considerations. While the use of numerical analysis overcomes these issues, and is continuing to grow in popularity, further work is required to improve the reliability

of predictions given inherent uncertainties associated with material models and soil properties.

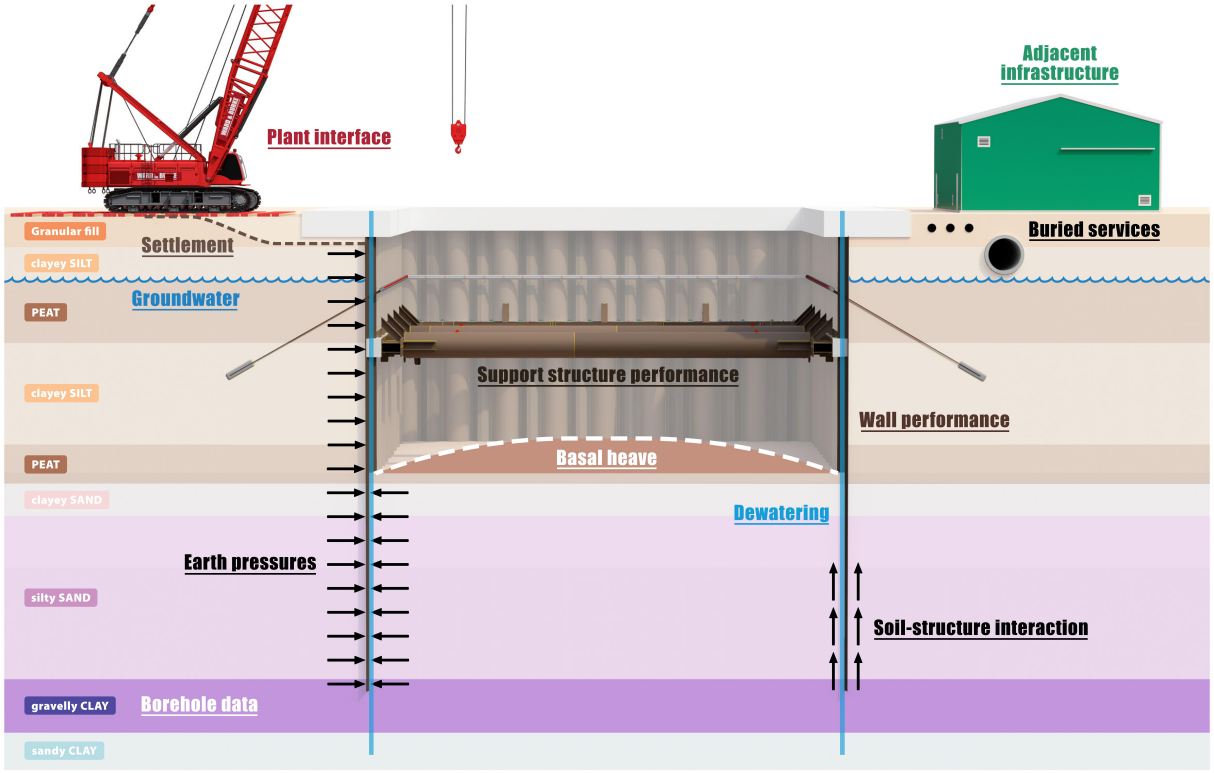


Figure 1.2: Sketch highlighting some of the design considerations involved for deep excavations and associated structures.

Advancements in *in situ* wall installation techniques has meant monitoring the performance of diaphragm and secant pile retaining walls has remained a popular topic in modern geotechnical literature. However, reported case histories involving the use of sheet pile walls are few in comparison. Modern cofferdam installation techniques have also led to an increase in the use of 'combi-wall' cofferdam solutions, involving sheet piles interspersed with stiffer king (often tubular) piles, to increase lateral stiffness and bearing capacity. High quality field data for this support system is much less common. There is also a general lack of reported case histories specific to the UK, which have been limited to diaphragm and secant pile walls in London Clay. The literature therefore points to a distinct lack of observations on the performance of combi-wall systems in UK soils.

1.2 Research objectives

The primary aim of this research is to achieve new understanding into the soil-structure interaction mechanisms involved in combi-wall supported deep excavations through state-of-the-art field monitoring of live construction sites together with complementary FE analysis to achieve new insight. The goal of this research is two-fold: firstly to investigate the structural performance of deep excavations and areas in which savings can be made through field monitoring, and secondly to provide confidence in the use of numerical models for the design of future deep excavation structures and evaluate the capability of these models to capture observed behaviours in the field. Numerical modelling and parametric analyses have the potential to be used to perform 'what-if' scenario forecasting and construction process optimisation in a safe virtual environment to achieve step-change construction efficiency. The application of this across the industry would lead to significant financial and environmental benefits. A summary of the key objectives and research areas are shown in Figure 1.3.

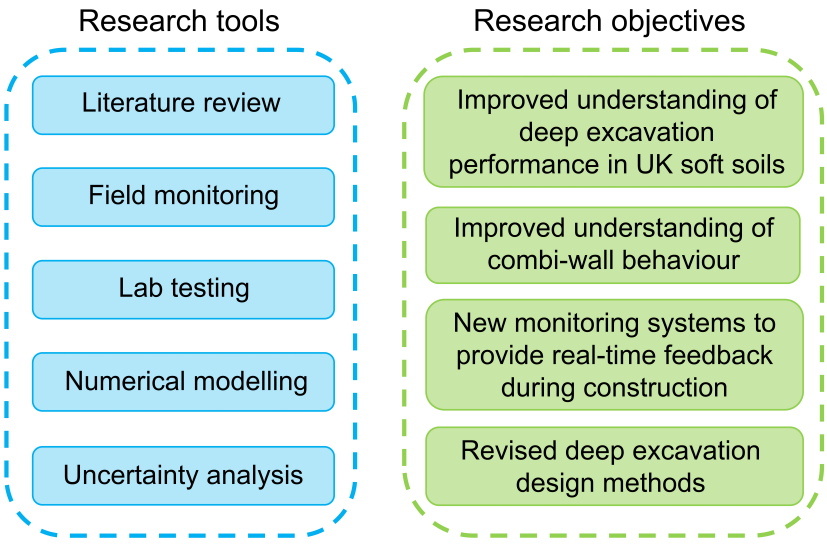


Figure 1.3: Summary of the research objectives and the main research tools available to achieve these.

1.3 Thesis outline

To achieve the research objectives, the research is presented in the following order:

Chapter 2 - Literature review

Background information and literature pertinent to this research is reviewed in this chapter. Firstly, typical deep excavation construction sequences and wall types are presented. Next, literature involving simplified theoretical design methods is presented. This is divided into methods for calculating lateral earth pressures and those for analysing basal stability. Historic limit equilibrium approaches are first introduced before more recent adaptations and developments are summarised. These typically conservative methods are commonly employed by industry designers. Previous research exploring empirical design methods is then presented, with a focus on methods for predicting ground settlements and lateral wall deflections, which are highly relevant to this research. Next, literature on the development of soil constitutive models and the application of numerical design methods and parametric analyses to deep excavation design are presented. Finally, previously published deep excavation field monitoring cases and databases are discussed, and the general trends observed in wall deflection data are summarised. Previous research involving the use of fibre-optic instrumentation systems to monitor geotechnical structures is also presented.

Chapter 3 - Field testing

This chapter outlines the methodology used to collect and interpret data from the monitoring scheme employed for the field study. Firstly, the field monitoring site at PROTOS Energy-from-Waste (EFW) facility is introduced, and the construction sequence for the bunker deep excavation and permanent reinforced concrete (RC) structure is outlined. The layout for the monitoring scheme is then shown, and the installation process for each component of the monitoring system is described. Finally, calculations used to determine key output parameters from raw instrument data are presented.

Chapter 4 - Field results

This chapter presents the monitored data and describes the observations from the instrumented deep excavation and RC bunker structure at the PROTOS EFW field monitoring site, with a focus on interpreting the monitored data with reference to previously published case history data to better contextualise the observed behaviours. Reported measurements include cofferdam wall deflections, bracing member loads, groundwater level and pumping data, and temperatures, strains and loads in the permanent RC bunker base and walls.

Chapter 5 - Numerical model development

This chapter details the development process for numerical models created to complement the field monitoring data in the commercially available finite element (FE) packages PLAXIS 2D and PLAXIS 3D (Brinkgreve et al. (2022)). Input parameters for the soil constitutive models used to model each soil layer are determined from site investigation data and laboratory elemental tests before structural models are selected for the deep excavation wall and support structures. The numerical construction sequence and the development and refinement of the FE mesh are also detailed.

Chapter 6 - Numerical model results and parametric study

This chapter describes the results of the numerical analyses and compares these to the field monitoring data and simplified limit equilibrium design predictions to assess the accuracy of the numerical predictions and to evaluate the model development process. Also, a probabilistic analysis is performed to analyse uncertainty in the model soil input parameters.

Chapter 7 - Conclusions

The final chapter of this thesis provides a summary of the key contributions of the work. It also highlights beneficial areas for future work.

1.4 Industry collaboration

This research has been carried out alongside industry collaborator Ward and Burke Construction Ltd. Ward and Burke specialises in the design and construction of underground infrastructure within the UK, Ireland and North America, with involvement in the utilities, road, bridge, energy and coastal sectors. The company focuses on the design and construction of micro-tunnels (up to 3 m diameter), deep excavations, shafts and caissons. The author has experience working on site as part of the design and construction of deep excavations, and other underground structures, with Ward and Burke. The field monitoring case study at PROTOS was carried out on a Ward and Burke project.

2 | Literature review

2.1 Introduction

The following chapter provides some background information about excavation construction methods and wall types, and a brief summary of literature relating to theoretical, empirical, and numerical deep excavation design literature and methods. A collection of key field case histories is also presented, and some of the trends observed in key monitored parameters are described. Finally, a summary of the literature review is presented, which highlights gaps in the literature which will be addressed by this research.

2.2 Typical excavation construction sequences

A deep excavation construction sequence typically starts with the installation of an embedded retaining wall. Several forms of temporary and permanent works can be used to provide additional support to the retaining wall (e.g. steel props, ground anchors, and permanent RC slabs). The construction sequence can typically be classified into one of three main categories: cantilever wall; top-down; and bottom-up, as described below.

2.2.1 Cantilever wall

Cantilever walls rely on the flexural strength and stiffness of the wall itself, and passive resistance provided by the soil within the excavation, with no additional structural anchorage or support. Cantilever walls are simple to design and construct, and the restrictions of working around temporary propping structures are avoided. However for deeper excavations, excessive deflections can occur at the top of the wall, and wall sections with a large bending stiffness are typically required, which can make this option economically unviable.

2.2.2 Top-down sequence

An alternative to a cantilever wall sequence involves propping of the retaining wall during excavation. A top-down (TD) sequence involves the use of the permanent works structure as

temporary propping, with higher level slabs cast before lower level slabs. Excavation occurs in stages below each new permanent propping slab, supported below by temporary vertical supports (e.g. piles), as shown in Figure 2.1a. This method eliminates the requirement for temporary support structures which can be economically beneficial. However, the excavated fill must be removed through small openings in the RC propping slabs, which can be a time-consuming and awkward process.

2.2.3 Bottom-up sequence

A bottom-up (BU) construction sequence involves constructing the permanent works from the lowest level upwards, with the foundation slab being cast before any permanent walls and high level slabs. Temporary propping structures such as steel props and ground anchorages are used to support the wall during excavation, and are often positioned at multiple levels (Figure 2.1b). RC capping beams and ring beams are typically used to prop the top of the retaining wall. BU sequences without the use of internal propping can be achieved through using a circular shaft or cofferdam, that relies on hoop compression to resist retained loads. The sequential construction of the substructure followed by the superstructure minimises conflicts between site operations, but this also means superstructure construction cannot take place concurrently with excavation works, which is common when using a TD approach.



(a) (b)

Figure 2.1: Example of a deep excavation constructed using (a) top-down construction method (Geotechnical Consulting Group (2011)) and (b) bottom-up construction method (Malcolm Drilling (2018)).

2.3 Excavation retaining wall types

There are several methods employed in industry to construct deep excavation walls. Factors that may influence the choice of method include site and ground conditions, nearby structures and utilities, excavation dimensions and the desired watertightness of the structure. The following provides an overview of commonly employed methods for excavation construction. Examples of each wall construction method are shown in Figure 2.2.

2.3.1 Contiguous piles

A contiguous pile wall consists of a series of bored cast *in situ* concrete piles installed along the line of the wall, with no intersection between piles (see Figure 2.2a). Piles are constructed using continuous flight augering (CFA) or rotary bored piling rigs, and temporary casings are sometimes used to improve the installation verticality tolerance. Contiguous pile walls are often cheaper and quicker to install than secant pile or diaphragm walls. However, the gaps between piles mean that they are not suitable for retaining water bearing course grained soils and that unstable sections of ground can fall into the excavation.

2.3.2 Secant piles

Secant pile walls are formed by a series of interlocking primary and secondary bored cast *in situ* piles (see Figure 2.2b). CFA or rotary bored piling rigs are used to install intervening secondary piles between primary piles. Secant pile walls can be further sub-classified as hard-soft, hard-firm or hard-hard, depending on the constituents of the primary piles. The maximum achievable depth is typically limited to 20 - 25 m by the verticality tolerance of the installation plant.

2.3.3 Diaphragm walls

Diaphragm walls are constructed by first excavating narrow trenches with grab arms or reverse circulation mills (for harder materials). The excavated void is retained through the use of construction support fluids. Prefabricated reinforcement cages are lowered into the trenches before the void is concreted using tremie pipes to displace the support fluid. An example of

an anchored diaphragm wall is shown in Figure 2.2c. Verticality tolerances are typically better than walls using CFA piles and have been shown to be as high as 1:400 (Gaba et al. (2017)). There are fewer joints compared with piled walls, making for effective water retaining ability. Diaphragm walls have been constructed to depths of up to 100 m in the UK.

2.3.4 Reinforced concrete caissons

An open dug caisson is a form of top-down construction, which involves a system of concurrent casting of the concrete walls at ground level and excavation of the soil within and beneath the caisson, which encourages the structure to sink into the ground. Caissons are typically circular (see Figure 2.2d) but there are examples of rectangular caissons being used in industry (Royston (2018)).

2.3.5 Segmental caisson shafts

Segmental caisson shafts consist of RC concrete segments bolted together to form a ring, as shown in Figure 2.2e. They can be constructed by jacking into the ground, adding sections at ground level, or by underpinning in stable ground. Each segment is bolted to the neighbouring elements, with rubber seals positioned in between to achieve water tightness. These structures are designed as compression structures and are not capable of withstanding large tensile forces.

2.3.6 Driven steel cofferdams

Cofferdams consist of long profiled steel pile sections, driven into the ground either by impact driving or vibratory equipment. Adjacent piles are connected by interlocking clutches, with sealants or welding used between clutches to inhibit water seepage into the excavation. Cofferdam depths are typically limited by the feasible lengths of sections, which depend on fabrication and transport requirements, with the maximum length typically between 20 m and 25 m. The most commonly used sheet sections are U piles and Z piles which can provide wall stiffness of up to 250,000 kNm^2/m (see Figure 2.2f). Where higher wall stiffness is required, 'combi-wall' solutions may be used. Combi-walls are composed of primary elements, typically steel tubular piles, I-sections or box piles, and interlocking secondary sheet piles, and can be

designed for stiffness values of up to 10,000,000 kNm^2/m. Sheet piling is not feasible in rock or soil containing large boulders. Driven steel cofferdams are the focus of this research.



Figure 2.2: Examples of deep excavation wall construction for: (a) contiguous pile wall (Martello Piling (2022)), (b) secant pile wall (Zakladani Staveb (2022)), (c) diaphragm wall (nscc International (2022)), (d) circular caisson, (e) segmental shaft wall (Donegan Civil Engineering (2019)), (f) sheet pile cofferdam (AGL Consulting (2018)).

2.4 Simplified theoretical methods

2.4.1 Limit equilibrium methods

Analysing the stability of a retaining structure is an important early design consideration. Preliminary wall stability calculations are typically performed using limit equilibrium analyses. Limit equilibrium analysis methods involve assessing the equilibrium of the wall under assumed lateral pressures, which are typically calculated using limiting values of lateral earth pressure coefficients.

Limit equilibrium methods have limitations in that they do not model the interaction between the ground and the structure, the wall flexibility or the construction sequence. They also cannot be used to calculate deformations of the wall or ground, and only drained or undrained conditions can be modelled. Despite this, limit equilibrium stability calculations remain an important component of analyses used in industry. However, the sole use of these methods without more complex subgrade reaction or numerical method checks can lead to overconservative designs, which can have financial and environmental implications.

Lateral earth pressure calculation

Traditionally two main approaches have been used to estimate the limiting active and passive earth pressures acting on a retaining wall. The Coulomb (1773) method considers the force that must be exerted on a wedge of soil to prevent it from sliding down a slip surface. By considering the forces acting on all three wedge boundaries, the magnitude of the resultant force exerted by the wedge to the wall can be calculated. The Rankine (1857) method is based on the maximum stress state which can achieve both equilibrium and not violate the maximum soil strength.

A limitation of these methods is that neither considers the wall deformation explicitly. This has been addressed through the development of idealised geo-structural deformation mechanisms such as those in Bolton and Powrie (1988), which offer a way of linking wall movement

to the mobilised soil strength. Another limitation is that both the Coulomb (1773) and Rankine (1857) methods consider every element of the soil mass to to be governed by the Mohr-Coulomb failure criterion. The omission of state- and pressure-dependency of soil dilation in simpler elastic-plastic models such as the Mohr-Coulomb failure criterion leads to an underprediction in the peak shear stress attainable at low normal effective stresses and an overprediction in its value at high normal effective stresses. Gaba et al. (2017) outlines some modified forms of the Mohr-Coulomb criterion which better describe the relationship between isotropic stress level and failure strength, including a tri-linear failure envelope (Schofield (1980), Wood (1990), Atkinson (2007), Powrie (2018)).

Methods developed by Caquot and Kérisel (1948), Sokolovskii (2016) and Absi (2017) incorporate additional realities such as wall friction and ground slopes into the Rankine (1857) approach, by assuming a soil failure mechanism shape and subsequently calculating the limiting force acting on the wall using equilibrium approaches. The calculated limits are not inherently safe, but experience demonstrates they provide a reasonable estimate of limiting lateral stresses (Gaba et al. (2017)).

Basal stability

Several researchers have also employed limit equilibrium methods to analyse the basal stability of deep excavations. Terzaghi (1943) suggested the weight of a soil column inside the excavation, and adhesion acting along the edges of the column, resists the bearing capacity failure of a corresponding soil column outside the excavation (Figure 2.3a). This method can be used to calculate an approximate factor of safety against basal heave (FOS_{BH}) as:

$$FOS_{BH} = \frac{5.7 c_{ub} B_1}{\gamma H B_1 - c_{uh} H} \tag{2.1}$$

where c_{uh} and c_{ub} are the values of average undrained shear strength above formation level and below formation level respectively, γ is the average bulk unit weight of soil above formation level, H is the maximum excavation depth and B_1 is equal to $0.7B$ or the depth to hard stratum

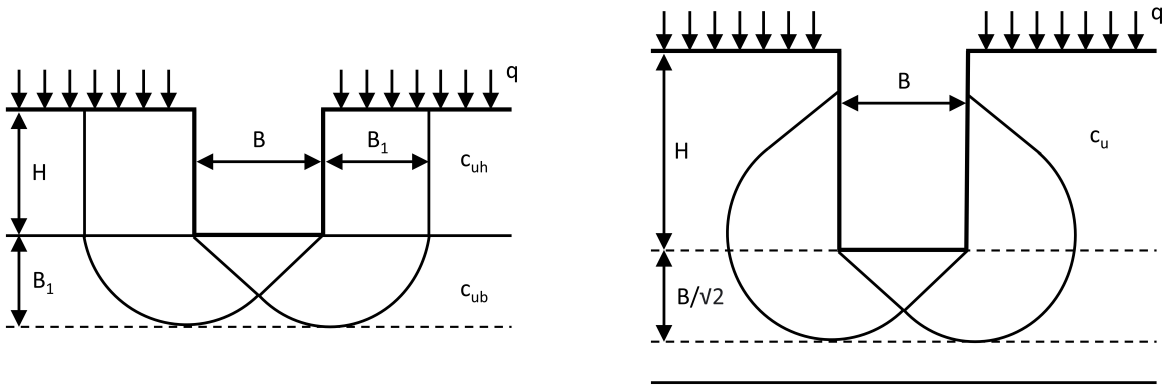
below formation.

Bjerrum and Eide (1956) treated the excavation base as a smooth footing (Figure 2.3b), with FOS_{BH} calculated as:

$$FOS_{BH} = \frac{c_u N_c}{\gamma H + q} \tag{2.2}$$

where N_c is the bearing capacity factor which is a function of shape and depth, c_u is the undrained shear strength at formation level, and q is the uniform surcharge applied to the ground surface. The method showed good agreement with several previously published case histories.

O'Rourke (1993) modified previous methods to consider the effect of wall flexure below the excavation level, anticipating an increase in stability due to the elastic strain energy stored. The approach also assumed that the embedded depth of the wall does not change the basal failure mechanism geometry.



(a) (b)

Figure 2.3: Illustration of assumed basal heave failure mechanisms for (a) Terzaghi (1943) method and (b) Bjerrum and Eide (1956) method (reproduced from Goh et al. (2008)).

2.4.2 Subgrade reaction and pseudo finite element methods

Subgrade reaction and pseudo FE methods are more complex than limit equilibrium methods, as they can be used to calculate wall movements in addition to wall bending moments and prop loads. The subgrade reaction method involves modelling the soil as a series of linear horizontal springs, with spring stiffness typically increasing with depth. Maximum spring forces are typically imposed, and correspond to active and passive limiting stresses. According to Simpson and Powrie (2002), while this method generally gives similar bending moment predictions to FE programs, it is challenging to determine suitable coefficients of subgrade reaction.

Pseudo FE methods involve replacing the soil with an elastic continuum, which realistically redistributes pressure (Simpson and Powrie (2002)). Both the subgrade reaction and pseudo FE methods use plane strain theory to compute earth pressures, leading to overconservative, 'safe' estimates. It is important that analyses undertaken using either of these methods are calibrated against data collected from well-monitored case histories.

2.5 Empirical methods

Empirical methods are those developed using previously published field data. The methods are typically only applicable within the validated range of each parameter. For the analysis of deep excavations, these parameters constitute ground conditions, construction sequences and structural components. Terzaghi et al. (1967) developed apparent earth pressure envelopes based on field data, which were then used to predict maximum strut loads for braced excavations. However, this method has been evaluated by many researchers such as Wong et al. (1997) and Hashash and Whittle (2002), and it has been shown the envelopes can differ significantly from measured load distributions.

Peck (1969) summarised data on lateral wall deflections and ground settlements, identifying three different settlement zones depending on ground conditions. Generally, where soil conditions were not challenging and workmanship was of a good standard, settlements are shown to

not exceed one percent of the excavation depth, with the surface settlement profile shown to extend laterally as far as twice the excavated depth. However, as the case histories considered were all constructed prior to 1969, all excavations were supported by flexible soldier and sheet piles, and the majority of data was collected from excavations with a depth of less than 15 m. Therefore, there are significant uncertainties in extrapolating such empirical observations to current cases involving much deeper excavations.

Mana and Clough (1981) analysed several case studies in soft to medium clays to correlate the maximum observed wall movements, normalised by excavation depth, to FOS_{BH}, calculated using the Terzaghi (1943) method. Upper and lower limits were suggested for predicting lateral wall movements. A key finding was that large increases in lateral wall displacement occurred at low values of FOS_{BH}, which was attributed to subsoil yielding mechanisms.

As part of a procedure to estimate wall movements induced by excavation in clay for multi-propped walls, Clough et al. (1989) defined a dimensionless system stiffness factor as:

$$S = \frac{EI}{\gamma_w s^4} \tag{2.3}$$

where EI is the bending stiffness of the wall calculated using the Young's modulus, E, and the second moment of area, I, γ_w is the unit weight of water, and s is the support spacing. The stiffness factor may be used in conjunction with the Terzaghi (1943) and Bjerrum and Eide (1956) (see Section 2.4.1) FOS_{BH} to provide an initial prediction of likely maximum wall displacements for an excavation of given depth as shown in Figure 2.4. Figure 2.4 shows that the horizontal wall movements increase rapidly as the risk of failure due to basal heave increases. The influence of S on the wall movements becomes less relevant with increasing FOS_{BH} but is of major importance in cohesive soils with $FOS_{BH} < 1.5$. The preliminary studies published in Mana and Clough (1981) conclude that for support systems with $FOS_{BH} = 1.4$, the horizontal wall movements are predicted to be $\delta_{h,max}/H < 2\%$. The wall movement prediction reduces to $\delta_{h,max}/H < 0.5\%$ for diaphragm walls. FOS_{BH} for walls considered in the literature is typically

larger than 3, meaning if workmanship is well controlled, wall displacements due to excavation should be relatively insensitive to the stiffness of the excavation wall.

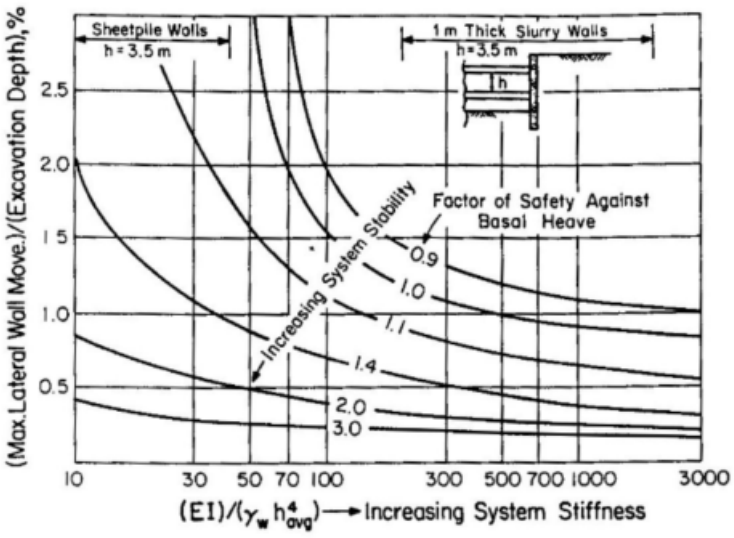


Figure 2.4: Empirical design curves to obtain maximum lateral wall movement for soft to medium clays (Clough et al. (1989)).

For multi-propped walls, Addenbrooke et al. (2000) defined a displacement flexibility factor, with units kN/m^4, which can be used to consider different propping structures and wall types for a specified lateral wall displacement value. This can be useful when considering value engineering options to satisfy a serviceability performance requirement.

2.6 Numerical methods

Finite element (FE) or finite difference (FD) packages are the most commonly used design tool for complex geotechnical structures, as they can consider various factors, such as complex soil constitutive behaviour, construction sequences, structural details, and groundwater and pore pressure variation. Typical target outputs of a numerical investigation include ground movements, wall movements and prop loads. The use of both a well-established and sufficiently advanced soil constitutive model is necessary to ensure the outputs are of value. Numerical analysis methods must be calibrated against reliable monitored case history data.

2D plane strain or axisymmetric analyses have been widely used to study deep excavations at the design stage due to the simplicity of these approaches (Clarke and Wroth (1984), Hubbard

et al. (1984), Potts and Fourie (1984), Powrie and Li (1991)). For many deep excavations, a 2D plane strain model can provide a reasonably accurate estimate of wall and ground movements that occur at the centre of a wall span. This approach is commonly adopted in practise across the industry. The extent of this capability has been quantified by Finno et al. (2007), who defined the plane strain ratio (PSR) as the maximum movement in the centre of an excavation wall computed by 3D analyses normalised to that computed by a plane strain simulation:

$$PSR = (1 - e^{-kC(L/H)}) + 0.05(L/B - 1) \tag{2.4}$$

where L is the length of the span considered, H is the depth of excavation, B is the length of the secondary span, and k and C are factors which depend on the support system stiffness and FOS_{BH} respectively, calculated as:

$$k = 1 - 0.0001S \tag{2.5}$$

$$C = 1 - 0.5(1.8 - FOS_{BH}) \tag{2.6}$$

where S is the wall system stiffness factor (Clough et al. (1989)) calculated using Equation 2.3. A PSR value of 1 indicates that a plane strain simulation will yield the same displacements in the centre of an excavation span as those computed by a 3D simulation. Using a plane strain model also has the benefits of being simpler and faster compared to 3D simulations.

However, the limitations of plane strain, 2D analyses have been widely reported, with these approaches unable to consider corner effects, whilst tending to overestimate ground movements compared to using simple 3D analyses (Ou et al. (1996), Finno et al. (2007)). Advances in computing power have enabled the application of 3D FE in routine design. Examples include the modelling of an excavation for an underground shopping centre in Shanghai using a 3D FE model in ABAQUS (Hou et al. (2009)), and the collapse of a railway transit deep trench in Singapore using a 3D FE model described in Lee et al. (2011).

2.6.1 Constitutive soil models

Aspects of real soil behaviour

The ability of a geotechnical numerical model to replicate observed behaviours in the field is heavily dependent on the extent to which the selected constitutive soil models are capable of capturing aspects of real soil behaviour. Brinkgreve (2005) categorised the basic aspects of real soil behaviour into five main areas:

1. The first aspect is the influence of water on the behaviour of soil. Total stresses in the soil can be divided into effective stresses and pore pressures. As the mechanical behaviour is dominated by effective stresses, it is essential to determine the pore pressure distribution in the soil.
2. The second aspect considers that soil stiffness is not a constant. It depends on various influences including stress state, stress path, strain level, loading time, density, permeability, overconsolidation and load direction.
3. The third aspect relates to the irreversible deformation of soils as a result of loading as most soils only have a very small elastic region.
4. The fourth aspect is related to soil strength. Soil strength is usually expressed in terms of shear strength which depends on the confining effective stress level, the loading speed, time, soil density, overconsolidation and load direction.
5. The fifth aspect relates to the time-dependency of soil behaviour. Time influences both soil stiffness and strength, and time dependent processes include consolidation, relaxation and swelling.

Other additional aspects of real soil behaviour to be considered include compaction, dilatancy and memory of pre-consolidation stress.

Brief history of constitutive soil model development

Soil constitutive models are mathematical representations used to describe the mechanical

behaviour of soils under various loading conditions. The foundations for the development of soil constitutive models were laid by contributions in the field of soil mechanics including those in Coulomb (1773), Darcy (1856), Rankine (1857) and Terzaghi (1925). The formulation of material behaviour in mathematical models started with relationships between stresses and strains to represent the material properties of stiffness and strength. The combination of Hooke's law, which provides a first order stiffness estimate involving isotropic linear elastic behaviour, and the maximum shear strength relationship in Coulomb (1773), formulated in a plasticity framework, led to the development of the Mohr-Coulomb (MC) model. The MC model is discussed further later in this section. Drucker et al. (1952) simplified the MC hexagonal shape of the failure contour in principal stress space to a simple conical surface. While the model was shown to be applied successfully to triaxial compression or extension scenarios, applications involving multiple stress paths were shown to capture failure behaviour poorly.

The introduction of critical state soil mechanics in the 1950s (Roscoe et al. (1958)) led to the development of the Cam-Clay model (Roscoe et al. (1963)). The model was originally meant to simulate the behaviour of near-normally consolidated clays under triaxial compression test conditions. The Cam-Clay model was soon revised using a modified flow rule which resulted in the Modified Cam-Clay model (Roscoe and Burland (1968)), which is still widely used in geotechnical applications to this day.

The Duncan-Chang model (Duncan and Chang (1970)), which is also known as the Hyperbolic model, introduced the concept of stiffness nonlinearity by considering Kondner's idea that the stress-strain curve in drained triaxial compression tests can be approximated by a hyperbola (Kondner (1963)) and Ohde's idea that soil stiffness can be formulated as a stress-dependent parameter using a power law (Ohde (1939)). Distinctions were also made between a stress-dependent primary loading stiffness and a constant unloading and reloading stiffness at a given confining pressure. Failure itself was still governed by the MC failure criterion.

Al-Tabbaa and Wood (1989) developed the 'Bubble' model, an extension of the Modified Cam Clay model and designed to capture more complex soil behaviour including softening, small-strain behaviour, and anisotropy. Stallebrass and Taylor (1997) further extended this model to develop a three surface of kinematic hardening (3-SKH) model, which incorporated the effects of recent stress history changes. The limitations and drawbacks of both models were reported by Grammatikopoulou (2004), who made further improvements by modifying the yield surface and flow rule.

Simpson (1992) developed an early computer model for elastic-plastic behaviour of London Clay, named the 'Brick' model, which incorporated small-strain stiffness nonlinearity. The model was used to back-analyse deep excavations in London Clay, with good agreement observed between the predicted and measured performance.

Whittle and Kavvadas (1994) later proposed the MIT-E3 soil model, a complex effective stress model that describes the rate-independent behaviour of normally and lightly overconsolidated clays. The model describes several important aspects of soil behaviour, including small-strain nonlinearity, anisotropic stress-strain-strength properties, and hysteretic behaviour due to cyclic loading. It has been validated through extensive comparisons between computed and measured effective stress-strain-strength behaviour in a variety of laboratory shear modes (Whittle et al. (1994b)). The model has been implemented into PLAXIS (Brinkgreve et al. (2022)) and ABAQUS (Abaqus (2020)) for predicting the performance of deep excavations (Whittle et al. (1994a), Hashash and Whittle (1996), Orazalin et al. (2015)).

Schanz et al. (1999) developed the Hardening Soil (HS) model in PLAXIS (Brinkgreve et al. (2022)), which uses three input soil stiffness values to define the variation of stiffness. The model also incorporates the stress dependency on soil stiffness and plastic straining due to primary deviatoric and compressive loadings. The HS-Small (HSS) soil model (Benz et al. (2009)) is an extension of the HS soil model and uses two additional parameters to better describe the

small-strain stiffness behaviour. Lim et al. (2010) evaluated the performance of the HS and the HSS soil models against measured field data from a deep excavation constructed at the Taipei National Enterprise Centre, finding very good agreement when using the HSS soil model. The HS model and HSS model are discussed in more detail later in this section.

Houlsby (1999) developed a soil model based on multi-surface plasticity which incorporates nonlinear small-strain stiffness, hysteresis, and soil stress history. The model was incorporated into OXFEM, a FE code developed at the University of Oxford, and has been used by several researchers in design analyses (Burd et al. (2000), Augarde and Burd (2001), Wisser et al. (2005), Dong (2014), Dong et al. (2016)). Potts et al. (2001) developed the nonlinear elasto-plastic Mohr-Coulomb model, which uses empirical equations derived from experiments in London Clay (Jardine et al. (1984)) to determine the nonlinear elasticity below the yield surface. It has been used frequently by the research group at Imperial College London as part of FE numerical analyses for designing deep excavations and tunnels (Franzius et al. (2005), Zdravkovic et al. (2005)). In recent years, the development of soil constitutive models has accelerated with advancements in computational methods and material modelling techniques.

Mohr-Coulomb model

The Mohr-Coulomb (MC) model is a simple and widely used linear elastic perfectly plastic model, which can be used as a first approximation of soil behaviour. In addition to the material unit weight γ, and the initial state soil parameters of overconsolidation ratio OCR, and at-rest lateral earth pressure coefficient K_0, calculated as:

$$K_{0(NC)} = 1 - sin\,\phi' \tag{2.7}$$

$$K_{0(OC)} = K_{0(NC)} \cdot OCR^{sin\,\phi'} \tag{2.8}$$

where $K_{0(NC)}$ and $K_{0(OC)}$ are the values of K_0 for normally consolidated and overconsolidated materials respectively, and ϕ' is the effective angle of friction, the model requires a total of five parameters, which are summarised in Table 2.1.

Table 2.1: Input parameters for the MC soil model.

Symbol	Description	Units
E	Young's modulus	kN/m^2
ν	Poisson's ratio	-
c	Cohesion	kN/m^2
ϕ	Friction angle	$^\circ$
ψ	Dilatancy angle	$^\circ$

In the plot of principal effective stress against principal strain in Figure 2.5, the linear elastic section is based on Hooke's law of isotropic elasticity, while the perfectly plastic section is based on the MC failure criterion. The MC failure envelope is typically defined using the effective strength parameters of effective cohesion c' and ϕ' as shown in Figure 2.6a. Alternatively, the cohesion parameter may be used to model the undrained shear strength s_u of the soil in combination with $\phi = 0$ as shown in Figure 2.6b. While the use of the effective strength parameters enables the change in shear strength with consolidation to be modelled, its value may deviate from s_u in reality due to a difference in the actual stress path being followed. The use of the total strength parameters when modelling enables direct control over the maximum available s_u.

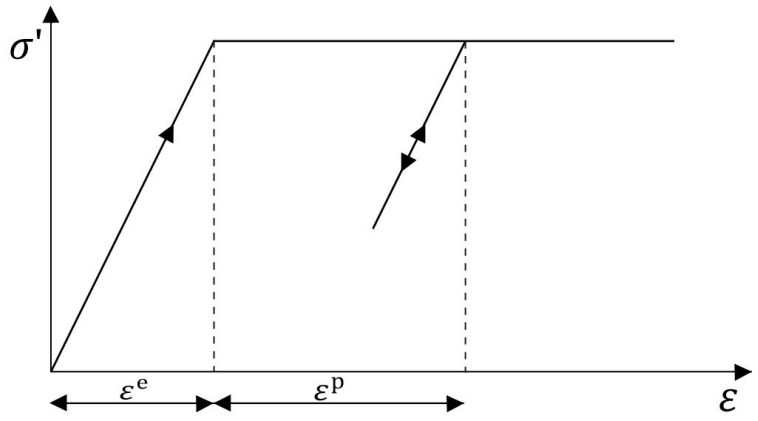


Figure 2.5: Principal effective stress against principal strain for a linear elastic perfectly plastic material (Brinkgreve et al. (2022)).

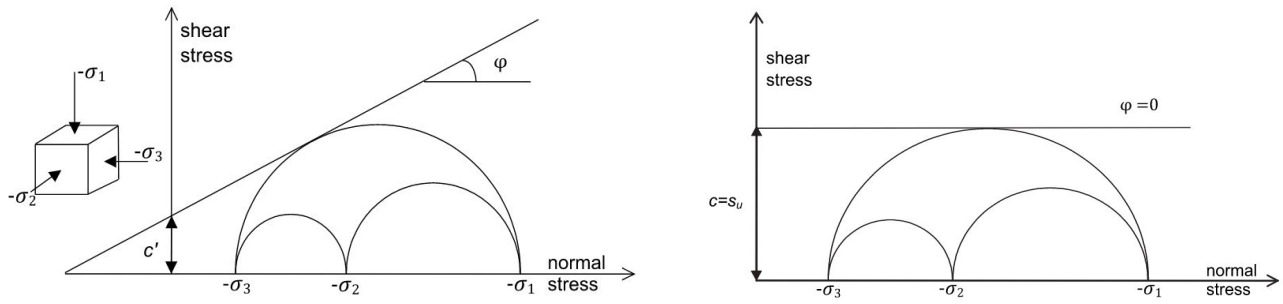


Figure 2.6: MC stress circles at yield using (a) effective strength parameters and (b) undrained strength parameters. (Brinkgreve et al. (2022))

Hardening Soil model

The Hardening Soil (HS) model is an advanced model for simulating the behaviour of both soft and stiff soils. When subjected to primary deviatoric loading, the material shows a decreasing stiffness (see Figure 2.7) and irreversible plastic strains develop simultaneously. The HS model deviatoric stress - axial strain relationship is modelled according to a power law with input parameter m, which supersedes the early Duncan and Chang (1970) hyperbolic relationship. Other characteristics of the HS model include plastic straining due to primary deviatoric loading (governed by secant stiffness E_{50}) and primary compression (governed by oedometric stiffness E_{oed}), elastic unloading and reloading (governed by unload-reload stiffness E_{ur}) and failure according to the MC failure criterion. In addition to the material unit weight γ, and the initial state soil parameters of overconsolidation ratio OCR and lateral earth pressure coefficients in Equation 2.7 and Equation 2.8, the HS model requires the input parameters listed in Table 2.2.

Direct parameter identification for the HS model requires the results of consolidated drained (CD) triaxial compression tests and oedometer tests performed on soil samples. A minimum of two CD triaxial compression tests are required at different confining pressures to determine the MC failure envelope. The stiffness moduli are determined from a CD triaxial compression plot of deviatoric stress against principle strain as shown in Figure 2.7. For this test the confining pressure should be approximately equal to the *in situ* vertical effective stress at the location

from which the soil sample was retrieved.

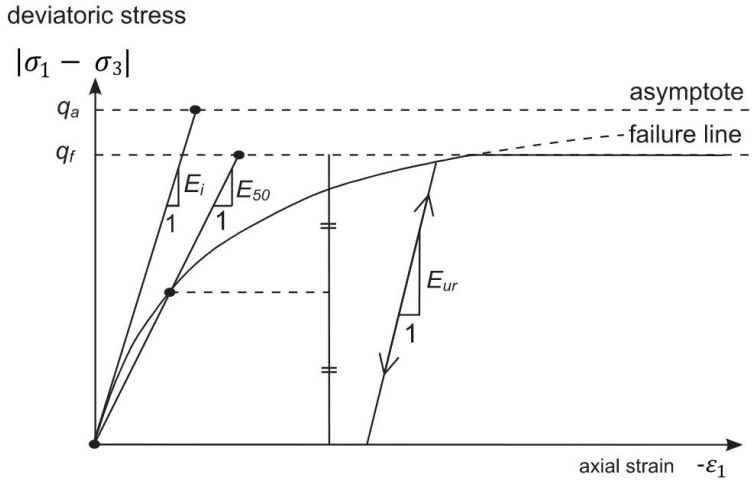


Figure 2.7: Stress dependent stiffness relation in primary loading for a standard drained triaxial test.(Brinkgreve et al. (2022))

Table 2.2: Input parameters for the HS soil model. Advanced parameters for which recommended value are typically taken are highlighted in bold.

Symbol	Description	Units
c'	Cohesion	kPa
ϕ'	Angle of friction	°
ψ	Dilatancy angle	°
E_{50}	Secant stiffness	kPa
E_{oed}	Oedometric stiffness	kPa
E_{ur}	Unloading/reloading stiffness	kPa
m	Power for stiffness stress dependency	-
ν_{ur}	**Unloading/reloading Poisson's ratio**	-
p_{ref}	**Reference stress for stiffnesses**	kPa
$K_{0(NC)}$	**Normally consolidated K_0**	-
R_{fa}	**Failure ratio**	-

Hardening Soil model with small-strain stiffness

Previous studies have highlighted the importance of stiffness degradation for soil-structure interaction scenarios at very small strain (Jardine et al. (1986), Burland (1989)). The accuracy of a numerical model therefore largely depends on the small strain characteristics of the chosen constitutive soil model. While the classical Mohr-Coulomb, Hardening Soil (Schanz et al. (1999)), Cam Clay (Roscoe et al. (1963)), and Modified Cam Clay (Roscoe and Burland (1968)) soil models have been used extensively to analyse deep excavation problems numerically, their inability to consider small-strain stiffness nonlinearity means they have been shown to generate

unusual ground movements and excessive basal heave.

With increasing strain amplitude, soil stiffness decays nonlinearly as shown in Figure 2.8. Plotting soil stiffness against the log of strain yields characteristicm S-shaped stiffness reduction curves. However, at the minimum strain which can be reliably measured in classical laboratory tests, the soil stiffness has typically already reduced to less than half of its initial value G_0 (Brinkgreve et al. (2022)). The Hardening Soil Small (HSS) soil model (Benz et al. (2009)) is an extension of the HS soil model and uses two additional parameters to better describe this small-strain stiffness behaviour. These are the initial shear modulus G_0, and the shear strain level $\gamma_{0.7}$ at which the secant shear modulus G_s has reduced to 72.2% of G_0. These additional parameters can be determined from *in situ* and laboratory seismic tests. The most frequently used relationship to model the stress-strain curve for small strains is that proposed in Hardin and Drnevich (1972), which describes the stress-strain behaviour using a simple hyperbolic law as:

$$\frac{G_s}{G_0} = \frac{1}{1 + 0.385\left|\frac{\gamma}{\gamma_{0.7}}\right|} \tag{2.9}$$

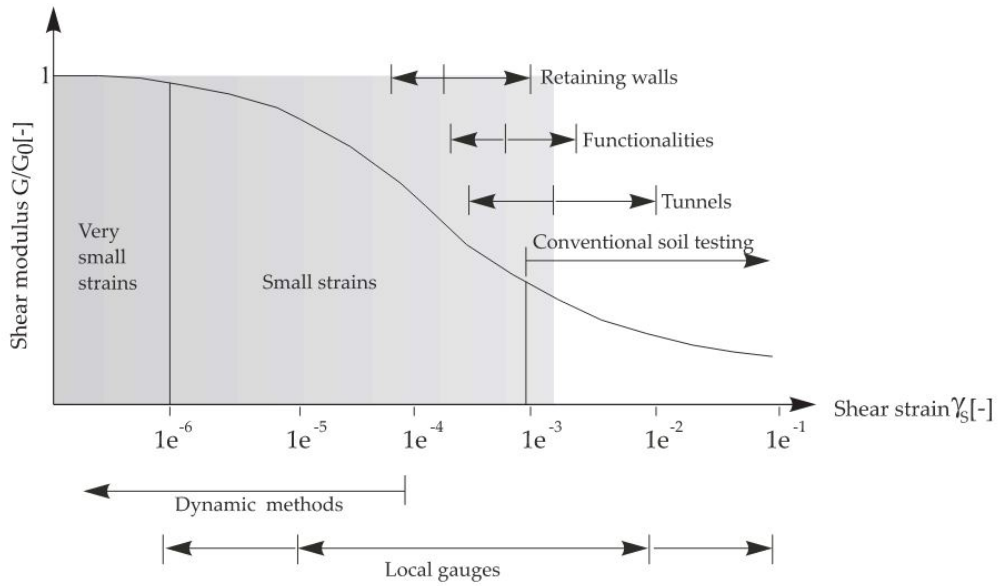


Figure 2.8: Characteristic stiffness-strain behaviour of soil with typical strain ranges for laboratory tests and structures (Atkinson (2000)).

2.6.2 Application to deep excavations

Previously published literature on the application of numerical methods to deep excavation design and analysis can be broadly divided into two categories. The first involves deep excavation behaviour prediction, where structural outputs predicted using numerical models and those measured in the field are compared. The second involves parametric analyses, where the influence of adjusting input parameters on structural outputs is assessed.

Deep excavation behaviour prediction

There are several examples in the literature involving the application of commercially available finite element packages such as PLAXIS 2D/3D (Brinkgreve et al. (2022)) and ABAQUS (Abaqus (2020)) to deep excavation design. These are typically associated with deep excavations constructed in soft and challenging ground due to the greater risks involved. Examples in the literature of comparisons between numerical models and field measurements for deep excavations include those in soft clays in Boston (Orazalin et al. (2015), Whittle et al. (2015)), Shanghai (Hou et al. (2009), Dong et al. (2016)) and Gothenburg (Karlsrud et al. (2006), Johansson and Sandeman (2014), Harlén and Poplasen (2019), Langford et al. (2021) and Tornborg et al. (2021)). While these cases provide useful references to evaluate the accuracy of numerical deep excavation models, additional cases involving different ground conditions and deep excavation wall types would be very beneficial to the industry. This is particularly important for deep excavations in the UK, as very few cases have been published due to company data protection policies and the high cost and challenges involved with field instrumentation installation.

Parametric studies

Deep excavation parametric studies are more prevalent in the published literature than detailed comparisons between field measurements and numerical calculations due to the reduction in cost achieved by avoiding the field monitoring altogether. Parametric analyses enable re-

searchers and designers to explore scenario forecasting and design optimisation in an affordable, safe environment. Examples of parameters considered in deep excavation parametric analyses include soil stratigraphy, soil properties, excavation geometry, structural parameters, groundwater flow parameters and construction sequences. The influence of excavation geometry on wall and ground movements is the most common component of parametric studies, with numerous examples in the literature. Ou et al. (1996), Hashash and Whittle (1996), Jen (1997), Roboski (2004), Blackburn (2005), and Finno et al. (2007) all investigated the effect of varying the excavation plan dimensions on lateral wall and vertical ground movements.

The influence of soil parameters on selected outputs is also a popular topic in the literature due to the inherent uncertainties associated with soil as a material. Soil parameters explored include lateral earth pressure coefficient (Potts and Fourie (1984), Powrie and Li (1991), Dong et al. (2016), Harlén and Poplasen (2019)), overconsolidation ratio (Hashash and Whittle (1996), Jen (1997), and Harlén and Poplasen (2019)) and soil stiffness (Powrie and Li (1991), Johansson and Sandeman (2014), Dong et al. (2016), and Schwamb (2014)). The influence of the selected soil constitutive model on wall and ground movements is also a popular topic. While the use of the MC model by Johansson and Sandeman (2014) and Schwamb (2014) provided first order estimates of ground and wall movements, the amplitudes of basal heave and lateral wall deflection were shown to be overestimated when compared to the use of the HS model. There are also cases of more complex constitutive models being used to accurately predict behaviours, such as the application of the MIT-E3 model to deep excavations in Boston Blue Clay (Whittle et al. (1994a), Hashash and Whittle (1996), Whittle et al. (2015), Hashash and Whittle (2002), (Orazalin et al. (2015)).

2.6.3 Probabilistic uncertainty analyses

Probabilistic modelling involves incorporating uncertainty and variability into the analysis of systems. Probabilistic approaches are commonly employed for geotechnical engineering applications, due to the inherent uncertainty and variability associated with soil and rock as materials.

Soil and rock variability is influenced by a number of factors, including stress history, pore fluid pressures and physical and chemical environmental changes. The use of several uncertainty analysis approaches have been reported in previously published literature for geotechnical applications. These approaches include the random field (Nguyen and Likitlersuang (2021), Zhang et al. (2022)), point estimate (Valley et al. (2010), Sekhavatian (2018)), random sets (Schweiger and Peschl (2005), Momeni et al. (2018)) and Monte Carlo (MC) simulation (Arabaninezhad and Fakher (2021), Bozkurt and Akbas (2023)) methods.

Of the listed uncertainty analysis methods, the MC simulation method is most frequently employed to analyse uncertainty in systems and has been used to perform probabilistic analyses for embankments (Cho (2007), Akbaş (2015), Jiang et al. (2015), Deliveris et al. (2022)), tunnels (Schweiger et al. (2007), Sheil et al. (2022)) and deep excavations (Sekhavatian (2018), Momeni et al. (2018), Arabaninezhad and Fakher (2021), Bozkurt and Akbas (2023)). Selected uncertain input parameters are modelled as random variables with probability distributions, before being randomly sampled for a system model simulation, from which the computed system output is recorded. The process is repeated many times to provide the range of possible output values and their associated probabilities. Statistical analyses can then be performed on the output probability distribution to inform design decisions. The simulation should be repeated a sufficient number of times to provide a representative system output probability distribution. In practise, determining the necessary simulation number to achieve this is often an iterative process (Phoon (1995)). While the application of the MC simulation method to FE system models is computationally expensive, it can effectively provide predictions of system behaviour (Arabaninezhad and Fakher (2021), Bozkurt and Akbas (2023)). Simplified representative surrogate FE models can be used to reduce the computational demands (Phoon (1995)). While several examples of the application of probabilistic approaches to analyse uncertainty in deep excavation behaviour predictions are provided above, none of these involve deep excavations

constructed in the UK or in soft ground , or deep excavations supported by combi-walls, and the number of examples are few in comparison to the number of deep excavation numerical model publications. Therefore, the literature points to a lack of probabilistic uncertainty analysis examples for deep excavation numerical models.

Prior to analysing uncertainty using the MC simulation approach, a sensitivity analysis should be performed. A sensitivity analysis provides a quantitative characterisation of the sensitivity of the model results to variations in the model input parameters. The purpose of the sensitivity analysis is to make an initial determination of the most influential input parameters to be included in the detailed MC uncertainty analysis. Sensitivity analyses are typically performed using the US Environmental Protection Agency TRIM sensitivity method (McKone (1999)). Sensitivity simulations are performed by varying each input parameter by plus and minus a small fixed percentage Δp. Firstly the sensitivity ratio η_s for each input parameter is calculated, which is defined as the relative change in the selected model output $f(x)$ to a relative change in the selected input parameter x:

$$\eta_s = \frac{\left(\frac{f(x_{L/U})-f(x))}{f(x)}\right)}{\left(\frac{x_{L/U}-x}{x}\right)} \tag{2.10}$$

where $f(x_{L/U})$ is the system response obtained by assigning the lower or upper bound of the selected range $x_{L/U}$ for each input variable and $f(x)$ is the system response obtained using the reference value for each input x. The sensitivity score η_{ss} is then calculated to normalise η_s:

$$\eta_{ss} = (\eta_{s,xL} + \eta_{s,xU})\frac{(x_L - x_U)}{x} \tag{2.11}$$

where $\eta_{s,xL}$ and $\eta_{s,xU}$ are the values of η_s for the lower value x_L and upper value x_U of the selected input variable range respectively. Finally, the relative sensitivity α is calculated for n input parameters:

$$\alpha(x_i) = \frac{\eta_{ss,i}}{\sum_{i=1}^{n} \eta_{ss,i}} \tag{2.12}$$

Input parameters with a value of α above a set threshold are considered to be the most influential

and are selected for a more detailed uncertainty analysis.

Prior to performing MC simulations to analyse soil property uncertainty, the most influential input parameters must be modelled as random variables with probability distributions. The main soil parameters represented as random variables with statistical distributions in previously published literature are angle of friction ϕ, cohesion c, undrained shear strength s_u, and stiffness modulus E_{50}. Each parameter is typically modelled using a lognormal distribution with mean μ and standard deviation σ, as this distribution best represents soil parameters that can only take positive values (Bozkurt and Akbas (2023)). In previously published literature, the degree of variability is more commonly reported as the coefficient of variability COV, which is calculated as:

$$COV = \frac{\sigma}{\mu} \tag{2.13}$$

Suggested COV values reported in literature for the geotechnical parameters ϕ, c, s_u and E_{50} are presented in Table 2.3.

Table 2.3: Summary of reported COV values for selected geotechnical parameters.

	COV (%)			
Reference	c	s_u	ϕ	E_{50}
Lumb (1974)	30	-	9	-
Kennedy (1979)	-	-	-	2-42
Harr (1987)	13-40	13-40	2-13	-
Kulhawy (1993)	13-40	13-40	7.5	-
Phoon (1995)	-	30	9	2-42
Cho (2007)	20	-	10	-
Orr and Farrell (2012)	20	-	10	-
Jiang et al. (2015)	-	30	-	-
Sekhavatian (2018)	10	-	3	-
Nguyen and Likitlersuang (2021)	-	40	-	-

2.7 Field case histories

Monitoring the behaviour of deep excavations in the field is primarily carried out to ensure the structure is performing within safe limits, and to provide live feedback to site personnel to inform the construction process. Additionally, the data collected can be contributed to

databases to verify and refine existing empirical design methods, and develop new ones. The observed performance of deep excavations constructed with diaphragm and secant pile walls, particularly in soft clays, has been a popular topic in the literature and dominates deep excavation field case histories, e.g. in Shanghai (Liu et al. (2005), Liu et al. (2011), Ng et al. (2012), Tan and Wei (2012)), in Chicago (Finno et al. (2002), Finno and Calvello (2005), Finno et al. (2015)), in Boston (Olsen (2001), Hewitt et al. (2003), Whittle et al. (2015)), in Taiwan (Ou et al. (1993), Ou et al. (1998), Ou et al. (2000), Wu et al. (2013)), and in the UK (Wood and Perrin (1984), Simpson (1992)). These case histories all vary in geological conditions and construction methods making comparisons between them difficult. However, they provide resources for calibrating numerical analyses and for understanding the more comprehensive behaviour of deep excavations. The uniqueness of each case history can also be valuable for the interesting site specific construction challenges, such as the complex excavation work for the construction of the Massachusetts Institute of Technology Campus (Orazalin et al. (2015)) and deep excavation works in the historical centre of Rome (Masini et al. (2021)).

Cases reporting the use of sheet pile retaining walls are relatively scant in comparison to those for in-situ walls. While recent research has significantly advanced understanding, insights are specific to Chicago (Finno et al. (1988), Finno et al. (1989), Finno and Calvello (2005), Finno et al. (2019)) and Gothenburg soft clays (Johansson and Sandeman (2014), Tornborg et al. (2021), Langford et al. (2021)). Typically, the reported behaviour includes wall deformations, prop loads, ground settlements, and pore water pressure measurements. The former two parameters are discussed below in more detail, as these are most relevant to the field monitoring work that was carried out at the PROTOS energy-from-waste (EFW) facility for this research.

2.7.1 Wall deformations

Lateral wall deflections are typically the primary concern when constructing a deep excavation, and are monitored in almost all field cases. The profile of deflected shape can be influenced by several factors, including wall type, support structure selection, construction method and

ground conditions. Wall deflections are typically measured with inclinometers, which can be portable and inserted manually into casings positioned on or within the wall, or in-place and automatically record measurements at specified time intervals.

In addition to the wall deformations reported in the individual deep excavation case histories listed previously, several researchers have collated databases comprising several hundred case histories, categorising these based on wall type and ground conditions. Long (2001) compiled a database of over 300 case histories, reporting horizontal deflections of walls divided into four categories based on support type and ground conditions. It was found that for $FOS_{BH} > 3$, the measured maximum wall deflections are largely influenced by the proportion of soft ground retained by the wall. It was also found that observed cantilever wall deflections are typically independent of the system stiffness S. Maximum wall displacement averages and recommended limits for each category were presented, with values normalised by the excavation depth.

Moormann (2004) compiled a database of over 500 international case studies, predominantly in soft clays. The studies were categorised by ground conditions and retaining wall type. Horizontal movements in soft clays showed a wide scatter but reported wall movements were typically less than 1% of the excavation depth (H), whilst cases in stiff clays were typically less than $0.4\%H$. Moormann (2004) also reported that the maximum lateral wall displacement is typically observed at the excavation depth, with 67% of cases having maximum values at depths between $0.5H$ and $1.0H$.

Wang et al. (2010) reported the wall movements of over 300 deep excavation case studies in soft soils in Shanghai. Mean values of maximum lateral displacement for different wall types and construction methods are presented. A significant average of $1.5\%H$ was observed for sheet pile walls, whilst that for *in situ* BU walls was found to be $0.4\%H$.

Observed maximum wall deflections relating to excavations in London Clay are presented by St John et al. (1992), Carder (1995) and Fernie and Sucking (1996). St John et al. (1992)

and Fernie and Sucking (1996) both reported an average maximum wall displacement value for top-down construction methods of $0.15\%H$, which is consistent with the average reported by Long (2001) of $0.16\%H$ for walls retaining largely stiff soils. The average for cantilever walls of $0.4\%H$ reported by St John et al. (1992) is consistent with the observations reported by Long (2001) for cantilever walls embedded in stiff soils. There are several general trends for the reported wall deflections:

- The wall initially deflects as a cantilever about the embedded toe prior to the installation of the upper propping mechanism.
- Adjustments of raw inclinometer data must be made to account for any translation of the retaining wall toe, which has been observed in the field (Simpson (1992)).
- The wall deflections measured closest to the corners of an excavation are typically smaller than those measured at the wall centre due to corner effects (Roboski (2004)).
- Wall deflection increases with excavation progression, with the vertical position of maximum lateral displacement progressing downwards close to the level of the excavation.
- Wall deflections may continue once formation has been reached, at a reduced rate, due to the dissipation of pore water pressure, as observed by Liu et al. (2005).

2.7.2 Prop loads

Monitoring of deep excavation prop loads is important to ensure the stability of deep excavations by reducing the risk of collapse and to collate data to validate and optimise numerical models. Prop loads have been shown to be influenced by ground conditions, excavation geometry and depth, groundwater levels and the construction sequence (Potts and Fourie (1984), (Boone and Crawford (2000)). Prop loads can be computed from strain gauge measurements, using a rosette layout around a steel prop, or a grid array in permanent slabs, to capture the axial loads and bending moments experienced.

Temperature effects are an important consideration, particularly in props with restrained ends, where thermal expansion and contraction can induce significant loads. Ignoring these

effects can lead to overstressing of prop members, or even failure of the support system. Bono et al. (1992) presented the performance of an internally braced diaphragm wall in Boston which experienced significant seasonal warming, resulting in overstressing of the strut members. Similarly, Zhang and Yao (2005) found that temperature effects in bracing structures caused incidents during the construction of several deep foundations in China.

Early empirical based design guidance on the issue was presented by Chapman et al. (1972), who evaluated earth and temperature induced loads in a braced excavation in Washington D.C. An empirical expression relating temperature dependent loads to the elastic modulus of the retained earth was developed. However, it was noted in Chapman et al. (1972) that a significant difference was observed between the initial elastic modulus measured by plate load tests, and that back-calculated from strut loads, highlighting the need for further research in this area. Boone and Crawford (2000) adjusted the empirical equations developed by Chapman et al. (1972) by incorporating case history data from a subway construction in glacial till, but found they were overestimating the temperature induced prop loads by $\sim 23\%$. Hashash et al. (2003) provided a further extension to this method, to incorporate the importance of the construction sequence selected, and validated this against a deep excavation case history in Boston and against numerical analyses.

Although the CIRIA C517 guide (Twine and Roscoe (1997)) provides valuable case data for temperature effects on bracing supporting sheet pile walls, they make up only 5 of 81 cases, as many don't provide details on prop load changes caused by temperature or cannot isolate temperature effects from other load changes. Gaba et al. (2017) proposed that the thermally induced load could be calculated using a factor representing the percentage degree of restraint of the prop FF, whose value is based on back-analysis of field case histories by Richards et al. (1999), Powrie and Batten (2000) and Chambers et al. (2016). The method suggests a level of restraint $FF = 50\%$ for stiff walls in stiff soils and $FF = 30\%$ for stiff walls in soft soils.

While this has led to the industry adopting a more consistent approach for incorporating prop temperature effects into design, only four main case histories have been used to select these values, and no guidance is provided for excavations supported by more flexible sheet pile walls and combi-walls.

A more thorough estimation of the restraint factor can be made on a case-by-case basis, by measuring the induced load during a period of no excavation or adjacent construction activity, and correlating this with the temperature measured by the thermistors in the strain gauges. Powrie and Batten (2000) obtained a restraint factor value of 59% during an 88-day period with no construction activity occurring, and minimal pore pressure variation, for a braced secant pile wall in stiff ground. This is in good agreement with the range of 40% - 60% quoted by Twine and Roscoe (1997) for stiff walls in stiff ground. However, this method relies on collecting prop data during an extended period of minimal construction activity, which is uncommon. Also, instrumentation must be present to ensure changes are not due to fluctuations in pore water pressure.

Wu et al. (2019) proposed a more complex empirical approach, which considers the interaction between temperature induced prop loads and the deformation of the retained soil, using Winkler's soil spring model. The case histories reported by Chapman et al. (1972) and Powrie and Batten (2000) were used to validate the approach, with the calculated values showing good agreement with those measured in the field, giving slightly conservative estimates. The temperature induced prop loads were found to be higher at lower-level bracings. This conclusion is consistent with that reported by Powrie and Batten (2000).

2.8 Fibre optic monitoring

The use of fibre optic (FO) sensing in civil engineering is a relatively new technology that owes its development to the invention of the laser and the low-loss optical fibre, which were initially driven by the telecommunications industry in the 1960s. The past 20 years has seen the

emergence of FO strain sensing, which uses the principles of FO light reflection and scattering as a tool to provide continuous strain profiling, which helps to determine rotations, deformations and other non-uniformly distributed soil-structure interaction forces. These problem areas can be missed when using conventional, discrete strain sensing instruments, such as vibrating-wire or metal foil strain gauges. Single fibre lengths have the potential to replace thousands of discrete strain sensing instruments, greatly simplifying the installation of the monitoring system. Unlike traditional electrical strain gauges, FO sensors are immune to electromagnetic interference, and can be used in high voltage environments. Fibre materials are also highly resistant against corrosion and can remain fully operational for several decades.

There are several FO sensing techniques that are relevant to strain sensing applications, including:

- Fibre Bragg sensors, which are short interference gratings that can be used to determine mechanical strain and temperature changes at discrete points along the fibre, by measuring the shift in the reflected Bragg wavelength at each grating.
- Distributed fibre optic detection (DFOS) systems, which use the fibre itself as the sensor (as opposed to discrete gratings). The backscattered light spectrum produced due to the deformation of the fibre by temperature or strain changes can be inferred by appropriate instruments. The spectrum contains three main components: Rayleigh scattering, Raman scattering, and Brillouin scattering. Strain sensing focuses on systems based on Brillouin scattering.
- Extrinsic Fabry-Perot interferometers (EFPIs), which can be used as discrete sensing points.

Fibre Bragg sensors and DFOS systems are the technologies most applicable to civil and geotechnical monitoring. Since variations in either temperature or mechanical strain can cause a shift in Bragg wavelength (for Fibre Bragg systems) or in Brillouin frequency (for DFOS

systems), it is necessary to distinguish between these two effects. One method of achieving this involves using a secondary temperature compensation fibre length positioned adjacent to the primary fibre. The secondary fibre can be positioned within a gel filled loose tube, to isolate it from any mechanical strain, or arranged such that sections of the fibre remain slack, by forming small loops positioned next to strained primary fibre regions. The former method is commonly adopted in the field, due to its ease of installation, and the protection to the fibre provided by the casing, and has been applied to monitor strains in tunnel linings (Beck et al. (2016)), in piles (Bell et al. (2013)), and in diaphragm wall segments (Schwamb et al. (2014)).

There are numerous case histories reporting the use of DFOS systems to monitor structural performance. Preliminary pile load tests in the UK have been monitored with DFOS systems by Vorster et al. (2006), Pelecanos et al. (2017) and Pelecanos and Soga (2018). The systems have also been used on existing pile foundation to prove the suitability of the piles for reuse (Bell et al. (2013)), and on energy piles to study the effect of thermal load (Bourne-Webb et al. (2009), Amatya et al. (2012), Bourne-Webb et al. (2013)). DFOS systems have been utilised in deep excavation construction to monitor secant pile walls (Mohamad et al. (2011)) and diaphragm wall segments (Schwamb et al. (2014), Nejjar et al. (2021)). It has also been applied to tunnelling monitoring, in an old tunnel to monitor the effect of proximity tunnelling (Mohamad et al. (2010)), and for monitoring strain in a concrete sprayed tunnel lining (De Battista et al. (2015)). The system has also been used to monitor the stability of embankments (Janmonta et al. (2008)).

Case histories involving the use of Fibre Bragg systems for geotechnical monitoring are scant in comparison, but there are cases of the technology being applied to monitor structural bridge health (Alavie et al. (1995), Chan et al. (2006)), and being applied to monitor marine structures (Mieloszyk et al. (2021)) and wind turbine blades (Park et al. (2011)).

2.9 Summary and gaps in knowledge

The literature review highlights the complexities involved when analysing soil-structure interaction for deep excavations. Monitoring the performance of diaphragm and secant pile walls has been a popular topic in the literature. However, case histories involving the use of cofferdams are few in comparison. There is a clear need to collect more high quality field data during the construction of cofferdams, particularly for those constructed in UK soft soils, and those using combi-wall cofferdams. This will enhance the database on which empirical methods are based, widening the calibration space, and enabling their use for the verification and refinement of design methods. The literature also points to a distinct lack of observations on the thermal performance of bracing frame structures supporting flexible walls in soft ground. The significant uncertainty surrounding the degree of restraint makes the influence of temperature very difficult to accurately quantify. The literature review also highlights a need for further research into numerical modelling of deep excavations, to improve the reliability of predictions, again for UK soft soils and for combi-wall cofferdams. High quality field data is essential for validating numerical base analyses, which can then be used for parametric studies to perform "what-if" scenario forecasting in a safe virtual environment. Also, the inherent uncertainties associated with soil as a material and the typical lack of high quality site investigation data mean that there are still significant uncertainties surrounding input parameters for design. This highlights a need for additional probabilistic uncertainty analyses to complement numerical model predictions and inform design decisions.

3 | Field testing and instrumentation setup

3.1 Introduction

To assess deep excavation performance during construction, a full-scale field monitoring project was carried out on a live construction site. The field monitoring project had three main focuses. Firstly, the live monitored data provided real-time feedback to inform decision making on site at key construction stages and provided a proactive approach to risk mitigation and management on site. Secondly, the field data can be compared to existing empirical methods to determine whether these can be reliably extended to the given scenario. Finally, well documented field data provide a valuable resource with which numerical analyses can be validated or refined. Though advanced numerical analyses are an effective tool to investigate deep excavation behaviour, their capacity to replicate observed performance in the field must be evaluated through validation against field data. Using the monitored data to refine design procedures could result in cost savings and increased efficiency by optimising support systems, improving soil characterisation and reducing over-design. The following sections introduce the field monitoring project at PROTOS Energy-from-Waste (EFW) Facility and describe the instrumentation components that comprised the employed monitoring scheme.

3.2 Project description

3.2.1 Project overview

The construction works described in this paper form part of the PROTOS EFW project in Chester, UK. The facility is designed to process over 400,000 tonnes of non-recyclable waste per annum to produce up to 49 MW of electrical power. The proposed site is situated on marshland, close to the Manchester Ship Canal and the River Mersey, as shown in Figure 3.1. A key aspect of the project involved the construction of a 40 m long, 18 m wide underground

waste storage bunker. Construction of the underground bunker section began with a 12 m deep excavation in May 2021 and was completed in March 2022 by Ward & Burke Construction Ltd.



Figure 3.1: PROTOS EFW Facility location in Chester, UK. Site boundary shown in red.

3.2.2 Ground conditions

Three main ground investigation (GI) schemes were undertaken at the site prior to construction in 2018, 2020 and 2021. The 2018 scheme comprised site-wide cable percussive boreholes, groundwater monitoring and geotechnical laboratory tests. The 2020 scheme comprised 15 site-wide cone penetrometer tests (CPTs) including 4 seismic CPTs (SCPTs), to provide interpreted soil parameter profiles to be used with the borehole data for design purposes. The layout of the 2018 boreholes and 2020 CPTs and SCPTs with reference to areas of the PROTOS EFW facility is shown in Figure 3.2. The 2021 site investigation comprised an additional 12 CPTs around the perimeter of the proposed bunker excavation, as shown in Figure 3.3.

The raw 2021 CPT measurements and selected inferred parameters are shown in Figure 3.4.

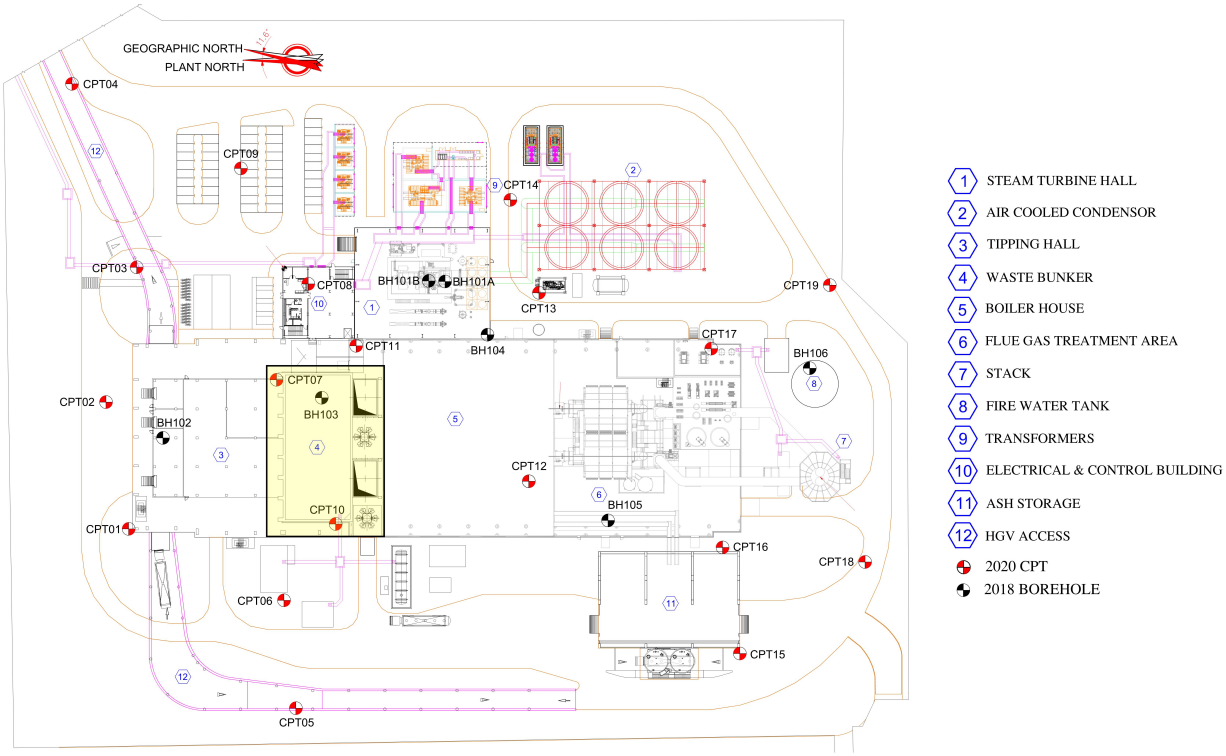


Figure 3.2: Schematic plan of PROTOS EFW Facility with layout of 2018 boreholes and 2020 CPTs. Bunker area highlighted in yellow.

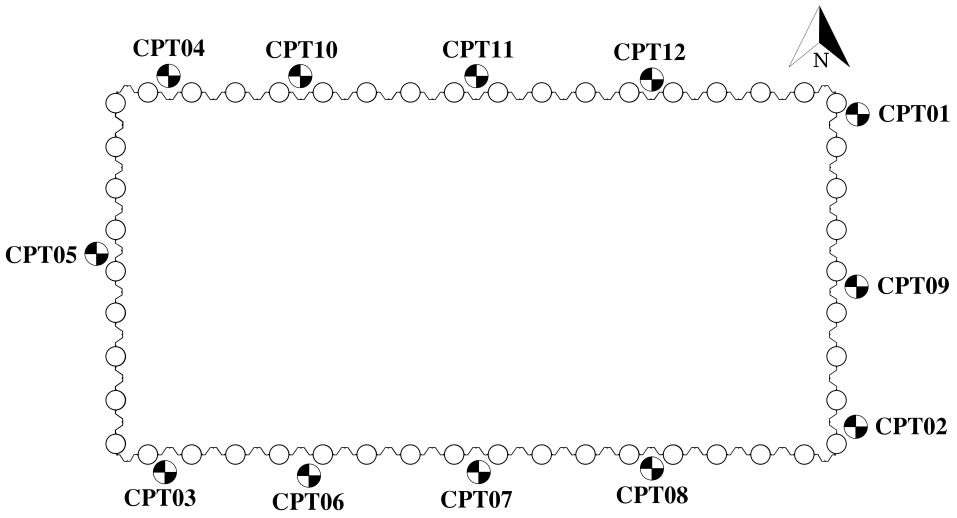


Figure 3.3: Plan view of excavation showing 2021 CPT locations and proposed excavation wall.

The inferred undrained shear strength s_u and angle of friction ϕ' were used with the borehole data to deduce the ground stratigraphy around the bunker perimeter as shown in Figure 3.5. The stratigraphy can be summarised as follows; a 1 m thick layer of made ground (MG) overlies tidal flat deposits (TF) which extend to 12 m below ground level (BGL). The TF deposits are predominantly very low strength silty clay with two bands of low strength fibrous peat (P) at 1.0 m – 1.8 m and 9.6 m – 10.3 m BGL. Below $\sim$ 12 m, there is a $\sim$ 7 m thick layer of glacial outwash (GO) deposits which consist of medium dense sands with some gravels. Beneath the outwash deposits lies glacial till (GT) consisting of a 4 m thick layer of stiff, sandy clay (C) with localised silt bands, followed by dense, silty, fine sand containing bands of sandy clay. The measured pore water pressure u closely matches the estimated hydrostatic pore pressure profile, particularly in the coarse-grained soils. From 0 m – 10 m BGL, measurements exceed the hydrostatic calculation, indicating the presence of normally to lightly overconsolidated clays. In contrast, measurements between 20 m – 25 m BGL are indicative of moderately to highly overconsolidated materials.

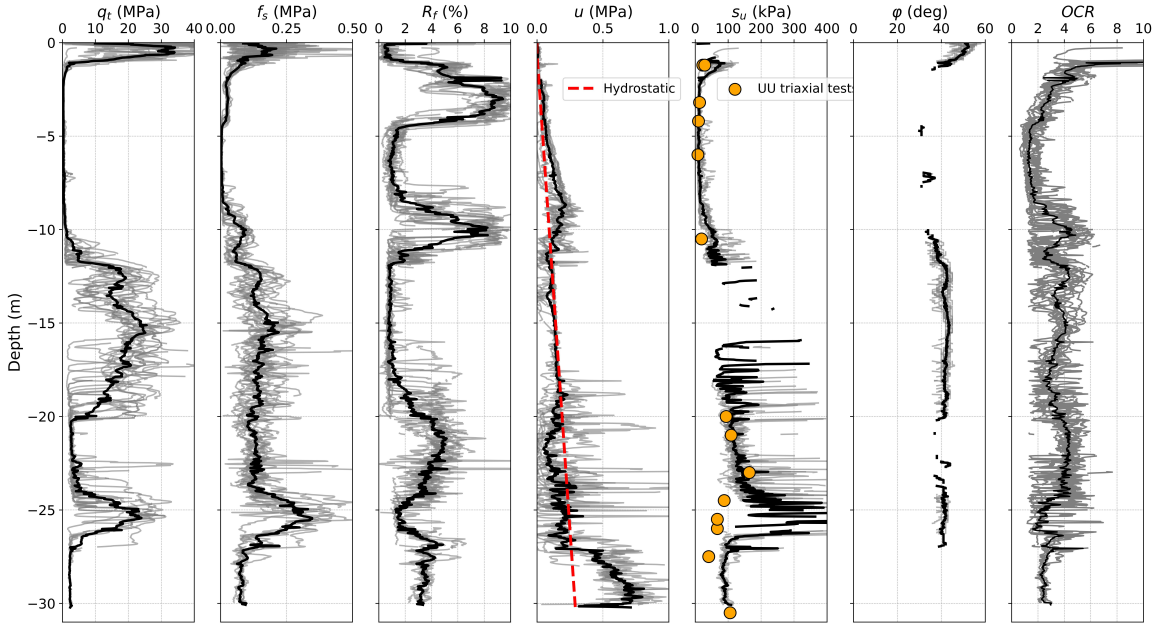


Figure 3.4: Raw CPT measurements and selected inferred soil properties from the 2021 CPTs around the bunker perimeter (see layout in Figure 3.3). Undrained shear strength data from 2018 unconsolidated undrained (UU) laboratory triaxial compression tests are also presented. Grey lines indicate individual CPTs whereas black lines denote the mean of all CPTs.

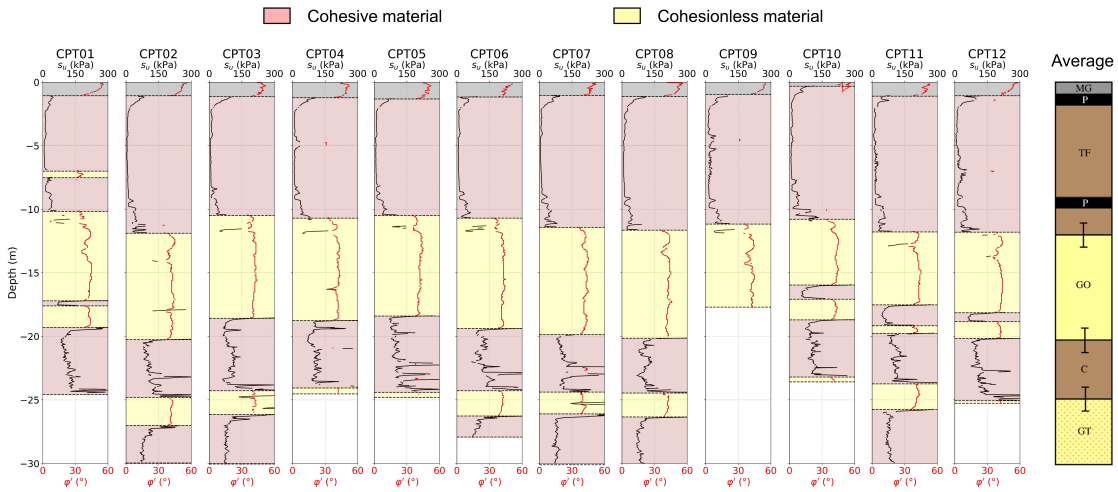


Figure 3.5: Ground stratigraphy around bunker perimeter inferred from 2021 CPT s_u and ϕ' and boreholes.

The undrained shear strength s_u, was determined using the relationship:

$$s_u = \frac{q_t - \sigma_{v0}}{N_{kt}} \tag{3.1}$$

where N_{kt} is the empirical cone factor. A value of $N_{kt} = 20$ was determined by fitting results from 14 unconsolidated, undrained (UU) triaxial compression tests. This value is in good agreement with those calibrated for other UK soft soils in Highbridge (Nkt = 19) (Royston (2018)) and in Hull (Nkt = 20) (Allievi et al. (2018)). The angle of friction of the soil ϕ', was calculated as follows (Kulhawy and Mayne (1990)):

$$\phi' = 17.6 + 11 \ln q_{t1} \tag{3.2}$$

where q_{t1} is the stress normalised cone resistance defined as:

$$q_{t1} = \frac{\left(\frac{q_t}{\sigma_{atm}}\right)}{\left(\frac{\sigma'_{v0}}{\sigma_{atm}}\right)^{0.5}} \tag{3.3}$$

where $\sigma_{atm} = 101.3$ kPa is the reference atmospheric stress and σ'_{v0} is the in-situ vertical effective stress.

Four of the 2020 CPTs in Figure 3.2 included *in situ* seismic testing: CPT10, CPT11, CPT12 and CPT17. The results of the seismic testing for that closest to the bunker area, CPT10, are shown in Figure 3.6. The measured shear wave velocity V_s, is compared to that inferred from the standard CPT measurements using the method in Robertson (2009), which estimates V_s

as a function of q_t and the soil behaviour type index I_c. The small strain shear modulus is calculated according to:

$$G_0 = \rho \cdot V_s^2 \tag{3.4}$$

where ρ is the soil density.

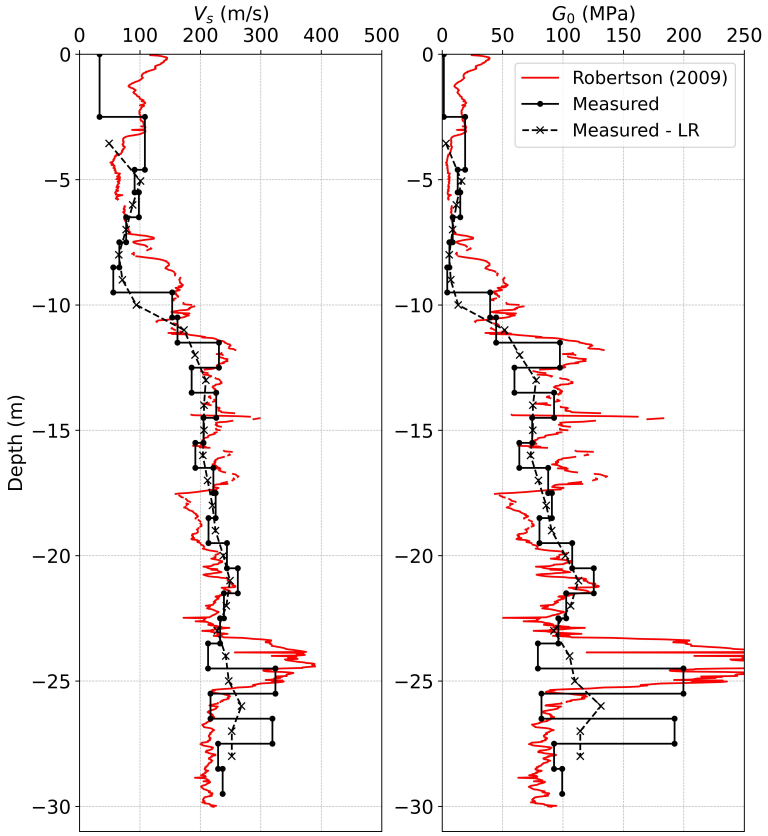


Figure 3.6: Measured shear wave velocity V_s, and inferred small strain shear stiffness G_0, from 2020 CPT10 seismic testing, with estimates from standard CPT data interpretation plotted for comparison (using the method in Robertson (2009)). The measured data are also plotted using a 3-interval linear regression (LR) model, which estimates the linear relationship between depth and inferred G_0 using a moving 3-point window.

Results from a series of laboratory density and index tests are presented in Figure 3.7, along with a depth profile of density inferred from the CPT data using the method in Robertson (2010) for comparison. The index data are plotted on a combined linear-log scale to highlight the considerable variability observed in the TF layer, which is indicative of the presence of bands of peat. Density and index tests performed on samples taken from the lower clay layer suggest a higher degree of uniformity, with density and plasticity remaining approximately

constant. The site water level was measured to vary between 0 m – 0.75 m BGL using four piezometers installed to a depth of 15 m, likely due to the proximity of the excavation to the River Mersey Estuary.

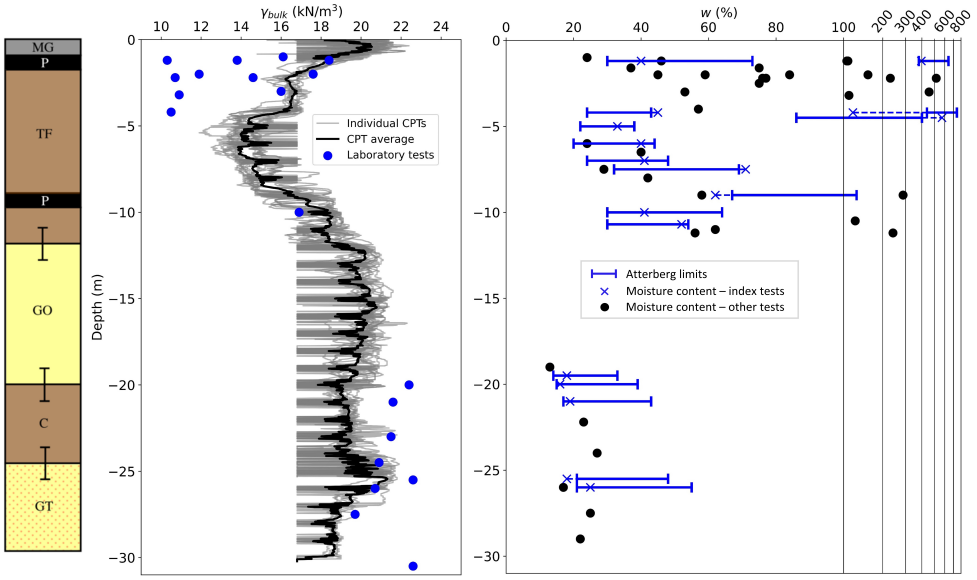


Figure 3.7: Data from density and index tests performed on soil samples in 2018 GI scheme. The density tests are compared to the density profile inferred from CPT data using the method in Robertson (2010). The index tests are plotted on a combined linear-log scale.

3.2.3 Construction sequence

The construction timeline is broken into 17 different construction stages as summarised in Table 3.1; schematic illustrations of the key stages during construction are shown using sections through the bunker in Figure 3.8. Prior to cofferdam installation, precast concrete piles were driven around the bunker area, to act as foundations for adjacent RC building slabs (see Figure 3.9). A bottom up construction sequence was adopted, with two levels of propping mechanisms used to support the excavation. A driven steel temporary works cofferdam was chosen for excavation support instead of *in situ* concrete due to concerns over potential losses of cement fines in the weak clay and peat layers. To minimize ground movements a combi-wall, comprising alternate tube and sheet piles, was used. The piles were driven to a depth of 21 m into the GT clay layer to minimize seepage into the excavation, with AZ28 sheet pile pairs subsequently driven between each tube (stage 2). The C9 clutches connecting the tube and

sheet piles were coated with bitumen to reduce water ingress into the excavation. A bracing frame structure (shown in Figure 3.10b) was assembled and positioned at ground level to be used as a guide for the cofferdam installation.

Table 3.1: Summary of PROTOS deep excavation and underground bunker construction sequence.

Stage	Construction works	Activity	Start date	End date	Duration (days)
1	Bunker excavation	Central frame assembly	11-05-21	18-05-21	7
2		Cofferdam installation	18-05-21	09-06-21	22
3		Excavate tube piles & concrete	14-06-21	17-06-21	3
4		Initial excavation below frame	17-06-21	20-06-21	3
5		Capping beam construction	18-06-21	09-08-21	52
6		Dewatering well installation	09-08-21	23-08-21	14
7		Top prop installation	15-08-21	31-08-21	16
8		Excavation phase 1	01-09-21	10-09-21	9
9		Central frame positioning	10-09-21	21-09-21	11
10		Excavation phase 2	21-09-21	29-09-21	8
11	Bunker piling	Piling bunker foundation slab	08-10-21	02-11-21	25
12	Bunker construction	Bunker base construction	02-11-21	25-11-21	23
13		Central frame removal	29-11-21	06-12-21	7
14		Bunker wall pour 1 construction	06-12-21	20-12-21	14
15		Bunker wall pour 2 construction	06-01-22	24-01-22	18
16		Top prop removal	31-01-22	03-02-22	4
17		Bunker wall pour 3 construction	03-02-22	25-02-22	22
		Underground waste bunker construction	**11-05-21**	**25-02-22**	**290**

The tube piles were then internally augered to 6.3 m BGL and filled with concrete to prevent local buckling at frame level 2 as shown in Figure 3.8a (stage 3). Following installation of the cofferdam, the bracing frame was lowered by excavating to a depth of 1.5m BGL to enable the area to be backfilled and create a working platform (stage 4). A 1.2 m thick RC capping beam was constructed around the perimeter of the cofferdam (Figure 3.8b) (stage 5), connected to the cofferdam using UC members partially cast into each tube. The cofferdam was supported by two sets of internal bracing at the levels shown in Figure 3.8e; a plan view of the top level 1 (0.6 m BGL) and lower level 2 (5.75 m BGL) bracings is shown in Figure 3.10a and Figure 3.10b respectively. Table 3.2 presents key properties of each structural member of the cofferdam and frame.

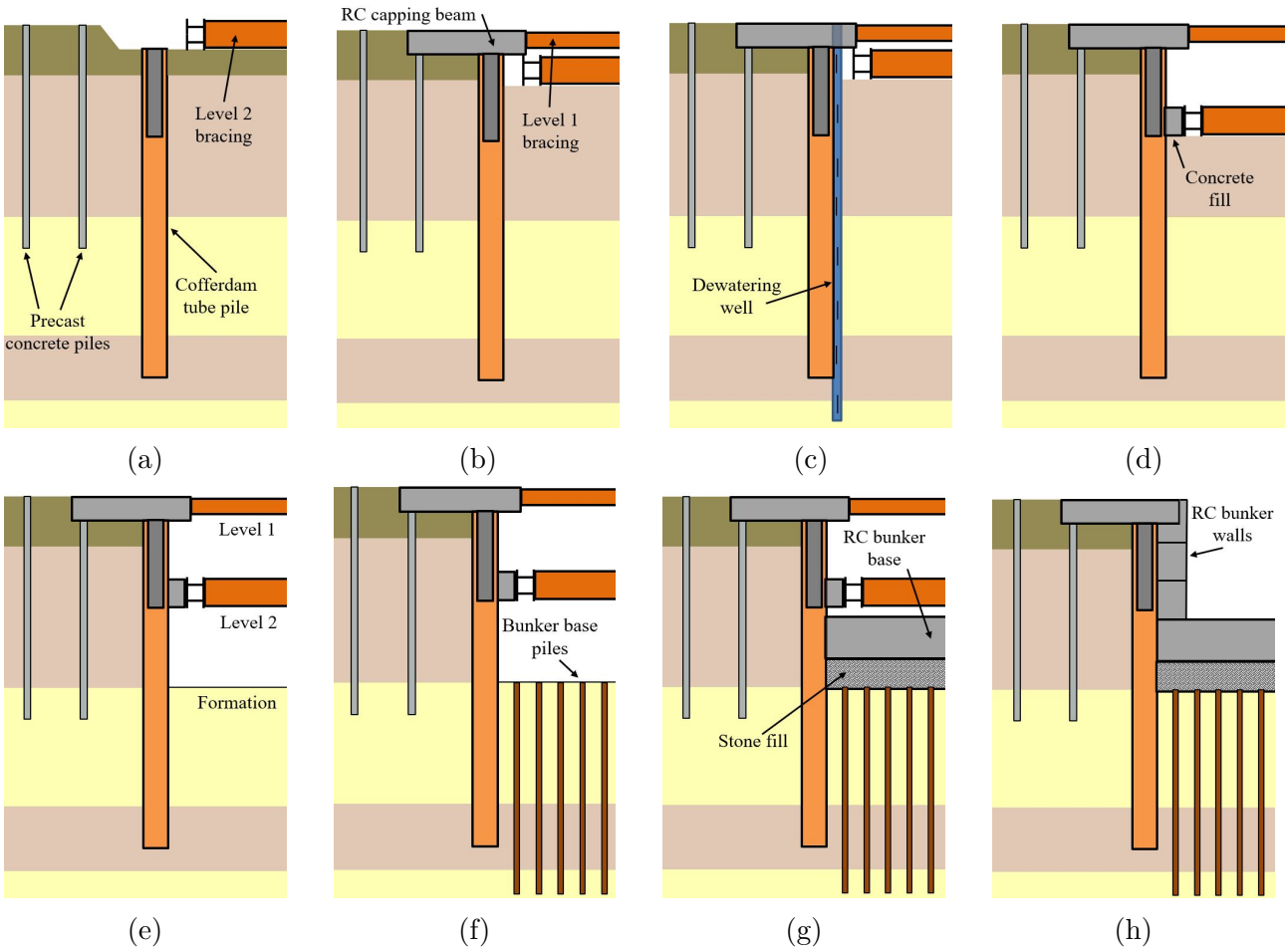


Figure 3.8: Typical section through excavation wall at key stages of the construction sequence: (a) stage 3, (b) stage 5, (c) stage 6, (d) stage 9, (e) stage 10, (f) stage 11, (g) stage 12, (h) stage 17.

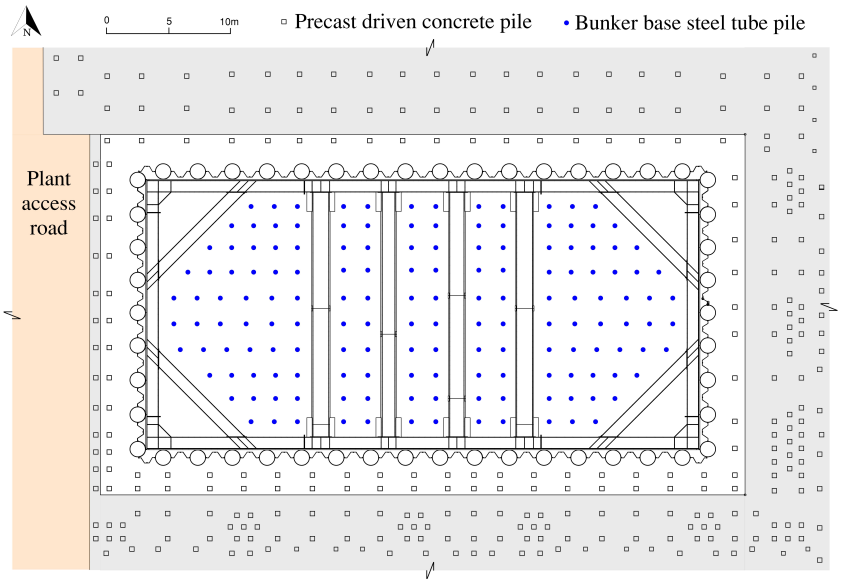
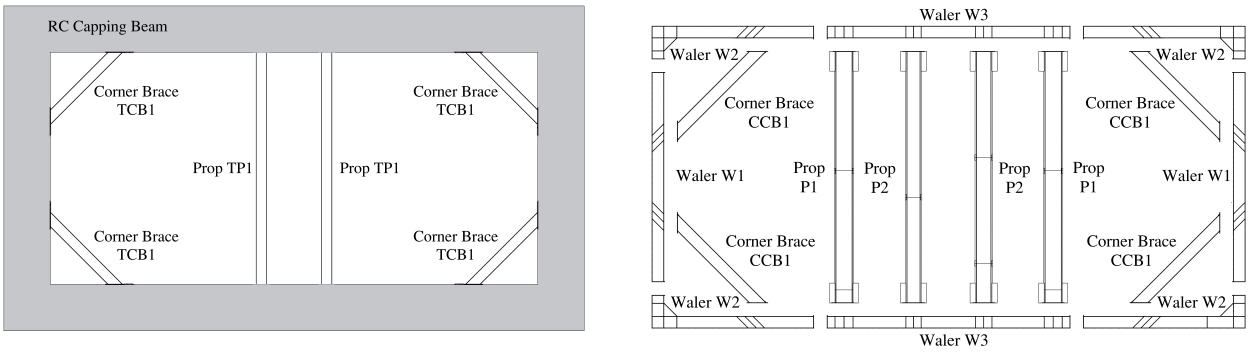


Figure 3.9: Plan view of the excavation showing the layout of RC precast piles for adjacent slab foundations and steel tube piles for the bunker base foundation; level 2 bracing shown for illustrative purposes.



(a) (b)

Figure 3.10: Schematic illustration of the plan view of the bracing arrangement and member loads for (a) level 1 (top) and (b) level 2 (lower).

Table 3.2: Member properties for excavation steel components.

Member type	**Label**	**Section geometry**	**Length (m)**	**Cross-sectional area, A (cm^2)**	**Elastic modulus, Z (cm^3)**
Perimeter waler	W1	Double 914/419/343 UB	15.84	874	27,452
	W2	Double 914/419/343 UB	12.23, 2.5*	874	27,452
	W3	Double 914/419/343 UB	18.36	874	27,452
Corner brace	CCB1	Double 914/419/343 UB	6.67	874	27,452
	TCB1	Double 914/419/343 UB	6.90	874	27,452
Central tube	P1	Tube: $OD = 1425$mm, $t = 22$mm	19.02	970	33,495
	P2	Tube: $OD = 1220$mm, $t = 20$mm	19.02	754	22,255
	TP1	Tube: $OD = 914$mm, $t = 20$mm	19.94	562	12,286
Cofferdam	-	Tube: $OD = 1220$mm, $t = 22$mm AZ28 sheet pile pairs	21.00	-	9513**

*L-shaped waler, length of each section provided
**Combined tube and sheet pile Z

Dewatering was carried out using internal wells, installed to a depth of 25 m BGL (Figure 3.8c) (stage 6), after which excavation commenced and the upper level 1 bracing was installed (stage 7). Excavation was paused to install the lower level 2 bracing frame at 5.75 m BGL (Figure 3.8d) (stage 9). Three types of end connection were employed between frame members in the level 2 bracing:

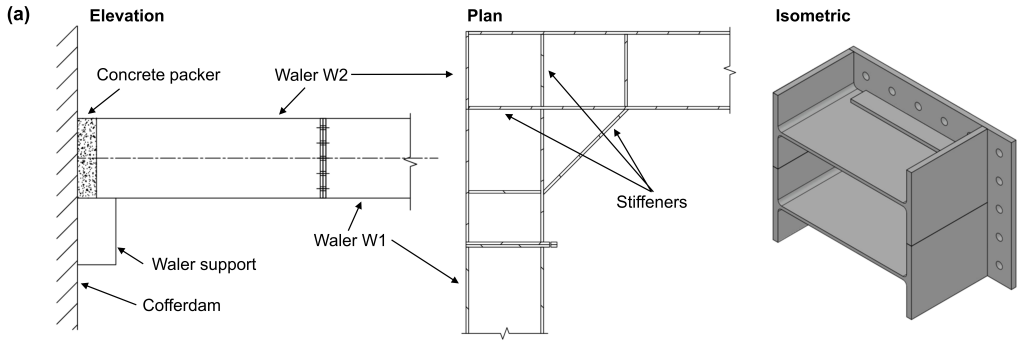
1. Waler-to-waler C1 connection comprised 15 grade 10.9, 39 mm diameter bolts connected

through flanged plates welded to the end of each member (Figure 3.11a).

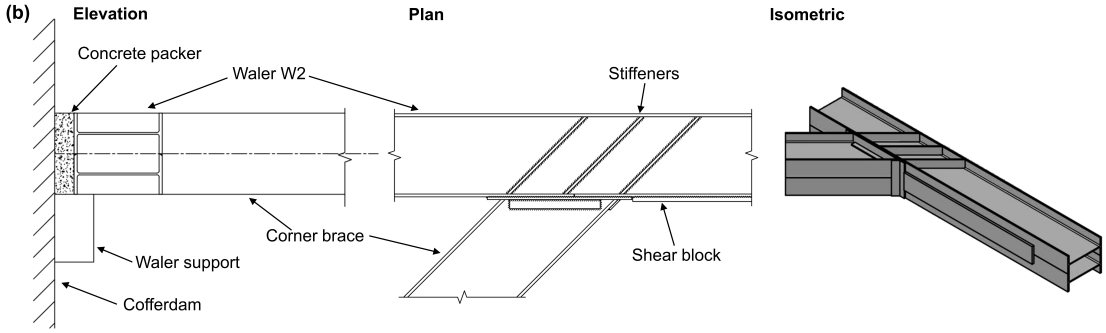
2. Corner brace-to-waler C2 connection comprised welds along either side of the corner brace endplate (Figure 3.11b).
3. Central tube-to-waler C3 connection comprised a steel L-section welded to the central tube endplate and positioned on top of the waler beam. UC sections were welded along the side of each central tube to stiffen the connection and to aid the transfer of load between members (Figure 3.11c).

The second and final excavation phase (to a depth of 12 m BGL) was then completed (stage 10). The formation depth ensured that the RC bunker base was founded on the GO silty sand deposits. Construction of the 2 m thick RC base began by installing 156 13 m long, 350 mm diameter steel tubal piles (stage 11), driven vertically from formation depth over the plan area of the excavation (see Figure 3.8f and pile layout in Figure 3.9). To increase the excavation level to that of the base underside, a layer of stone fill was installed. A waterproofing bentonite liner was installed onto the base underside and internal cofferdam surfaces to improve the watertightness of the bunker structure. The 2000 m^3 base pour took place across an eight-hour period prior to a subsequent curing period (Figure 3.8g) (stage 9). Key properties for the base concrete mix are summarised in Table 3.3. The level 2 bracing structure was then removed (stage 12/13) before bottom-up (BU) construction of the 1.5 m thick RC bunker walls using a one-sided hydraulic climbing formwork structure. Each wall pour had a height of 3 m, with three wall pours required to complete the underground section of the bunker (Figure 3.8h). The level 1 bracing was removed following the second wall pour. Photographs of the excavation at 8 different construction stages are presented in Figure 3.12.

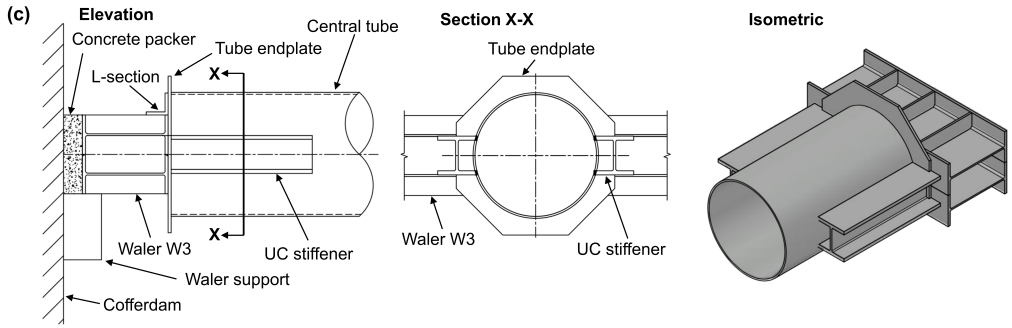
The construction of the 21 m high bunker superstructure followed the completion of the underground bunker section. A simplified construction timeline for the bunker superstructure is summarised in Table 3.4. Eight wall pours were required to construct the 1 m thick bunker



(a)



(b)



(c)

Figure 3.11: Schematic illustrations of the member end connection detail for (a) C1 connection, (b) C2 connection and (c) C3 connection.

superstructure walls using a modified two-sided hydraulic climbing formwork (stage S1). Following wall pour 4, the bunker was filled with water to preload the bunker structure for an 11-week period to accelerate the process of consolidation induced settlement (stages S2 and S3). The water was filled to just below to a depth of 15 m from the top of the bunker base to

Table 3.3: Summary of base concrete properties.

Strength class	C40/50
DC class	DC-2
Cement type	CIIIA+SR
Min. cement content (kg/m^3)	340
Cement content (kg/m^3)	380
Max. water/cement ratio	0.5
Water/cement ratio	0.46
GGBS proportion (%)	50
Target consistency	S4



(a) (b) (c)

(d) (e) (f)

(g) (h)

Figure 3.12: Photographs of the excavation and bunker structure during construction: (a) stage 3, (b) stage 5, (c) stage 6, (d) stage 9, (e) stage 10, (f) stage 11, (g) stage 12, (h) stage 17.

just below openings in the north wall for waste deposition truck access. Following the completion of the bunker superstructure walls and bunker preloading, connections were constructed between the bunker and the adjacent boiler building to the south (stage S4). The connections were formed intermittently over a period of several months. The dewatering system was decommissioned during this period (stage S6). Photographs of the bunker during the preloading phase and following superstructure completion are presented in Figure 3.13. The description of the bunker superstructure construction process allows the long-term monitored wall bending moment data in section 4.5.2 to be interpreted with reference to site construction activities.

Table 3.4: Summary of bunker superstructure construction sequence.

Stage	Construction activity	Start date	End date	Duration (days)
S1	Bunker superstructure walls	26-02-22	10-06-22	104
S2	Bunker filling	05-05-22	27-05-22	23
S3	Bunker preloading	27-05-22	12-08-22	78
S4	Bunker to boiler building connections	20-06-22	10-12-22	174
S5	Bunker emptying	12-08-22	23-08-22	12
S6	Dewatering system decommissioning	30-08-22	31-08-22	2
	Waste bunker superstructure	**26-02-22**	**10-12-22**	**288**



(a) (b)

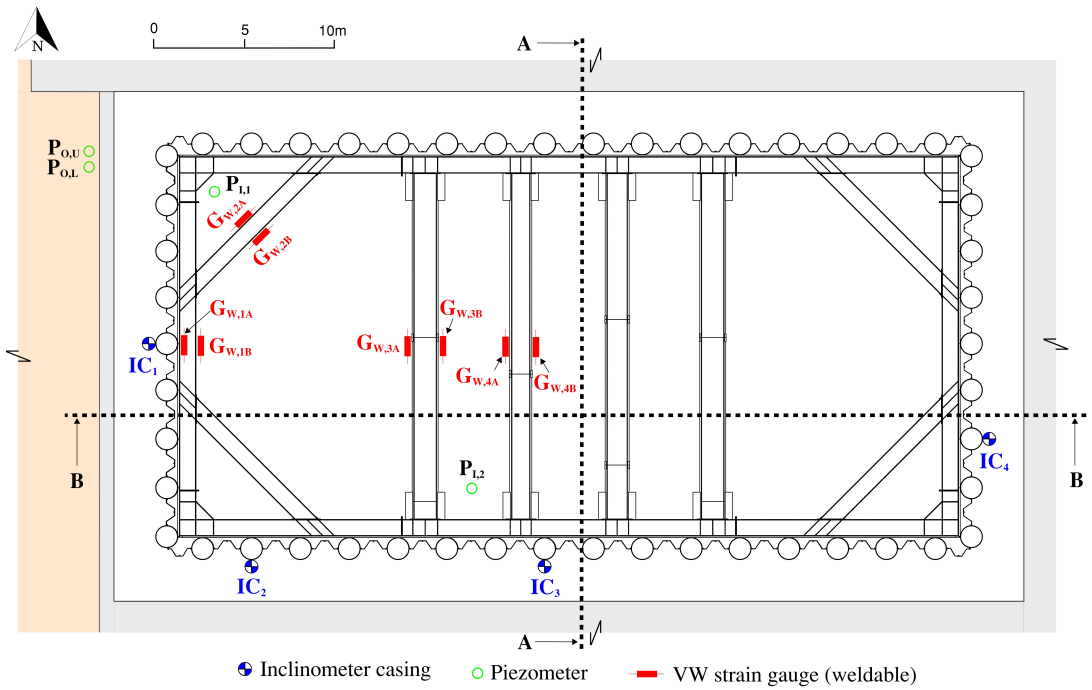
Figure 3.13: Photographs of the bunker superstructure (a) during preloading and (b) following wall construction.

3.3 Instrumentation plan

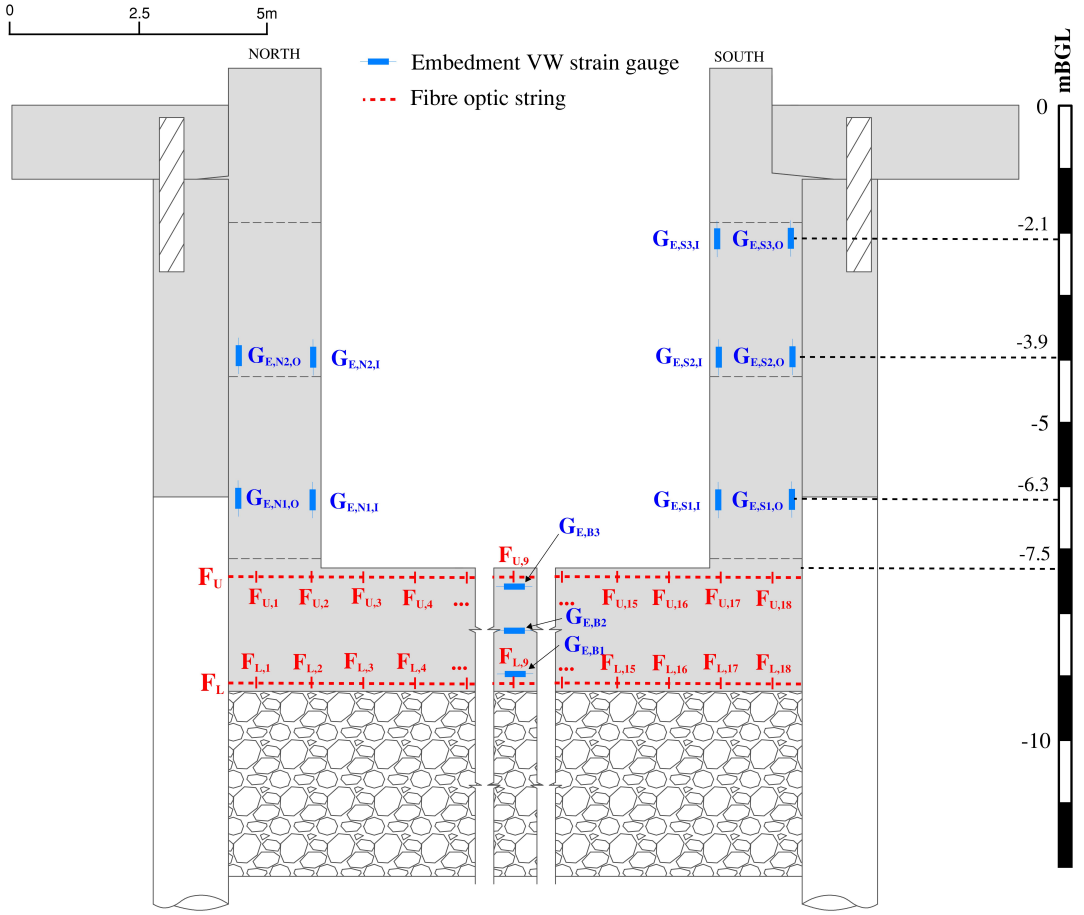
The adopted instrumentation setup for the excavation and bunker construction processes are shown in Figure 3.14 and are summarised in Table 3.5 along with their notation. The information obtained included cofferdam pile deflections, prop member axial loads and bending moments, RC bunker base and wall strains and temperatures, and water level monitoring data. Video monitoring was undertaken using time-lapse cameras positioned around the site and drones, operating once a week. All data were displayed in real time on a bespoke online platform developed by Dr Zhandos Orazalin as shown in Figure 3.15. This was made accessible to site personnel via tablets and computers. The information was used to inform decisions made by the site team at critical construction stages. The monitored data were continuously compared to trigger levels for "early warning" and "work stoppage" limits determined from the excavation design calculations. If exceeded, email and text message alerts were to be automatically distributed to the site engineering team.

Table 3.5: Deep excavation and RC bunker instrumentation summary.

Measurement	**Sensor type**	**Quantity**	**Notation**
Horizontal wall deflections	Portable inclinometer	4	IC
Prop axial loads and bending moments	Weldable vibrating wire (VW) strain gauge	8	G_w
RC bunker base strains and temperatures	Fibre optic Bragg grating (FBG) - bottom	18	F_L
	Fibre optic Bragg grating (FBG) - top	18	F_U
	Embedment VW strain gauge	3	G_E
RC bunker wall strains and temperatures	Embedment VW strain gauge	10	G_E
Water levels - inside and outside of bunker	Piezometer	4	P



(a)



(b)

Figure 3.14: (a) Plan layout of instrumentation used during excavation, taken through level 2 bracing. (b) Section A-A showing RC bunker base and wall instrumentation.

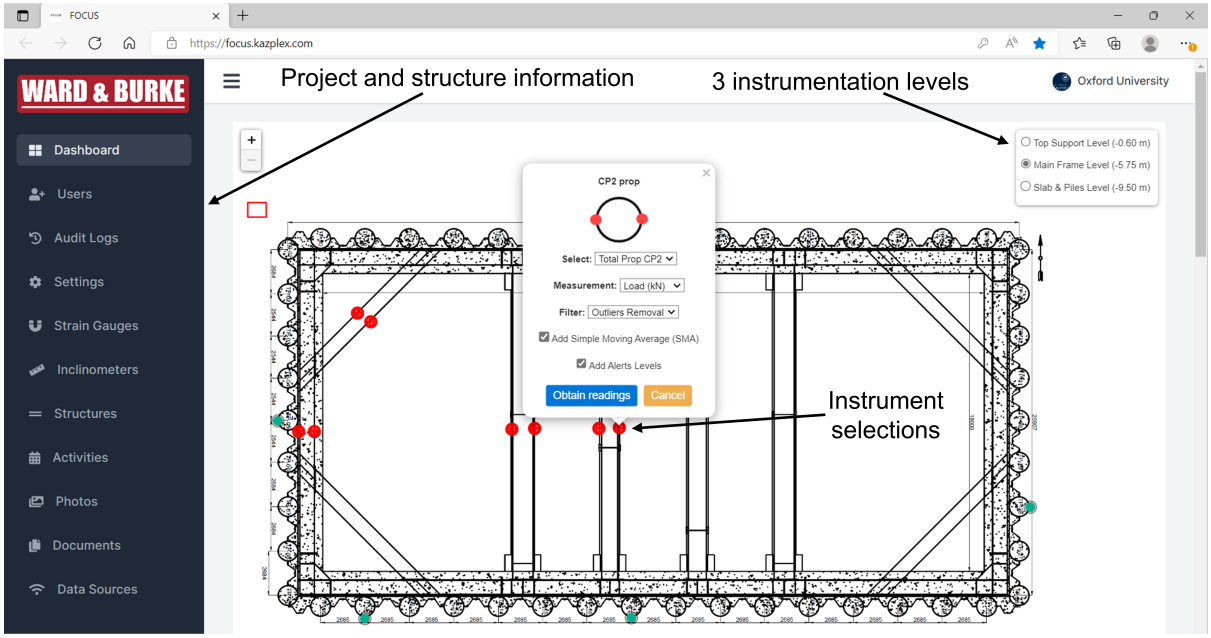
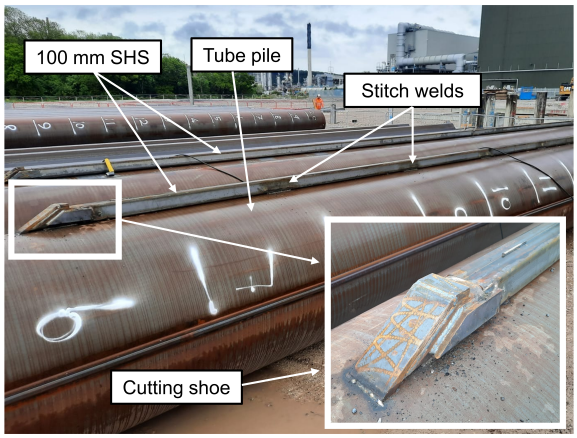


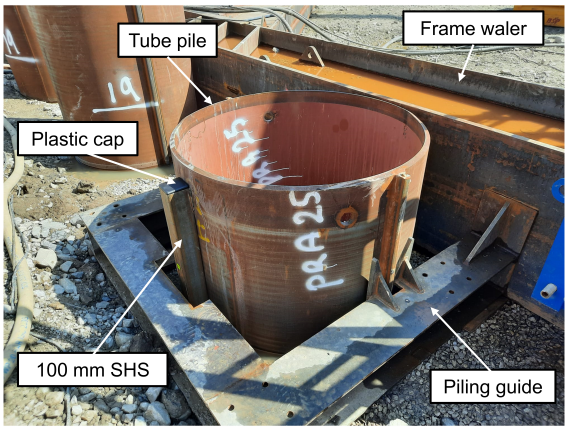
Figure 3.15: Online dashboard used to present and analyse data in real-time.

3.3.1 Inclinometers

The lateral deflection of the cofferdam was monitored using a portable MEMS inclinometer, in casings installed on four of the tube piles (IC_1 – IC_4) as shown in Figure 3.14a. Each 15 m long casing was installed in a void formed by stitch welding a 100 mm SHS length with a tapered cutting base to the tube piles before installation. The void was continued up through the capping beam and access was provided through cast in covers. Prior to casing installation, pumping at the base of the void was necessary to remove fine soil particles that had entered during tube pile installation. Each casing was held within the void using a single size 1 mm filter sand. Measurements were taken in an axis both parallel and perpendicular to the cofferdam wall, at 0.5 m intervals starting from the bottom of the casing. Measurements were taken 2-3 times a week during excavation and piling works, and weekly outside of these periods. Corresponding excavation level surveys were taken using a Trimble total station at the time of each inclinometer measurement. Photographs of the installation process and inclinometer instrument are shown in Figure 3.16.

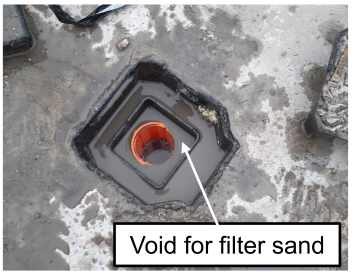


(a)



(b)







(c)



(d)

Figure 3.16: Photographs of inclinometer casing installation process: (a) SHS section installation, (b) tube pile installation, (c) casing installation within void. (d) Photograph of inclinometer instrument.

3.3.2 Weldable VW strain gauges

The intention at the instrumentation planning stage was to monitor the loads in the level 1 and level 2 bracing members, and to utilise the quarter-symmetry of the excavation to reduce the instrumentation requirements. To obtain axial loads and lateral bending moments, two vibrating wire (VW) strain gauges were tack welded to a level 1 corner brace (TCB1) and tube prop (TP1) and each of the four instrumented level 2 members as shown in Figure 3.14a. Base readings were taken using a GEOSENSE VWR1 readout immediately following gauge

installation and also following prop removal. Protective covers were tack welded over each gauge following installation. Initially, the VW gauge cables were routed along the support structures into an enclosure containing three Soil Instruments eight-channel VWlog8 GPRS dataloggers. The enclosure was powered by a GEOSENSE WI-SOS 480 solar panel kit and data were transmitted every 5 minutes to an online server to be displayed on the dashboard. Photographs of the VW gauge installation process and logging systems are shown in Figure 3.17.

Strains were determined from the measured frequency, f, as follows:

$$\mu\varepsilon = \frac{1}{1000}(f^2 \cdot C_G \cdot C_B) \tag{3.5}$$

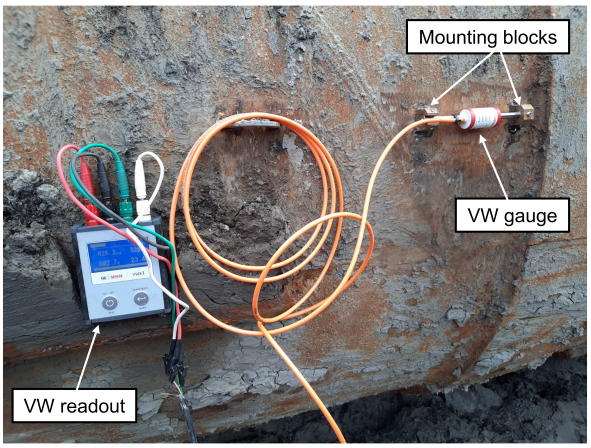
where C_G and C_B are the calibration factors for the gauge type and batch respectively. The average axial prop load, F, and bending moment, M, were subsequently calculated as:

$$F = \frac{(\mu\varepsilon_A + \mu\varepsilon_B)}{2}EA \tag{3.6}$$

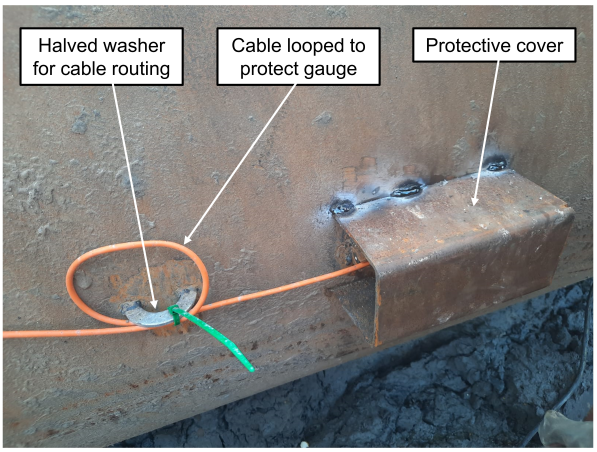
$$M = \frac{(\mu\varepsilon_A - \mu\varepsilon_B)}{2}EZ \tag{3.7}$$

where Z, E and A are the elastic modulus, Young's modulus (taken as 210 GPa for steel) and cross-sectional area of the member considered respectively, and subscripts 'A' and 'B' denote the microstrain measurement on either side of a given member.

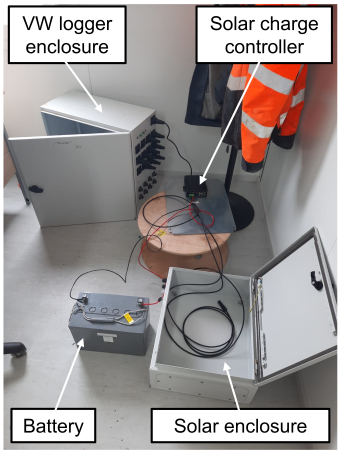
During excavation phase 1, issues with the data loggers and power supply to the enclosure meant that the initial load development data for the monitored level 1 props were lost. Two of the four gauges were also damaged by a suspended boat skip as shown in Figure 3.17f. The decision was taken to focus on monitoring loads in the level 2 bracing frame, for which much larger loads were predicted during design, and to use the lessons learned from the problems encountered during the initial level 1 prop monitoring to inform the later level 2 frame monitoring. At this stage, the data logging system was replaced with five battery powered GEOSENSE WI-SOS 480 vibrating wire nodes which transmitted data to the server via a 4G Gateway Cloud device located in the site office. This addressed the power supply and data logging issues.

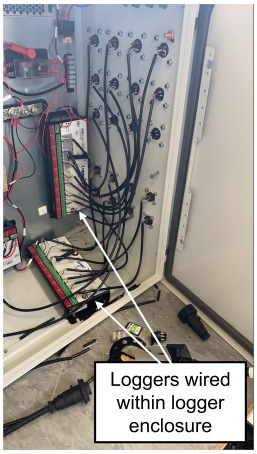


(a)

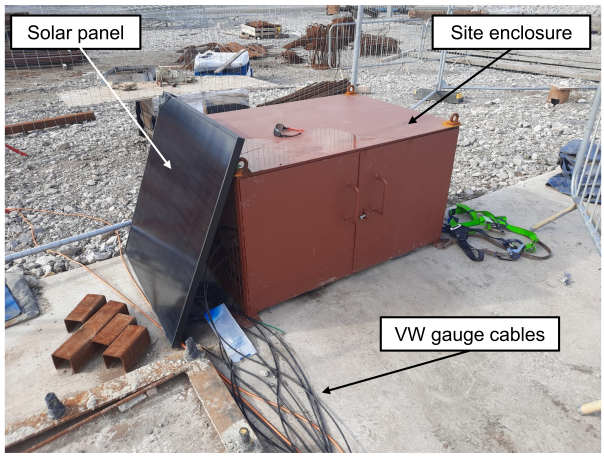


(b)

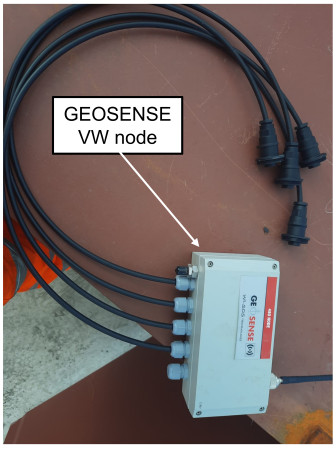


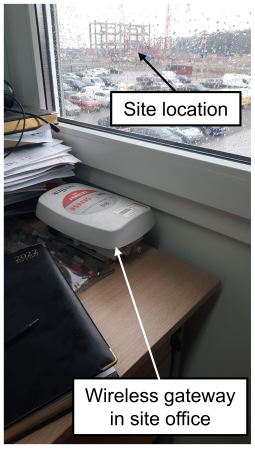


(c)

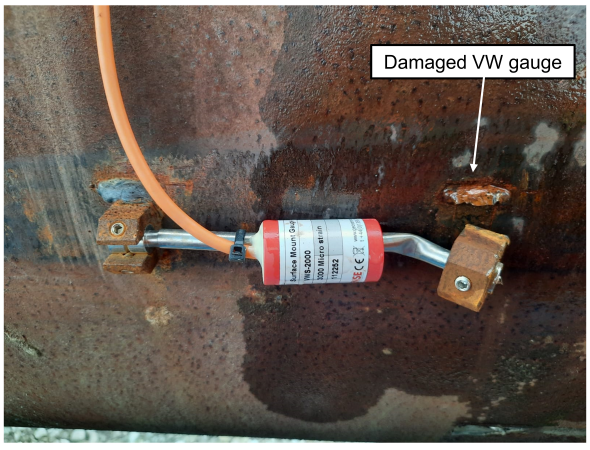


(d)





(e)



(f)

Figure 3.17: Photographs of prop VW gauge installation process and logging systems: (a) VW gauge base reading, (b) VW gauge installation, (c) initial data logging setup, (d) site enclosure and power supply, (e) revised data logging setup, (f) damaged VW gauge on level 1 tube prop.

3.3.3 Embedment type VW strain gauges

Ten embedment type VW strain gauges were installed at three different levels to monitor the development of temperatures, strains and bending moments in the 1.5 m thick RC bunker walls, as shown in Figure 3.14b. The gauges were operational from wall construction until several months after the completion of the bunker superstructure to monitor the influence of early soil consolidation on wall behaviour. At each location, the VW strain gauges were positioned on both the internal and external reinforcement mat, with concrete cover of approximately 50 mm. Photographs of the wall VW gauge installation process and logging systems are shown in Figure 3.18. Three embedment type VW strain gauges were also located in the bunker base ($G_{E,B1}$, $G_{E,B2}$, $G_{E,B3}$ in Figure 3.14b): one each positioned beside the central fibre-optic FBGs on the top and bottom mats as a means of verifying the adopted FBG temperature compensation strategy as shown in Figure 3.21d. The third VW strain gauge was in the centre of the base slab and was used to measure temperature. The GEOSENSE WI-SOS 480 vibrating wire nodes and 4G Gateway Cloud were used to transmit data to the server and dashboard. To continue to monitor the walls following bunker construction, enclosures were cast into the top of each wall on the north and south sides to house the data logging systems. As the gauges were embedded in concrete, the calculated strains needed to be compensated for the difference in the thermal expansion coefficients of concrete, α_c, and the steel gauges, α_g:

$$\mu\varepsilon_{corrected} = \mu\varepsilon + (\alpha_g - \alpha_c)\Delta T \tag{3.8}$$

where $\mu\varepsilon$ is calculated using Eq. 3.5 and ΔT is the current temperature difference from the base reading taken after installation. Values of 10 με/°C and 12.6 με/°C (Bamforth (2007), Royston et al. (2022)) are taken for α_c and α_g respectively. The use of strain measurements to infer forces is less straightforward for concrete due to the time dependent E which is estimated

as (Eurocode 2: Part 1-1 (2004)):

$$E(t) = \left(\frac{f_{cm}(t)}{f_{cm}} \right)^{0.3} \tag{3.9}$$

where:

$$f_{cm}(t) = \beta_{cc}(t) \cdot f_{cm} \tag{3.10}$$

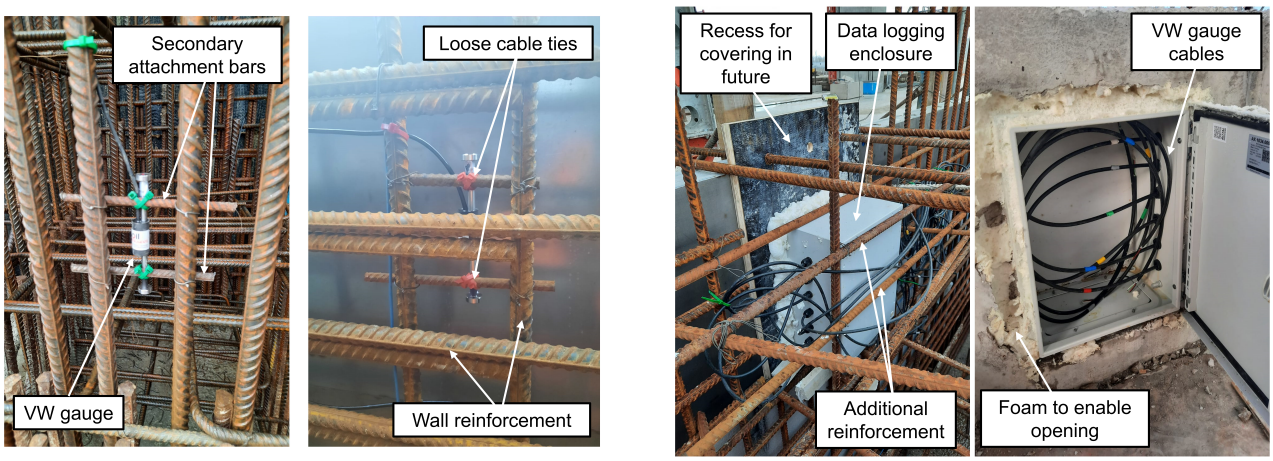
$$\beta_{cc}(t) = e^{s(1-(\frac{28}{t})^{0.5})} \tag{3.11}$$

where t is the age of the concrete in days, E_{cm} and f_{cm} are the values of E and mean compressive strength taken at an age of 28 days, $f_{\mathrm{cm}}(t)$ is the mean compressive strength at time t, $\beta_{cc}(t)$ is a time dependent concrete coefficient and s is a coefficient which depends on the cement type used. The value '28' and parameter s in Eq. 3.11 were adjusted to fit $E(t)$ to the results of concrete cube strength tests carried out on 112, 36 and 32 samples for the bunker base, bunker wall pour 1, and bunker wall pour 2 respectively, as shown in Figure 3.19. The replacement of a significant proportion of cementitious material with Ground granulated blast-furnace slag (GGBS) led to a lower initial rate of reaction and corresponding strength development but a larger long term peak strength than predicted by the Eurocode 2 method. The GGBS was included as the lower initial rate of reaction helped to control early-age thermal cracking. The axial load and bending moment per m run for each gauge pair can then be calculated as:

$$F = \frac{(\mu\varepsilon_A + \mu\varepsilon_B)}{2} E(t) h \tag{3.12}$$

$$M = \frac{(\mu\varepsilon_A - \mu\varepsilon_B)}{2} E(t) Z \tag{3.13}$$

where h is the thickness of the concrete element.



(a) (b)

Figure 3.18: Photographs of wall embedment type VW gauge (a) installation and (b) enclosure.

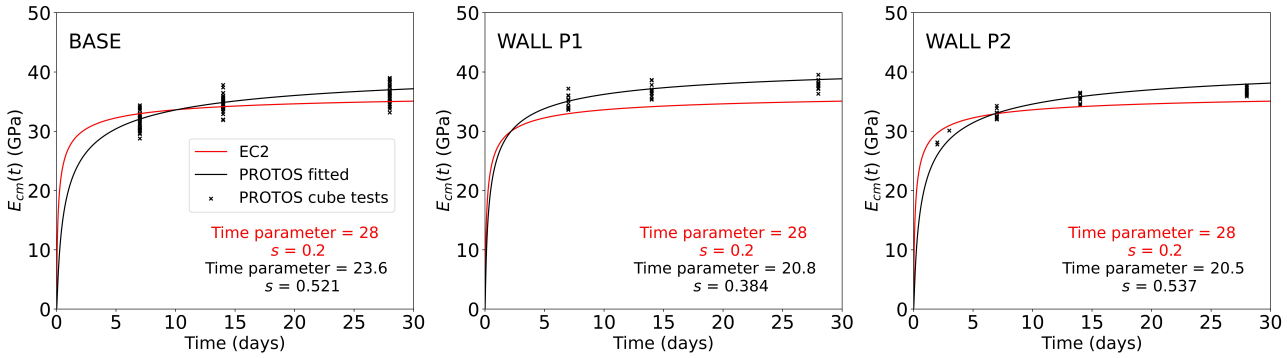
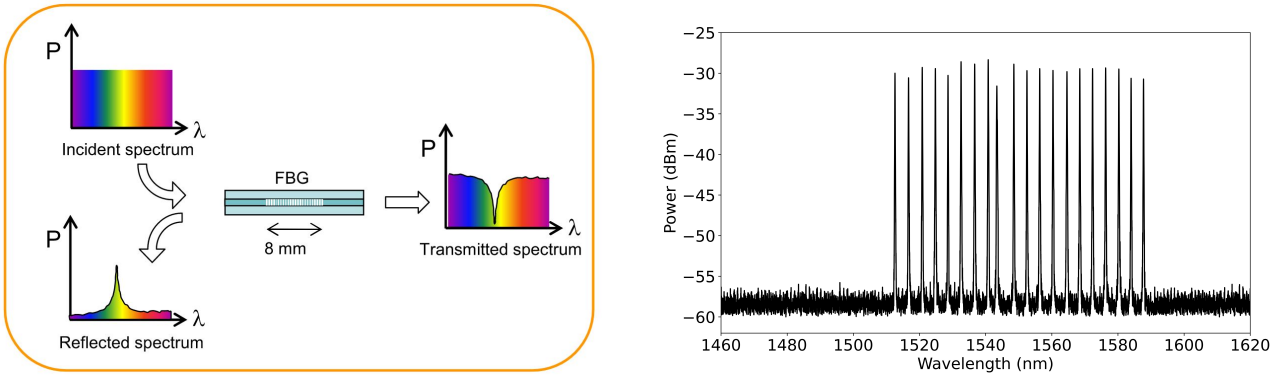


Figure 3.19: Concrete $E_{cm}(t)$ series fitted to sample cube tests for the bunker base, wall pour 1 and wall pour 2 mixes. Eurocode 2 prediction also plotted for comparison.

3.3.4 Fibre optics

Two 'strings' of FBG strain sensors each comprising 20 FBGs spaced 1 m apart were used to measure strain development in the 2 m thick RC bunker base. An FBG consists of a short section of single-mode optical fibre into which a periodic modulation of the core refractive index is formed. The core refractive index is modulated over a number of grating periods forming a grating length. When a broadband spectrum of light is incident on a FBG within a fibre, a narrow band of the spectrum is reflected through coherent scattering at the grating index variations. The reflected spectrum is characterised by a specific wavelength called the Bragg wavelength, λ_B. FBGs can be exploited as sensing elements by measuring the shift in the reflected wavelength that occurs when the grating is exposed to mechanical strain or a

temperature change (Figure 3.20a). An example of a reflected spectrum for the one of the FBG fibre lengths deployed in the bunker base is shown in Figure 3.20b.



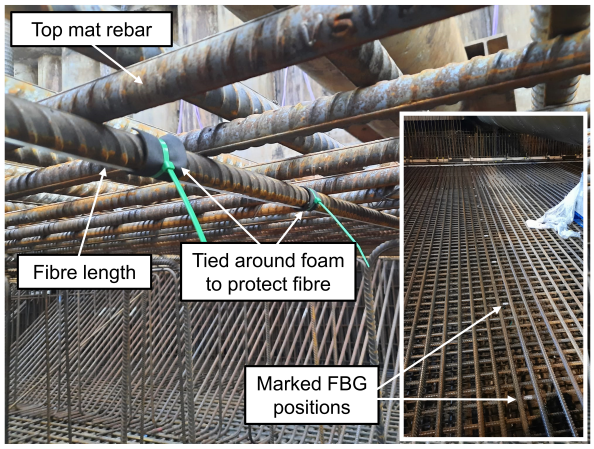
(a) (b)

Figure 3.20: (a) Illustration of the reflection and transmission behaviour of a FBG (FBGS (2019)). (b) Reflected spectrum for base bottom fibre on 20/12/2021.

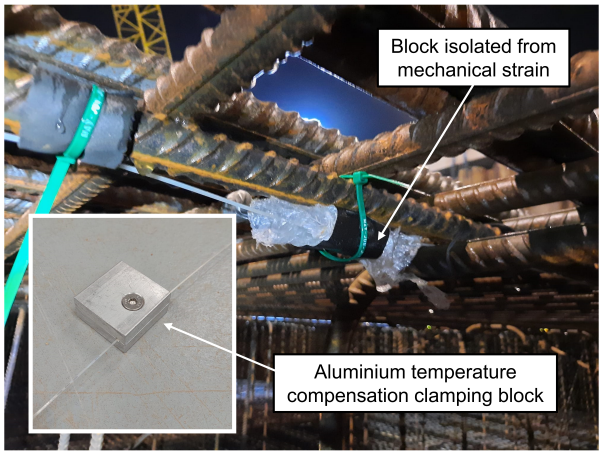
The two 20 m long FBG strings were installed along the short span of the bunker base, one each located on the top and bottom mats of reinforcement, with a concrete cover of approximately 50 mm, as shown in Figure 3.14b. The fibres were secured to the underside of reinforcing steel bars to prevent aggregate causing damage during the base concrete pour. 18 of the 20 FBGs in each fibre were positioned to measure strain, with the other 2 part of the spare fibre length required for connection to the transmission cable. The wire reinforced transmission cable connected the fibre lengths to a Micron Optics si255 8-channel interrogator. The system was operational from bunker base curing until the casting of the first bunker wall pour. While it was intended for the system to be operational until completion of the underground bunker walls, the failure of an electrical component within the interrogator led to the early demobilisation of the system for repairs. Photographs of several installation stages and system components are shown in Figure 3.21.

The change in wavelength, $\Delta\lambda$, of each FBG measured by the optical interrogator is sensitive to both strain and temperature as follows:

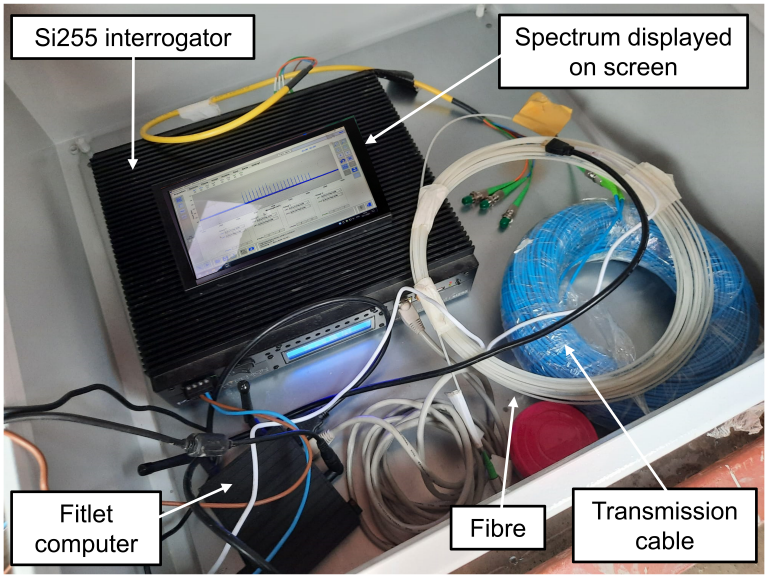
$$ln\left(\frac{\lambda}{\lambda_0}\right) = (1 - P_o)\Delta\mu\varepsilon_{mech} + (\alpha + \zeta)\Delta T \tag{3.14}$$



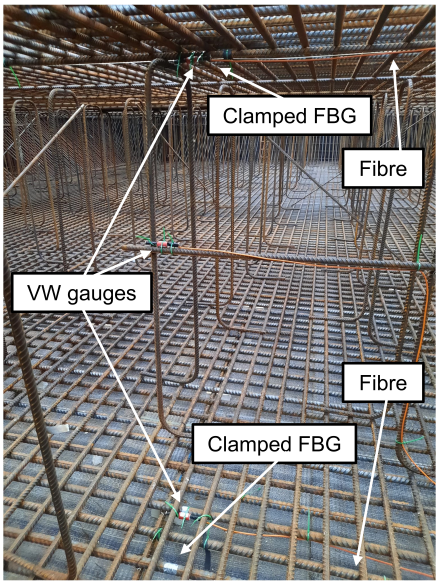
(a)



(b)



(c)



(d)

Figure 3.21: Photographs of fibre system and component installation: (a) fibre length, (b) aluminium temperature compensation clamping block, (c) interrogator system, (d) VW gauge arrangement.

where λ_0 is the base wavelength reading, P_o is the photo-elastic coefficient of the fibre, $\Delta\mu\varepsilon_{mech}$ is the mechanically applied microstrain, and α and ζ are the thermal expansion and thermal-optic coefficient of the fibre respectively. When an FBG is bonded or embedded within a structure, Eq. 3.14 is modified as (Magne et al. (1997)):

$$ln\left(\frac{\lambda}{\lambda_0}\right) = (1 - P_o)\Delta\mu\varepsilon_{mech} + (\alpha + \zeta + (1 - P_o)(\alpha_s - \alpha))\Delta T \tag{3.15}$$

where α_s is the coefficient of thermal expansion of the structure (in this case concrete); the modification accounts for the additional strain induced by the difference in thermal expansion

of the fibre and structure.

To isolate the 'true' applied mechanical strain from any temperature effects, precisely machined aluminium blocks were clamped onto one FBG in each string as a temperature gauge as shown in Figure 3.21b. The aluminium block was isolated from the concrete using a highly flexible foam such that the clamped FBG could be assumed to experience zero mechanical strain and any wavelength shift could then be directly related to expansion/contraction of the aluminium block due to ΔT as:

$$\Delta T = \frac{ln\left(\frac{\lambda}{\lambda_0}\right)}{(1-P_o)(\alpha_s - \alpha_f) + S_1} \tag{3.16}$$

where α and ζ have been grouped into a single temperature coefficient S_1 and α_s = 20.92 x 10^{-6} °C^{-1} is the coefficient of thermal expansion of aluminium in this case. Prior to installation on site, four of the FBGs on the fibre string were clamped and calibrated in a laboratory temperature chamber across two tests such that $\ln(\lambda/\lambda_0)$ could be related to ΔT as shown in Figure 3.22. The gradient of the linear fit in Figure 3.22 was used to calculate S_1 = 6.49 με/°C. This is in good agreement with S_1 = 6.3 με/°C provided on the specific datasheet for this fibre. The ΔT time series calculated using Eq. 3.16 could then be used to compensate the rest of the embedded FBGs to determine $\Delta\mu\varepsilon_{mech}$ as follows:

$$\Delta\mu\varepsilon_{mech} = \frac{1}{(1-P_o)}\left[ln\left(\frac{\lambda}{\lambda_0}\right) - S_1\Delta T\right] - (\alpha_s - \alpha_f)\Delta T \tag{3.17}$$

Microstrains measured by pairs of FBGs positioned in the same plan position on the top and bottom mat were used to calculate the axial load and bending moment per m run in the bunker base slab using Eq. 3.12 and Eq. 3.13.

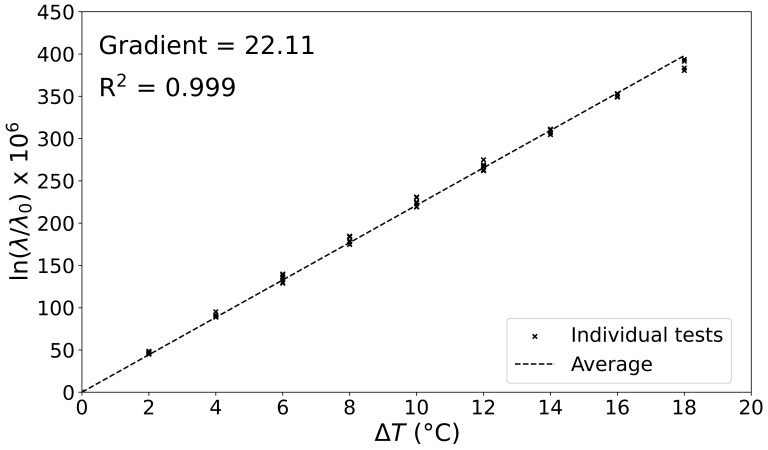


Figure 3.22: Results of laboratory clamped FBG temperature calibration tests for four FBGs on fibre string.

3.3.5 Piezometers

Two inner piezometers ($P_{I,1}$, $P_{I,2}$) and two outer piezometers ($P_{O,U}$, $P_{O,L}$) were installed to monitor internal and external bunker water levels respectively. A section showing the installation level of each of the monitoring wells is shown in Figure 3.23a. The external boreholes were positioned to determine whether groundwater was being drawn into the excavation by the internal pumps through infiltration through the walls or seepage beneath the cofferdam toe. Water levels in the upper GO layer and lower GT sand layer were monitored separately to determine whether the GT clay layer achieved an effective seal. The wells were installed using a Soilmec SM14 drilling rig through pipe openings cast into the capping beam to a depth of 25 mBGL. Six internal wells (four for pumping, two for monitoring) and two external monitoring wells were installed. The monitored water levels and total pumped flow rate were recorded continuously using a WJ groundwater datalogger system. Photographs of the well installation process and logging container are shown in Figure 3.23.

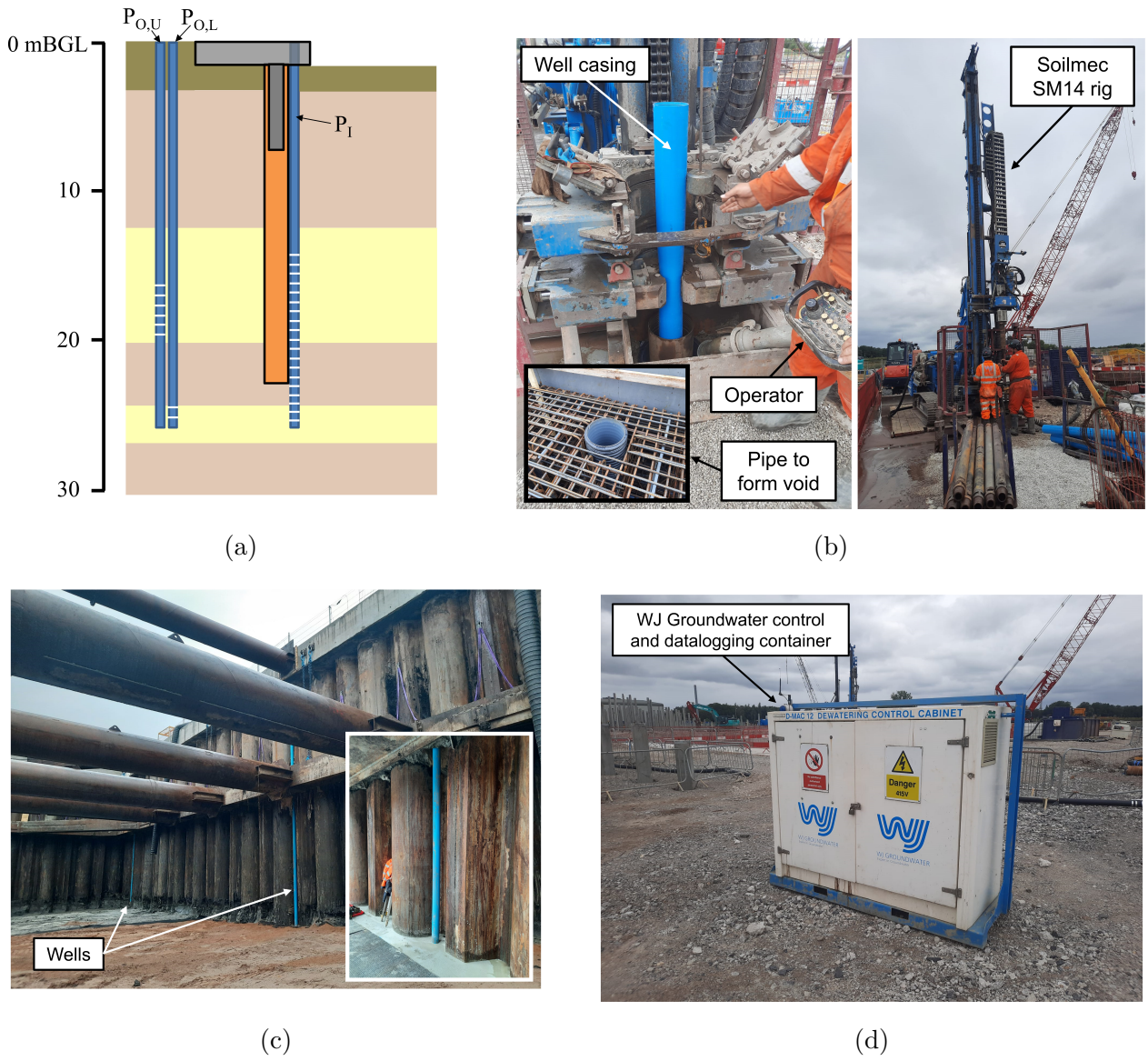


Figure 3.23: (a) Section through excavation showing piezometer installation levels. Perforated pipe lengths are indicated by the dashed lines. Plan locations are given in Fig. 3.14a. (b) Photographs of well installation. (c) Photograph of wells within bunker excavation. (d) Photograph of logging enclosure.

3.4 Lessons learnt and areas for improvement

A comprehensive instrumentation and monitoring system was developed to improve understanding of structural behaviour and to provide information in real-time to the site team. The following lessons were learnt during the instrumentation installation, operation, and maintenance processes:

- Working on live construction sites is challenging and the ability to be flexible and adaptable to changing structure and plant layouts is critical. The monitoring scheme must be rigorously planned and organised not to impede the main construction works. Monitoring systems should be assembled and tested off site prior to installation.
- While the steel monitoring enclosure (Figure 3.17d) was effective in preventing damage and waterproofing, the setup offered a poor ergonomic environment in which to perform electrical installations and maintenance works. The use of a purpose-built monitoring cabin would greatly improve the ergonomics of the setup, reduce installation times and further reduce equipment exposure to the site environment. The cabin would also address issues with sourcing power on site, as difficulties were encountered using the solar power system and site generators.
- Using the battery powered GEOSENSE WI-SOS 480 vibrating wire nodes greatly simplified the VW gauge logging and data transmission process. Short cable lengths with end connection plugs should be installed for each channel connection to prevent the node casing being opened in a site environment (Figure 3.17e).
- Increasing the number of gauges positioned around each prop from 2 to 4 would provide a full 360 degree profile of prop bending moment and incorporate some redundancy into the system in the case of gauge damage. Positioning gauges on the side of props increases the likelihood of damage from excavation plant during excavation. Protective covers should be tack welded on at 2 points orthogonal to the direction of strain measurement to prevent

a local increase in stiffness. Cables adjacent to VW gauges should be looped to prevent damage in the event of a cable tug (Figure 3.17b).

- For VW gauges embedded in concrete, cable connector plugs should be positioned towards the top of the pour to reduce the head of concrete fluid pressure driving water ingress into the connection. Connections should be waterproofed using heat shrinking.
- Fibre optic cables are highly susceptible to damage in a construction site environment and cables were replaced on numerous occasions. Cables should be sheathed within armoured tubing for protection where exposed. The connection point between the fibre end and the cable should be made accessible through a cast-in junction box to facilitate access to easily replace damaged cables. This prevents the need to splice fibres or cables in a site environment which is highly challenging. Ensure that protective caps are always kept on to prevent the optical core becoming dirty or scratched. This will reduce the transmitted/reflected signal power and make it more difficult to distinguish between FBG peaks and noise.

4 | Field monitoring results

4.1 Introduction

Chapter 3 outlined the instrumentation scheme employed to monitor the construction of the deep excavation and RC bunker at PROTOS EFW. This chapter presents the results of the monitoring scheme, with an emphasis on contextualising the data with reference to previously published case histories and empirical guidelines to evaluate the performance of the excavation support system, the dewatering system, and the permanent RC bunker structure.

4.2 Wall deflections

4.2.1 Initial cantilever deflection

All tube piles around the perimeter of the cofferdam were surveyed before and after the initial 1.5m deep excavation (stage 4 in Table 3.1) to monitor lateral deflection at the cantilever stage. The average ratio of cantilever deflection to maximum deflection for the surveyed tube piles along each side of the excavation $\delta_{h,c}/\delta_{h,max}$ are plotted against the ratio of cantilever depth to excavation formation depth h_c/H in Figure 4.1 and compared to data reported in Gaba et al. (2017) for excavations in London Clay. The north side is omitted as no tube piles were instrumented with inclinometer casings to obtain maximum wall displacement ($\delta_{h,max}$) data. The average $\delta_{h,c}/\delta_{h,max} = 1.19$ for the surveyed tube piles is significantly larger the Gaba et al. (2017) range of 0.3 - 0.6 and design recommendation of 0.7, indicating the passive resistance provided by the soft TF layers following removal of the stiffer MG band is much less than that by the stiffer London Clay. The largest displacements occur along the south side due to the closer proximity to a dense layout of precast concrete piles (see Figure 3.9). Long (2001) examined over 35 deep excavation cases which reported unusually large lateral wall movements and found that the inclusion of an initial cantilever stage was the primary cause for excessive

deformation, making up over one-third of these cases. It is therefore critical that additional monitored data is contributed towards the Gaba et al. (2017) database to aid designers and contractors in reducing risks associated with excessive ground movements at the cantilever stage.

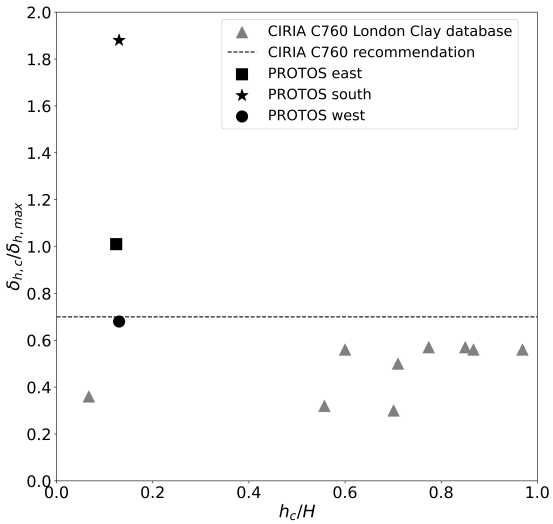


Figure 4.1: Average initial cantilever stage $\delta_{h,c}/\delta_{h,max}$ plotted against h_c/H for the surveyed tube piles on each excavation side. Data for cases in London Clay and the design recommendation both reported in CIRIA C760 (Gaba et al. (2017)) are plotted for comparison.

4.2.2 Maximum wall deflection time series

A time history of the maximum lateral displacement, $\delta_{h,max}$, experienced by the four monitored tubes (IC_1 – IC_4) is presented in Figure 4.2. For reference, the average surveyed excavation level is plotted using a secondary axis and key construction activities are indicated using shaded regions. The development of $\delta_{h,max}$ for all four monitored tubes during construction show similar trends. The largest $\delta_{h,max}$ (= 23.2 mm) during excavation was recorded for IC_1 which was 1.4 – 1.7 times greater than those recorded for IC_2 – IC_4 due to its position at the centre of the West wall and the presence of a plant access road, and therefore additional surcharging, on the West side. It is also likely that IC_2 and IC_4 benefited from increased stiffness at the excavation corners (Roboski (2004)). A significant increase is observed for IC_3 during the bunker piling indicating a much greater effect of this activity on the long span of the support system. Negligible changes are observed following base construction.

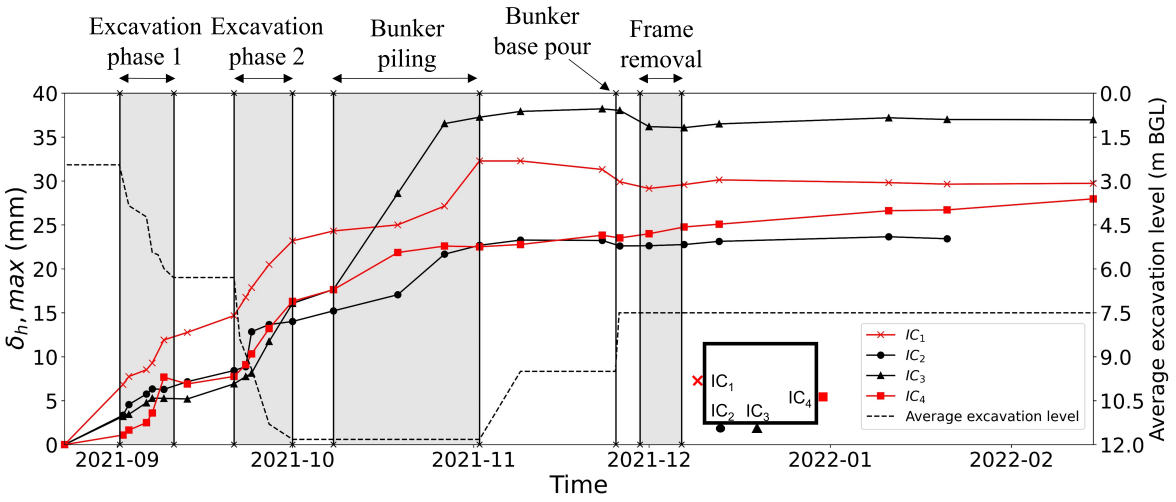
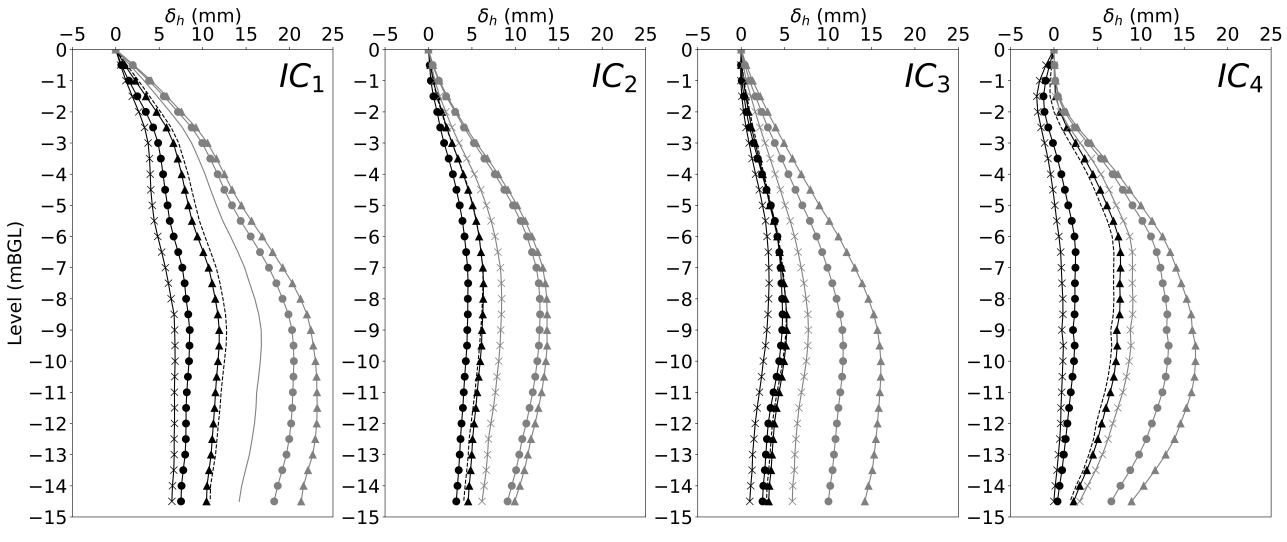


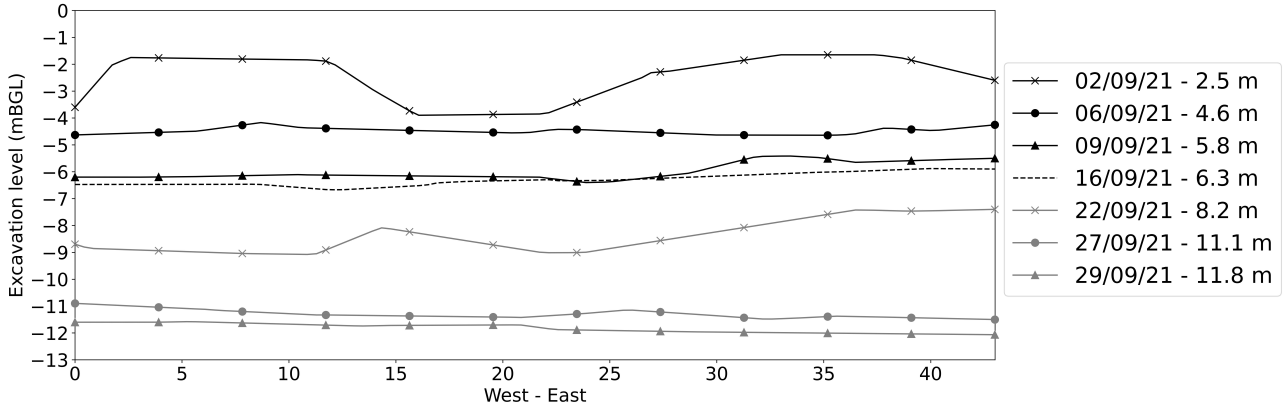
Figure 4.2: Time history of instrumented tube pile maximum lateral displacements and average internal level. Short span and long span tube piles indicated by red and black lines respectively.

4.2.3 Deflected wall shape during excavation

Figure 4.3 shows the horizontal displacement, δ_h, profiles with depth measured for IC_1 – IC_4 at several stages during excavation together with (long span) cross-sections of the corresponding excavation surface profiles shown in Figure 4.4. It can be seen that the RC capping beam was highly effective at 'anchoring' the top of the cofferdam. Interestingly, negative lateral displacements initially develop at 1.5 m BGL for IC_4 due to shallow excavation works (to a depth of 1 m) occurring behind the capping beam during the construction of a RC slab. As excavation depth, H, increases, there is a steady increase in both $\delta_{h,max}$ and its corresponding depth, to the point where $\delta_{h,max}$ occurs near the dig level at the end of excavation. The largest percentage increases in $\delta_{h,max}$ caused by excavation phase two were 210% and 136% for IC_3 and IC_4 respectively on the East side of bunker, whereas 82% and 95% increases were observed for IC_1 and IC_2 respectively. This may be attributed to the additional 0.5 m depth excavated on the East side, compared to the West side during this period.



(a)



(b)

Figure 4.3: (a) Horizontal displacement profiles for instrumented tube piles during bunker excavation, (b) Corresponding bunker excavation level surveys taken through section B-B on Figure 3.14a, and legend. Phase 1 excavation and phase 2 excavation indicated by black and grey lines respectively.

4.2.4 Deflected wall shape during bunker construction

Figure 4.5a shows the profiles of δ_h with depth during bunker piling which is broken into four different 'piling weeks' (WK1 – WK4), as shown in the pile installation layout in Figure 4.5b. Bunker piling causes substantial increases in δ_h for all four monitored tube piles. In contrast, no appreciable changes to the corresponding depths to $\delta_{h,max}$ or the overall deflected shapes are observed. Measured displacements are strongly influenced by nearest proximity piling whereas other piling has only a secondary effect. For example, WK1 piling causes a significant increase in IC_4 displacements which then show negligible changes during subsequent piling. In contrast,

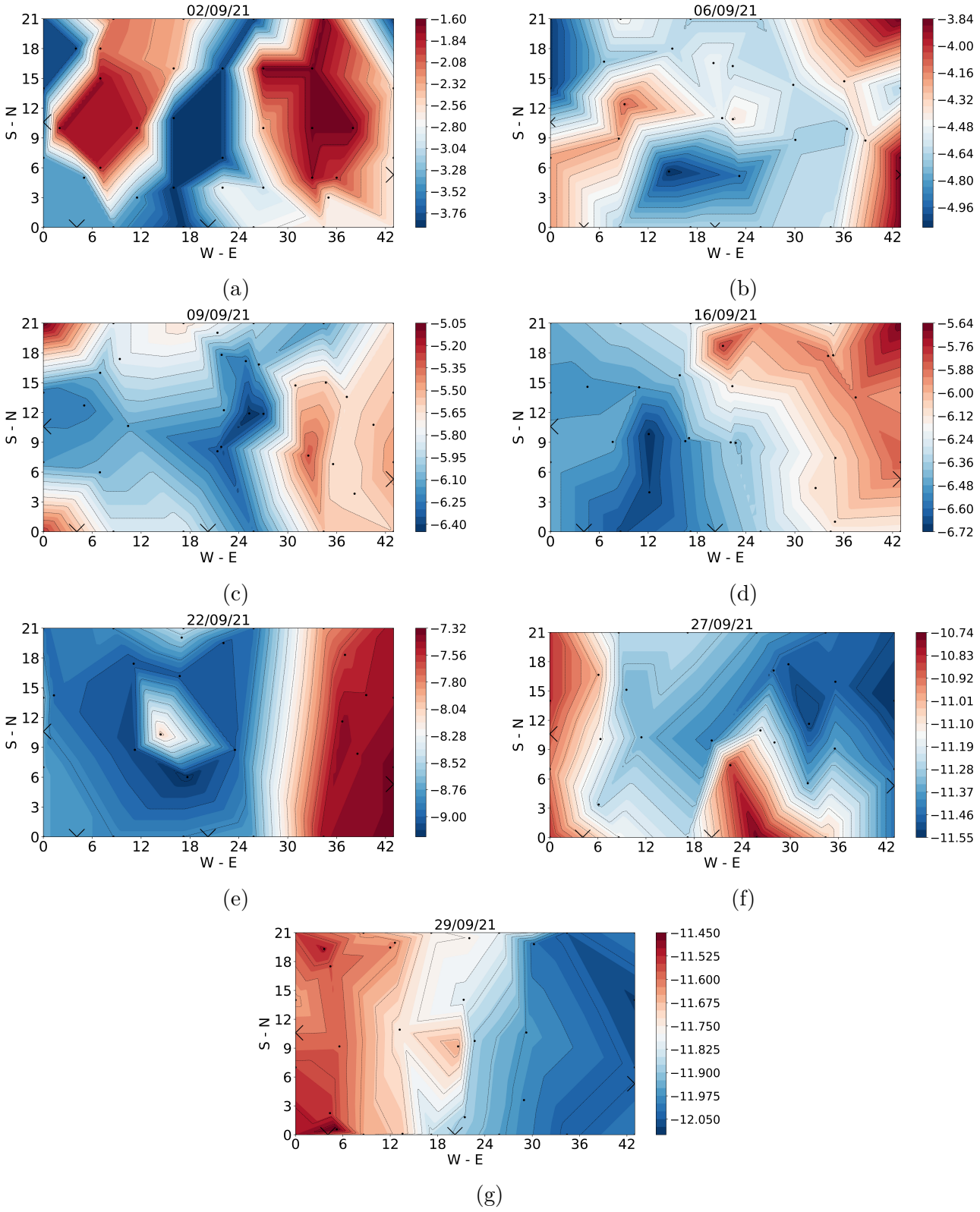


Figure 4.4: Contour plots produced from level surveys taken during excavation. Each survey corresponds to a deflected wall profile measurement in Figure 4.3b. Levels provided in mBGL.

there is a steady increase in $\delta_{h,max}$ for IC_2 and IC_1 during this period as the piling progressed towards the West side of the bunker. The piling process had the greatest impact on the long span IC_3 measurements with an increase in $\delta_{h,max}$ of 111%, likely due to its closer proximity to

the bunker piles.

Following piling, the 2 m thick RC base is cast with all temporary propping still in place. From Figure 4.5a, base installation causes a small decrease in $\delta_{h,max}$ for IC_1 and IC_3 and a small increase in $\delta_{h,max}$ for IC_2 and IC_4. This suggests a competing influence of the outward concrete head pressure and the subsequent concrete shrinkage during curing.

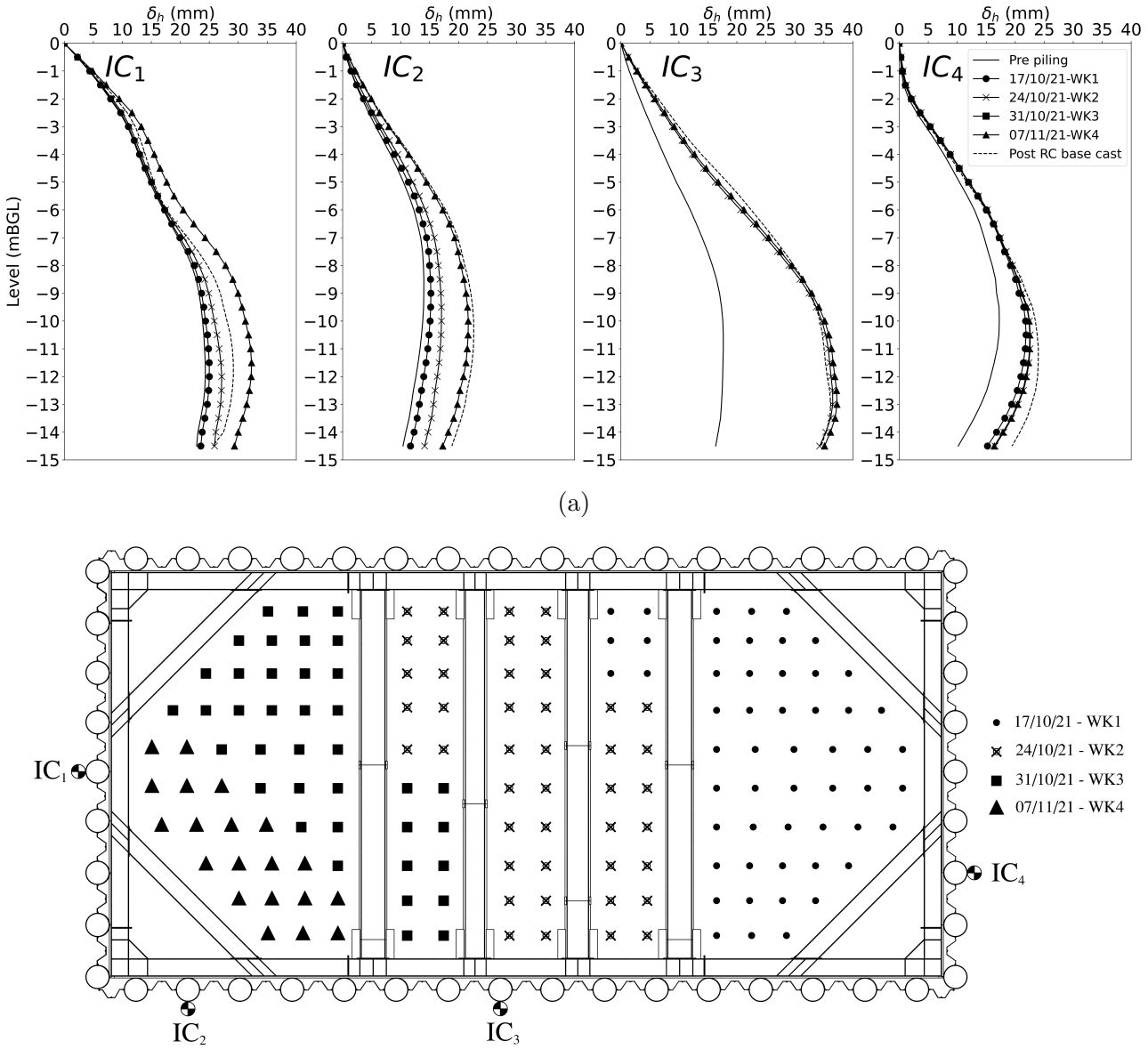


Figure 4.5: (a) Measured δ_h profiles with depth for all four instrumented tube piles during internal piling works and RC bunker base construction (WK3 profiles omitted due to sensor fault), and (b) corresponding weekly pile installation layout.

4.2.5 Comparison to case histories and empirical methods

The monitored wall deflection data have been normalised to enable comparisons to previously published case history data and empirical methods in Figure 4.6. Data from individual case histories in relevant sections of the databases published in Long (2001) and Moormann (2004) have been plotted for comparison. The plotted data in Figure 4.6 published in Long (2001) comprises the "set 2" category, which is defined as support structures embedded in stiff soils supporting a soft soil majority and having a high factor of safety against basal heave failure (FOS_{BH}). The plotted data in Figure 4.6 published in Moormann (2004) comprises the "soft clay" and/or the "layered soils" categories. These categories have been selected as their definitions bear close similarities to the ground conditions and support structure properties for the PROTOS bunker excavation.

The maximum wall displacement is plotted as a function of the final excavation depth in Figure 4.6a. The adopted selection of empirical guidance superimposed on Figure 4.6a represents a mix of average expected displacements and recommended upper limits for use in design and are defined in Table 4.1. The final "post bunker" $\delta_{h,max}$ are consistent with the Moormann (2004) recommended average of $\delta_{h,max}/H = 0.27\%$ (defined '[6]') and lower than the Long (2001) recommended average of $\delta_{h,max}/H = 0.39\%$ (defined '[5]'). Despite the conclusion in Long (2001) that $\delta_{h,max}/H$ appears to be relatively independent of wall stiffness, the monitored $\delta_{h,max}/H$ align closer to those reported for cases employing stiffer contiguous, secant pile and diaphragm walls than those employing more flexible sheet and soldier pile walls. The Fernie and Sucking (1996) (defined '[4]') recommended average of $\delta_{h,max}/H = 0.15\%$ provides a reasonable fit to the data during the excavation process, whereas the upper limit of $\delta_{h,max}/H = 0.5\%$ (Clough (1990)) represents a safe design bound for the present data. These comparisons highlight the effectiveness of the employed combi-wall and support system in reducing ground movements in soft and challenging ground conditions. Bunker piling and construction causes

the displacements to increase above several average and bound lines at the end of construction thus highlighting the importance of considering all stages of construction in design.

The depth BGL of the maximum wall displacement ($z[\delta_{h,max}]$) is plotted as a function of the final excavation depth in Figure 4.6b and compared with those reported in Moormann (2004). Present measurements are well described by the $z[\delta_{h,max}] = 1.0$ guideline (Moormann (2004)) indicating that the point of maximum displacement is approximately located at the dig level during excavation. The Moormann (2004) data suggests the maximum lateral wall deflections in stiffer layered clays typically occurs further above the excavation level, highlighting the soft nature of the TF layers. This is consistent with the reported behaviour of walls supporting soft clays in China (Tan and Wei (2012)).

The ratios of $\delta_{h,max}/H$ are plotted as a function of the system stiffness factor S for the instrumented tube piles in Figure 4.6c and are compared with the Clough et al. (1989) prediction curves (see section 2.5) and relevant case histories published in Long (2001) and Moormann (2004). The large calculated $FOS_{BH} \simeq 4.5$ for the PROTOS bunker excavation can be attributed to the large excavation width and stiff nature of the GO and GT clay layers. Long (2001) and Moormann (2004) concluded that while the published cases in soft clays exhibit wide scatter without a clear dependency of S on $\delta_{h,max}/H$, there are signs that the Clough et al. (1989) curves may be broadly confirmed with regard to the effect of FOS_{BH} on ground movements. The monitored data support this conclusion, with good agreement observed between the ground movement predictions made using the Clough et al. (1989) method and those recorded at excavation formation.

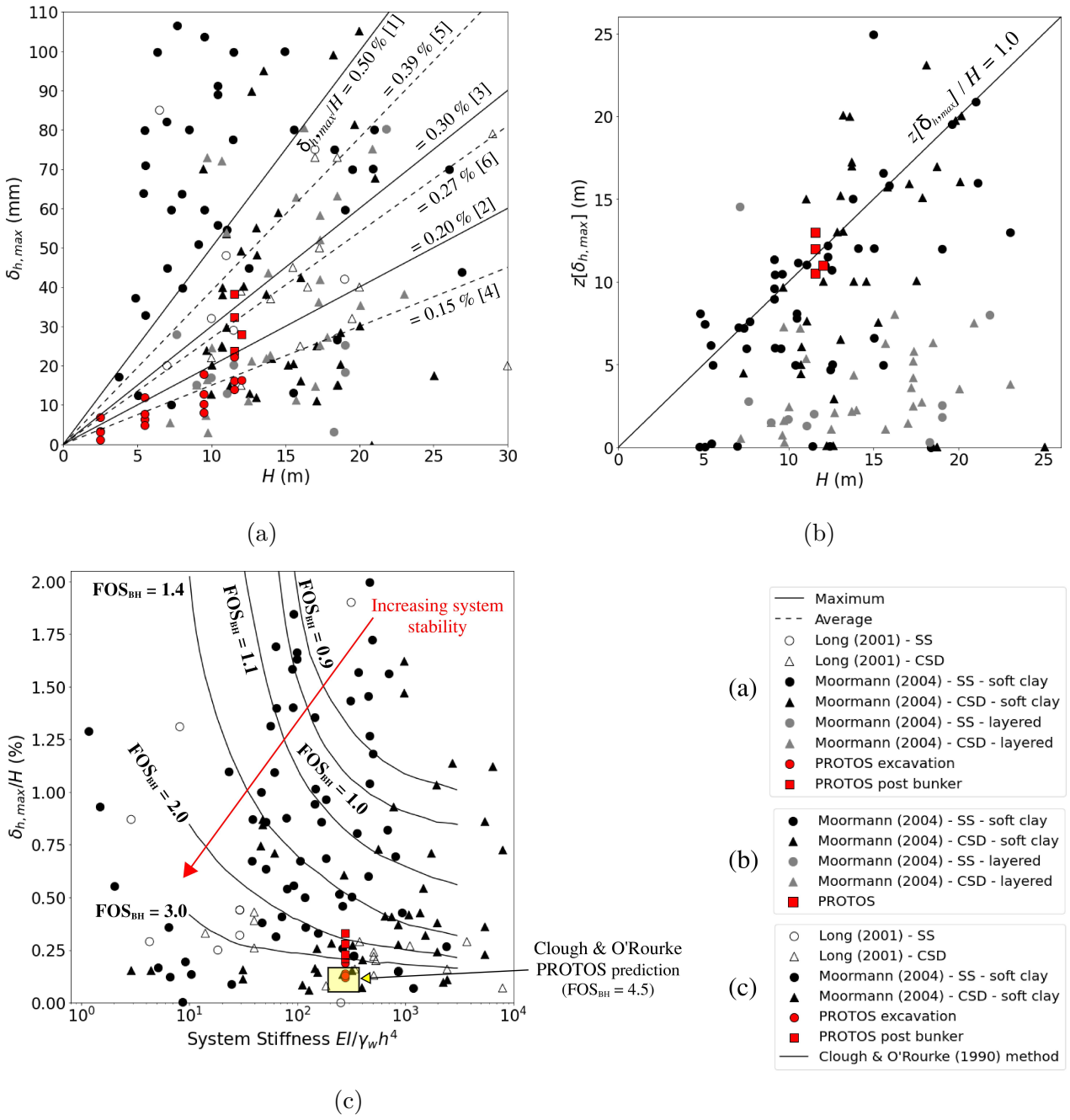


Figure 4.6: Comparison between present monitored data and empiricism reported elsewhere in the literature. (a) variation of $\delta_{h,max}$ with H both during excavation and post bunker construction (refer to Table 4.1 for empirical design guideline definition and notation), (b) variation of $z[\delta_{h,max}]$ with H, and (c) variation of $\delta_{h,max}/H$ with system stiffness S. SS denotes sheet and soldier pile walls, CSD denotes contiguous, secant pile and diaphragm walls.

Table 4.1: Empirical $\delta_{h,max}/H$ ratios reported in the literature. SS denotes sheet and soldier pile walls, CSD denotes contiguous, secant pile and diaphragm walls.

Design guidance notation	**Reference**	**Support system type**	$\delta_{h,max}/H$ **(%)**	**Description**	**Soil conditions**
[1]	Clough (1990)	SS, CSD	**0.5**	Maximum	Soft clays
[2]			**0.2**	Maximum	Stiff clays
[3]	Fernie and Sucking (1996)	CSD	**0.3**	Maximum	Stiff London clay
[4]			**0.15**	Average	
[5]	Long (2001)	SS, CSD	**0.39**	Average	Retaining soft soils, embedded in stiff soils ("Case 2")
[6]	Moormann (2004)	SS, CSD	**0.27**	Average	Layered soils

4.3 Prop axial loads and bending moments

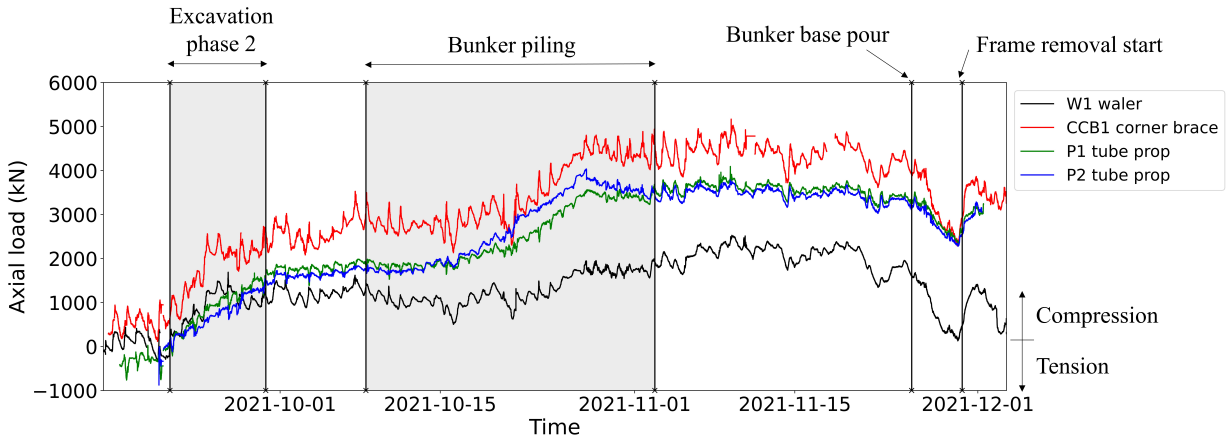
4.3.1 Raw measurements

A time history of the overall axial and bending loads for each instrumented level 2 bracing member is shown in Figure 4.7a and Figure 4.7b respectively; key construction stages are again identified using grey shading. The measured axial loads show similar trends for all four bracing members. The largest measured axial load is experienced by the corner brace on account of this member being at an angle to the cofferdam wall and having the largest tributary area (vice versa for the perimeter waler). Predictably, there is a noticeable increase in axial loads during the excavation phase, due to stress redistribution from the internal soil to the support structure.

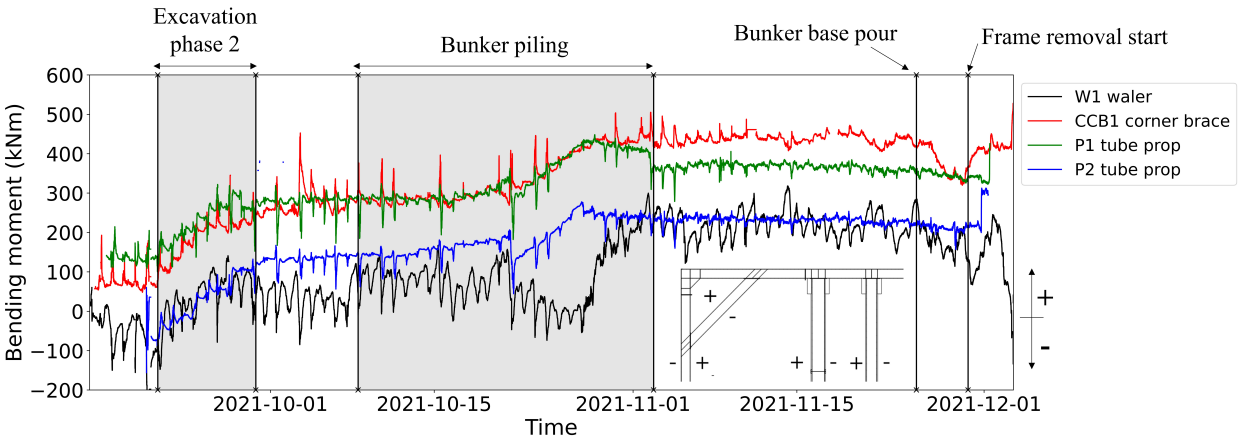
Significant increases in axial loads are also caused by the vibratory piling. While WK1 and WK2 piling had little influence on the axial loads, significant increases occurred during WK3 and WK4 as piling progressed towards the instrumented members on the West side of the bunker (see Figure 4.5b). These considerable load increases and the associated increases in lateral wall deflection in Figure 4.5a are due to a loss of strength of glacial till clay (C) inside the excavation consequent upon remoulding and excess pore pressure generation caused by pile driving. The vibratory piling may have also induced liquefaction effects in the saturated GO layer. These results highlight the importance of considering the impact of the full construction

process on the adopted support system.

Following the casting of the RC bunker base, significant reductions in compressive axial load of 91%, 41%, 29% and 36% were observed for B1, CCB1, P1 and P2 respectively. This is due to a redistribution of the bracing forces into the RC base which undergoes thermal expansion during cement hydration. This behaviour is consistent with the reductions in prop loads of 10% and 20% following base slab installation reported in Powrie and Batten (2000) and Chambers et al. (2016) respectively. Finally, post-excavation removal of the frame caused notable increases in axial load, as removed frame member loads re-distributed into adjacent members.



(a)



(b)

Figure 4.7: (a) Level 2 instrumented frame member (a) axial load time series, (b) bending moment time series.

Similar findings may be deduced from an examination of the bending moments in Figure 4.7b. The largest bending moments developed in the corner brace, which may be attributed to the

significant eccentricity of the applied cofferdam load. The two central tube props experience bending towards the West side of the bunker, which suggests the long span waler on the North side of the bunker is exhibiting curvature towards the excavation, which is symmetric about the centre of the span. The magnitude of the bending moment measured in P1 is significantly larger than that in P2, due to P2's closer proximity to the centre of symmetry on the North waler.

4.3.2 Temperature compensation method

From Figure 4.7a, significant daily fluctuations are observed in the data, due to thermal effects as the props warm during the day and cool at night. As the bracing members were installed during September 2021 and were removed in December 2021, the temperatures encountered varied considerably: Figure 4.8 shows the temperatures measured by a typical VW gauge thermistor ranged from -2°C to +25°C. The temperature encountered by gauge $G_{W,1A}$ is plotted for comparison to highlight the insulating effect of embedding this gauge in concrete fill. If the bracing members had been fully restrained, the corresponding increase in load per degree Celsius would have been 247 kN/°C, 290 kN/°C, 230 kN/°C and 179 kN/°C for members W1, CCB1, P1 and P2 respectively (taking the coefficient of thermal expansion $\alpha = 11.3$ x 10-6 / °C). To estimate the load component attributable solely to the construction process, it is necessary to determine how the prop loads respond to temperature changes.

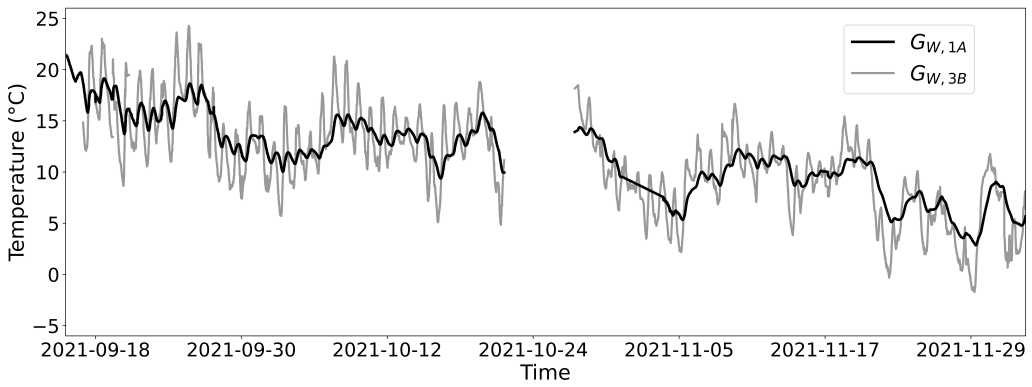


Figure 4.8: Temperature time series measured by a typical VW gauge thermistor (gauge $G_{W,3B}$) and an insulated VW gauge thermistor (gauge $G_{W,1A}$).

To compensate for temperature fluctuations, the method outlined in Richards et al. (1999) and Powrie and Batten (2000) was employed, which involves monitoring load fluctuations during downtime periods. The downtime period selected occurred between 02-11-21 and 20-11-21, during which the RC base reinforcing steel was fixed (stage 12 in Table 3.1), and minimal plant movement occurred. It was assumed that changes in load during this period could be solely attributed to thermal effects, enabling the load-temperature relationship to be determined, and the degree of restraint to be quantified. Figure 4.9 shows that approximately linear relationships between measured microstrain (multiplied by EA to give an apparent load in kN) and temperature are apparent for all 8 gauges, indicating temperature causation. Interestingly, the relationship for $G_{W,1A}$ differs from that of the other gauges as it follows a more defined cyclic load path. This is likely to be due to the insulating effect caused by embedding this gauge in the concrete fill on the external face of waler W1.

Some scatter and deviation from the linear approximation is observed for all gauges in Figure 4.9. This is likely to be due to a difference in temperature between the frame member surfaces and the gauge measurements. This is caused by the exposure of each prop to direct sunlight, while the gauges are sheltered by protective covers. In future monitoring schemes, to achieve stronger correlations in Figure 4.9, a secondary thermistor should be positioned adjacent to each gauge outside of each protective cover. Scatter from the linear approximation may also be caused by a temperature differential along the length of each frame member, as some regions are subjected to sunlight, while others remain in the shade. If the gauge were to be in a shaded region, a rise in load would be recorded but no rise in temperature. It would then be incorrectly assumed that the load increase was due to construction activity. In future, this issue could be addressed by positioning gauges at several points along each member.

By calculating the gradient of the assumed linear relationship, f' in Figure 4.9 the end fixity

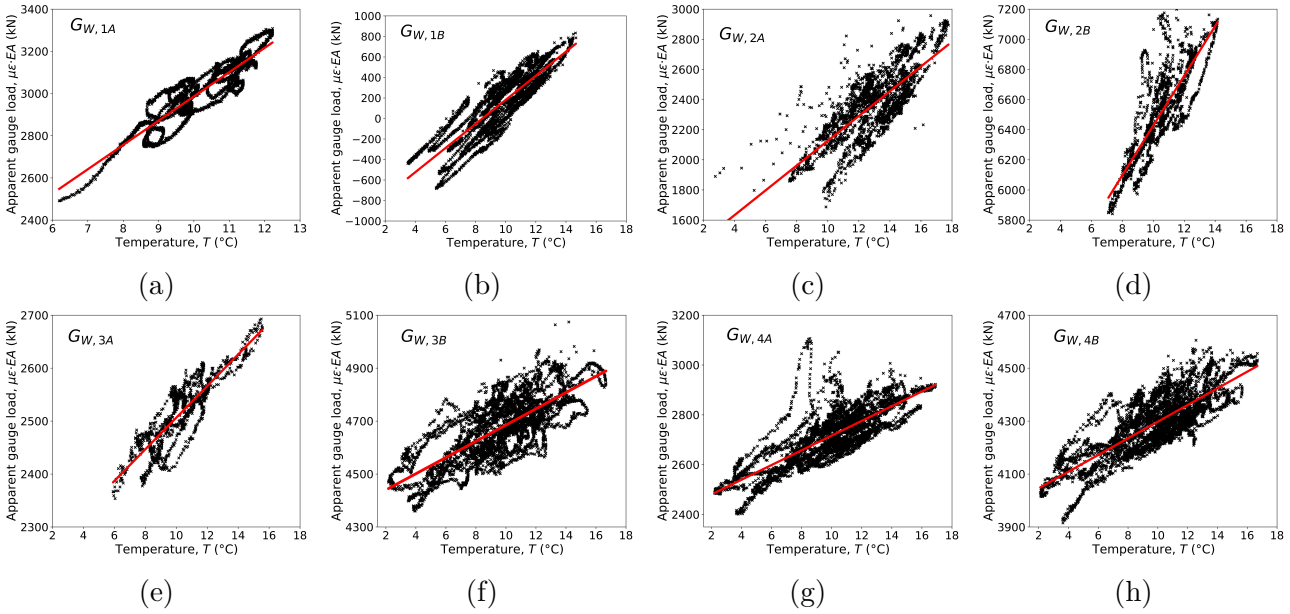


Figure 4.9: Relationship between temperature and apparent gauge load during a period of no construction activity in the bunker area for (a) $G_{W,1A}$, (b) $G_{W,1B}$, (c) $G_{W,2A}$, (d) $G_{W,2B}$, (e) $G_{W,3A}$, (f) $G_{W,3B}$, (g) $G_{W,4A}$, (h) $G_{W,4B}$.

factor, FF, can be calculated as:

$$FF = \frac{f'}{EA\alpha} = \frac{f'}{f_t} \tag{4.1}$$

where f_t is the theoretical thermally induced load assuming rigid end restraint. Table 4.2 summarises the calculation of FF for each of the level 2 frame gauges. There is good consistency between the values of FF for pairs of gauges on each frame member. The largest values of FF were calculated for waler W1, which is to be expected due to the high degree of restraint provided by the bolted C1 end connection (see Figure 3.11a) and the increased wall stiffness at the corner of the excavation (Richards et al. (1999), Roboski (2004)). The smallest values of FF were calculated for the tube props P1 and P2, as these members are hung from the waler frame with no method of fixed connection applied to their ends (see C3 end connection in Figure 3.11c). Except for W1 due to significant restraint provided by the C1 connection, the calculated FF values are reasonably consistent with the 10% – 25% range recommended in Twine and Roscoe (1997), based on previous sheet pile wall case history data. This finding is surprising given that the ground conditions for this project are significantly softer than almost all cases in the database. The current industry adopted approach for incorporating

prop temperature effects into design in Gaba et al. (2017) suggests using FF values of 30% and 50% for stiff walls in soft soils and in stiff soils respectively. However, no guidance is provided for excavations supported by more flexible sheet pile walls and combi-walls. While data from more cases will be necessary to verify or refine the calculated FF, the values from this project can be contributed towards this database to provide initial guidance on the selection of FF values for these more flexible wall types.

Table 4.2: Summary of the end fixity factor, FF, calculation for each level 2 frame member gauge.

Level 2 frame member	**Gauge**	f' **(kN/°C)**	f_t **(kN/°C)**	FF **(%)**
W1 waler	$G_{W,1A}$	115.1	247.3	**46.5**
	$G_{W,1B}$	117.6	247.3	**47.5**
CCB1 corner brace	$G_{W,2A}$	82.2	290.5	**28.3**
	$G_{W,2B}$	81.0	290.5	**27.9**
P1 tube prop	$G_{W,3A}$	29.9	230.1	**13.0**
	$G_{W,3B}$	30.7	230.1	**13.3**
P2 tube prop	$G_{W,4A}$	29.5	178.9	**16.5**
	$G_{W,4B}$	31.5	178.9	**17.6**

As the relationship between measured strain and temperature for each gauge is approximately linear, the measured prop loads can be adjusted to account for thermal expansion as follows:

$$F_{adjusted} = F - f'\Delta T \tag{4.2}$$

where $F_{adjusted}$ are the loads that would have been recorded in each prop had the construction occurred without variation in temperature. Figure 4.10 presents a comparison between F and $F_{adjusted}$ for all four instrumented frame members. The loads induced by construction activities alone are significantly more than the actual loads measured in the props. The largest difference between F and $F_{adjusted}$ is observed for W1 (61.1%) due to the large FF combined with a period of seasonal cooling from September until December. In contrast, there is little difference between F and $F_{adjusted}$ for props P1 and P2 due to the reduced FF enabling almost uninhibited thermally induced movement. Although daily fluctuations in $F_{adjusted}$ are considerably less than those in F, temperature fluctuations have not been eliminated completely. From Figure 4.11,

the daily temperature cycling effect is greatly reduced except for very sunny days on which a greater rate of rise in temperature occurred. The deviation of the load-temperature relationship may therefore be due to the rate of loading. Alternatively, the deviation may be caused by the actual prop temperature being higher than that recorded by the gauges, for the reasons already discussed.

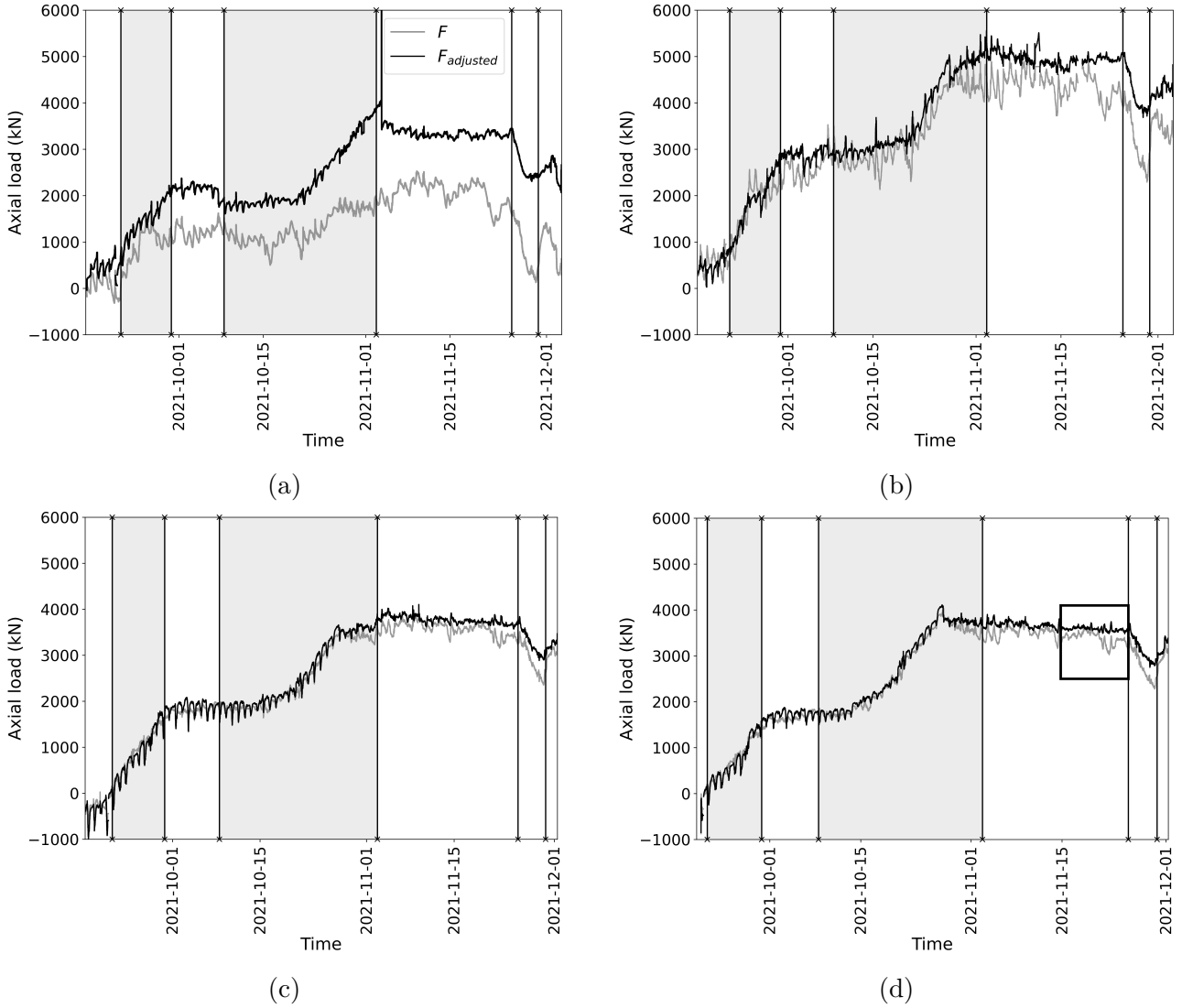


Figure 4.10: Comparison between axial load, F, and temperature adjusted axial load, $F_{adjusted}$, for (a) waler W1, (b) corner brace CCB1, (c) prop P1, and (d) prop P2. The construction activities indicated by vertical lines and shaded regions are the same as those annotated in Figure 4.7. Figure 4.11 window outlined by box in (d).

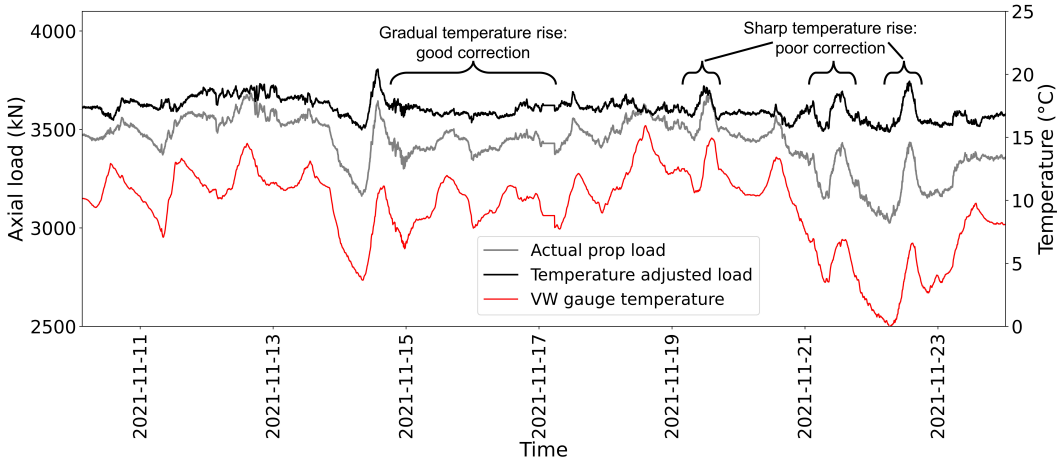


Figure 4.11: Exploded period from Figure 4.10d showing the daily cycling of load due to temperature effect and the effectiveness of the temperature compensation approach.

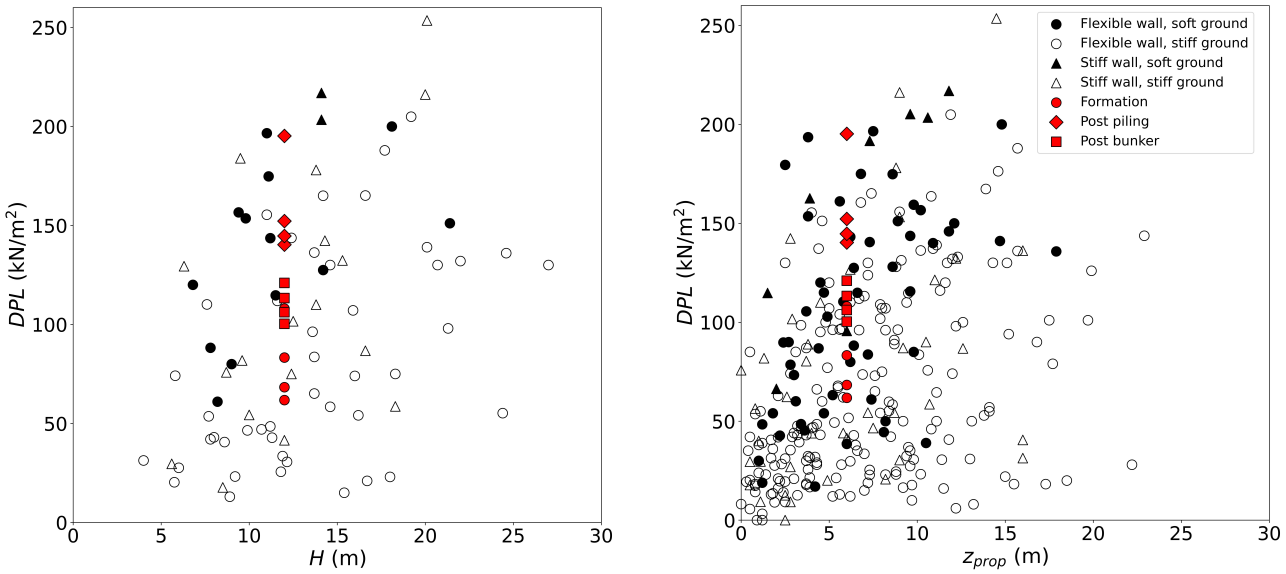
4.3.3 Comparison to case histories

To enable comparisons to previously published case history data, the level 2 frame member load data have been normalised as:

$$DPL = \frac{F_{adjusted,max}}{A_T} \tag{4.3}$$

where DPL is the maximum distributed prop load in kN/m^2 and A_T is the tributary area that is assumed to apply load to each member. The calculated DPL at formation level, post base piling, and following bunker construction are compared to those from 81 case histories published in Twine and Roscoe (1997) in Figure 4.12. Figure 4.12a compares the reported maximum DPL for each case to the excavation depth H and Figure 4.12b compares the reported DPL for each individual prop to the prop depth z_{prop}. While the published case history data in Figure 4.12 exhibit wide scatter, the reported DPL appear to show a weak positive correlation with H in Figure 4.12a, and with z_{prop} in Figure 4.12b. In general, props supporting deep excavations in soft ground conditions exhibit greater DPL values than those in stiff ground conditions. The maximum DPL occur following base piling and are calculated as 195 kN/m^2, 152 kN/m^2, 140 kN/m^2 and 145 kN/m^2 for B1, CCB1, P1 and P2 respectively. Of the values of DPL for over 300 prop members in Figure 4.12b, 86% fall below DPL = 140 kN/m^2 for prop P1. This

suggests a large proportion of lateral earth loads are transferred into the support structure, highlighting the low strength of the TF layers. The calculated DPL values are consistent with those reported for props supporting excavations in soft clays in Oslo (NGI (1962), Chicago (Swatek et al. (1972)), and Rotterdam (Tschebotarioff (1973)) (cases AF8, AF11, AF12, AF13, AF25, AF26 and AF27 in Twine and Roscoe (1997)).



(a) (b)

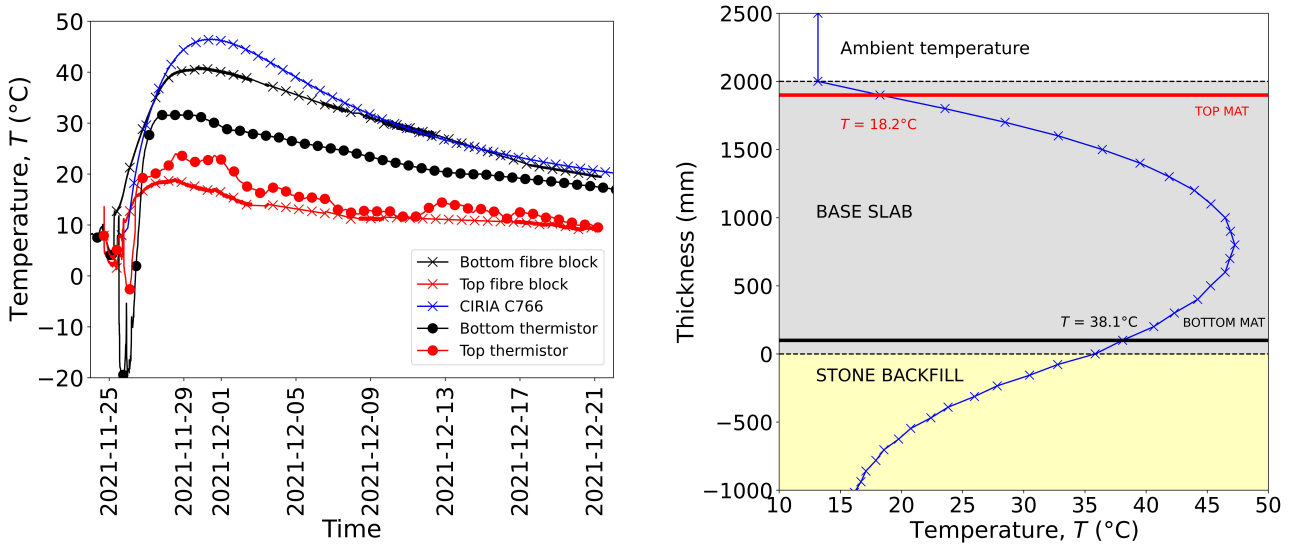
Figure 4.12: Comparison between present monitored data and previously published case history data reported in Twine and Roscoe (1997). (a) Variation of DPL with H at formation, post piling, and post bunker construction compared to largest DPL from each case, (b) variation of DPL with z_{prop} compared to case history data from all prop members.

4.4 Bunker base structural response

4.4.1 Base temperature response

The temperature series inferred from the top and bottom clamped FBG measurements using Eq. 3.16 is presented alongside that measured by the thermistors in the VW gauges $G_{E,B3}$ and VW gauges $G_{E,B1}$, and the CIRIA C766 (Bamforth (2018)) predicted peak temperature series in Figure 4.13a. There is good agreement between the temperature series inferred from the top mat clamped FBG and that measured by the adjacent thermistor ($G_{E,B3}$). Less fluctuation is measured by the clamped FBG due to the slight insulating effect of the flexible foam used to isolate the FBG from mechanically applied strain. While there is a difference in the peak tem-

perature inferred from the bottom clamped FBG and that measured by the bottom thermistor ($G_{E,B1}$) of 23%, the peak occurs at the same time, and the rate of temperature decrease is very similar. The disparity in temperature may be due to difficulties encountered when aligning the fibre length within the aluminium block, as very precise positioning is necessary to replicate the laboratory calibration test arrangement. This may also explain the small difference between measurements for the top instruments, with presence of small voids between the fibre and the aluminium block enabling some thermal expansion before the FBG is engaged, leading to a lower temperature prediction for the FBG. There is also some uncertainty surrounding the thermistor measurements due to their unusual transient response to becoming embedded within the wet concrete during the pour on 2021-11-25, as measured temperatures dropped to below 0°C. The problems could potentially be attributed to water from the concrete causing interference with the thermistor electrical systems.



(a) (b)

Figure 4.13: (a) Temperature series inferred from clamped FBG measurements and measured by thermistors. CIRIA C766 (Bamforth (2018)) predicted peak temperature series included for comparison. (b) CIRIA C766 (Bamforth (2018)) predicted peak temperature profile through ground bearing bunker base slab.

The CIRIA C766 (Bamforth (2018)) predicted peak temperature profile through the ground bearing bunker base slab is shown in Figure 4.13b. The peak temperature measured by each

of the bottom (40.5°C) and top (18.1°C) clamped FBGs agrees well with those predicted at the bottom (38.1°C) and top (18.2°C) rebar mat positions, providing confidence in the adopted temperature compensation strategy. The measured cooling rate is very consistent with that predicted using CIRIA C766 (Bamforth (2018)) in Figure 4.13a, providing further confidence in the application of this approach. The base slab temperature measurements show that providing 50% of the cementitious requirement as Ground Granulated Blast-furnace Slag (GGBS) regulated the generated peak temperature and slowed the rate of temperature increase. This was critical in ensuring thermal crack widths remained within acceptable limits.

4.4.2 Base strains

The development of the strain derived from each of the 18 FBGs with time immediately post casting of the concrete base are shown in Figure 4.14a and Figure 4.14b for the bottom and top mat respectively. The measured microstrain readings were zeroed 24 hours after the conclusion of the base pour to analyse base behaviour during concrete curing and assess the structural loads induced in the base during subsequent bunker wall construction. Data has been interpolated during periods where the logging system failed due to power supply issues. For both the bottom and top mat, there is good consistency between the individual strain readings such that the measurements are well-characterised by the average value. A comparison between the microstrains measured by the base embedment VW gauges $G_{E,B1}$ and $G_{E,B3}$, and those measured by the adjacent FBG to each gauge on the bottom and top mats is shown in Figure 4.14c. For the top mat, following a slight difference in induced microstrain during early curing, there is good agreement between the VW gauge measurements ($G_{E,B3}$) and the adjacent FBG measurements. For the bottom mat, the development of microstrain measured by the VW gauge ($G_{E,B1}$) follows a very similar trend to that measured by the adjacent FBG. The considerable difference in the amplitudes of measured microstrain on the bottom mat may be due to water from the concrete causing interference with the VW gauge electrical systems. The disparity may also be due to differences in temperature along the fibre profile, as a single

temperature series was used to compensate all FBG's along each of the top and bottom fibre lengths.

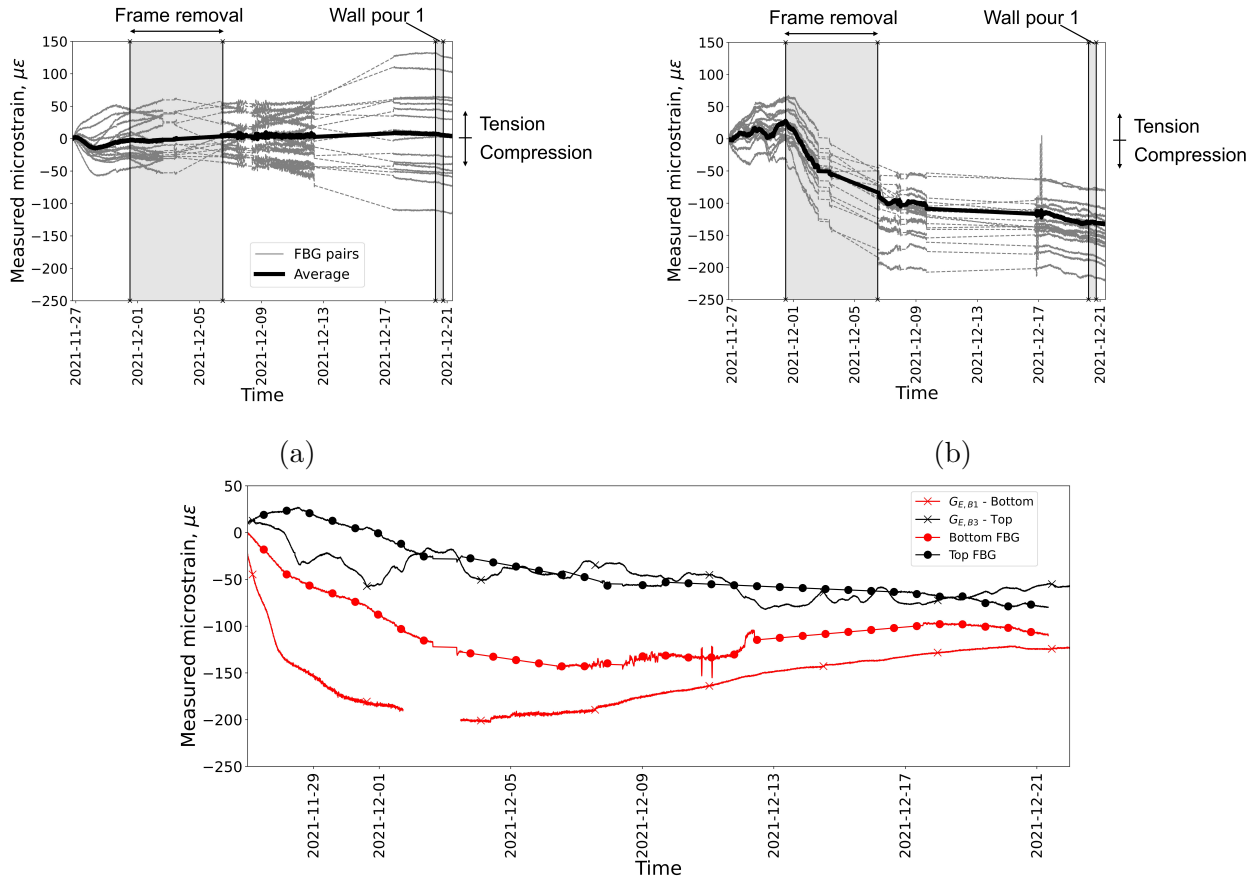
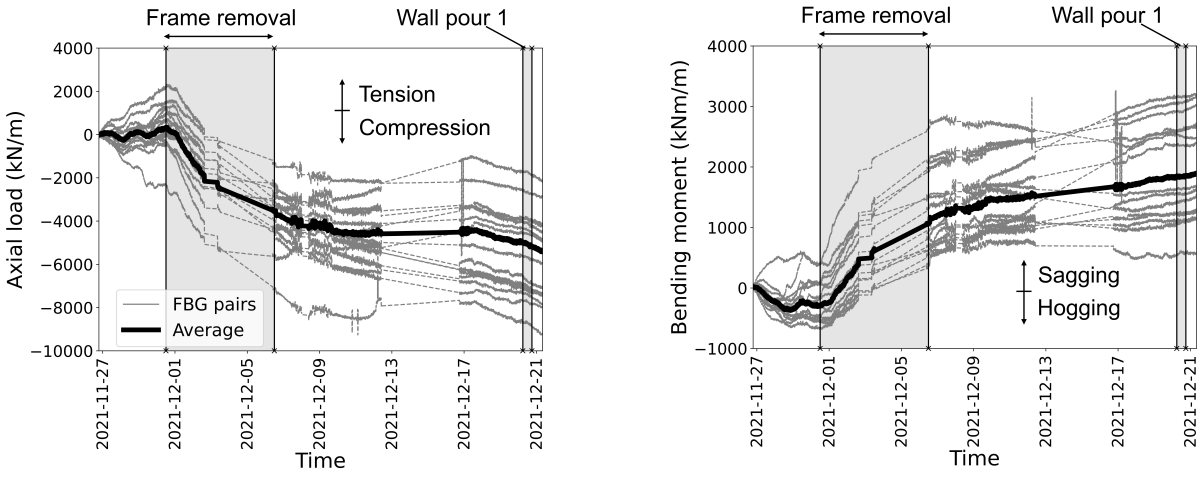


Figure 4.14: Time series of strains calculated from individual FBG measurements for (a) bottom mat, (b) top mat. (c) Comparison between microstrain measured by base embedment VW gauges $G_{E,B1}$ and $G_{E,B3}$, and measured by adjacent FBGs. Dashed sections indicate periods of interpolated data due to issues with the data logging system.

4.4.3 Axial load and bending moment time series

The axial load and bending moment data calculated from Eq. 3.12 and Eq. 3.13 are plotted in Figure 4.15a and Figure 4.15b respectively. From Figure 4.15a, a significant increase in axial compressive load is observed during the frame removal process, with an average value of approximately 2000 kN/m, due to re-distribution of loads into the base, followed by a more gradual longer-term increase during subsequent soil consolidation. A large sagging (positive) moment is observed during the frame removal process as shown in Figure 4.15b. This is caused by the redistribution of the frame loads into cofferdam bending which, in turn partly translates into

an applied moment on the bunker base. Thereafter, a gradual increase in sagging is observed as excess pore pressure dissipation increases the lateral pressure retained by the cofferdam. Little change in bending moment is observed during the first wall pour, with the large thickness and bending stiffness of the base slab leading to minimal load distribution across the slab width.



(a) (b)

Figure 4.15: Bunker base (a) axial load and (b) bending moment time series calculated from measured FBG microstrains.

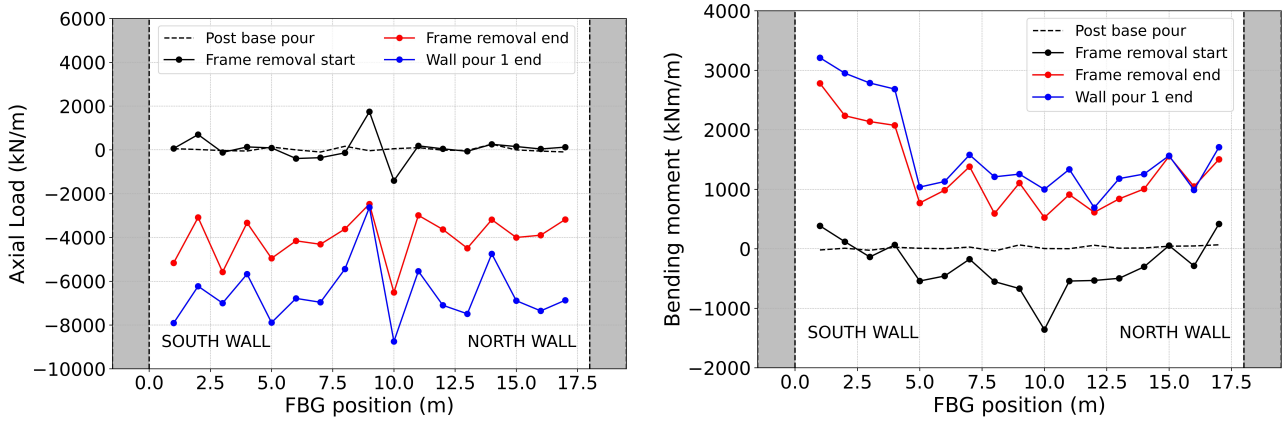
4.4.4 Axial load and bending moment profiles

The axial load and bending moment profiles across the bunker width at selected times are shown in Figure 4.16a and Figure 4.16b respectively. The increases in axial compressive load due to frame removal and longer-term consolidation are reasonably consistent across the bunker width, suggesting a uniform load distribution across the slab. Some variation in the axial load measurements is observed, particularly close to the centre of the slab, which may be caused by temperature differentials along the fibre profile. In future, this issue could be addressed by positioning additional thermistors or clamped temperature FBGs along the length of the fibre string.

During base curing, a hogging moment is induced in the bunker base. This is due to a differential shrinkage strain rate caused by the temperature differential across the 2 m base thickness shown in Figure 4.13. The insulating influence of the ground causes temperatures in

the lower portion of the base slab to reach a higher peak and to reduce slower, increasing the rate of reaction and consequently the rate of shrinkage. The hogging moment is at its largest at the centre of the slab and reduces towards the slab edges, as the reduction in insulation from adjacent slab sections at the perimeter causes a smaller temperature differential.

The increase in sagging moment during frame removal and long-term pore pressure dissipation is consistent with that observed in Figure 4.15b. The sagging bending moment is largest at the slab edges at the point of application and reduces towards the slab centre, emphasising the large bending stiffness of the slab. The moment applied to the south side of the slab is larger than that applied to the north which can be attributed to additional surcharge loading on this side caused by the construction of a 22 m high incinerator building to the south of the bunker excavation.



(a) (b)

Figure 4.16: Bunker base (a) axial load and (b) bending moment profiles across bunker width at selected times. Sign convention is as that defined in Figure 4.15.

4.5 Bunker wall structural response

4.5.1 Wall temperature response

The temperature series measured by each of the 10 VW gauge thermistors cast into the bunker walls is presented alongside the CIRIA C766 (Bamforth (2018)) predicted peak temperature series and predicted peak profile through the bunker wall in Figure 4.17. The CIRIA C766 (Bamforth (2018)) prediction was generated for the air-wall-ground system using the sheet for

ground bearing slabs. The temperature series data have been plotted until completion of the underground bunker section as their early-age periods are of most interest to analyse. Several of the thermistors exhibit an unusual transient response to becoming embedded in the wet concrete, which is consistent with the behaviour of the base VW thermistors reported in section 4.4.1. Again, this is likely due to water infiltration into the electrical systems. The thermistors positioned on the outer faces of the bunker walls measured greater temperatures throughout the displayed period than those on the wall inner faces due to the insulating influence of the combi-wall and ground. The outer face thermistor measurements were not influenced by daily fluctuations in temperature, while inner face thermistors measurements followed the ambient T trend closely at a reduced amplitude. The peak temperature measured by the level 1 thermistors ($T = 52.8$°C) is greater than those measured by the level 2 ($T = 38.6$°C) and level 3 ($T = 34.9$°C) thermistors. This is due to the increased insulation provided around the level 1 thermistors close to the centre of the first wall pour, while the level 2 and level 3 thermistors are positioned close to the second pour invert and top level respectively. Interestingly, the occurrence of the second wall pour on 24/01/2022 causes a small increase in the temperatures measured by the level 1 thermistors due to thermal conductance of thermal energy generated during concrete curing through the first wall pour.

The occurrence of the peak temperature and the measured cooling rate for each thermistor are consistent with the CIRIA C766 (Bamforth (2018)) prediction. The CIRIA C766 (Bamforth (2018)) peak generated temperature predictions on both the outer ($T = 35.1$°C) and inner ($T = 17.6$°C) faces show reasonable agreement with those measured by the outer (level 1 $T = 52.8$°C, level 2 $T = 38.6$°C, level 3 $T = 34.9$°C) and inner (level 1 $T = 19.2$°C, level 2 $T = 29.2$°C, level 3 $T = 22.9$°C) thermistors respectively. The monitored bunker wall temperature data provides some interesting insights into the insulating influence of the retained combi-wall and adjacent ground. These can be applied to thermal crack width design for RC deep excavation walls.

These findings also support the application of the CIRIA C766 (Bamforth (2018)) ground slab temperature prediction to underground RC wall design.

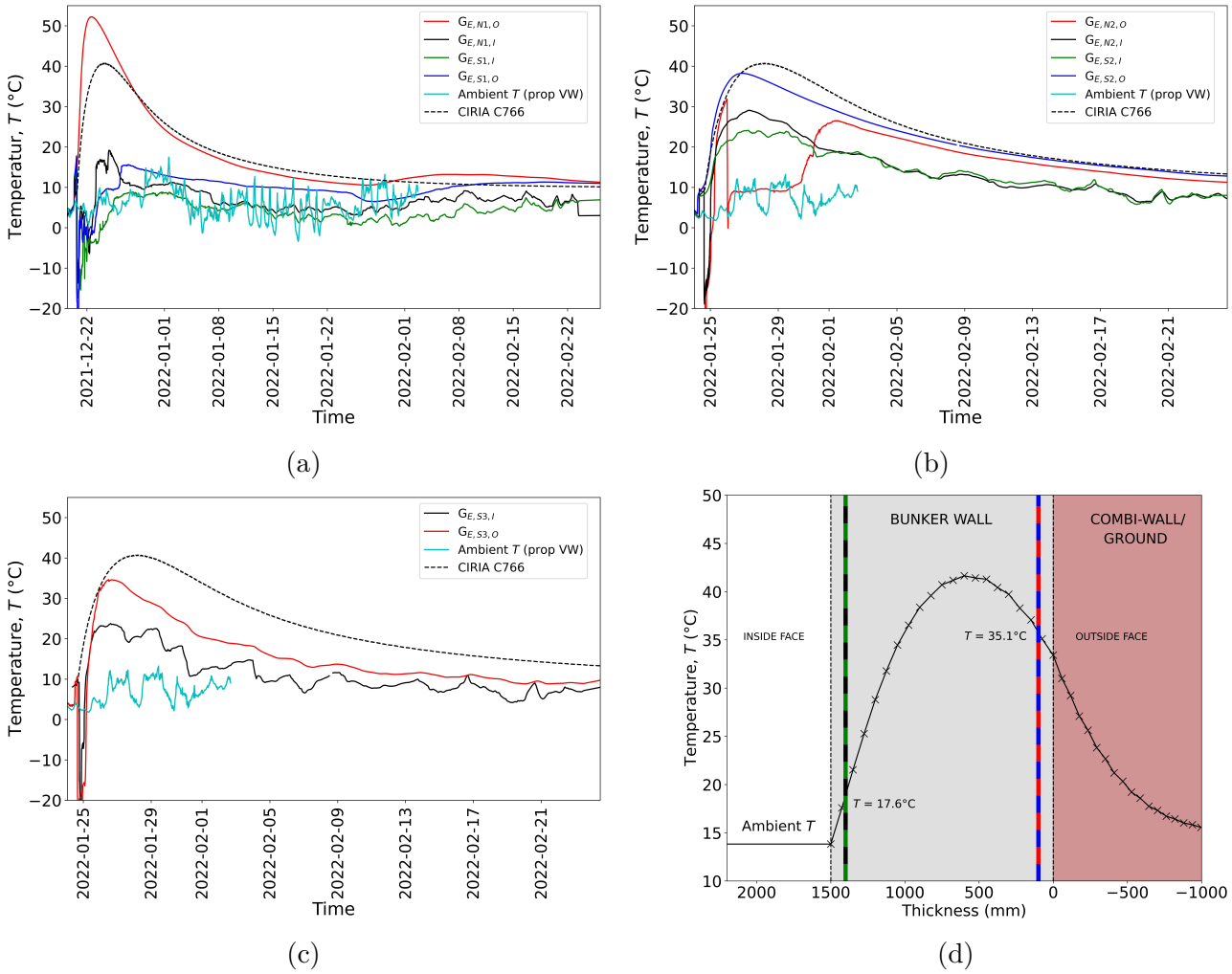


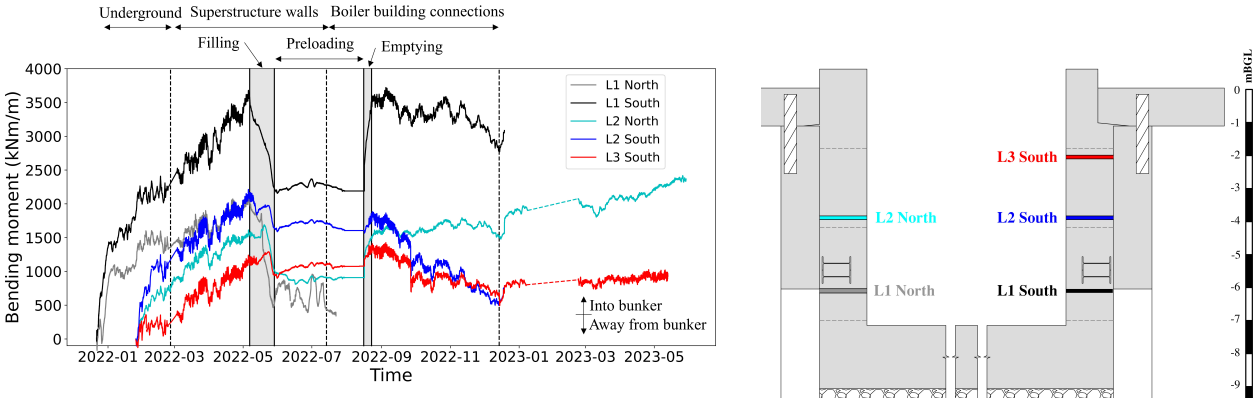
Figure 4.17: Bunker wall temperature development compared to CIRIA C766 (Bamforth (2018)) peak temperature prediction for (a) level 1 gauges (6.3 mBGL), (b) level 2 gauges (3.9 mBGL) and (c) level 3 gauges (2.1 mBGL). (d) CIRIA C766 (Bamforth (2018)) peak temperature profile prediction through bunker wall.

4.5.2 Wall bending moments

Bending moment data for each of the VW gauge pairs calculated from Eq. 3.13 are plotted in Figure 4.18. Several of the bending moment series finish early due to VW gauge or cable damage. Prior to bunker preloading, a consistent increase in bending moment towards the excavation is observed due to transfer of load from the cofferdam into the bunker structure. These moments continue to increase at a steady rate due to subsequent pore pressure dissipation, which is consistent with the behaviour observed in the bunker base. The largest bending

moment values are recorded at the lowest monitoring point because of the greater associated lever arm of the applied cofferdam loads. The larger bending moments measured in the south bunker wall prior to preloading can be attributed to additional surcharge loading on this side, which is caused by the construction of a 22 m high incinerator building to the south of the bunker which began on 16/12/2021.

The filling of the bunker to a depth of 15 m caused a large reduction in the measured bending moments due to the internal hydrostatic fluid pressure exerting a moment on the walls. The largest moment reductions occurred at the level 1 position due to the application of the largest hydrostatic loads at the greatest water depths. During the preloading stage, less temperature induced fluctuation in the measurements occurs due to the insulating effect of the water on the inner wall face. During bunker emptying following preloading, the largest moment increases occurred at the lowest level as the hydrostatic fluid pressures were removed.



(a) (b)

Figure 4.18: (a) Bunker wall bending moment time series calculated from embedment VW gauge pairs. (b) Section through bunker showing VW gauge pair positions.

During the subsequent months, decreases in the wall moments on the south side were observed. This was due to connections being constructed between the south bunker wall superstructure and the adjacent boiler building, which propped the wall at 3 different superstructure levels, reducing the moments measured in the underground south bunker wall section. The reduction may also be due to the decommissioning of the dewatering system on 30/08/2022

which led to large hydrostatic uplift pressures being applied to the base underside which induces an outward wall bending moment at the very stiff fixed base to wall connections. Following the completion of the bunker to boiler building connections, a small long term increase in moments is observed due to pore pressure dissipation during consolidation.

4.6 Water levels

The observed water level time series for all piezometers are shown in Figure 4.19. For reference, the corresponding time history of the total pumped flow rate, Q, is also plotted on a secondary axis. The data are plotted until two months after the completion of the underground bunker section, once the reduced water level had been brought up to the underside of the RC bunker base. The site water table outside the excavation ($P_{O,U}$) remained consistently high throughout construction, varying between 2-3 m above ordnance datum (AOD), due to the close proximity of the river Mersey. Initially three pumping wells were operational, with an average Q = 5.5 l/s, reducing the water table within the bunker ($P_{I,1}$, $P_{I,2}$) to approximately -5.5 m AOD. This was still 0.7 m above the estimated formation depth, which led to the mobilisation of a fourth pumping well on 01/09/2021, which increased Q to 7 l/s and reduced the level to -7 m AOD. During unexpected shutdowns of the pumping system (reflected by $Q = 0$), the water level increased rapidly at a rate of 100 mm/min. To reduce the risk to personnel within the excavation and prevent damage to plant, the capacity of the pumping system was increased further by repurposing the $P_{I,1}$ monitoring well for a fifth pumping well on 07/09/2021. This reduced the water level to -8.5 m AOD and increased Q to 8 l/s.

The internal ($P_{I,2}$) and external ($P_{O,L}$) water levels in the lower GT sands show very similar trends except $P_{I,2}$ is consistently $\sim$1.5 m higher indicating groundwater is being drawn into the bunker through seepage beneath the cofferdam toe. The water level in the GO sand layer remains at the site water table level, indicating the GT clay layer acts as a highly effective seal to prevent flow between the GO and GT granular layers. The mobilisation of bunker piling

towards the monitoring well locations (early October 2021) caused an increase in water level of ∼2.2 m in both $P_{I,2}$ and $P_{O,L}$, despite no apparent change in system setup and a constant $Q = 8$ l/s. This reduction in performance may be due to the disturbance and restriction of flow passages in the ground adjacent to the monitoring wells caused by the vibratory piling equipment. The dewatering and water level monitoring schemes directly mitigated and helped manage the risks of flooding, excessive pumping rates and wall infiltration posed by the deep excavation and bunker construction.

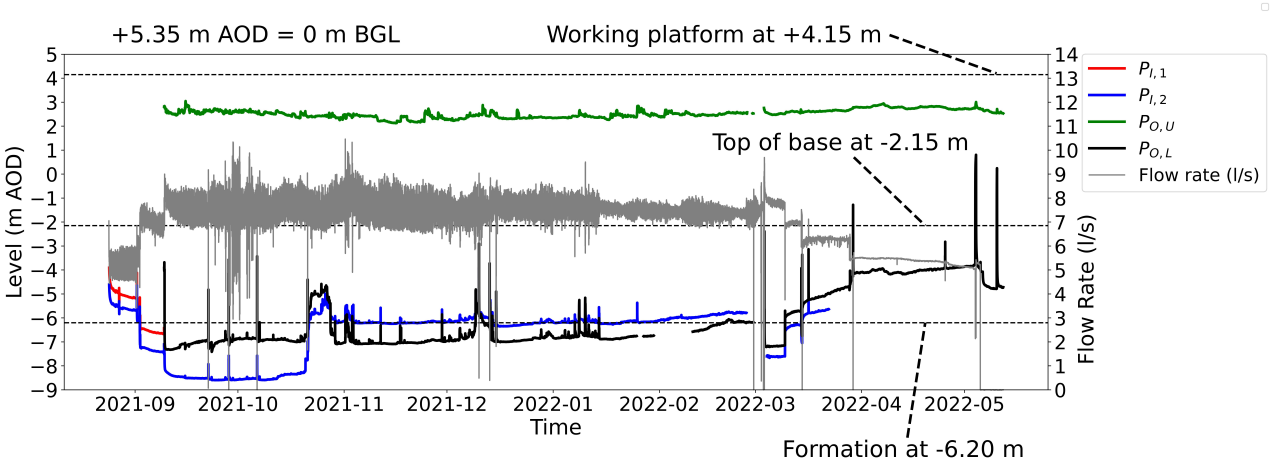


Figure 4.19: Piezometer water level data and total pumped well flow rate.

4.7 Summary of key findings

This chapter has presented the findings of a comprehensive instrumentation layout to monitor the performance of the deep excavation support structures, dewatering system and RC bunker structure during construction. The key findings from this work are summarised below:

- Measured wall displacements were well-represented by average values reported elsewhere in the literature and were close to lower bounds reported for deep excavations in soft clays; these results highlight the potential applicability of existing solutions and design methods to combi-wall design in soft UK soils.
- The axial loads measured in the bracing members increased steadily during excavation with the largest load developed in the corner brace (2300 kN) due to its relatively large tributary length and it being at an angle to the cofferdam wall. As the lifetime of the

support structure occurred from autumn to winter, a significant decrease in the frame member loads occurred due to seasonal cooling. The calculated FF values for members CCB1, P1 and P2 are reasonably consistent with the 10% – 25% range recommended in Twine and Roscoe (1997), based on previous sheet pile wall case histories. The value of $FF = 47\%$ calculated for member W1 aligns closely with the recommendation of 50% for members supporting stiff walls in stiff ground. This is likely to be due to the high degree of restraint provided by the C1 end connection and the increased wall stiffness at the corner of the excavation.

- Vibratory piling internally within the excavation cause an increase to the horizontal wall displacements of up to 111% and increases in level 2 frame member loads of between 700 – 2100 kN, revealing the importance of considering the full construction process on the support system performance.
- There is good agreement between the temperature series inferred from the base top mat clamped FBG and that measured by the adjacent thermistor. The peak temperature measured by the base bottom mat clamped FBG is 23% lower than that measured by the bottom thermistor, which can be attributed to difficulties encountered when aligning the fibre length within the aluminium block. The peak temperature and cooling rate measured by each of the bottom and top clamped FBGs agrees well with the CIRIA C766 (Bamforth (2018)) predictions.
- A significant axial compressive load was observed in the bunker base during the frame removal process due to re-distribution of frame loads into the base. Subsequent soil consolidation caused gradual increases in axial compression thereafter. This behaviour was consistent with that observed in the bunker walls, with wall bending moments increasing gradually over time.
- Continuous groundwater pumping, with flow rates consistently above 7 l/s, was neces-

sary to retain the internal excavation water level below formation level, due to seepage occurring below the cofferdam toe. Piling within the excavation led to a reduction in the performance of the pumping system due to the introduction of additional flow paths.

5 | Numerical model development

5.1 Introduction

The following chapter describes the development of numerical models for the PROTOS EFW bunker deep excavation. The models are developed in the commercially available FE packages PLAXIS 2D and PLAXIS 3D (Brinkgreve et al. (2022)) because they are arguably the most commonly adopted in industry. The numerical models are developed to enable comparisons to the field monitoring data, to assess the ability of the models to replicate observed field behaviours. Firstly, the input parameters for the soil constitutive models used to model each soil layer are determined from site investigation data and laboratory tests performed on samples retrieved from the excavation. The soil constitutive model parameters are used to simulate laboratory tests. The simulated test data are compared to real laboratory test data to calibrate and refine the initial parameter values. The selection of the structural models for the wall and support structures for both the 2D and 3D models is then discussed, and the numerical model construction sequence which most closely simulates its real counterpart is outlined. Finally, the development and refinement of the FE mesh for the 2D and 3D models is discussed.

5.2 Constitutive soil modelling

Components of the PROTOS bunker structure penetrated several ground layers (Figure 3.5). For the numerical analyses, the inferred stratigraphy from the ground investigation data was simplified into five distinct layers as shown in Figure 5.1. For simplicity, the thin peat (P) layers were not explicitly modelled and the glacial till layer was evenly divided into cohesive clay (GT-C) and cohesionless sand (GT-S) layers. The five soil layers were modelled using either the Mohr-Coulomb (MC), the Hardening Soil (HS) or the Hardening Soil with small strain stiffness (HSS) constitutive models as these models are applicable to a variety of soil types and are widely adopted in industry for the numerical analysis of deep excavations as reported in the

geotechnical literature in Section 2.6.2. The three ground models employed for the numerical modelling scheme are shown in Table 5.1. These were used to compare the influence of using each of the MC, HS and HSS constitutive models. For ground models 1 and 2, each of the five layers is modelled with the same soil constitutive model. For ground model 3, only the TF and GO materials were modelled using the HSS consitutive model, as these materials were assumed to most influence the behaviour of the deep excavation, and limited SI for the MG, GT-C and GT-S layers meant some HSS model parameters could not be determined.

While the ground investigation schemes in 2018, 2020 and 2021 described in Section 3.2.2 could be used to determine several model input parameters for each layer through direct determination or the use of empirical relationships, it was decided that additional laboratory elemental tests would be performed on samples collected from the TF and GO layers. This would help to more accurately determine parameters for the more complex HS and HSS models by eliminating the requirement to use weakly correlated empirical relationships and by providing stress-strain curves for model calibration. Due to cost restraints, only samples from the TF and GO layers were selected for laboratory testing. These layers were assumed to most influence the behaviour of the deep excavation structure. The soil sampling process, the laboratory elemental scheme and the determination of parameters for each of the selected soil constitutive models are discussed in more detail in this section.

Table 5.1: Summary of each ground model (GM) employed for the numerical modelling scheme.

Soil layer	**GM 1 (MC)**	**GM 2 (HS)**	**GM 3 (HSS)**
MG	MC	HS	HS
TF	MC	HS	HSS
GO	MC	HS	HSS
GT-C	MC	HS	HS
GT-S	MC	HS	HS

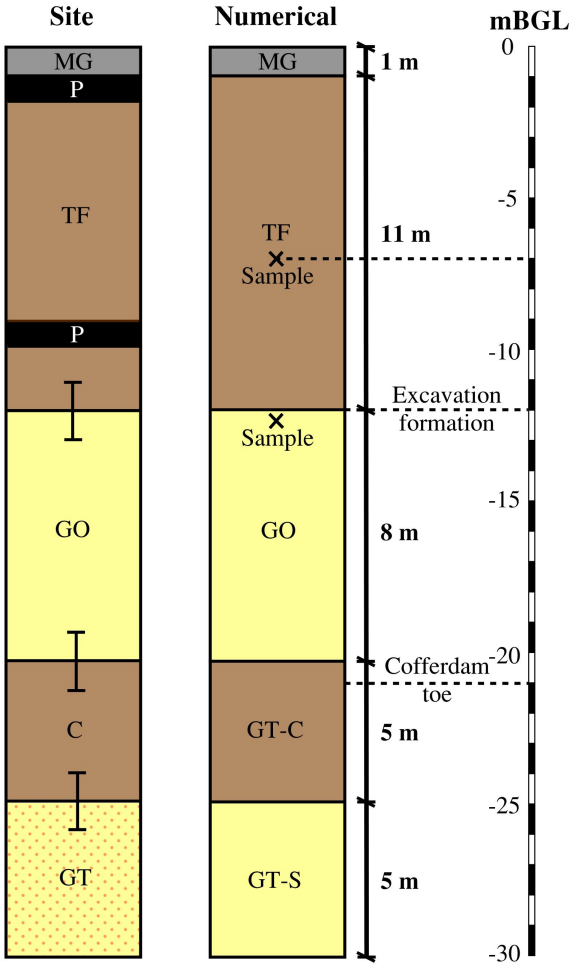


Figure 5.1: Assumed ground stratigraphy for numerical analyses. Sampling levels for laboratory elemental tests indicated by crosses.

5.2.1 Field soil sampling

The TF sample was taken in the form of a block sample, with efforts made to minimise disturbance of the sample during retrieval, transportation, and storage to attempt to preserve the *in situ* stress conditions within the sample. The block sample was taken close to the centre of the TF layer, at a level of -7 mBGL as shown in Figure 5.1. Photographs of the block sampling process are presented in Figure 5.2. A small excavator removed soil either side of a 400 mm x 400 mm marked area. A hand saw was then used to cut the base of the sample before the sample was wrapped in shrink wrap. The sample was then placed inside a timber box and expanding foam was inserted into voids on all sides of the sample to maintain stresses. While wax is commonly used to ensure water-tightness, it was deemed unnecessary here as the soil was

to be tested within several weeks of sample retrieval and difficulties would be encountered in avoiding disturbance during the wax removal process due to the soft nature of the TF material.

The granular GO sample was retrieved at excavation formation. This involved simply shovelling the material into a timber box. For the laboratory testing the sample was reconstituted to a specified bulk density γ_{bulk}, and moisture content w. These parameters were determined from empirical recommendations using the 2021 CPT data presented in Section 3.2.2.



(a) (b) (c)

Figure 5.2: Photographs of block sampling process for TF layer. (a) Sample trimmed with hand saw, (b) sample wrapped in shrink wrap, (c) voids in box filled with expanding foam.

5.2.2 Laboratory elemental testing

For the TF layer sample, the following laboratory elemental tests were specified:

- **TF triaxial 1**: Consolidated undrained (CU) triaxial, compressive, $\sigma'_1 = 77$ kPa, $\sigma'_3 = 27$ kPa, K_0 consolidated.
- **TF triaxial 2**: Consolidated undrained (CU) triaxial, compressive, $\sigma'_1 = 153$ kPa, $\sigma'_3 = 101$ kPa, K_0 consolidated.
- **TF CRS**: Constant rate of strain (CRS) one-dimensional compressive load test.

Here, σ'_1 and σ'_3 are the confining pressures in the axial direction and radial direction respectively at the end of the consolidation stage. K_0 consolidation involves adjusting axial load, cell pressure and pore pressure during the consolidation phase to maintain zero radial strain leading to one-dimensional consolidation. While this consolidation approach is more difficult to implement in the laboratory than isotropic consolidation, it most closely mimics *in situ*

conditions.

For the GO layer sample, the following laboratory elemental tests were specified:

- **GO triaxial 1**: Consolidated drained (CD) triaxial, compressive, $\sigma'_3 = 50$ kPa, isotropically consolidated.
- **GO triaxial 2**: Consolidated drained (CD) triaxial, compressive, $\sigma'_3 = 100$ kPa, isotropically consolidated, seismic bender element test.
- **GO triaxial 3**: Consolidated drained (CD) triaxial, compressive, $\sigma'_3 = 150$ kPa, isotropically consolidated, local radial strain measurement.
- **GO oedometer**: One-dimensional compressive oedometer test with single unload-reload stage.

Here, σ'_3 is the confining isotropic cell pressure at the end of the consolidation stage and isotropic consolidation involves simply applying a hydrostatic cell pressure to the sample prior to the shearing stage. Radial strain measurement was included for GO triaxial 3 to determine a value for Poisson's ratio ν. A vertical bender element was fitted to the sample for GO triaxial 2 to measure V_s and correlate this to a value of G_0. Often laboratory tests are performed on multiple samples taken from different depths to determine whether any variation in soil parameters within each layer is present, enabling depth profiling of each parameter. However for this research only one sample was retrieved and tested for each of the TF and GO layers due to the high cost associated with additional laboratory testing. Also the relatively small thickness of these strata compared to other reported case histories meant that it was reasonable to assume that some soil parameters remain constant throughout the depth of each layer. The laboratory elemental tests were performed by Geolabs Ltd.

Some of the key parameter relationships from the laboratory testing scheme are presented in Figure 5.3. The triaxial test deviator stress q data are plotted against both the full test axial strain ε_a range and a small strain region, to provide information about the strength (determined

from the deviator stress at failure q_f) and the small strain stiffness of the material. Both the TF and GO material exhibit an initially stiff response, with stiffness degrading rapidly with increasing ε_a thereafter. These small strain stiffness data are crucial for effectively calibrating constitutive soil models to most accurately simulate *in situ* ground conditions. Interestingly, the q-ε_a response for TF triaxial 2 in Figure 5.3a indicates dilatant behaviour for the TF material, as q continues to increase after reaching q_f, due to dilatancy reducing excess pore pressures and thus increasing effective stresses. The results of the laboratory testing scheme are used alongside data from the *in situ* ground investigation scheme outlined in Section 3.2.2 to determine the input parameters for the MC, HS and HSS soil constitutive models in Section 5.2.3, Section 5.2.4 and Section 5.2.5 respectively.

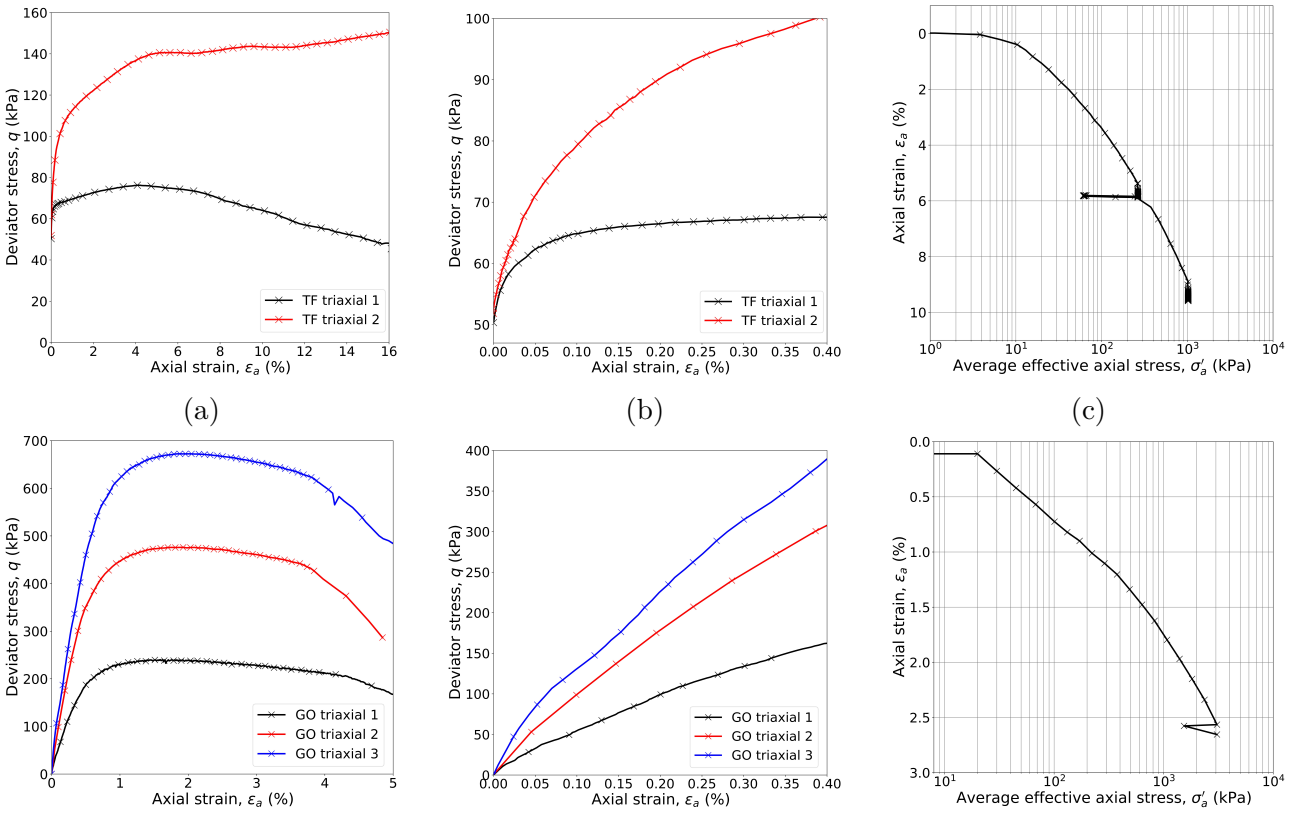


Figure 5.3: Key parameter relationships from laboratory elemental testing scheme: (a) & (b) TF triaxial test q - ε_a plots, (c) TF CRS test ε_a - σ'_a plot, (d) & (e) GO triaxial test q - ε_a plots, (f) GO oedometer test ε_a - σ'_a plot.

5.2.3 Mohr-Coulomb Model parameter determination

The main five input parameters for the MC constitutive model are summarised in Table 2.1. In addition to these, the material unit weight γ, and the initial state soil parameters OCR and K_0 are required. Firstly, data from the ground investigation schemes in 2018, 2020 and 2021 were analysed to determine whether γ or any initial state or MC model parameters could be obtained. The soil unit weight was estimated from the correlation proposed in Robertson (2010) as:

$$\gamma = \gamma_w(0.27\,log(R_f) + 0.36\,log\left(\frac{q_t}{R_f}\right) + 1.236) \tag{5.1}$$

where γ_w is the unit weight of water, R_f is the CPT friction ratio and q_t is the corrected cone tip resistance. Individual density tests performed on samples are compared to the γ profile in Figure 3.7, with a reasonable fit to the profile observed. OCR was estimated from the correlation proposed in Mayne and Campanella (2005) as:

$$OCR = \frac{k_1(q_t - \sigma'_{v0})^{m'}}{\sigma'_{v0}} \tag{5.2}$$

where k_1 is a compressibility dependant constant, σ'_{v0} is the in situ effective overburden pressure and m' is a power law exponent related to grain size. The inferred OCR profile is shown in Figure 3.4. The effective angle of friction ϕ', was estimated from the correlation proposed in Kulhawy and Mayne (1990) using Equation 3.2. However, this correlation can only be applied to raw CPT data for granular materials as shown in Figure 3.4, meaning additional laboratory tests are necessary to determine ϕ' for cohesive materials. K_0 was then calculated for the granular material layers using Equations 2.7 and 2.8.

While the undrained shear strength s_u, is not a direct input parameter for the MC model, it is important to compare the available strength predicted using the MC failure envelope governed by the effective cohesion c', and ϕ', to s_u as an upper limit, to prevent strength overprediction. s_u was estimated using Equation 3.1, using a site specific N_{kt} value which was correlated to

UU triaxial tests as shown in Figure 3.4. Dilatancy angle ψ for each layer was calculated from ϕ' as recommended in Brinkgreve et al. (2022) as:

$$\psi = \phi' - 30^{\circ} \tag{5.3}$$

The final MC model input parameter that was estimated using the ground investigation data was the secant stiffness E_{50}. E_{50} is the secant modulus taken through the point at which $q = q_f/2$ from the deviator stress at the start of shearing q_i (zero for isotropically consolidated samples). Prior to the availability of laboratory triaxial test data, Hooke's law was applied to the inferred G_0 from the seismic CPT test in the bunker area to obtain an estimate of E_0. Obrzud (2010) recommends taking E_{50} to be between one-half and one-sixth of E_0 depending on the material type. While this provided an initial estimate of E_{50}, the approach incorporates significant uncertainty. To address this issue, it was decided to directly determine E_{50} using the results of laboratory tests.

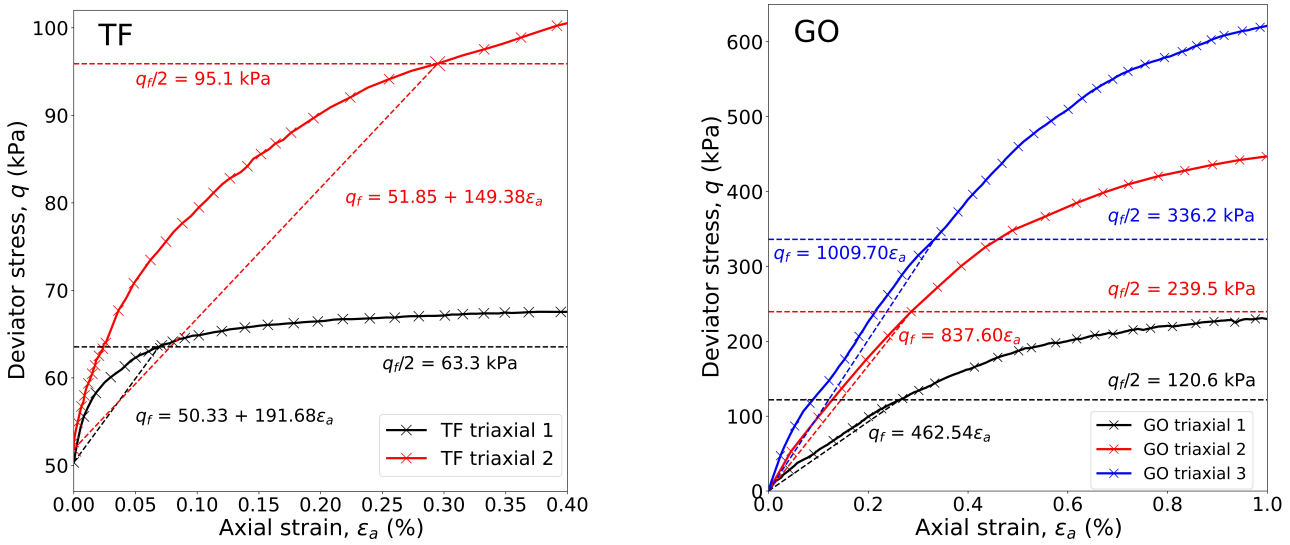
While several of the required parameters were determined using the ground investigation data, values of c' and ϕ' for modelling the failure envelope in cohesive layers were absent, and the inferred E_{50} for each layer was highly unreliable. These parameters were therefore determined for the TF and GO layers from the results of the laboratory testing scheme outlined in Section 5.2.2.

Figure 5.4 shows the calculation of E_{50} from q-ε_a data from each of the triaxial tests. For the CU triaxial tests on the TF material, the calculated stiffness is the undrained secant modulus E_{50}^u. The drained stiffness modulus E_{50} was calculated from E_{50}^u using the equation in Obrzud (2010) as:

$$E_{50} = \frac{2(1+\nu)E_{50}^u}{3} \tag{5.4}$$

Unusually, E_{50} for TF triaxial 1 is larger than that for TF triaxial 2. Typically stiffness increases with depth (and hence confining pressure) as reported in Brinkgreve et al. (2022). This is likely due to disturbance to the soft material sample occurring during retrieval, which caused a

reduced q_f when the material was consolidated using smaller stresses, which drives the high stiffness calculation. Therefore, E_{50} calculated from the results of TF triaxial 2 was assumed throughout the full layer thickness. E_{50} for the GO material was taken as that calculated from the results of GO triaxial 2, as the test consolidation pressure most closely replicated the *in situ* stress state at the depth from which the sample was retrieved.



(a) (b)

Figure 5.4: Stiffness determination from triaxial laboratory tests: (a) E_{50}^u for TF material samples and (b) E_{50} for GO material samples.

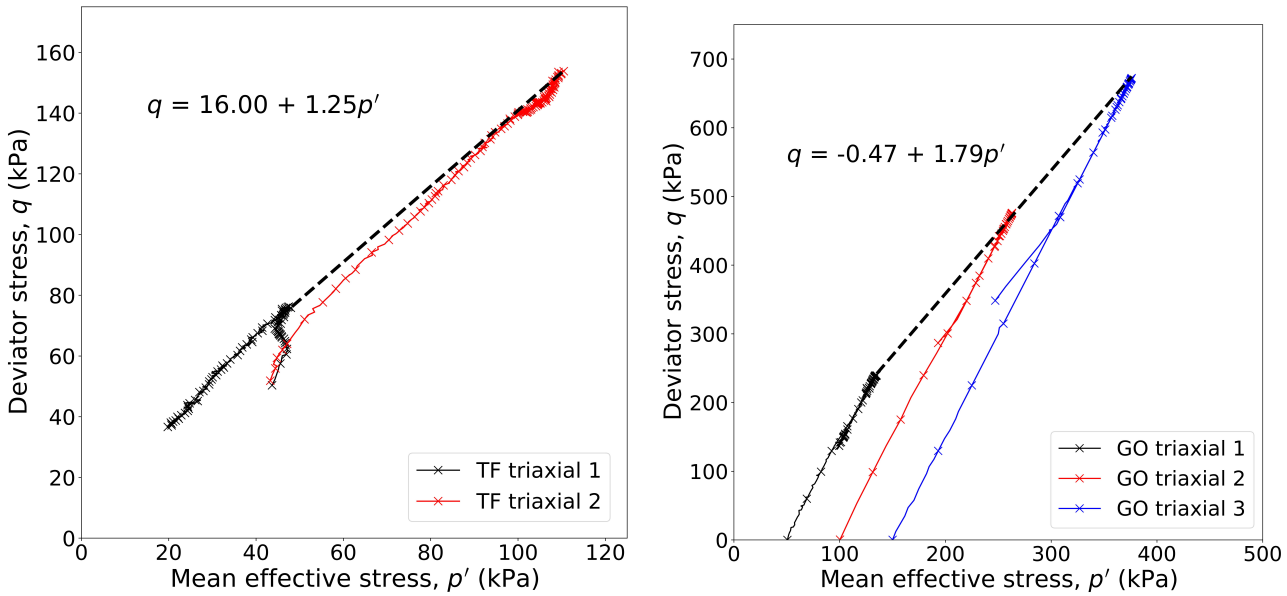
c' and ϕ' were determined by first plotting the MC failure envelope in q - p' space as shown in Figure 5.5. The gradient M^*, and intercept c^*, calculated in q - p' space were then used to determine c' and ϕ' using the equations in Obrzud (2010) as:

$$\phi' = sin^{-1}\left(\frac{3M^*}{6 + M^*}\right) \tag{5.5}$$

$$c' = \frac{c^*(3 - sin\ \phi')}{6\ cos\ \phi'} \tag{5.6}$$

The parameters were calculated as $c' = 7.7$ kPa and $\phi' = 31.1°$ for the TF material data in Figuree 5.5a and as $c' = 0$ kPa and $\phi' = 43.5°$ for the GO material data in Figure 5.5b. The GO ϕ' determined from the triaxial tests is reasonably consistent with that inferred from the CPT data in Figure 3.4. K_0 was then calculated for the TF material using Equations 2.7 and 2.8.

ν for the GO material was calculated using the axial and radial strain measurements from GO



(a) (b)

Figure 5.5: MC failure envelope plotted in q - p' space determined from triaxial laboratory tests on (a) TF material samples and (b) GO material samples.

triaxial 3 and is presented in Figure 5.6. The ν calculation is valid up until $\varepsilon = 0.4\%$. Above this strain value the angled shear plane deformation caused the radial strain measurement instrument to distort. The approximate $\nu = 0.25$ is in good agreement with the widely adopted recommended values in Brinkgreve et al. (2022). This justified adopting the recommended ν values in Brinkgreve et al. (2022) for the other strata.

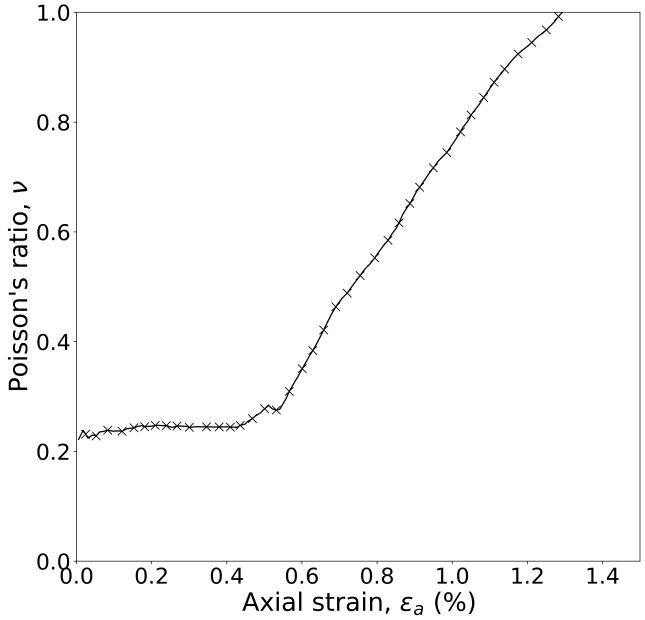


Figure 5.6: Poisson's ratio ν, against axial strain ε_a, for GO triaxial 3 test.

The majority of the density, initial soil state and MC input parameters for the less critical made ground (MG), glacial till clay (GT-C) and glacial till sand (GT-S) layers were determined from the CPT correlations in Figure 3.4 and Figure 3.7, and other the other empirical relationships and recommendations presented previously in this section. c' for the granular MG and GT-S layers was assumed to be zero. In the absence of c' and ϕ' values for the GT-C layer to predict the MC failure envelope, the total stress parameter s_u was used to define material strength. While this typically leads to poorer deformation prediction due to the absence of stress dependent strength, it provides a safe upper limit which cannot be exceeded. The use of s_u to govern material strength is defined as an Undrained B analysis in PLAXIS, whereas the use of the effective strength parameters c' and ϕ' is defined as an Undrained A analysis. In the absence of a ϕ' value for the GT-C layer, the assumption was made that $K_0^{NC} = 0.5$. Although c' values for the granular materials were determined as being approximately zero, non-zero values were inputted to avoid distortion and "flying" of FE elements when unloaded during excavation simulation. The soil permeabilities k, were taken as $k = 1$ x 10^{-4} m/day and $k = 1$ m/day for the cohesive and granular materials respectively. A summary of the input parameters for each of the soil layers in Figure 5.1 is presented in Table 5.2.

Table 5.2: Summary of density, initial soil state and MC model input parameters for each soil layer in Figure 5.1.

Soil layer	**MG**	**TF**	**GO**	**GT-C**	**GT-S**
PLAXIS drainage type	Drained	Undrained A	Drained	Undrained B	Drained
γ (kN/m^3)	18	15	18	18	19
γ_{sat} (kN/m^3)	20	19	20	20	21
E_{50} (MPa)	50.0	12.4	83.8	80.0	100.0
ν (-)	0.25	0.25	0.25	0.25	0.25
c' (kPa)	1.0	7.7	1.0	-	1.0
ϕ' (°)	43.0	31.1	43.5	-	40.0
s_u (kPa)	-	-	-	100	-
ψ (°)	13.0	1.1	13.5	1.0	10.0
OCR (-)	10.0	1.4	3.5	4.0	3.0
$K_{0,NC}$ (-)	0.32	0.48	0.31	0.50	0.36
$K_{0,OC}$ (-)	1.54	0.57	0.73	1.00	0.73

5.2.4 Hardening Soil Model parameter determination

The input parameters for the HS constitutive model are summarised in Table 2.2. The parameters that were to be determined in addition to those defined in Table 5.2 were E_{oed}, E_{ur}, m, p_{ref} and R_{fa}. For the TF and GO materials, E_{oed} was calculated from the results of the CRS and oedometer tests respectively. By determining the tangential gradient of the σ'_a - ε_a curve at the ε_a corresponding to the *in situ* effective stress σ'_v, E_{oed} was calculated as 5.80 MPa and 26.80 MPa for the TF sample and GO sample respectively. For the MG, GT-S and GT-C layers, E_{oed} = E_{50} as recommended in Obrzud (2010). Typically, accurate E_{oed} definition is less important than that for E_{50} for deep excavation applications as hardening and softening responses are largely governed by shearing behaviour rather than compressive behaviour. Conversely for bearing foundation design, accurate E_{oed} definition is important due to the system response being governed by compressive behaviour. In the absence of unload-reload stages for the TF and GO triaxial tests due to cost and time implications, it was assumed that $E_{ur} = 3E_{50}$ as recommended in Obrzud (2010).

The power exponent m governs the stress dependency of stiffness according to a power law and was calculated as the gradient of the linear approximation to triaxial test points plotted as $\ln(E_{50})$ against x_1 defined as:

$$x_1 = \frac{\sigma'_3 + c' \cdot cot(\phi')}{p_{ref} + c' \cdot cot(\phi')} \tag{5.7}$$

Here, p_{ref} is taken as σ'_3 from the test which consolidates the sample to its approximate *in situ* σ'_v. The combination of the inputted E_{50} and p_{ref} is used to simulate the variability in stiffness with stress level throughout each layer. m was calculated using this approach for the GO material as $m = 0.69$, which is in good agreement with both the range of $0.55 < m < 0.7$ for well-graded sand in von Soos (1991), and the typical m values observed for 17 sands and gravels presented in Benz (2007). m for the TF material could not be determined using this approach due to the issue with E_{50} being larger for the test with lower σ'_3 as described

in Section 5.2.3. m for the other strata were determined using empirical relationships in von Soos (1991) and Viggiani and Atkinson (1995) for the cohesive layers and in von Soos (1991) and Benz (2007) for the granular layers. The HS model feature of stress dependent stiffness governed by m is highly advantageous over the MC model single stiffness input for accurate ground deformation prediction.

For the TF and GO materials, the reference stress p_{ref} was taken to be σ'_3 from the triaxial test which consolidates the sample to its approximate *in situ* σ'_v. In the absence of triaxial test data, p_{ref} = 100 kPa for the other strata as recommended in Brinkgreve et al. (2022). The failure ratio R_{fa} = 0.9 was taken for all materials as recommended in Brinkgreve et al. (2022). A summary of the HS model-specific input parameters is presented in Table 5.3. These constitute the HS model input parameters along with the parameters in Table 5.2.

Table 5.3: Summary of HS model-specific input parameters for each soil layer in Figure 5.1.

Soil layer	**MG**	**TF**	**GO**	**GT-C**	**GT-S**
E_{oed} (MPa)	50.0	5.8	26.8	80.0	100.0
E_{ur} (MPa)	150.0	37.2	251.4	240.0	300.0
m (-)	0.50	0.90	0.58	0.70	0.70
p_{ref} (kPa)	100	100	100	100	100
R_{fa} (-)	0.9	0.9	0.9	0.9	0.9

5.2.5 Hardening Soil with Small-Strain Stiffness Model parameter determination

The additional input parameters for the HSS constitutive models are the small-strain shear modulus G_0 and the shear strain parameter $\gamma_{0.7}$. While the *in situ* seismic CPT data in Figure 3.6 provides a profile of G_0 with depth, $\gamma_{0.7}$ is typically determined using highly sensitive local strain gauges. These gauges were not employed as part of the laboratory testing scheme outlined in Section 5.2.2 due to their limited availability and high cost. A more suitable method to determine the HSS model input parameters involved fitting the Hardin and Drnevich (1972) S-shaped stiffness reduction curve (Figure 2.8) to the larger strain portion of triaxial test data, by adjusting the input parameters G_0 and $\gamma_{0.7}$ in Equation 2.9, as shown in Figure 5.7 for the

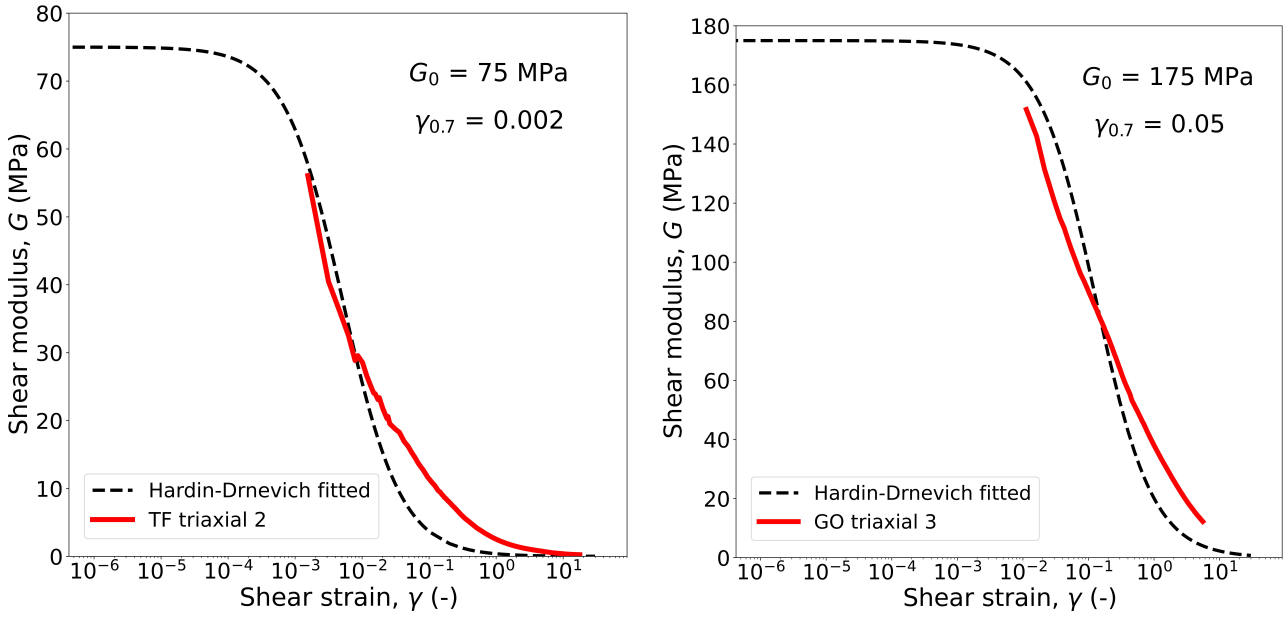
TF and GO materials. The triaxial test parameters E_{50} and ε_a were first used to calculate shear modulus G, and shear strain γ, using Hooke's law as:

$$G = \frac{E_{50}}{2(1+\nu)} \tag{5.8}$$

$$\gamma = \varepsilon_a - \varepsilon_r \tag{5.9}$$

where ε_r is the radial strain measured during the test. Only the TF and GO materials were modelled using the HSS constitutive model, as these materials were assumed to most influence the behaviour of the deep excavation, and very few empirical relationships to determine $\gamma_{0.7}$ have been published. The HSS input parameters were determined as $G_0 = 75$ MPa and $\gamma_{0.7} = 0.002$, and $G_0 = 175$ MPa and $\gamma_{0.7} = 0.05$ for the TF and GO materials respectively. The data from GO triaxial 3 was used as this was the only GO triaxial test with ε_r measurement for use in Equation 5.9.

For the GO triaxial test 2 sample, $G_0 = 105.3$ MPa was calculated from V_s measured by the bender element. This result is consistent with G_0 fitted to GO triaxial test 3 in Figure 5.7, as G_0 is expected to be larger for material samples consolidated to a larger σ'_3.



(a) (b)

Figure 5.7: Hardin and Drnevich (1972) small-strain stiffness reduction curve fitted to results of triaxial tests for (a) TF material and (b) GO material.

5.2.6 Model calibration

To be confident that the chosen soil constitutive model is accurately simulating real soil behaviour, data from laboratory elemental tests performed on real samples should be compared to simulated single element laboratory tests with behaviour defined by the constitutive model and its input parameters. The PLAXIS SoilTest program can simulate basic soil laboratory tests on the basis of a single point algorithm without the need to create a complex FE model. The comparison between real and simulated laboratory test data also offers the possibility to optimise model parameters such that a best fit is obtained between the data.

The initial input parameters for each of the MC and HS constitutive models for the TF and GO materials were used to simulate triaxial tests with test input parameters as defined in Section 5.2.2. This was done to assess the accuracy to which real soil behaviour is approximated by the constitutive model and the initial input parameters defined in Table 5.2 and Table 5.3. This was also used to revise any uncertain input parameters to best fit the simulated soil behaviour to the real soil behaviour. The triaxial tests outlined in Section 5.2.2 were simulated for the TF and GO materials. A comparison between the real q - ε_a response, and that simulated using the MC model, for the TF and GO materials is presented in Figure 5.8. The comparisons have been plotted across both large-strain and small-strain regions to compare the overall failure behaviours and small-strain stiffness behaviours respectively.

From Figure 5.8a and Figure 5.8b, there is reasonably poor agreement between the real and simulated triaxial test results for the TF material. The simulated test data underpredicts the available strength for TF triaxial 1 and overpredicts the available strength for TF triaxial 2, which suggests different strength properties for the triaxial samples retrieved from the main block sample for each of the real laboratory tests. This may have been caused by sample disturbance during retrieval, transportation or test preparation due to the soft nature of the material, as only a single large block sample was used. From Figure 5.8c and Figure 5.8d,

there is reasonably poor agreement between the real and simulated triaxial test results for the GO material. However, the simulated test data provides a good approximation of the available strength for each of the triaxial tests. The single stiffness input E_{50}, for the MC model was determined from GO triaxial 2 as σ_3' most closely replicated the *in situ* conditions from which the sample was retrieved. This means the simulated test data overpredicts soil stiffness at lower stress states and underpredicts stiffness at higher stress states than the *in situ* stress conditions. This is a limitation of the MC constitutive model. This can be addressed by specifying E_{50} as a linear function of depth in the model. The results of the comparison demonstrate the reasonably poor ability of the MC constitutive model with the input parameters defined in Table 5.3 to reasonably simulate real soil behaviour.

Next, the triaxial tests outlined in Section 5.2.2 were again simulated for the TF and GO materials, with material behaviour being governed by the HS constitutive model with input parameters defined in Table 5.2 and Table 5.3. A comparison between the real and simulated q - ε_a responses for the TF and GO materials is presented in Figure 5.9. Again, the comparisons have been plotted across both large-strain and small-strain regions.

From Figure 5.9a and Figure 5.9b, there is improved agreement between the real and simulated triaxial test results for TF triaxial 2. While the agreement between the real and simulated results for TF triaxial 1 is still relatively poor, the consolidation pressure for triaxial test 2 more closely centres within the *in situ* stress range for the TF layer. Also, the input E_{50} for the TF material models was determined from the results of triaxial test 2, which has likely caused the small-strain disparity in real and simulated soil behaviour for triaxial test 1. From Figure 5.9c and Figure 5.9d, there is good agreement between the real and simulated triaxial test results for the GO material. The strain-softening behaviour simulated using the HS model results in more accurate real soil q - ε_a behaviour predictions when compared to the use of the MC model. While the PLAXIS SoilTest parameter optimisation feature was utilised with the HS model

parameters for the TF and GO layers, only minor variations from the parameters in Table 5.2 and Table 5.3 were recommended. The soil model input parameters in Table 5.2 and Table 5.3 were therefore used to model each of the soil layers in Figure 5.1 for the numerical modelling scheme outlined in Section 5.3 and Section 5.4.

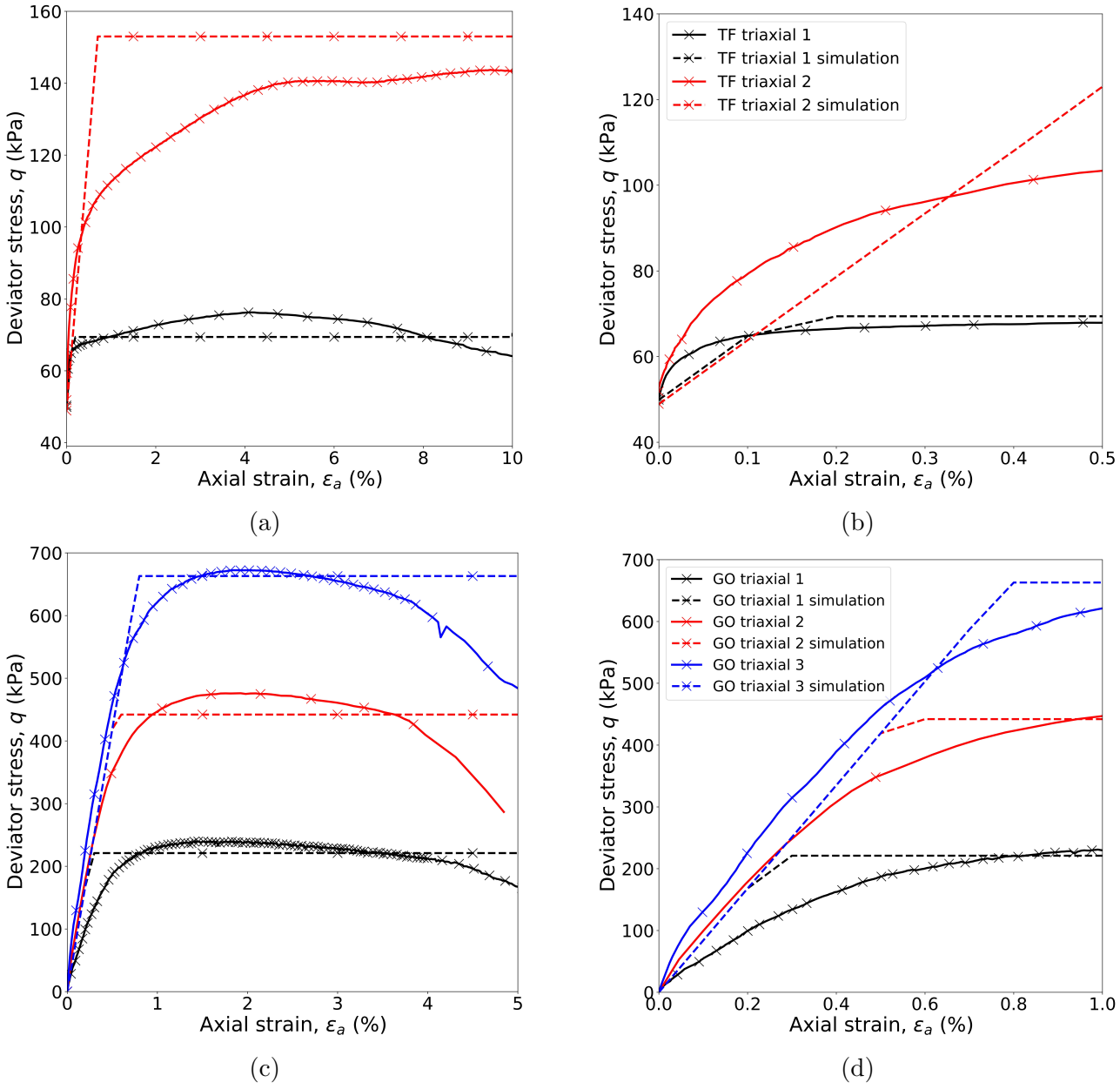


Figure 5.8: Comparison between real and simulated triaxial test q - ε_a responses for (a) & (b) TF material and (c) & (d) GO material. Soil behaviour governed by the MC constitutive model with input parameters defined in Table 5.2.

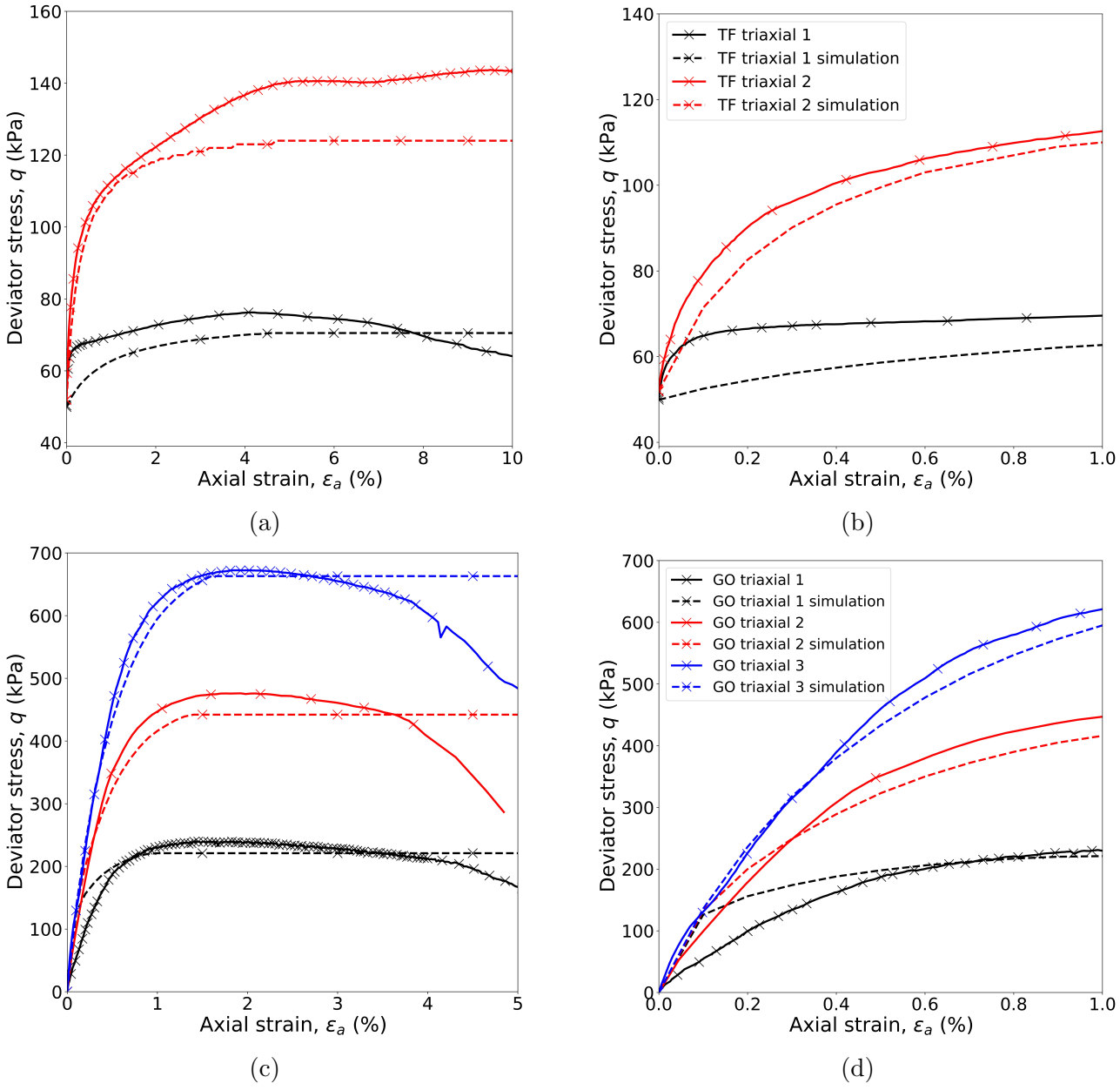


Figure 5.9: Comparison between real and simulated triaxial test q - ε_a responses for (a) & (b) TF material and (c) & (d) GO material. Soil behaviour governed by the HS constitutive model with input parameters defined in Table 5.2 and Table 5.3.

5.3 2D numerical model development

2D plane strain or axisymmetric FE and FD analyses have been widely used to study deep excavations at the design stage, primarily owing to the substantial reduction in the quantity of elements and nodes (and thus simulation time and computational requirements) compared to that for 3D analyses. The extent to which a 2D plane strain analysis can estimate wall movement at the centre of a wall span is quantified as the plane strain ratio PSR (Finno et al. (2007)) calculated as:

$$PSR = (1 - e^{-kC(L/H}) + 0.05(L/B - 1) \tag{5.10}$$

where L is the length of the span considered, H is the depth of excavation, B is the length of the secondary span, and k and C are factors which depend on the support system stiffness and FOS_{BH} respectively, calculated in Equation 2.5 and in Equation 2.6. A PSR value of 1 indicates that a plane strain simulation will yield the same displacements in the centre of an excavation span as those computed by a 3D simulation. For the PROTOS deep excavation, $PSR = 1.05$ and $PSR = 0.96$ for the long and short wall spans respectively. This suggested performing a 2D plane strain analysis was an appropriate approach to initially predict the behaviour of the PROTOS deep excavation. In this section, the structural models for the deep excavation wall and support structures, the construction sequence and the refinement of the FE mesh are outlined for the PROTOS deep excavation numerical model developed in PLAXIS 2D.

5.3.1 Structural models

The structural components in the PROTOS deep excavation adopted the properties of structural steel or reinforced concrete. It was deemed appropriate to model these as linear elastic materials. Structural components can be modelled as plates, anchors, beams or embedded beams. The deep excavation retaining wall at PROTOS was designed as a "combi-wall", comprising alternate tube and AZ-28 sheet pile pairs as shown in Figure 5.10. The wall was modelled

as a linear elastic plate with its mechanical input properties being the length-weighted average of the tube piles input properties and the sheet pile pair input properties. The mechanical input parameters required included the unit weight γ_{wall}, axial stiffness EA, bending stiffness EI, and Poisson's ratio ν. To calculate EA and EI, the cross-sectional area A and second moment of area I, were taken as that for the overall system A_{sys} and I_{sys} calculated as:

$$A_{sys} = \frac{\left(\frac{b_{tube}}{b_{sys}}\right) A_{tube} + \left(\frac{b_{sheet}}{b_{sys}}\right) A_{sheet}}{b_{sys}} \tag{5.11}$$

$$I_{sys} = \frac{\left(\frac{b_{tube}}{b_{sys}}\right) I_{tube} + \left(\frac{b_{sheet}}{b_{sys}}\right) I_{sheet}}{b_{sys}} \tag{5.12}$$

where A_{tube} and A_{sheet} are the cross-sectional area of the tube and sheet pile pair respectively, I_{tube} and I_{sheet} are the second moment of area of the tube and sheet pile pair respectively, b_{tube} and b_{sheet} are the width of the tube and sheet pile pair respectively and b_{sys} is the combined system width. The plate was assumed to exhibit isotropic axial stiffness in planes parallel and perpendicular to the length of the wall. The walls were assumed to be impermeable to groundwater as the clutches between tube and sheet piles were coated with bitumen to reduce water ingress.

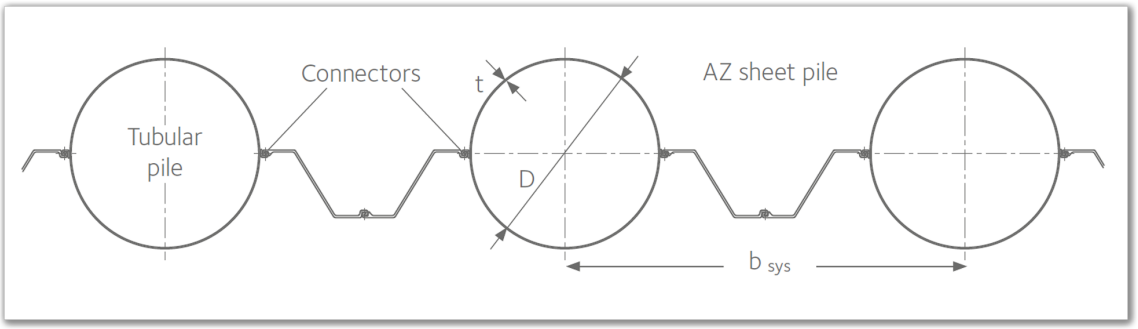


Figure 5.10: Sketch showing "combi-wall" tube and AZ sheet pile pair arrangement (ArcelorMittal (2020)).

The RC capping beam in Figure 3.10a was modelled as a row of closely spaced anchors with extremely high EA to prevent any compressive deformation and consequently any deflection at the top of the walls. This realistically simulates the highly stiff behaviour of the 4 m wide capping beam, as no wall deflection was measured at ground level in the field. The level 2 frame

structure in Figure 3.10b was modelled as a row of anchors at 5 m spacing which approximately equates to that between each of the corner brace and tube prop supports along the waler length. EA was taken as the average of that for the P1 and P2 tube props in Table 3.2. The wall plates and support structure anchors were modelled with pinned connections, as the anchors have no moment carrying capacity. While this is a limitation of modelling the support structures as anchors rather than plates, the use of plates in this case was not possible due to the variation in lateral bending stiffness along the length of the supporting frame waler. A summary of the input parameters for the structural component models in PLAXIS 2D is presented in Table 5.4. w denotes the unit weight per unit area and $L_{spacing}$ denotes the anchor spacing.

Table 5.4: Summary of structural components and input parameters for PLAXIS 2D numerical model.

Structure	**Wall**	**Capping beam**	**Frame**
Numerical component	Plate	Anchor	Anchor
w (kN/m^3)	0.13	-	-
E (GPa)	210	-	210
A (cm^2)	-	-	862
A_{sys} (cm^2/m)	202	-	-
I_{sys} (cm^4/m)	276,000	-	-
EA (kN)	-	1 x 10^9	18.10 x 10^6
EA_{sys} (kN/m)	4.23 x 10^6	-	-
EI_{sys} (kNm^2/m)	0.58 x 10^6	-	-
ν (-)	0.3	-	-
$L_{spacing}$ (m)	-	0.1	5.0

At a soil-structure interface, a reduction in the soil shear strength and soil stiffness is typically observed (Tiwari et al. (2010)). The extent of the reduction depends on both the soil type and the structure material. The properties of soil-structure interface elements are governed by the interface strength reduction factor R_{inter}. By default, the soil shear strength is reduced by a factor of R_{inter} and the soil stiffness is reduced by a factor of R_{inter}^2. A value of $R_{inter} = 0.8$ was assumed for all soil layers. This was conservatively selected based on the calculated steel-clay $R_{inter} = 0.81$ and steel-silty sand $R_{inter} = 0.83$ from interface test data presented in Tiwari et al. (2010).

5.3.2 Construction sequence

The aim when developing the simulated construction sequence was to most accurately mimic the real PROTOS deep excavation sequence in Table 3.1. The numerical model was developed to simulate the bunker excavation works (stages 1 - 10 in Table 3.1). The numerical construction sequence comprised ten phases and is presented in Table 5.5. The 2D numerical model setup at each of the phases in Table 5.5 is presented in Figure 5.11. Each phase was simulated as a plastic phase with a subsequent, associated coupled consolidation phase. A plastic phase is the name given to an elastic-plastic deformation analysis in which it is not necessary to take the change of pore pressure with time into account. A coupled consolidation phase is then conducted to analyse the development and dissipation of excess pore pressures in saturated cohesive materials as a function of time. In a coupled consolidation phase, the governing equations for fluid flow and soil deformation are solved together to incorporate the influence of pore pressure on soil deformation and vice versa.

Prior to simulating the construction of the deep excavation, the initial soil stress field must be generated. This was done using the K_0 procedure, where the initial soil state parameters K_0 and OCR are used with soil unit weight γ (all from Table 5.2) to generate the initial stress field. Phase 1 involved modelling the wall installation. The wall installation was modelled using the wished-in-place (WIP) approach, which assumes the installation process has no influence on the initial *in situ* stress state. The WIP approach is widely adopted for modelling driven steel walls (Potts et al. (2001)), which induce fewer soil stress state changes during installation than alternative secant pile or diaphragm walls. While the driven sheet pile installation process is likely to lead to increases in the *in situ* lateral earth pressure coefficient K_0, O'Brien (1991) suggested that the WIP approach is suitable as the bending moments in the wall are unlikely to be particularly sensitive to the initial *in situ* horizontal stresses. The initial excavation to 1.5 mBGL was modelled in phase 2, and a construction plant and materials surcharge of 10 kPa

was applied across an 8 m width from the excavation edge. The surcharge was determined as the weight of construction plant and materials distributed over the area of the capping beam on the most heavily loaded west side of the PROTOS excavation. The installation of the capping beam and the dewatering process were modelled in phase 3. The dewatering process was simply modelled as a lowering of the water table from a depth of 2 mBGL to the excavation formation depth of 12 mBGL. The groundwater head was assumed to increase linearly with depth from excavation walls to the edges of the meshed area located 40 m from the excavation edge, as this is in agreement with the hydraulic gradient inferred from the difference in the levels of the internal and external groundwater monitoring wells in Figure 4.19.

Table 5.5: Summary of construction sequence for PLAXIS numerical model.

Phase	**Construction activity**	**Duration (days)**	**Simulation type**
Initial	Initial stress field	-	K_0 procedure
1	Wall installation	-	Plastic
1C		30	Consolidation
2	Initial excavation &	-	Plastic
2C	construction load	30	Consolidation
3	Capping beam installation	-	Plastic
3C	& dewatering	50	Consolidation
4	Excavate to -2.5 mBGL	-	Plastic
4C		3	Consolidation
5	Excavate to -4.5 mBGL	-	Plastic
5C		3	Consolidation
6	Excavate to -7 mBGL	-	Plastic
6C		10	Consolidation
7	Frame installation	-	Plastic
8	Excavate to -8 mBGL	-	Plastic
8C		3	Consolidation
9	Excavate to -11 mBGL	-	Plastic
9C		3	Consolidation
10	Excavate to formation	-	Plastic
10C	at -12 mBGL	10	Consolidation

The excavation phases were modelled so as to compare the results of the numerical model with each of the wall deflection surveys in Figure 4.3. Phases 4, 5 and 6 involved modelling excavation to depths of 2.5 mBGL, 4.5 mBGL and 6.0 mBGL respectively, which correspond to the depths measured on 02/09/21, 06/09/21 and 09/09/21 respectively, at which wall deflection

surveys were taken in Figure 4.3. The level 2 frame installation was modelled in phase 7. Phases 8, 9 and 10 involved modelling excavation to depths of 8.0 mBGL, 11.0 mBGL and 12.0 mBGL respectively, which correspond to the depths measured on 22/09/21, 27/09/21 and 29/09/21 respectively, at which wall deflection surveys were also taken.

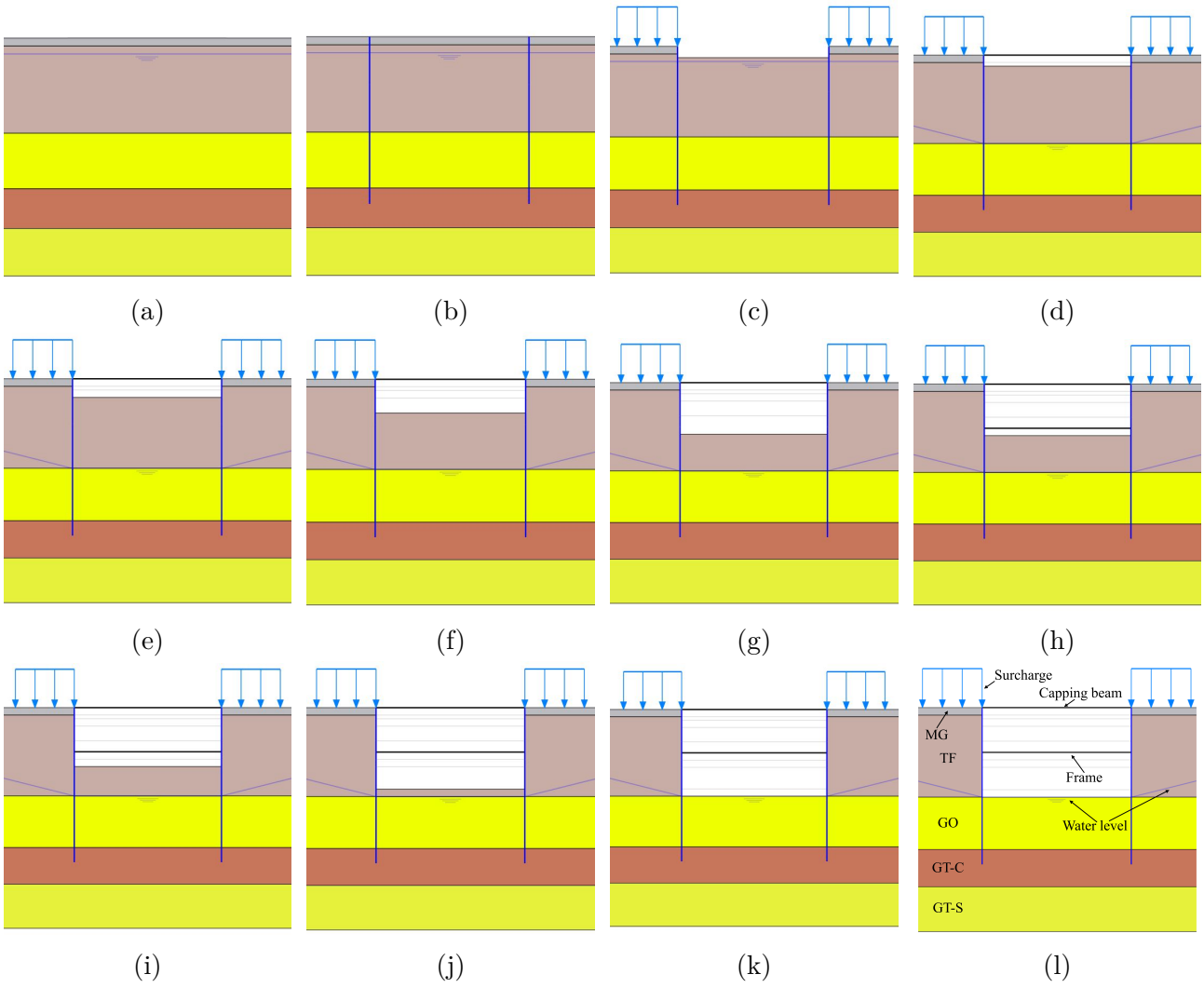


Figure 5.11: PLAXIS 2D model setup for construction sequence in Table 5.5. (a) Initial phase, (b) phase 1, (c) phase 2, (d) phase 3, (e) phase 4, (f) phase 5, (g) phase 6, (h) phase 7, (i) phase 8, (j) phase 9, (k) phase 10, (l) phase 10 annotated with numerical model components.

5.3.3 Mesh refinement

The ability of a numerical FE model to accurately replicate observed behaviours in the field can be largely influenced by the FE mesh discretisation. The mesh should adequately cover all regions of interest and its extents should be sufficiently large to capture the full range of desired output parameters. The mesh refinement process involves striking a balance between accuracy

and computational efficiency. To achieve this, the mesh density should be adjusted by using smaller elements in regions with complex geometries or interfaces and larger elements in regions with fewer components and interfaces. Elements with very high or very low aspect ratios should be avoided as these can lead to inaccuracies and significant computational demand.

To determine the domain size of the meshed area, a sensitivity study was performed to investigate the influence of the meshed area on key output parameters. A mesh width and depth of 100 m and 30 m respectively was found to provide a good balance between capturing boundary effects by ensuring the mesh extends beyond the area of interest, and computational requirements. The mesh was formed of 15-noded triangular elements. Prior to in-depth analysis of the numerical simulation results, a convergence study was performed to assess the accuracy and reliability of the numerical solution. The convergence study can be used to determine whether the numerical solution converges to a well-defined solution as the mesh is refined, ensuring the results are not sensitive to the mesh density and discretisation.

The six mesh arrangements employed for the convergence study are presented in Figure 5.12. M1 - M5 were generated using the five global refinement options. M6 was additionally, locally refined around the soil-structure interfaces. The number of elements and nodes, and the model calculation time, for each arrangement is presented in Table 5.6. The two output parameters used to assess the sensitivity of the mesh were the maximum wall displacement $\delta_{h,max}$ and compressive frame anchor load N_{max} following phase 10C at formation. The simulations resulted in outputted ranges of $\delta_{h,max} = 13.8$ - 14.7 mm, and $N_{max} = 1953$ - 1970 kN, which correspond to percentage differences of 6.51% and 0.87% respectively. These values were deemed sufficiently small to conclude the results are not highly sensitive to the mesh density. The most densely arranged mesh (M6 in Figure 5.12 and Table 5.6) was selected for the analyses as its calculation time was still suitably small for this numerical scenario.

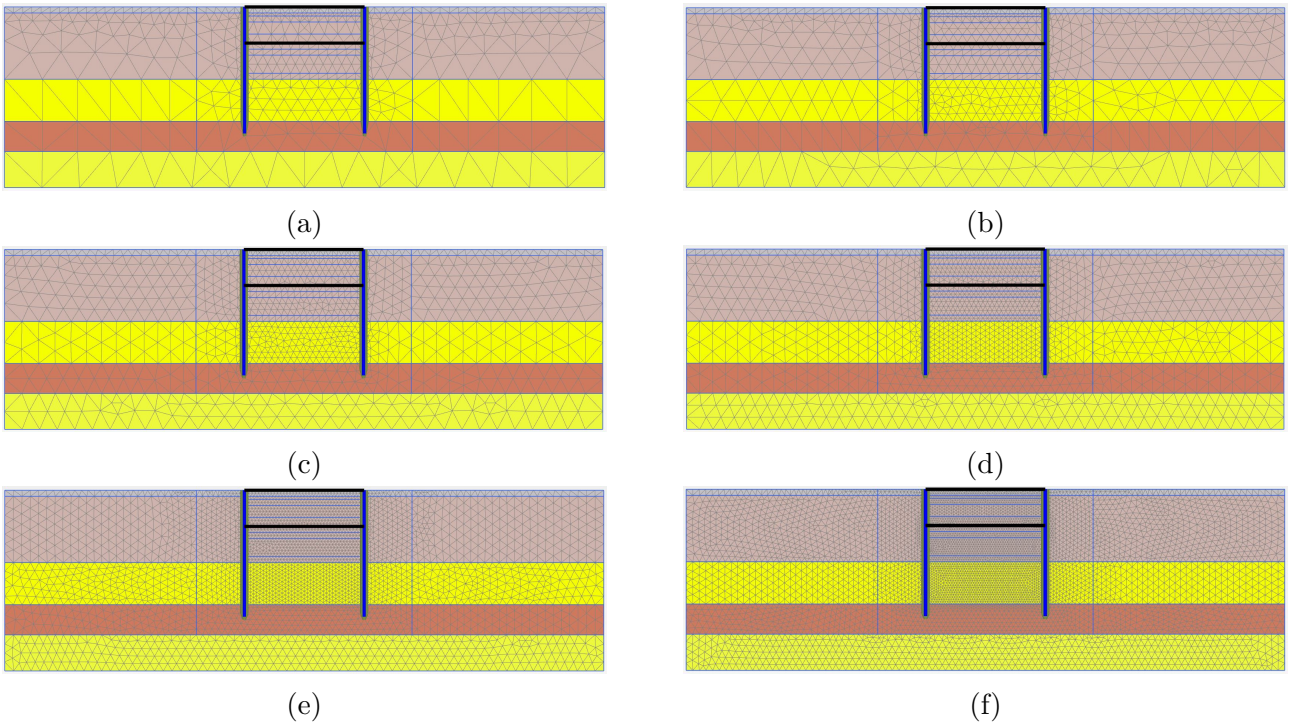


Figure 5.12: PLAXIS 2D mesh arrangements for convergence study. (a) M1, (b) M2, (c) M3, (d) M4, (e) M5, (f) M6.

Table 5.6: Summary of mesh and calculation parameters for PLAXIS 2D convergence study.

Mesh arrangement	**Elements**	**Nodes**	**Calculation time (s)**
M1	937	7929	152
M2	1262	10567	159
M3	2005	16665	177
M4	3141	25921	197
M5	6776	55359	248
M6	12349	100345	301

5.4 3D numerical model development

The limitations of 2D plane strain analyses have been widely reported, with these approaches unable to consider corner effects, whilst tending to overestimate ground movements compared to 3D analyses. 3D analyses provide an opportunity to investigate corner effects at wall joints and to explicitly model each member of the supporting frame structures. 3D analyses also provide an opportunity to model each separate element of a combined wall. The PLAXIS 2D model outlined in Section 5.3 was progressed into a 3D numerical model to investigate some of the forementioned more complex numerical features. In this section, the structural models for the deep excavation walls and support structures, the construction sequence, and the refinement

of the FE mesh are outlined for the numerical model developed in PLAXIS 3D.

5.4.1 Structural models

In PLAXIS 3D, the "combi-wall" retaining walls in Figure 5.10 were modelled in two ways as shown in Figure 5.13. The first involved modelling the walls as four linear elastic plates, with their mechanical input properties being the length-weighted average of those for the tube piles and the sheet pile pairs (using Equation 5.11 and Equation 5.12) as in Table 5.4. This is denoted as WM1. The second involved modelling each of the tube pile and sheet pile pair elements resulting in the creation of 100 individual linear elastic plates. This is denoted as WM2. PLAXIS 3D allows for orthotropic material behaviour in plate elements, which is defined by the following input parameters:

- E_1 (GPa): Young's modulus in first axial direction.
- E_2 (GPa): Young's modulus in second axial direction.
- G_{12} (GPa): In-plane shear modulus.
- G_{13} (GPa): Out-of-plane shear modulus related to shear deformation over first direction.
- G_{23} (GPa): Out-of-plane shear modulus related to shear deformation over second direction.
- ν_{12} (-): Poisson's ratio.
- γ_N (kN/m^3): Numerical unit weight input.

The type of loading to which the plate is subjected influences the input parameter calculation. For this case, bending was considered the most important loading type. The wall structure is geometrically orthotropic with largely different stiffnesses in the horizontal and vertical direction. The axial stiffness in the vertical direction is larger than the effective stiffness in the horizontal direction ($E_1 > E_2$). Also, the moment of inertia against bending over the vertical direction I_1, is much larger than the moment of inertia against bending over the horizontal direction I_2. Brinkgreve et al. (2022) recommends taking $I_1 \approx 20I_2$ and $I_1 \approx 10I_{12}$, where I_{12} is the moment of inertia against torsion, and recommends taking the equivalent thickness d equal to the height of the wall cross-section. Brinkgreve et al. (2022) also recommends taking

the cross-sectional area effective against shear deformation over the vertical and horizontal directions A_{13} and A_{23}, equal to 1/3 and 1/10 of the total cross-sectional area A_w, respectively. These recommendations were combined with Equations 5.13 - 5.19 to calculate the PLAXIS 3D plate input parameters. Equations 5.13 - 5.19 are recommended for situations where bending is considered the most important loading type and result in the bending stiffnesses $E_1 d^3/12$ and $E_2 d^3/12$, and shear stiffnesses $G_{13}d$ and $G_{23}d$, being independent of the chosen value for d.

$$E_1 = \frac{12E_w I_1}{d^3} \tag{5.13}$$

$$E_2 = \frac{12E_w I_2}{d^3} \approx \frac{I_2}{I_1} E_1 \approx \frac{E_1}{20} \tag{5.14}$$

$$G_{12} = \frac{6E_w I_{12}}{(1+\nu)d^3} \approx \frac{6E_w I_1}{10d^3} \tag{5.15}$$

$$G_{13} = \frac{E_w A_{13}}{2(1+\nu)d} \approx \frac{E_w(A_w/3)}{2d} = \frac{E_w A_w}{6d} \tag{5.16}$$

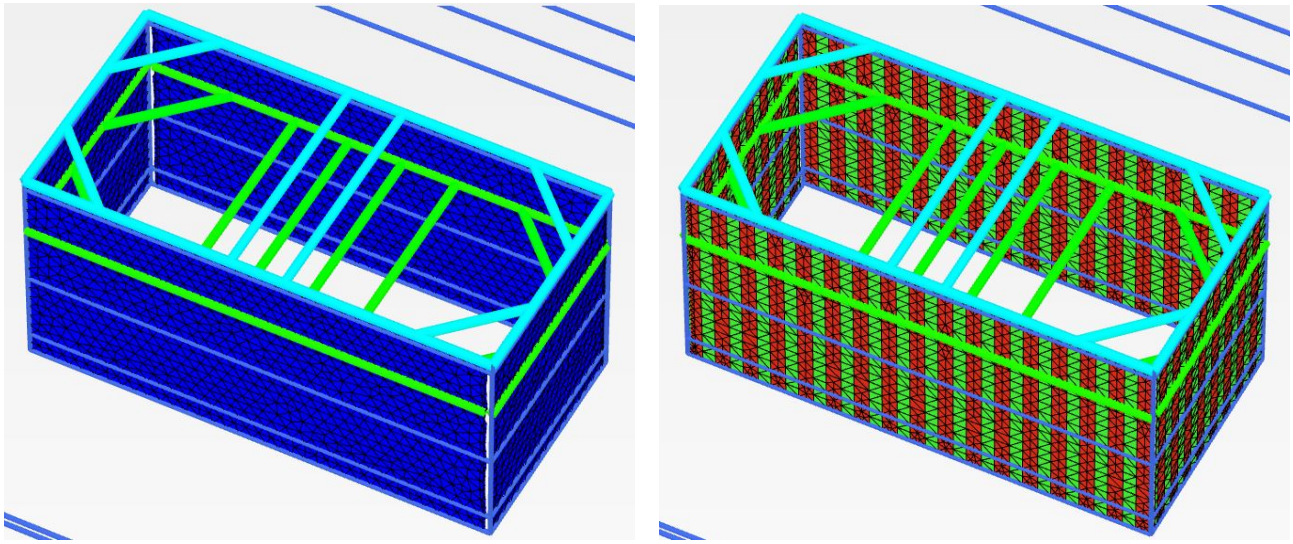
$$G_{23} = \frac{E_w A_{23}}{2(1+\nu)d} \approx \frac{E_w(A_w/10)}{2d} = \frac{E_w A_w}{20d} \tag{5.17}$$

$$\nu_{12} \approx 0 \tag{5.18}$$

$$\gamma_N = \frac{A_w \gamma_w}{d} \tag{5.19}$$

Here, E_w and γ_w are the Young's modulus and unit weight of the wall material respectively, and A_w and I_1 are the cross-sectional area per m wall width and second moment of area per m wall width of the wall section respectively. A summary of the input and output parameters from Equations 5.13 - 5.19 for each of the wall model components is presented in Table 5.7. The wall-to-wall corner pile clutch connections were modelled as hinged joints with no moment capacity. The behaviour at soil-structure interfaces was again governed by R_{inter} as described in Section 5.3.1.

The RC capping beam and level 2 frame in Figure 3.10a and Figure 3.10b respectively were modelled with linear elastic 3D beam elements, as shown in Figure 5.14. A summary of input parameters for the 3D beam elements in Figure 5.14 is presented in Table 5.8. I_x and I_y denote



(a) (b)

Figure 5.13: Deep excavation retaining walls modelled in PLAXIS 3D with (a) WM1 model (averaged input properties) and (b) WM2 model (separate tubes and sheet pile pairs).

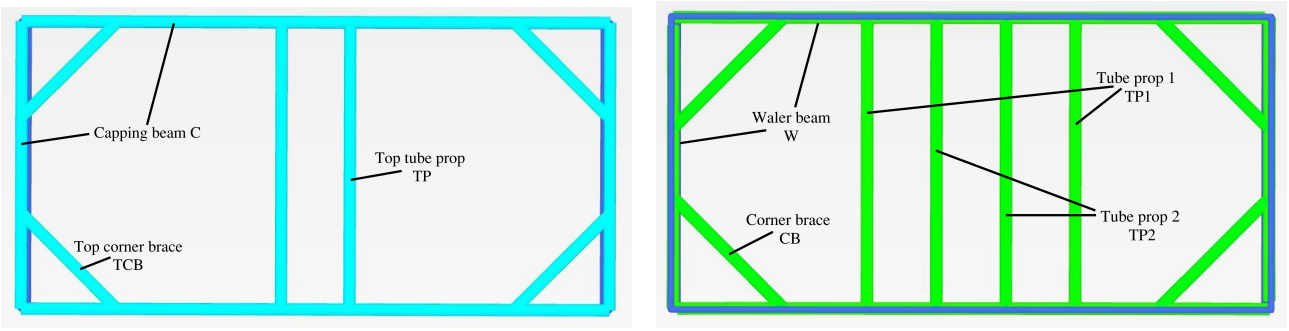
Table 5.7: Summary of parameters for PLAXIS 3D wall models. Top and bottom parameters are inputs and outputs from Equations 5.13 - 5.19 respectively.

Plate model	**Averaged (WM1)**	**Tube (WM2)**	**Sheet pile pair (WM2)**
Section width (m)	1.00	1.22	1.40
d (m)	0.80	1.22	0.46
γ_w (kN/m^3)	78.5	78.5	78.5
A_w (cm^2/m)	202	670	200
I_1 (cm^4/m)	2.76 x 10^5	1.20 x 10^6	6.40 x 10^4
E_w (GPa)	210	210	210
γ_N (kN/m^3)	1.98	4.31	3.41
E_1 (GPa)	13.60	16.70	16.60
E_2 (GPa)	0.68	0.84	0.83
ν_{12} (-)	0	0	0
G_{12} (GPa)	0.68	0.83	0.83
G_{13} (GPa)	0.88	1.92	1.52
G_{23} (GPa)	0.27	0.58	0.46

the second moment of area of the beam section in planes parallel and perpendicular to the ground surface respectively. The waler beams in Figure 5.14b were modelled as spanning the full length of each side as the waler-to-waler connections were bolted and fully fixed. All other member connections were also modelled as fully fixed and had moment carrying capacity.

5.4.2 Construction sequence

The construction sequence adopted for the 3D numerical model is outlined in Table 5.5. The 3D numerical model setup at each of the phases in Table 5.5 is presented in Figure 5.15.



(a) (b)

Figure 5.14: Summary of 3D beam elements used to model (a) RC capping beam, and (b) level 2 frame.

Table 5.8: Summary of parameters for PLAXIS 3D beams in Figure 5.14. RC and S denote reinforced concrete and steel respectively.

Beam	**C**	**W**	**TCB**	**CB**	**TP**	**P1**	**P2**
Material	RC	S	S	S	S	S	S
γ (kN/m^3)	25.0	78.5	78.5	78.5	78.5	78.5	78.5
E (GPa)	50	210	210	210	210	210	210
A (cm^2)	4.80 x 10^4	874	874	874	562	970	754
I_x (cm^4)	6.40 x 10^8	1.25 x 10^6	1.25 x 10^6	1.25 x 10^6	5.61 x 10^5	2.39 x 10^6	1.36 x 10^6
I_y (cm^4)	5.80 x 10^7	7.83 x 10^4	7.83 x 10^4	7.83 x 10^4	5.61 x 10^5	2.39 x 10^6	1.36 x 10^6

5.4.3 Mesh refinement

The length, width and depth of the meshed area were chosen to be 155 m, 85 m and 30 m respectively. These dimensions were determined using a mesh dimension sensitivity study similar to that described in Section 5.3.3 for the 2D numerical model. For the 3D model, soil elements were modelled with 10-noded tetrahedral elements. For beams and plates, 3-noded line elements and 6-noded plate elements were used respectively. At soil-structure interfaces, 12-noded interface elements were used. Similarly to the 2D model development in Section 5.3.3, a convergence study was performed with five mesh arrangements generated using the five global mesh refinement options. These five mesh arrangements are presented in Figure 5.16, and the number of elements and nodes, and the model calculation time, for each arrangement is presented in Table 5.9.

The convergence simulations resulted in outputted ranges of $\delta_{h,max,LC}$ = 15.7 - 17.1 mm, and N_{max} = 1903 - 2133 kN, which correspond to percentage differences of 8.9% and 12.1%

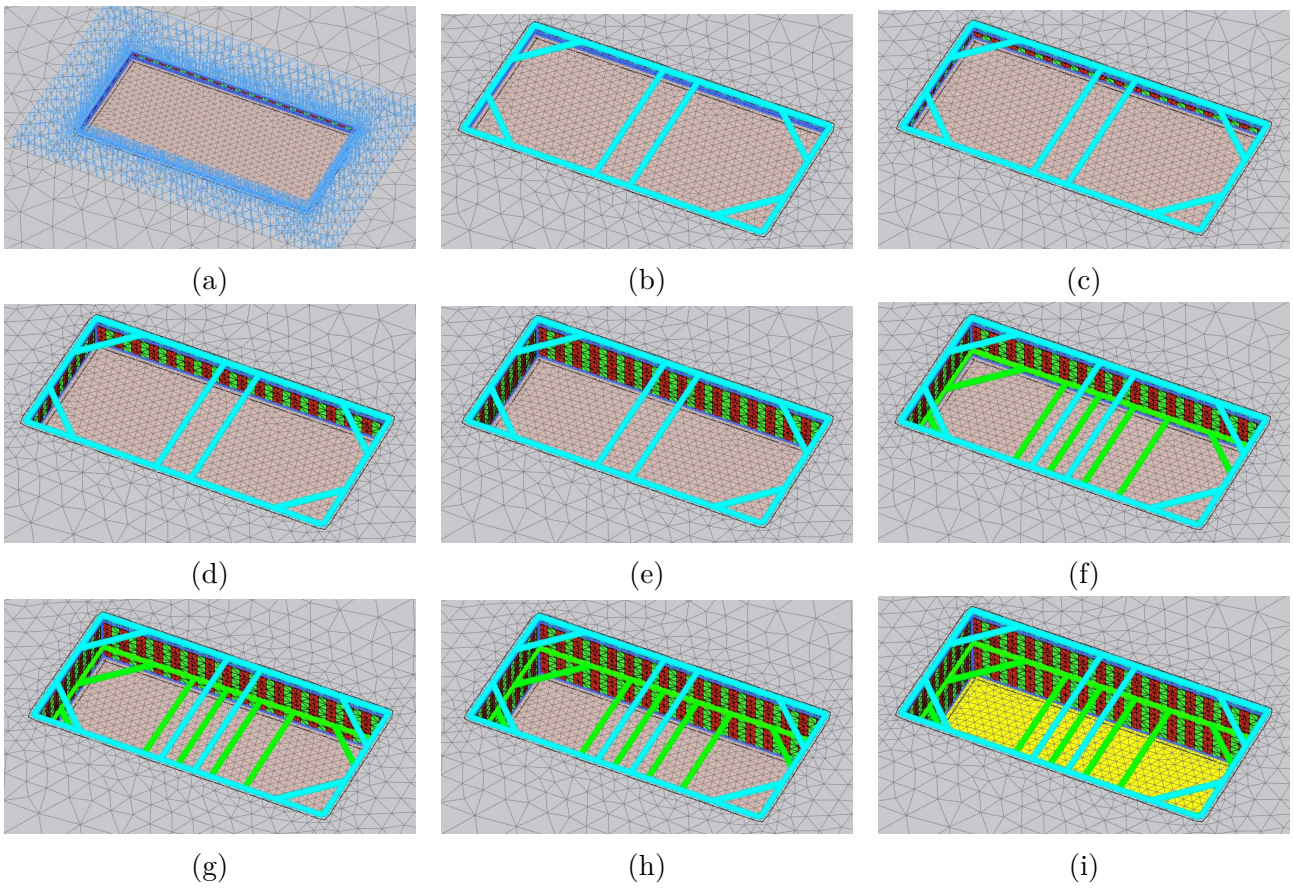


Figure 5.15: PLAXIS 3D model setup for construction sequence in Table 5.5. (a) Phase 2, (b) phase 3, (c) phase 4, (d) phase 5, (e) phase 6, (f) phase 7, (g) phase 8, (h) phase 9, (i) phase 10. Surface load hidden in phases 3 - 10.

respectively. With increasing element and node numbers, the simulations converged towards a well-defined solution, as the percentage differences decreased from those in the preceding simulation each time. Also, the depth profile of δ_h became smoother from simulation 3D-M1 to 3D-M5 due to the increase in mesh density. The mesh arrangement 3D-M4 was selected for the 3D numerical analyses as it provided a good balance between accuracy and computational efficiency. Simulation 3D-M5 resulted in only a 1.4% difference in $\delta_{h,max,LC}$ compared to that outputted from simulation 3D-M4. However 3D-M5 required significantly more time to complete, highlighting the importance of performing a mesh refinement exercise to carry out time efficient numerical analyses.

Table 5.9: Summary of mesh and calculation parameter for PLAXIS 3D convergence study.

Mesh arrangement	Elements	Nodes	Calculation time (mins)
3D-M1	19769	42991	20
3D-M2	27004	55319	25
3D-M3	50000	90362	50
3D-M4	107521	184737	102
3D-M5	242492	408333	990

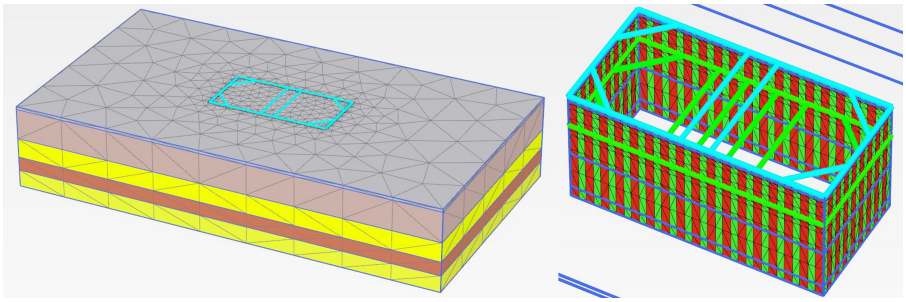
5.5 Lessons learnt and areas for improvement

A numerical modelling scheme was developed to enable comparisons to be made to the field monitoring data, to assess the ability of the models to accurately simulate real structural behaviours. The following lessons were learnt during the numerical model development process:

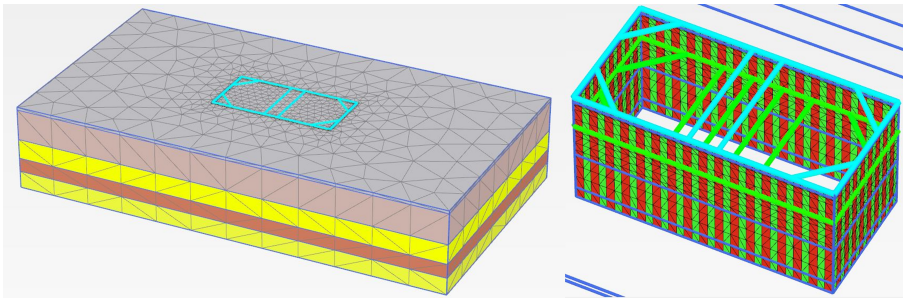
- Difficulties were encountered when retrieving and storing the soft TF material sample prior to its use for laboratory testing. Laboratory tests should be performed on sensitive, cohesive materials as soon as possible following retrieval to preserve the soil state and minimise the effects of drainage and consolidation. Multiple laboratory elemental tests with the same test parameters should be performed on low strength materials to evaluate the repeatability of the tests and the influence of sample disturbance.
- For the laboratory testing scheme described in this chapter, a sample from only a single depth was tested for each of the TF and GO materials, due to cost restraints. Performing laboratory tests on samples retrived from several depths into each material layer would enable profiling of parameters, and result in more accurate ground behaviour simulation.
- If numerical modelling is to be utilised during the design process for a geotechnical structure, and CPT tests are commissioned as part of the site investigation works, then seismic CPT (SCPT) tests should also be included. While these come at an additional cost to standard CPT tests, the inferred G_0 profile they provide can be correlated to laboratory tests to provide continuous information about soil stiffness along a depth profile. If highly accurate small-strain stiffness simulation is necessary, then advanced laboratory

tests with highly sensitive displacement measurement capability should be specified to obtain an accurate value for $\gamma_{0.7}$.

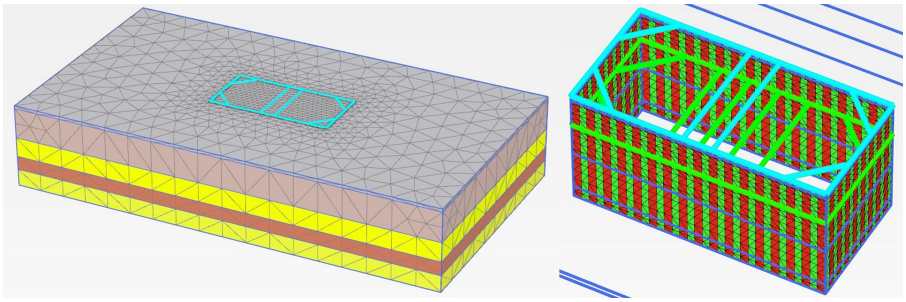
- When incorporating consolidation phases into the numerical construction sequence, it is challenging to predict exact durations for each phase in advance of the works. Conservative durations should be assumed to ensure consolidation does not cause lateral earth pressures to exceed those allowable. The sensitivity of key output parameters to changes in consolidation duration should be investigated as part of the design process.
- When modelling deep excavation walls in 3D, determine the primary loading type to which the plate is subjected, as this influences the determination of its parameters. For example, if bending is considered to be the primary load type, then deformation predictions under orthogonally applied loads are unlikely to be accurate.



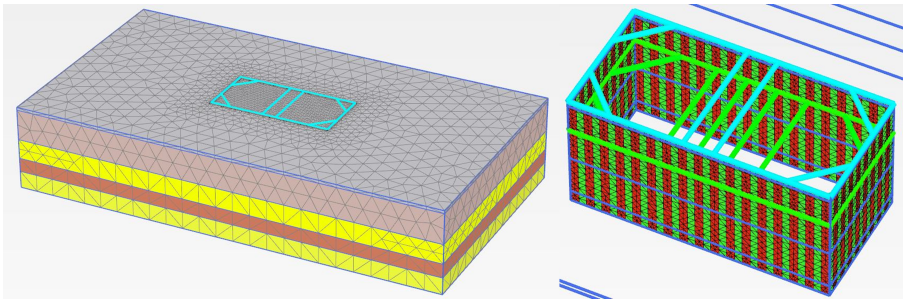
(a)



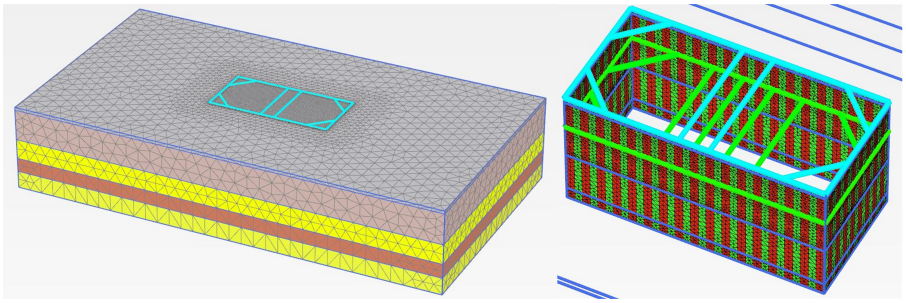
(b)



(c)



(d)



(e)

Figure 5.16: PLAXIS 3D mesh arrangements for convergence study. (a) 3D-M1, (b) 3D-M2, (c) 3D-M3, (d) 3D-M4, (e) 3D-M5.

6 | Numerical modelling results

6.1 Introduction

Chapter 5 outlined the numerical modelling scheme developed to complement the field monitoring data. This chapter details the results of the numerical modelling scheme, which are compared to the field monitoring data to assess the accuracy of the numerical predictions and to evaluate the model development process. The key output parameters selected for these comparisons are the lateral wall displacement δ_h, profile with depth, and the loads in the level 2 frame structure. The numerical predictions are also compared to those simulated using simplified limit equilibrium (LE) design methods.

6.2 2D model results

The output parameters presented are the wall deflected shape and the support structure reaction loads. The influence of the selected soil constitutive model on the output parameters is assessed, as results from models using the MC, HS and HSS models are compared. The numerical results are compared to the field measurements at PROTOS EFW (presented in Chapter 4) to assess the ability of the numerical models to capture observed field behaviours. The numerical results are presented for phase 7 and phase 10C in Table 5.5, as these correspond to the completion of the first and second phases of excavation in Table 3.1 respectively. The numerical results are also compared to the results of limit equilibrium analyses performed in the commercially available software CADS Piled Wall Suite (PWS) (CADS (2011)) for comparison.

6.2.1 Wall deflections

Figure 6.1 shows the horizontal displacement δ_h, profiles with depth predicted by the PLAXIS 2D numerical models together with both those measured in the field at PROTOS EFW, and the width profile of basal heave at formation. The results are presented for phase 7 and phase 10C. Ground models 1, 2 and 3 in Table 5.1 are denoted by MC, HS and HSS respectively in

Figure 6.1 and for all results and discussion sections in this chapter. As the simulated excavation depth H, increases, there is an increase in both $\delta_{h,max}$ and its corresponding depth, which is consistent with the wall behaviour observed in the field. The use of the MC model yields the largest δ_h across the full depth profile for both phase 7 and phase 10C, and the largest basal heave at phase 10C in Figure 6.1h. This is due to the inability of the MC constitutive model to model the greater unloading stiffness exhibited by real soils (Obrzud (2010)), as only a single input stiffness E_{50} governs the linear-elastic, perfectly-plastic stress-strain behaviour. This leads to unrealistically large soil swelling and heave when unloading during excavation is simulated, which results in the large heave displacement $\delta_{y,heave}$, and δ_h predictions in Figure 6.1. The inability to model the increased unloading stiffness means typically the MC model is unsuitable for accurately predicting ground and structure movements for excavation scenarios (Tjie-Liong (2014)).

The additional stiffness input E_{ur}, for the HS and HSS constitutive models results in more accurate simulation of real soil behaviour when unloading during excavation. This results in the smaller $\delta_{y,heave}$ predictions presented in Figure 6.1h. The more accurate modelling of unloading behaviour, alongside the other more complex features of real-soil behaviour simulated using the HS and HSS models, also result in the smaller δ_h predictions in Figure 6.1g. The HS model simulation results in the most accurate δ_h predictions, with close agreement with the field measurements observed. Modelling the increase in soil stiffness at very small strains using the HSS model results in significantly reduced δ_h profiles compared to those predicted using the HS model.

While the δ_h profiles predicted using the HSS model are much smaller than those measured in the field, the HSS model most closely simulates real-soil behaviour, which suggests the use of the averaged wall properties in Table 5.4 overestimates the combined wall stiffness, which results in an underprediction of δ_h. This is supported by the reasonably close agreement between the

δ_h predictions made using the MC model and the field measurements, as typically the use of the MC model overpredicts deep excavation wall movements (Tjie-Liong (2014)). The results of the PLAXIS 3D analyses presented in Section 6.3 provide an opportunity to investigate this finding, by comparing two different wall models.

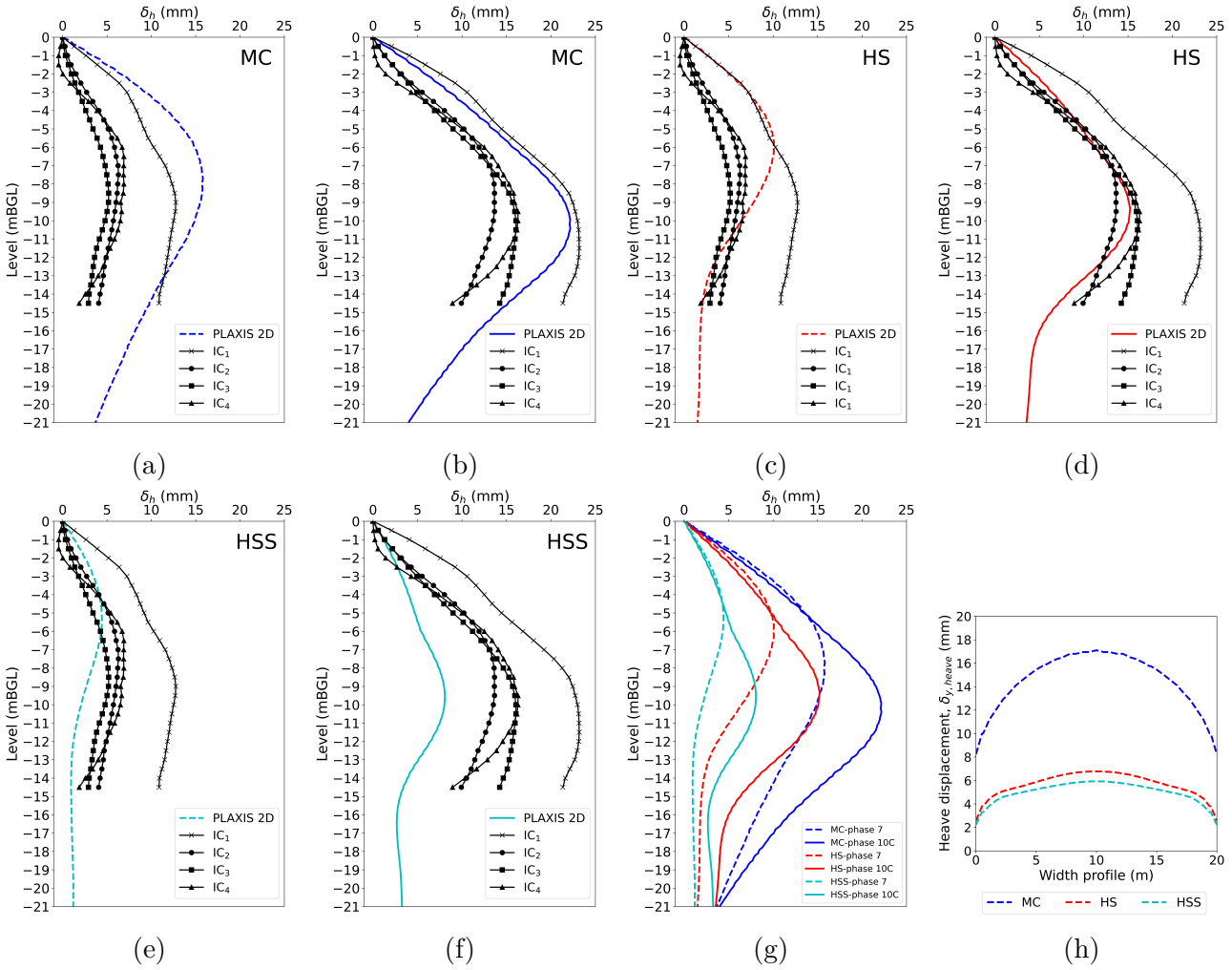


Figure 6.1: δ_h profiles with depth predicted by the PLAXIS 2D numerical models together with those measured in the field at PROTOS: (a) MC model δ_h for phase 7, (b) MC model δ_h for phase 10C, (c) HS model δ_h for phase 7, (d) HS model δ_h for phase 10C, (e) HSS model δ_h for phase 7, (f) HSS model δ_h for phase 10C, (g) comparison between use of soil models, (h) width profile of basal heave at formation.

6.2.2 Prop loads

A summary of the level 2 frame reaction loads predicted by the PLAXIS 2D numerical models following phase 10C is presented in Table 6.1. The observed axial loads in the level 2 frame at formation in the field are also included for comparison. The axial load N, is divided by the tributary length L_t, to determine the axial load per m run N', which enables direct

comparisons between the predicted and observed frame loads to be made. N' predicted by a limit equilibrium analysis in CADS PWS for two different Eurocode 7 (EC7 (2004)) design combinations are also included for later discussion in Section 6.2.3.

In general, the three PLAXIS 2D simulations provide reasonably accurate frame load predictions with good agreement observed between the simulated and observed N'. A lower N' is predicted by the MC model simulation than those predicted by the HS and HSS model simulations, which is likely due to a greater proportion of the lateral earth pressures being distributed into wall bending when using the MC model as shown in Figure 6.1 and Figure 6.2.

Table 6.1: Summary of level 2 frame reaction loads predicted by PLAXIS 2D numerical models at phase 10C together with those measured in the field at formation. CADS limit equilibrium N' included for later discussion in Section 6.2.3.

Simulation/member	**Load,** N **(kN)**	**Tributary length,** L_t **(m)**	**Load per m,** N' **(kN/m)**
PLAXIS MC	1506	5.0	**301**
PLAXIS HS	2044	5.0	**409**
PLAXIS HSS	2050	5.0	**410**
Field - W1	1966	4.0	**492**
Field - CCB1	2126*	6.7	**317**
Field - P1	1722	5.8	**297**
Field - P2	1639	5.3	**309**
CADS LE - Comb 1	-	-	**1399**
CADS LE - Comb 2	-	-	**1250**

*Resolved at 45° angle to horizontal

6.2.3 Comparison to limit equilibrium methods

Limit equilibrium (LE) design methods are commonly employed in industry for the design of deep excavations. It is important to compare the results from the PLAXIS 2D numerical analyses to those calculated from LE analyses to compare their ability to simulate observed deep excavation behaviour in the field. The commercially available LE design program CADS PWS (CADS (2011)) was used to model the PROTOS deep excavation. The program uses the Rankine (1857) method to calculate lateral earth pressures and requires the geotechnical input parameters γ, γ_{sat}, c and ϕ to calculate the active and passive earth pressure coefficients K_a and K_p and the lateral earth pressures. The values used for these were taken from Table 5.2.

The construction sequence used for the LE analysis was the same as that outlined in Table 5.5 with the consolidation phases removed, as the program is unable to simulate drainage and consolidation behaviour. Two LE analyses were performed which involved using Eurocode 7 (EC7 (2004)) design approach 1 (DA1) combination 1 (Com 1) and 2 (Com 2), which involve applying factors to increase loads and decrease soil strengths respectively.

To enable comparisons to be made between the wall behaviour predicted by the PLAXIS numerical and CADS PWS LE analyses, and that observed in the field, the field deflected wall shapes were first converted to the bending moment M depthwise variation, as CADS PWS is unable to predict ground and wall deformations and can only estimate the depthwise variation of M. The wall M is proportional to its curvature Ψ and can be calculated as:

$$M = EI\Psi = EI\frac{d^2\delta_h}{dz^2} \tag{6.1}$$

where z is the depth down the wall. Before the curvature can be calculated as the second derivative of δ_h with respect to z, the δ_h profile must be fitted with a series of curves. A variety of curves have been fitted to δ_h profiles as described in Ooi and Ramsey (2003), including quadratic curves, cubic curves and circular arcs. Ooi and Ramsey (2003) recommends fitting cubic splines, which are piecewise cubic functions that are fitted to moving point windows. A three-point window was used to fit cubic splines to the measured δ_h data in Figure 4.3. The δ_h profiles measured following the first and second phases of excavation were selected as these correspond to numerical phases 7 and 10C in Table 5.5. The fitted δ_h profiles were then inputted into Equation 6.1 which resulted in the depthwise variations of M as presented in Figure 6.2a and Figure 6.2b for tube pile IC_3.

Ooi and Ramsey (2003) also recommends fitting a higher degree polynomial function to the δ_h profile using the method of least squares as this results in a smoother depthwise variation of M. The lowest possible degree polynomial that 'adequately' describes the data should be used (Ooi and Ramsey (2003)). The fitting of a fourth-degree polynomial function to the δ_h was

found to provide a smooth and reasonable fit to the depthwise variation of M resulting from the cubic spline fitting, as shown in Figure 6.2a and Figure 6.2b. The successful application of this approach is reported in Price and Wardle (1984), Soares (1984) and Poh et al. (1997), in which ninth-degree, sixth-degree and seventh-degree polynomials respectively were fitted to the deflected profiles of diaphragm walls.

The depthwise variations of M in Figure 6.2a and Figure 6.2b exhibit negative M at shallow depths, due to the initial cantilever deflections described in Section 4.2.1 causing curvature away from the excavation when the top of the wall is retained and passive earth resistance is removed. Interestingly, the propping of the wall with the frame at a depth of 6 mBGL has no influence on the inferred depthwise variation of M. This is potentially due to issues with the connection between the wall and frame, which are discussed later in Section 6.3.1.

Figure 6.2c and Figure 6.2d present a comparison between the inferred depthwise variations of M in Figure 6.2a and Figure 6.2b, and those predicted by the PLAXIS 2D and CADS PWS simulations following excavation phase 1 (PLAXIS phase 7) and excavation phase 2 (PLAXIS phase 10C) respectively. The depthwise variations of M predicted using each of the MC, HS and HSS models in PLAXIS 2D are presented. While the PLAXIS 2D simulations provide a reasonable prediction of the maximum bending moment M_{max} following both phases of excavation, the predictions of the depthwise variations of M are relatively poor due to the failure to predict the negative M at shallow depth. Instead, the model predicts $M = 0$ at ground level due to the inability to model a fixed connection between the wall and the anchors which model the capping beam in PLAXIS. In reality, the top of the wall is fixed within the capping beam as a fully fixed connection with moment capacity.

The MC model simulation in PLAXIS 2D predicts greater M down the full depth profile compared to the HS and HSS model simulations, which is consistent with the predicted δ_h profiles in Figure 6.1. The CADS PWS Com 1 simulations overpredict the inferred field M_{max}

by factors of 2.4 and 4.0 for excavation phases 1 and 2 respectively, due to the use of the limit equilibrium Rankine (1857) earth pressure calculation approach which provides conservative predictions.

The level 2 frame reaction loads following excavation phase 2 predicted by the CADS PWS simulations are compared to those predicted using PLAXIS 2D and those measured in the field in Table 6.1. While the PLAXIS 2D simulated N' are in good agreement with those measured in the field, the CADS LE simulations significantly overpredict N' by factors of 3.95 and 3.53 for Com 1 and Com 2 respectively. The M and N' comparisons highlight the typically conservative nature of limit equilibrium design approaches and support the use of numerical design methods to provide significant improvements in accuracy.

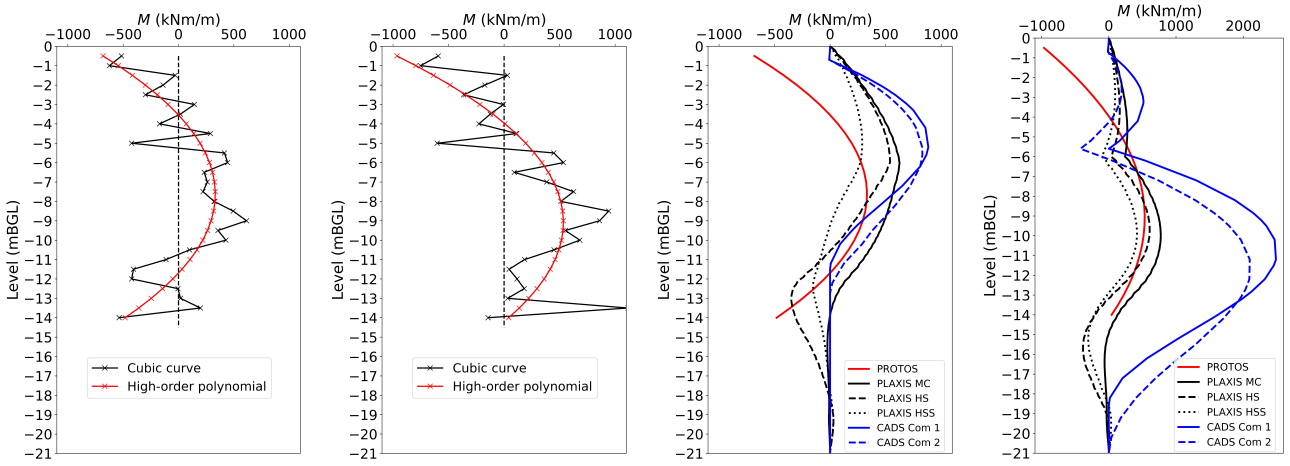


Figure 6.2: Depthwise variations of M calculated from δ_h depth profiles fitted with cubic splines and higher-order polynomial functions for (a) excavation phase 1 and (b) excavation phase 2, and comparison between these and the depthwise variations of M predicted by the PLAXIS 2D and CADS PWS simulations for (c) excavation phase 1 and (d) excavation phase 2.

6.3 3D model results

The PLAXIS 3D model provides an opportunity to investigate increased wall stiffness at the excavation corners and to model the 'combi-wall' components as separate 3D elements. Also each of the capping beam and frame members can be modelled explicitly, enabling a more rigorous investigation into the ability of the numerical model to replicate observed field

behaviours than that for the PLAXIS 2D model. Firstly, the simulated δ_h depth profiles using the two wall models (WM1 and WM2) and the HS and HSS soil models are compared to the field measurements. PLAXIS simulations using the MC soil model have been excluded from this section. The PLAXIS 3D model using the WM2 wall model and the HSS soil model is then used to produce more complex time series outputs, including the wall $\delta_{h,max}$ and frame member F and M. Finally, the PLAXIS 3D numerical results are again compared to the CADS PWS LE analyses.

6.3.1 Wall deflections

Figure 6.3 shows the PLAXIS 3D WM1 model simulated vertical ground and mesh deformations following excavation phases 1 and 2. Negative settlement deformation is simulated around the excavation edges, with positive heave deformation predicted at excavation formation. The predicted maximum settlements are -13.9 mm and -37.9 mm, and the predicted maximum heave displacements are 11.6 mm and 14.6 mm, following excavation phases 1 and 2 respectively. The plan views of mesh deformation in Figures 6.3c and 6.3d show the increase in wall stiffness towards the excavation corners, which along with the settlement contour profiles in Figures 6.3a and 6.3b, are consistent with the monitored behaviours of real deep excavations reported in Finno and Roboski (2005).

Figure 6.4 shows the horizontal displacement δ_h, profiles with depth predicted by the PLAXIS 3D numerical models together with those measured in the field at PROTOS EFW. The use of the WM2 wall model results in larger δ_h down the full depth than those predicted using the WM1 wall model following both excavation phases. The WM1 HSS δ_h predictions are also significantly lower than those measured in the field following both excavation phases. These results suggest the WM1 model overpredicts wall stiffness and highlight the importance of performing a 3D analysis when modelling a combined wall to enable each of the wall components to be modelled individually. This finding is consistent with that concluded from the PLAXIS 2D δ_h depth profile comparisons in Figure 6.1.

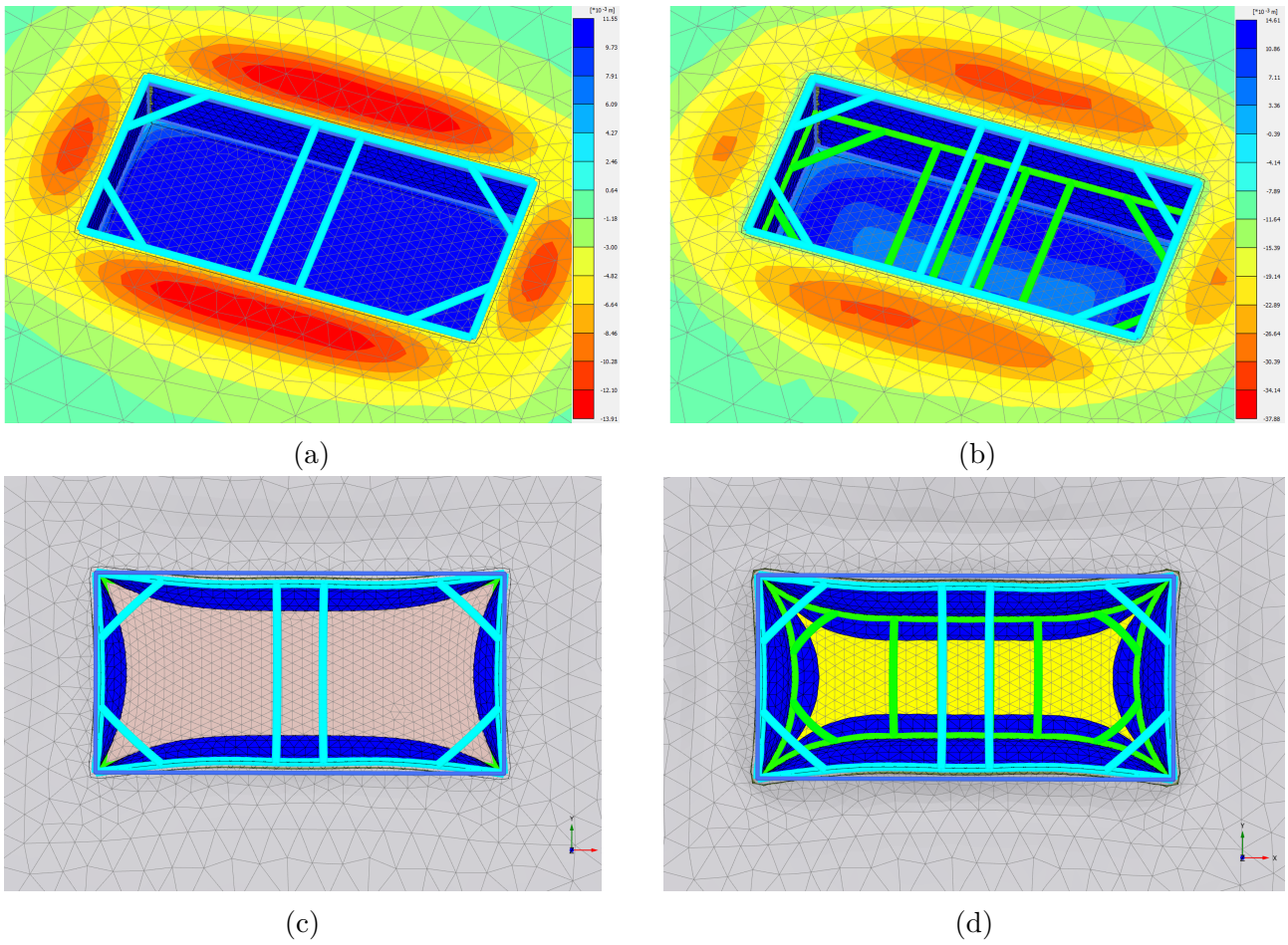


Figure 6.3: PLAXIS 3D WM1 model simulated vertical ground deformations following (a) excavation phase 1 and (b) excavation phase 2, and plan view of exaggerated mesh deformation following (c) excavation phase 1 and (d) excavation phase 2.

While the WM1 HS simulations predict $\delta_{h,max}$ values which agree well with the field measurements, the predictions are not simulated through accurate means, due to the competing influence of the wall stiffness overprediction using the WM1 model and the soil small-strain stiffness underprediction using the HS model. For IC_2, IC_3 and IC_4, the WM2 HSS model $\delta_{h,max}$ predictions agree reasonably well with the field measurements. The differences in $\delta_{h,max}$ between the WM2 HSS predictions and field measurements for IC_1 are likely due to the presence of a plant access road, and therefore additional surcharging, adjacent to IC_1. This load was not incorporated into the numerical models for simplicity as the magnitude and distribution of the load was uncertain.

Interestingly, the δ_h depth profiles predicted using the more flexible WM2 wall model include a point of inflection at the frame level of -5.75 mBGL following excavation phase 2 in Figures 6.4e

- 6.4h, which was not observed in the field. This is likely due to the constitution of the wall-frame connection as the presence of compressive plywood to form the concrete fill (Figure 6.5) enabled additional lateral displacement at frame level above that predicted by the numerical analyses which assume a fully restrained connection.

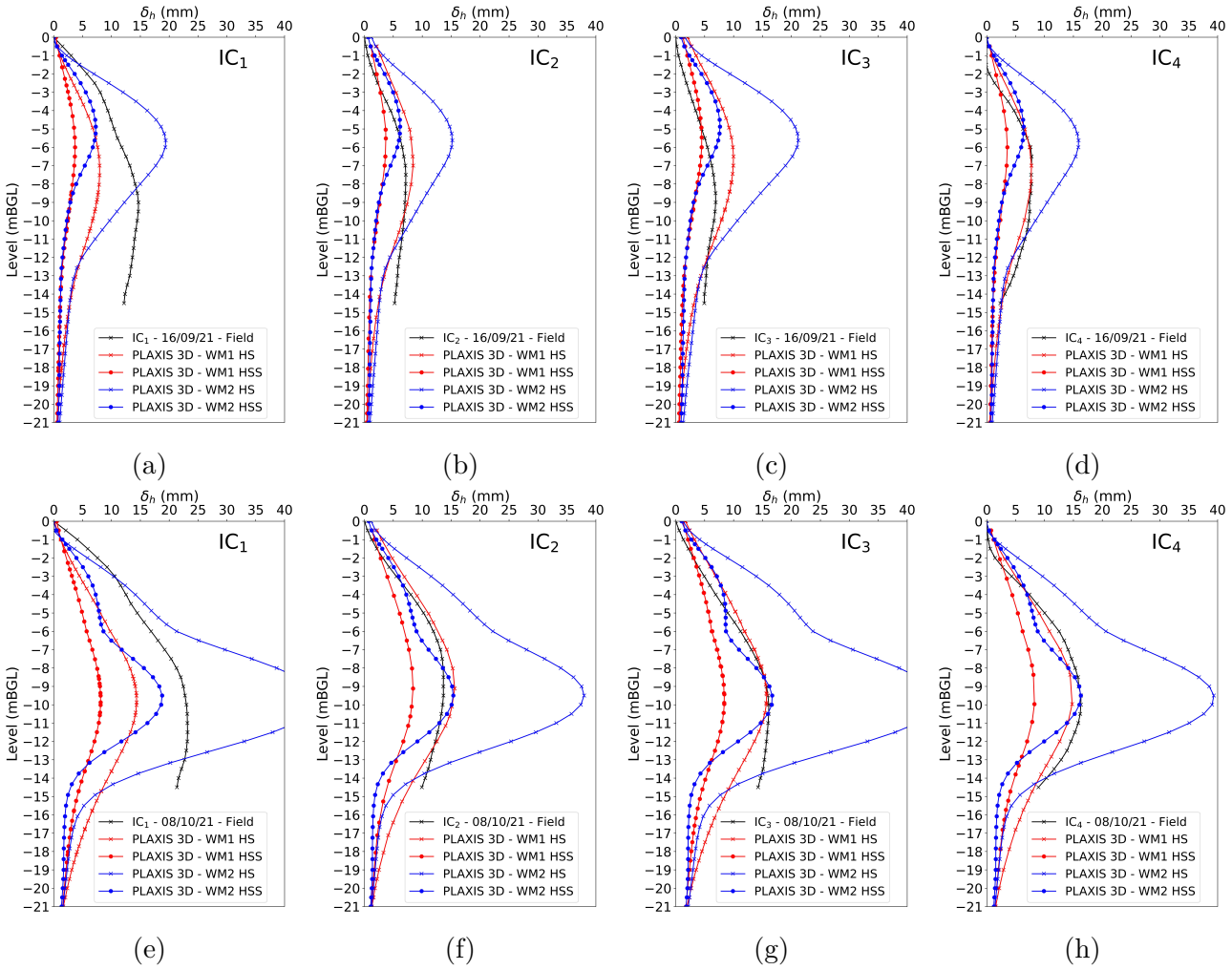


Figure 6.4: δ_h depth profiles predicted by the PLAXIS 3D numerical models together with those measured in the field. Excavation phase 1 (PLAXIS phase 7) IC_1, IC_2, IC_3, IC_4 comparisons presented in (a), (b), (c) and (d) respectively. Excavation phase 2 (PLAXIS phase 10C) IC_1, IC_2, IC_3, IC_4 comparisons presented in (e), (f), (g) and (h) respectively.



(a) (b) (c)

Figure 6.5: Photographs of connection between excavation wall and level 2 frame waler showing (a) plywood formwork and reinforcement, (b) concrete pour and (c) cured concrete connection.

The WM2 HSS model was selected to perform more advanced time dependent drainage and consolidation analyses due to its relatively accurate $\delta_{h,max}$ predictions, and the more complex features of soil and wall behaviour incorporated into this model. A time history of $\delta_{h,max}$ predicted using the PLAXIS 3D WM2 HSS model is presented in Figure 6.6, together with those measured in the field for IC_1 - IC_4 and the average excavation depth z_{ex}. There is very good agreement between the predicted $\delta_{h,max}$ and that observed for IC_2 - IC_4. The $\delta_{h,max}$ prediction is lower than that observed for IC_1 for the reasons discussed previously. The simulated increases in $\delta_{h,max}$ during periods of no excavation are in line with those measured, highlighting the ability of the numerical model to accurately model drainage and consolidation behaviour.

6.3.2 Prop loads

The WM2 HSS model was selected to perform more advanced time dependent drainage and consolidation analyses to predict the development of frame member loads, for the reasons previously discussed above. Time histories of axial load F and bending moment M predicted using the PLAXIS 3D WM2 HSS model are presented in Figure 6.7, together with those measured in the field at PROTOS. The presented field F data are those compensated for temperature in Figure 4.10. There is reasonably good agreement between the predicted and observed F data for members CCB1, P1 and P2. The large disparity between the predicted

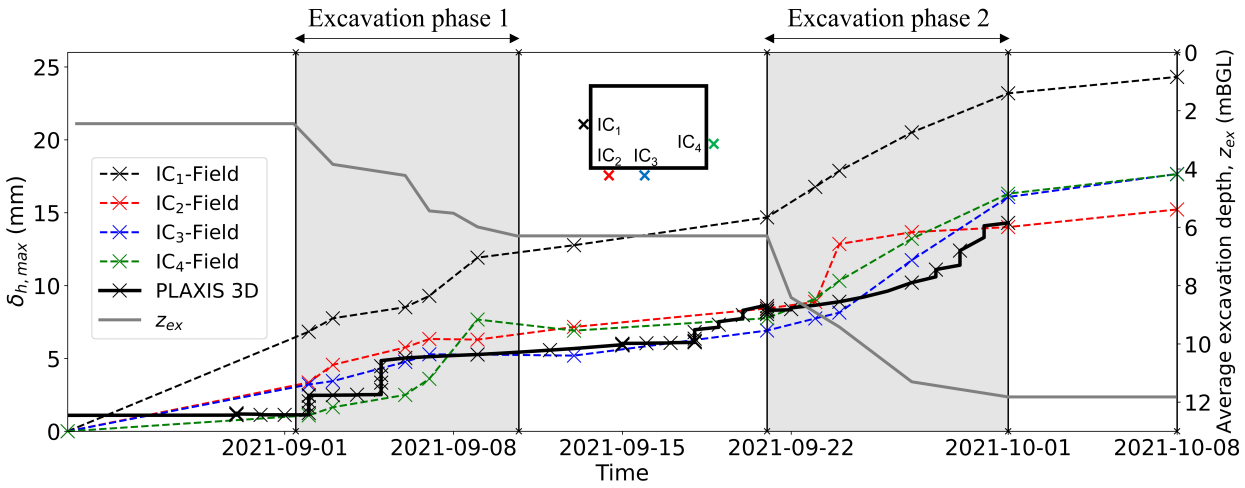


Figure 6.6: Time history of PLAXIS 3D WM2 HSS model $\delta_{h,max}$ predictions together with those measured in the field for IC_1 - IC_4 and average excavation depths.

and observed F for member W1 in Figure 6.7a is likely due to the combined wall on the short side of the excavation model taking a larger proportion of the laterally applied load than in the field. This is related to the anisotropic wall modelling approach described in Section 5.4.1, as bending was considered the most important loading type and the selection of accurate stiffness properties in the direction perpendicular to the waler was prioritised.

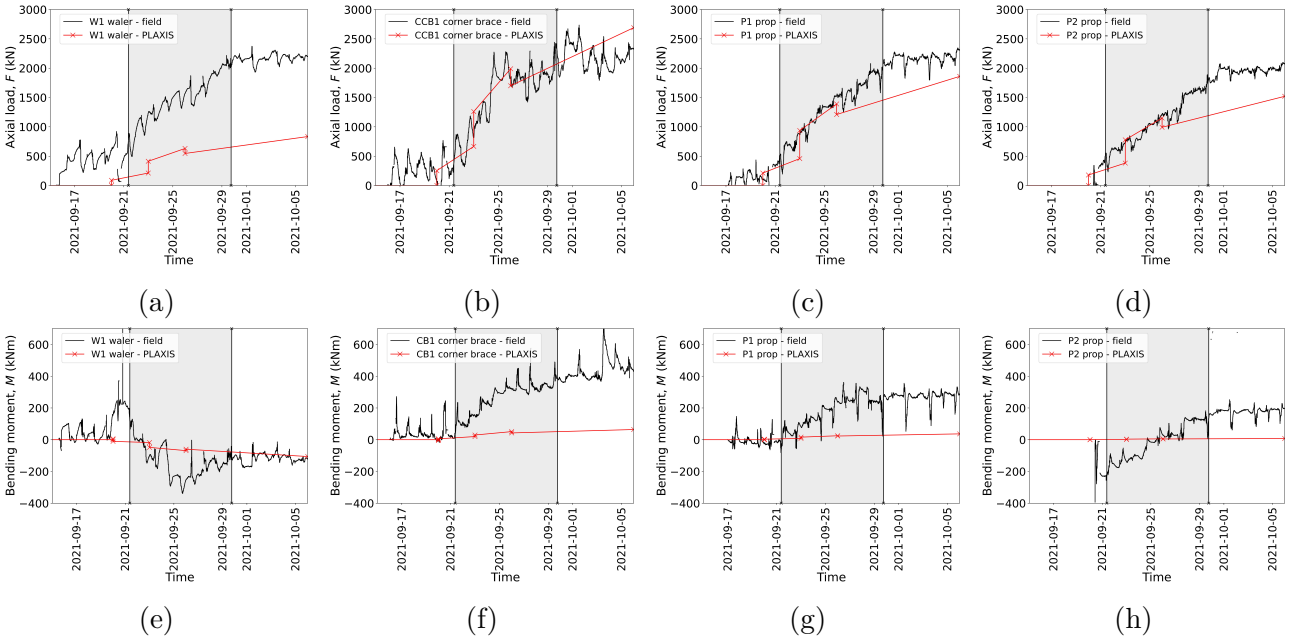


Figure 6.7: Time history of PLAXIS 3D WM2 HSS model F and M predictions together with those measured in the field for (a) & (e) W1 waler, (b) & (f) CCB1 corner brace, (c) & (g) P1 prop and (d) & (h) P2 prop. Excavation phase 2 period shaded in grey. Field measurements are compensated for temperature.

The M predictions in Figures 6.7e - 6.7h are significantly lower than the observed M in the field. The induced M is largely dependent on the degree of fixity at each structural connection and the interaction between frame members. The capabilities within geotechnical FE programs to model beam-to-beam connections are limited. These comparisons highlight a requirement to analyse advanced structural behaviour in a dedicated structural FE software.

6.3.3 Comparison to limit equilibrium methods

Figure 6.2c and Figure 6.2d present a comparison between the depthwise variations of M predicted using the PLAXIS 3D WM2 HSS and 2D CADS PWS simulations and those inferred from the measured δ_h field data (IC_3) following excavation phase 1 (PLAXIS phase 7) and excavation phase 2 (PLAXIS phase 10C) respectively. The M_{max} values predicted by the PLAXIS 3D simulations are in good agreement with those inferred from the field data, being significantly more accurate than those predicted by the CADS PWS simulations which are highly conservative.

An advantage of using the PLAXIS 3D model rather than the PLAXIS 2D model is the ability to model the fixed connection between the capping beam PLAXIS beam elements and the combined wall plate elements. This results in a non-zero M prediction at the top of the wall which is consistent with the inferred field M at ground level, with very good agreement between M values following both phases of excavation.

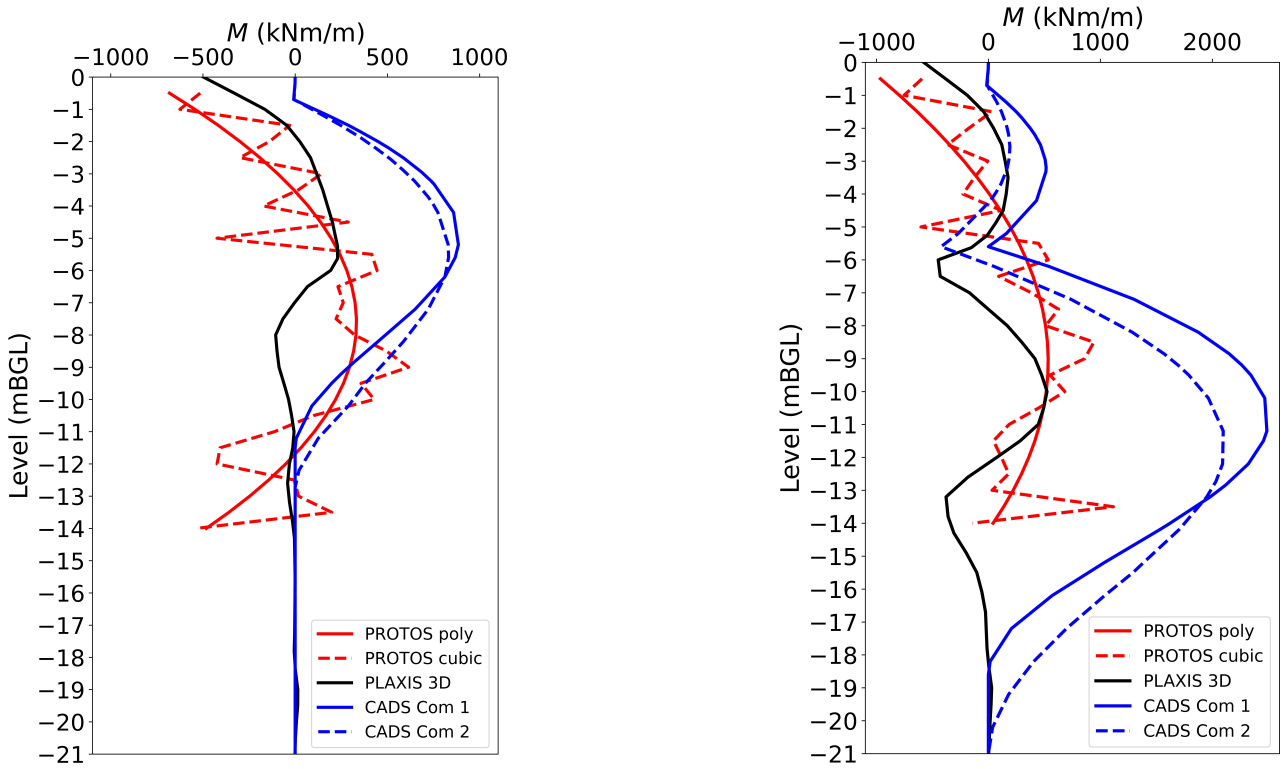


Figure 6.8: Comparison between depthwise variations of M predicted by PLAXIS 3D WM2 HSS model and CADS PWS simulations, and M inferred from field measurements in Figure 6.2a and Figure 6.2b for (a) excavation phase 1 (PLAXIS phase 7) and excavation phase 2 (PLAXIS phase 10C).

6.4 Probabilistic uncertainty analysis

The evaluation of the reliability of the numerical model prediction merits the analysis of soil property variability using a probabilistic analysis. Probabilistic uncertainty analyses are vital as part of a civil and structural design process as they provide insight into where resources and efforts should be focused to obtain accurate data for critical input parameters. These analyses also allow for quantification of the impact of inherent material uncertainties on model predictions by exploring a range of plausible parameter values to estimate the range of possible outcomes. This is particularly important for geotechnical applications due to the significant uncertainties associated with soil input parameters, which is often due to the limited availability of high quality site investigation data.

An uncertainty analysis forms an important part of the numerical modelling process for the

PROTOS deep excavation, due to the limited availability of high quality laboratory elemental test data. c' and ϕ' for the 11 m thick TF layer and stiffness parameters for the TF and GO layers have been determined using laboratory tests performed on a sample taken from a single level within each layer as shown in Figure 5.1. Also, the depth profile of G_0 in Figure 3.6 exhibits significant variability.

A flowchart of the adopted uncertainty analysis process is presented in Figure 6.9. A simplified surrogate form of the 2D FE model outlined in Section 5.3 was used for the analysis. The surrogate model had a reduced number of construction sequence steps and a coarser mesh than the 2D FE model outlined in Section 5.3, to reduce the computational runtime, and was validated by comparing its δ_h profiles following excavation phases 1 and 2 to those resulting from the 2D model in Section 6.2, with good agreement observed. Firstly, a sensitivity analysis was carried out to determine the most influential soil input parameters on $\delta_{h,max}$ at excavation formation. The analysis involves systematically varying each of the selected input parameters, while keeping all other parameters constant and provides insights into the relative importance of different input parameters and helps identify key drivers of system behaviour. The resulting parameters were then modelled as random variables with lognormal distributions as recommended in Bozkurt and Akbas (2023). MC simulations were then performed by randomly sampling each random variable for a surrogate FE model simulation. The process was repeated numerous times to provide a range of possible wall $\delta_{h,max}$ and M_{max} values at formation and their associated probabilities. The influence of the number of MC simulations n on the probability distributions of $\delta_{h,max}$ and M_{max} at formation was also explored. The MC simulation sequence was automated and the output data was extracted using the PLAXIS remote scripting server API and the in-built python interpretor.

6.4.1 Sensitivity study

The sensitivity study was performed using the USA EPA TRIM method outlined in Section 2.6.3. The parameters selected for the sensitivity study were the stiffness parameters E_{50},

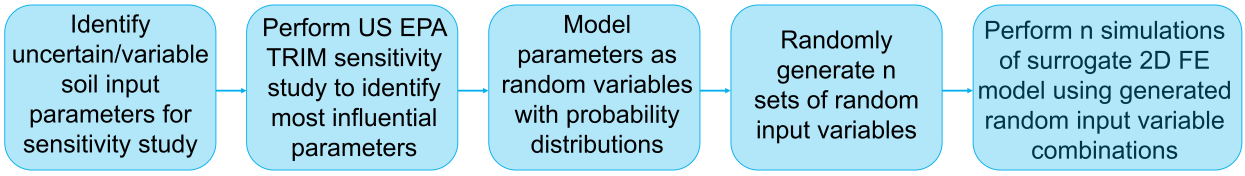


Figure 6.9: Flowchart depicting sensitivity analysis and MC simulation process.

E_{oed} and E_{ur} for all five soil layers and the strength parameters c' and ϕ' for the MG, TF, GO and GTS layers and s_u for the GTC layer as these are those typically incorporated into deep excavation probabilistic analyses as recommended in Phoon (1995). The relationship:

$$E_{50} = E_{oed} = \frac{E_{ur}}{3} \tag{6.2}$$

was assumed for the stiffness parameters. A value for the adjustment percentage $\Delta p = 10\%$ was adopted as recommended in McKone (1999). A comparison between the relative sensitivity α for each of the selected soil input parameters is presented in Figure 6.10. A threshold $\alpha = 5\%$ was chosen as recommended in Sekhavatian (2018). The most influential parameters on $\delta_{h,max}$ at excavation formation were determined to be E, c' and ϕ' for the TF layer and E and ϕ' for the GO layer. In practise, $\Delta p = 10\%$ should be applied to a realistic ranges for each soil parameter taken from literature or from preliminary site investigation data.

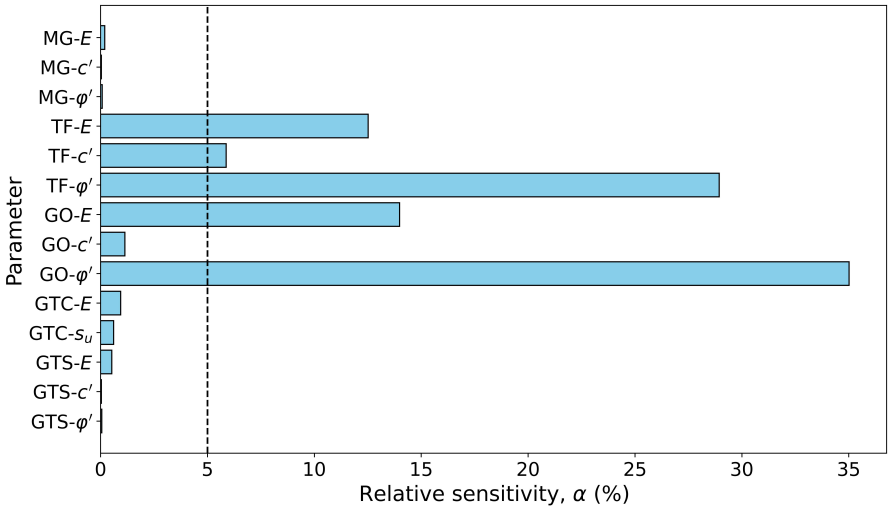


Figure 6.10: Relative sensitivities of selected soil input variables for $\delta_{h,max}$ at excavation formation.

6.4.2 Soil input parameter distributions

Each of the five most influential soil input parameters resulting from the sensitivity analysis was modelled as a random variable characterised by a lognormal probability distribution defined by a mean μ_X and standard deviation σ_X. The lognormal distribution ranges between zero and infinity and is positively skewed, making it well suited for parameters that cannot take on negative values. Once μ_X and σ_X are expressed in terms of the coefficient of variation COV, where:

$$COV = \frac{\sigma_X}{\mu_X} \tag{6.3}$$

and the mean $\mu_{\ln X}$ and standard deviation $\sigma_{\ln X}$ of the lognormal distribution can be calculated as:

$$\sigma_{lnX} = \sqrt{ln(1 + COV^2)} \tag{6.4}$$

$$\mu_{lnX} = ln\mu_X - 0.5\sigma_{lnX}^2 \tag{6.5}$$

μ_X and COV taken for each of the five soil input parameters are summarised in Table 6.2. μ_X for the parameters were taken as the values in Table 5.2 used for the soil constitutive modelling in Chapter 5. COV values were adopted from those published in literature in Table 2.3, and were evaluated with reference to the site specific SI and laboratory elemental test data in Section 3.2.2 and Section 5.2.2. The uncertain nature of the stiffness profile through the TF and GO ground layers due to limited laboratory elemental tests led to the selection of a large COV value characterising the TF and GO E_{50} statistical distributions. Conversely, as the profile of ϕ' inferred from the CPT test data exhibits little variation with depth, relatively low COV values were selected for ϕ', which is in agreement with the COV data reported in the literature (Table 2.3).

The MC simulation method involved randomly sampling each of the five soil input parameters n times to generate combinations for surrogate FE model simulations. The soil input

Table 6.2: Characteristic statistical parameters for soil input parameter lognormal distributions.

Soil input parameter	μ_X	COV **(%)**	COV **reference**
TF E_{50}	12.4 MPa	40	Kennedy (1979), Phoon (1995)
TF c'	7.7 kPa	30	Lumb (1974), Phoon (1995)
TF ϕ'	31.1 °	8	Kulhawy (1993), Phoon (1995)
GO E_{50}	83.8 MPa	40	Kennedy (1979), Phoon (1995)
GO ϕ'	43.5 °	8	Kulhawy (1993), Phoon (1995)

parameters were modelled by lognormal distributions characterised by the statistical parameters in Table 6.2. The generated soil input parameter statistical distributions for $n = 100$, $n = 250$, $n = 500$ and $n = 1000$ are presented as histograms in Figure 6.11. A probability density function (PDF) has been fitted to each of the histograms in Figure 6.11. μ_X and COV estimated from each of the histograms are annotated. Each of the histograms in Figure 6.11 exhibit positive skewness as expected for a lognormal distribution, with those with larger COV displaying greater positive skewness. The histograms for $n = 100$ exhibit the most variability, with variability from the fitted PDF decreasing with increasing n. While there is good agreement between μ_X in Table 6.2 and the estimated μ_X in Figure 6.11 for each input parameter, there is some disparity in the values of COV due to the random nature of parameter generation using the MC approach.

6.4.3 Results and discussion

The statistical distributions of the surrogate FE model output parameters simulated using the MC method are presented in the form of histograms in Figure 6.12 and Figure 6.13. The output parameters presented are $\delta_{h,max}$ and M_{max} in Figure 6.12 and Figure 6.13 respectively, following the first and second phases of excavation. Again a probability density function (PDF) has been fitted to each of the histograms in Figure 6.11. μ_X and COV estimated from each of the histograms are annotated. Figure 6.12 and Figure 6.13 show the variability in the soil

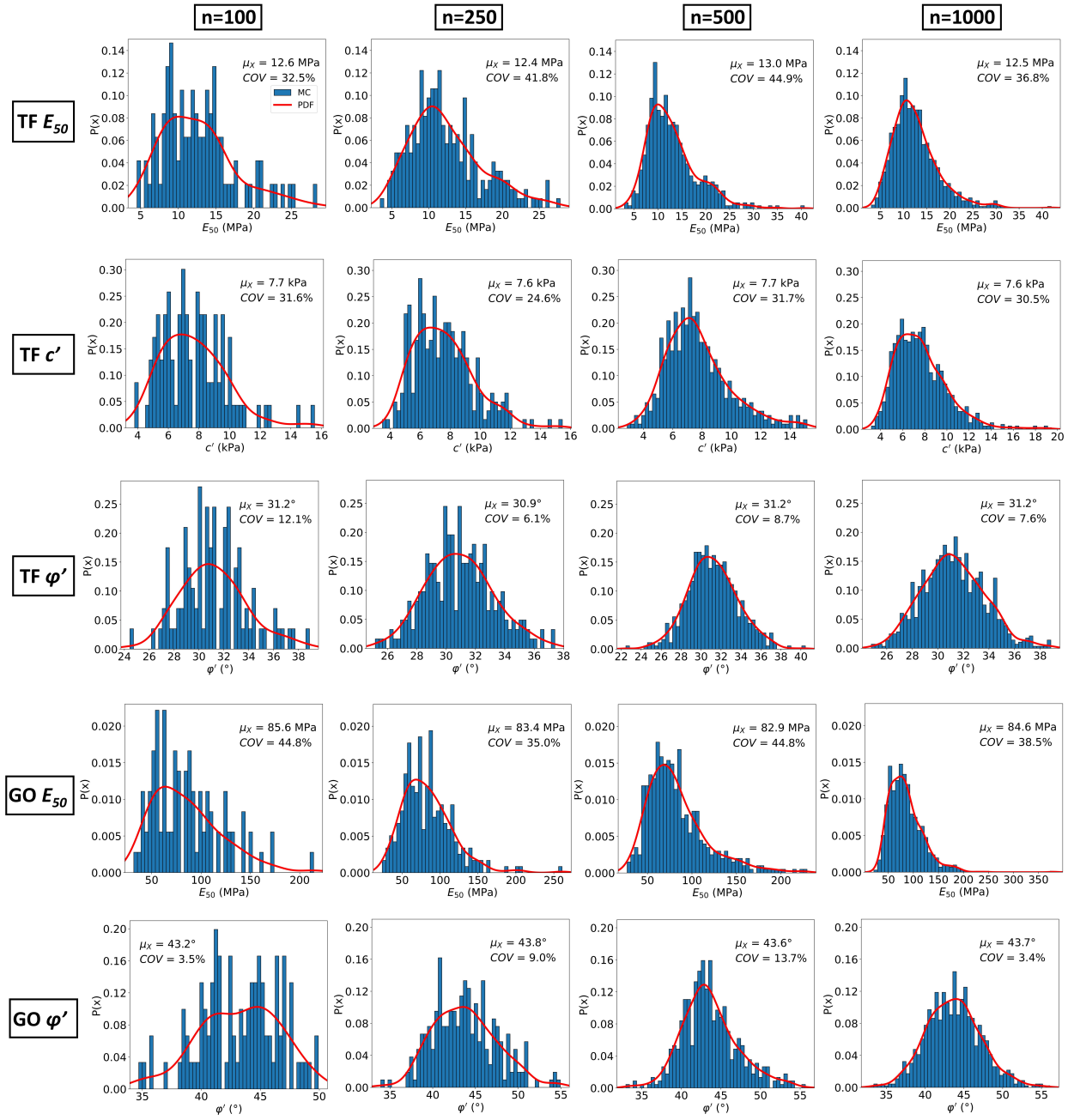


Figure 6.11: Soil input parameter distributions generated using MC simulation procedure for $n = 100$, $n = 250$, $n = 500$ and $n = 1000$. MC denotes MC simulated distribution and PDF denotes the fitted probability density function.

input parameters has a significant influence on the simulated $\delta_{h,max}$ and M_{max}, with the largest generated values being 58.8% and 67.3% greater than μ_X for each distribution respectively.

Again, the generated statistical distribution for each output parameter for $n = 100$ exhibits significant variability from the fitted PDF, with the estimated COV values being largely different from those estimated for other n. For increasing n, COV appears to converge and less

variability from the fitted PDF is observed. Figure 6.14 shows the cumulative average of $\delta_{h,max}$ following excavation phase 2 with increasing simulation number for each n, which acts as an indicator for MC simulation convergence. Convergence refers to the process of the simulated values approaching a stable mean as the number of simulations increases. Initially, significant fluctuation in $\delta_{h,max}$ μ_x is observed for each set of simulations. While, fluctuation reduces significantly at approximately $n = 50$, the large variability in Figure 6.12 and Figure 6.13 at $n = 100$ indicates more simulations ($n = 250$) are required to achieve a representative distribution of output parameters.

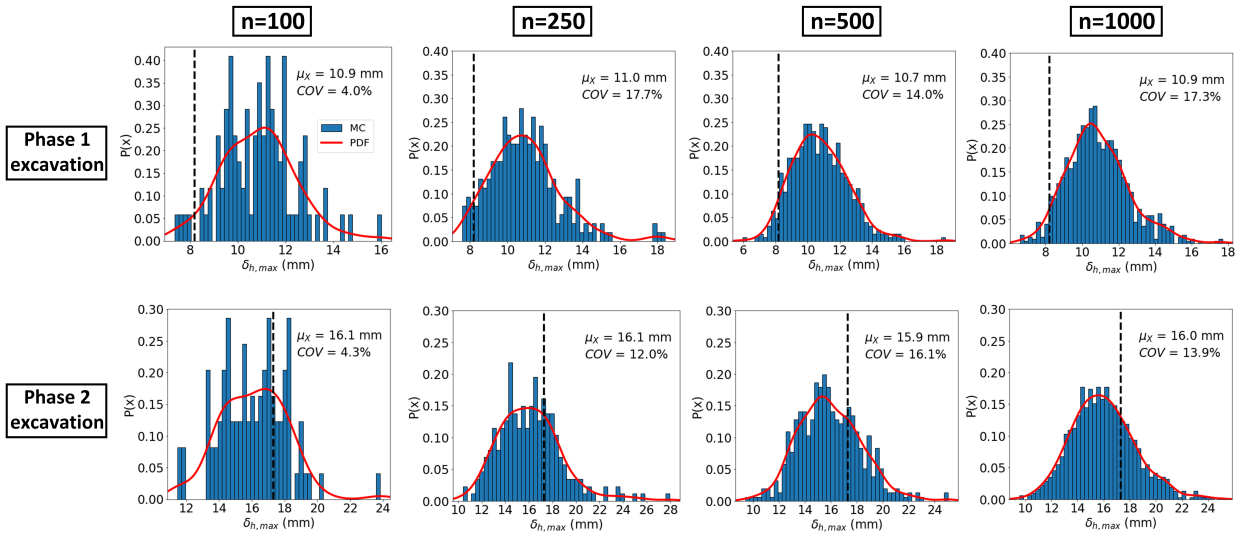


Figure 6.12: Predicted $\delta_{h,max}$ distributions generated using MC simulation procedure for $n = 100$, $n = 250$, $n = 500$ and $n = 1000$. MC denotes MC simulated distribution and PDF denotes the fitted probability density function. Average field measurement indicated by black dashed line.

Figure 6.15 shows the output M_{max} following excavation phase 1 for each FE simulation for $n = 1000$. M_{max} predicted using the limit equilibrium analysis in CADS PWS in Figure 6.2c is shown to determine the probability of exceeding this value p_e. Only 5 of the 1000 simulations predicts the FE model M_{max} being greater than the design limit predicted by the LE analysis ($p_e = 0.5\%$). This approach can be used in industry design to provide a quantitative assessment of the risk associated with uncertainty in geotechnical input parameters to estimate the probability of various outcomes. Also the soil parameters which most influence system perfor-

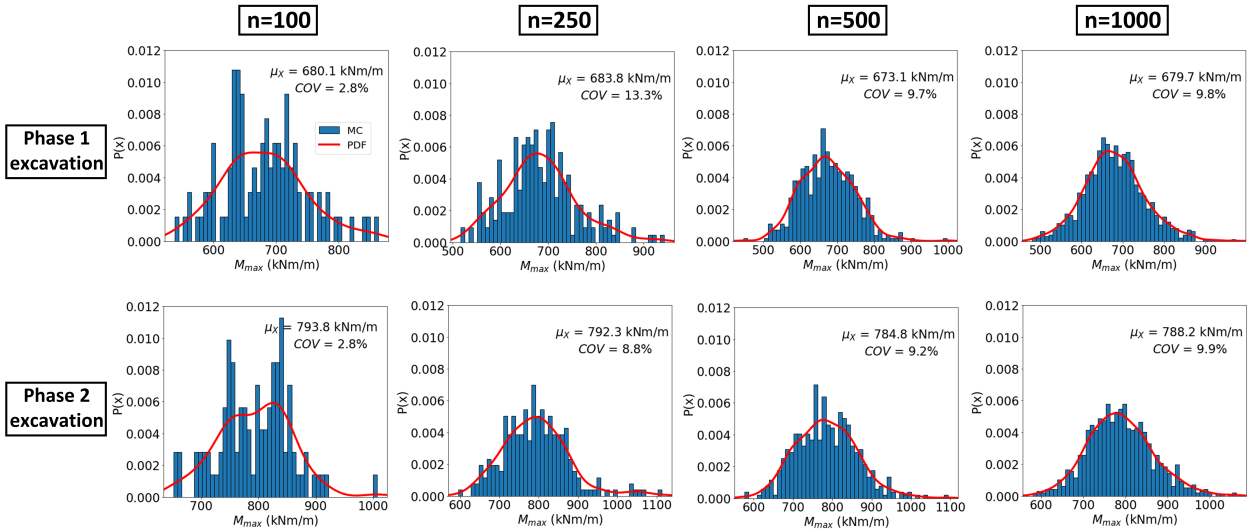
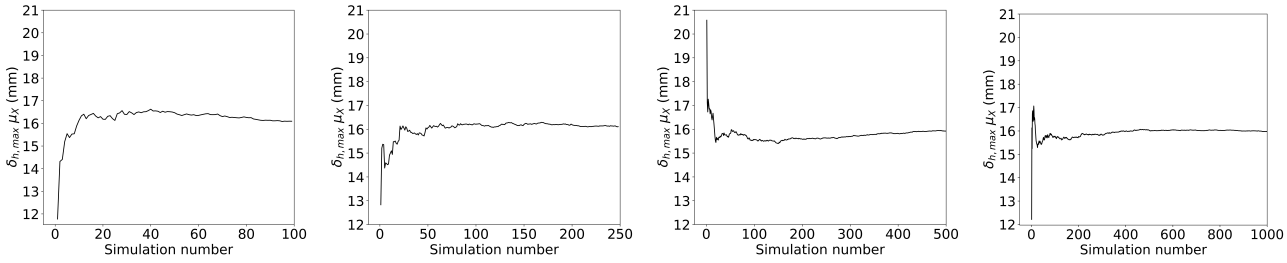


Figure 6.13: Predicted M_{max} distributions generated using MC simulation procedure for $n = 100$, $n = 250$, $n = 500$ and $n = 1000$. MC denotes MC simulated distribution and PDF denotes the fitted probability density function.

mance can be identified so that testing schemes used for their determination are prioritised. Employing a probabilistic design approach for numerical analyses is a crucial process which is often overlooked in modern design practise. It enables data-driven and informed decisions to be made to achieve target levels of reliability.



(a) (b) (c) (d)

Figure 6.14: Cumulative $\delta_{h,max}$ mean for excavation phase 2 with increasing simulation number for (a) $n = 100$, (b) $n = 250$, (c) $n = 500$ and (d) $n = 1000$.

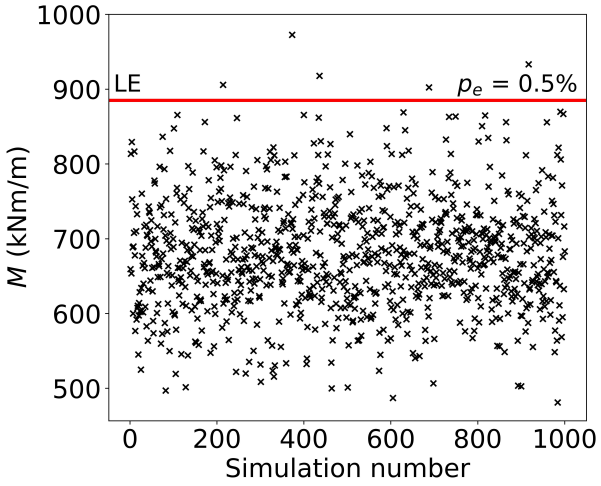


Figure 6.15: Simulated M_{max} following excavation phase 1 for each FE simulation for $n = 1000$. CADS LE M_{max} prediction plotted for probability of exceedance p_e calculation.

6.5 Summary of key findings

This chapter has presented the findings of a numerical modelling scheme to simulate the behaviour of the deep bunker excavation at PROTOS EFW. The numerical results have been compared to those measured in the field, and those predicted using simplified LE design methods to evaluate the accuracy of the model predictions. The key findings from this chapter are summarised below:

- The use of the MC constitutive model yields the largest δ_h along the full depth profile and induces the largest basal heave. This is due to the inability of the MC model to simulate the greater unloading stiffness exhibited by real soils, as only E_{50} is provided as an input, which leads to unrealistically large swelling during unloading, and poorer deformation predictions than those made by simulations using more complex soil constitutive models.
- The comparison between the results of the 2D numerical models and the measured field data suggests that modelling the combined wall with the length-weighted average of tube and sheet pile pair properties overpredicts the wall bending stiffness. This is supported by the comparison between the 3D WM1 and WM2 wall model results, as the δ_h predictions made by separately modelling the combined wall elements (WM2) agree better with

the field measurements than those predicted using WM1. This suggests a 3D numerical analysis should be performed when modelling a deep excavation supported by a combined wall.

- The δ_h depth profiles predicted using the WM2 HSS 3D simulation most accurately simulates those measured in the field. The model also accurately simulates the development of $\delta_{h,max}$ with time and provides reasonable predictions of the development of F with time in the support frame members.
- The δ_h profiles predicted using the WM2 wall model include a point of inflection at the frame level following excavation phase 2 which was not observed in the field. This is likely due to the use of compressive plywood to form the concrete fill connection, which enabled some additional lateral displacement above that predicted by the numerical models. This highlights the importance of constructing connections and joints which replicate the degree of fixity modelled at the design stage.
- M predicted by the numerical models are significantly lower than those observed in the field, due to limited capabilities within PLAXIS to model different degrees of fixity at beam-to-beam connections. This suggests analysing more advanced structural interactions and behaviours in a dedicated structural FE software package.
- The δ_h and prop loads predicted by the CADS PWS LE analyses are significantly larger than those measured in the field, with the numerical simulations providing more accurate predictions.
- Overall, when designing deep excavations supported by combined walls, 3D numerical simulations should be employed over 2D simulations, as they provide an opportunity to model each of wall elements and support frame members separately, they incorporate increased wall corner stiffness and they can be used to model fixed connections between support structures and walls.

7 | Conclusions

7.1 Introduction

This research has explored the soil-structure interaction mechanisms involved in combi-wall supported deep excavations to achieve improved and new insight into the behaviour of the support system. This has been achieved through field monitoring of a live construction site together with complementary numerical analysis. This chapter summarises the key findings and contributions, and makes suggestions for areas of future research.

7.2 Key contributions

Monitored field data

High quality monitored data was provided for a combi-wall supported deep excavation in soft and challenging ground conditions in the UK. Case histories reporting the behaviour of deep excavations in UK soft soils are almost non-existent with the vast majority of data relating to London Clay. Also, field data for the combi-wall support system is very uncommon. For example, 16 of the 296 case studies reported in Long (2001) related to a combi-wall design, and only one involved a tube and sheet pile combination. With cofferdam installation technology having advanced significantly in recent years, the combi-wall solution has the potential to become a more conventional method in soft and challenging ground to eliminate the risks associated with *in situ* concrete solutions (contiguous, secant pile and diaphragm walls) in those conditions, which involve significant losses of cementitious material and out-of-shape piles. The contextualization of the performance of the combi-wall with reference to more typically employed wall types reported in this research provides consultants, contractors and researchers with a useful reference to improve confidence in their use.

High quality monitored data was also provided for temperature effects on prop loads for props supporting combi-walls in soft ground. The current method adopted by the industry to

determine temperature induced loads for the design of temporary props is outlined in Gaba et al. (2017), which recommends values of FF based on only 4 case histories – all of which involve the use of *in situ* secant pile and diaphragm walls in stiff London Clay. There are currently no recommended values of FF in Gaba et al. (2017) for props supporting deep excavations in soft soils due to a lack of reliable case history data. While the database of case history FF values published in Twine and Roscoe (1997) provides guidance on FF selection for more flexible sheet pile walls, only 5 cases are reported and no details of ground conditions are provided. The temperature induced prop load data collected during this research provides a valuable contribution to the databases in Twine and Roscoe (1997) and in Gaba et al. (2017) and provides guidance on the selection of FF values for props supporting combi-walls in soft soils.

Measured wall displacements were well represented by average values reported elsewhere in the literature and were close to lower bounds reported for deep excavations in soft clays; these results highlight the potential applicability of existing solutions and design methods to combi-wall design in soft soils in the UK and suggest that combi-wall supported deep excavations can successfully control ground deformations in soft and challenging soils.

Vibratory piling internally within the excavation caused an increase to the horizontal wall displacements of up to 111% and increases in level 2 frame member loads of between 700 – 2100 kN due to a loss of strength of glacial till clay (C) inside the excavation consequent upon remoulding and excess pore pressure generation caused by pile driving. Vibratory piling also led to a reduction in the performance of the pumping system due to the introduction of additional flow paths. This reveals the importance of considering the full construction process on the support system performance and suggests that vibratory piling works should be conducted prior to excavation works if possible. These findings also suggest that impact piling methods may be preferable over vibratory ones for pile driving within excavations in soft clays and

saturated granular materials.

Field monitoring systems

Monitored data was presented for the application of strain sensing fibre optic FBG systems to monitor the structural performance of the RC bunker base. This is one of very few cases involving the use of FBG systems to monitor strains in concrete and the first case in which FBGs are used to monitor an underground RC base slab. Typically, discrete embedment type VW strain gauges are used for this application, whereas FBGs provide pseudo-continuous strain profiles. The highly sensitive nature of FBG systems make them suitable for strain monitoring within very stiff concrete structures.

A novel method for distinguishing between temperature-induced and mechanically-induced fibre optic FBG strains was outlined, which uses precisely machined aluminium blocks clamped onto one FBG in each string. The method was validated by comparing the inferred temperature series to that measured by an adjacent thermistor and that predicted using the CIRIA C766 industry adopted approach (Bamforth (2007)) for both the top and bottom of the RC bunker base, with good agreement observed. Typically a secondary temperature compensation fibre length is positioned adjacent to the primary fibre to determine temperature effects. Although more cases using the block temperature method are necessary to support or contradict the findings from this research, the method could provide significant financial benefits by avoiding the requirement for a secondary fibre length. This is particularly applicable to FBG strain sensing systems, for which the cost of fibre lengths is typically much greater than for distributed systems.

The bespoke dashboard developed for this research to display field monitoring data in real-time provided the site team with crucial feedback during the construction process. The data were used to actively inform the construction process during high risk activities including the final excavation stages and bunker piling, and promoted a proactive approach to risk mitigation

and management on site. The positive impact of the feedback system on this project has already led to Ward & Burke Construction deploying the same system on other more recent deep excavation and caisson shaft projects.

Numerical modelling

The use of the MC constitutive model predicted the largest δ_h along the full depth profile and induced the largest basal heave. This is due to the inability of the MC model to simulate the greater unloading stiffness exhibited by real soils, as only E_{50} is provided as an input, which leads to unrealistically large swelling during unloading, and poorer deformation predictions than those made by simulations using more complex soil constitutive models.

The δ_h profiles predicted using the 3D numerical model included a point of inflection at the frame level following excavation phase 2 which was not observed in the field. This is likely due to the use of compressive plywood to form the concrete fill connection, which enabled some additional lateral displacement above that predicted by the numerical models. Large differences in M for the level 2 corner brace between the numerical predictions and field measurements were also observed due to limited capabilities for modelling the degree of fixity at connections in the numerical model. This highlights the importance of constructing connections and joints which replicate the degree of fixity modelled at the design stage.

The comparison between the results of the 2D numerical models and the measured field data suggested that modelling the combined wall with the length-weighted average of tube and sheet pile pair properties overpredicts the wall bending stiffness. This suggests the combined wall is better represented in 3D by modelling separate tube and sheet pile elements. When designing deep excavations supported by combined walls, 3D numerical simulations should be employed over 2D simulations, as they provide an opportunity to model each of wall elements and support frame members separately, they incorporate increased wall corner stiffness and they can be used to model fixed connections between support structures and walls.

7.3 Recommendations for future research

Areas for further research which would contribute to this area are suggested below:

- Additional monitoring of combi-wall supported deep excavations in a variety of ground conditions would provide further monitored data to which the observations of structural behaviours and soil-structure interactions can be compared. Additional prop temperature effect data taken from combi-wall supported deep excavations in soft ground could be used to check the FF values determined from this research. Future monitoring should include surface settlement and basal heave monitoring using extensometers or shape arrays, particularly if the excavation is constructed in an urban area. In many previously published deep excavation case histories, lateral wall deflection is normalised using surface settlement to enable comparisons to be made to empirical databases and design methods. This would provide some additional insight into the performance of the combi-wall support system and its ability to control ground deformations.
- Several key improvements could be made to the instrumentation and monitoring setup. The development of a purpose-built monitoring cabin would greatly improve the ergonomics of the setup, reduce installation times, address issues with sourcing power, and further reduce equipment exposure to the site environment. Distributed FO strain sensing technology should be deployed for monitoring deep excavation components to provide fully continuous strain profiling. The reduced cost of distributed fibre lengths would also enable the deployment of additional fibres to provide profiling in two planes across deep excavation walls and base slabs. The aluminium block FBG temperature compensation approach should be used in additional RC structural monitoring projects alongside thermistors to qualify the assertions made from this research. The use of FO monitoring to measure lateral wall deflections would provide pseudo-continuous or continuous data which would be advantageous over the discrete points measured using inclinometers. For

steel tube and sheet piles, this could be achieved by cutting a notch along the length of the pile and securing a fibre length within the notch using resin.

- Additional monitoring of combi-wall supported deep excavations would also provide an opportunity to develop a numerical model to predict its behaviour. This would enable the hypotheses drawn from this research related to the advantages of 3D modelling over 2D modelling for combi-wall support structures and prop members to be tested on deep excavations with different dimensions and in different ground conditions.
- There is scope to incorporate the numerical model developed to predict deep excavation performance into the real-time monitoring feedback system through the use of machine learning techniques. Bayesian inference can be used for real-time "model updating", which involves using early stage field measurements to revise model input parameters and consequently revise later stage design predictions. This approach has the potential to create "early warning" systems to reduce risk, by inferring input parameters and comparing these to the safe ranges specified in the design of the deep excavation. Also, artificial neural networks could be trained to perform FE software calculations, which would eliminate the need for the associated significant computational requirements.

7.4 Concluding remarks

This research has investigated the soil-structure and structural interaction mechanisms involved in combi-wall supported deep excavations to achieve improved and new insight into the behaviour of the modern support system. This has been achieved through field monitoring of a live construction site together with complementary numerical analysis. The conclusions drawn from this research highlight the potential for significant financial and environmental savings to be made by adopting more accurate design methods and reducing overconservatism in industry design. This research, alongside future cases, can provide confidence in the use of more accurate numerical design methods and highlight their advantages.

Bibliography

Abaqus (2020). Abaqus user manual. *Abaqus*.

Absi, E. (2017). *Active and passive earth pressure tables*. Routledge.

Addenbrooke, T. I., Potts, D., and Dabee, B. (2000). Displacement flexibility number for multipropped retaining wall design. *Journal of geotechnical and geoenvironmental engineering*, 126(8):718–726.

AGL Consulting (2018). Deep excavation. URL: https://agl.ie/project-item/ [Online; accessed August 15, 2022].

Akbaş, B. (2015). Probabilistic slope stability analysis using limit equilibrium, finite element and random finite element methods. Master's thesis, Middle East Technical University.

Al-Tabbaa, A. and Wood, D. M. (1989). An experimentally basedbubble'model for clay. In *International Symposium on Numerical Models in Geomechanics (3rd: 1989).*, pages 91–99. Elsevier Applied Science Publishers.

Alavie, A., Maaskant, R., Ohn, M., Karr, S., Huang, S., et al. (1995). A structurally integrated bragg grating laser sensing system for a carbon fiber prestressed concrete highway bridge. *Smart Materials and Structures*, 4(1):20.

Allievi, L., Curran, T., Deakin, R., and Tyldsley, C. (2018). On the use of cpt for the geotechnical characterization of a normally consolidated alluvial clay in hull, uk. In *Cone Penetration Testing 2018: Proceedings of the 4th International Symposium on Cone Penetration Testing (CPT'18), 21-22 June, 2018, Delft, The Netherlands*, page 73. CRC Press.

Amatya, B., Soga, K., Bourne-Webb, P., Amis, T., and Laloui, L. (2012). Thermo-mechanical behaviour of energy piles. *Géotechnique*, 62(6):503–519.

Arabaninezhad, A. and Fakher, A. (2021). A practical method for rapid assessment of reliability in deep excavation projects. *Iranian Journal of Science and Technology, Transactions of Civil Engineering*, 45:335–357.

ArcelorMittal (2020). Kiel cruise & ferry terminal combined wall. URL: https://sheetpiling.arcelormittal.com/products-services/production-range/combined-walls/combined-walls-steel-tubes/ [Online; accessed August 15, 2023].

Atkinson, J. (2000). Non-linear soil stiffness in routine design. *Géotechnique*, 50(5):487–508.

Atkinson, J. (2007). *The Mechanics of Soils and Foundations*. CRC Press.

Augarde, C. and Burd, H. (2001). Three-dimensional finite element analysis of lined tunnels. *International Journal for Numerical and Analytical Methods in Geomechanics*, 25(3):243–262.

Bamforth, P. (2007). *Early-age thermal crack control in concrete*, volume 660. Ciria.

Bamforth, P. (2018). Ciria c766. *Control of cracking caused by restrained deformation in concrete*.

Beck, Y., Di Murro, V., Pelecanos, L., Soga, K., Kechavarzi, C., Morton, R., and Scibile, L. (2016). Distributed fibre optic long-term monitoring of concrete-lined tunnel section tt10 at cern. In *Transforming the Future of Infrastructure through Smarter Information: Proceedings of the International Conference on Smart Infrastructure and ConstructionConstruction, 27–29 June 2016*, pages 27–32. ICE Publishing.

Bell, A., Soga, K., Ouyang, Y., Yan, J., and Wang, F. (2013). The role of fibre optic instrumentation in the re-use of deep foundations. In *Proceedings of the 18th International conference on Soil Mechanics and Geotechnical Engineering, Paris*, pages 1863–1866.

Benz, T. (2007). *Small-strain stiffness of soils and its numerical consequences*, volume 5. Univ. Stuttgart, Inst. f. Geotechnik Stuttgart.

Benz, T., Vermeer, P., and Schwab, R. (2009). A small-strain overlay model. *International journal for numerical and analytical methods in geomechanics*, 33(1):25–44.

Bjerrum, L. and Eide, O. (1956). Stability of strutted excavations in clay. *Géotechnique*, 6(1):32–47.

Blackburn, J. T. (2005). *Automated sensing and three-dimensional analysis of internally braced excavations*. PhD thesis, Northwestern University.

Bolton, M. and Powrie, W. (1988). Behaviour of diaphragm walls in clay prior to collapse. *Géotechnique*, 38(2):167–189.

Bono, N. A., Liu, T. K., and Soydemir, C. (1992). *Performance of an internally braced slurry-diaphragm wall for excavation support*. ASTM International.

Boone, S. and Crawford, A. (2000). Braced excavations: Temperature, elastic modulus, and strut loads. *Journal of geotechnical and geoenvironmental engineering*, 126(10):870–881.

Bourne-Webb, P., Amatya, B., Soga, K., Amis, T., Davidson, C., and Payne, P. (2009). Energy pile test at lambeth college, london: geotechnical and thermodynamic aspects of pile response to heat cycles. *Géotechnique*, 59(3):237–248.

Bourne-Webb, P. J., Amatya, B., and Soga, K. (2013). A framework for understanding energy pile behaviour. *Proceedings of the Institution of Civil Engineers-Geotechnical Engineering*, 166(2):170–177.

Bozkurt, S. and Akbas, S. O. (2023). Finite element-based geotechnical risk analysis for anchor-supported deep excavations. *Arabian Journal of Geosciences*, 16(8):470.

Brinkgreve, R., Kumarswamy, S., and Swolfs, W. (2022). Plaxis 2022. *Reference manual*.

Brinkgreve, R. B. (2005). Selection of soil models and parameters for geotechnical engineering application. In *Soil constitutive models: Evaluation, selection, and calibration*, pages 69–98.

Burd, H., Houlsby, G., Augarde, C., and Liu, G. (2000). Modelling tunnelling-induced settlement of masonry buildings. *Proceedings of the institution of civil engineers-geotechnical engineering*, 143(1):17–29.

Burland, J. (1989). Ninth laurits bjerrum memorial lecture:" small is beautiful"—the stiffness of soils at small strains. *Canadian geotechnical journal*, 26(4):499–516.

CADS (2011). Cads piled wall suite user manual.

Caquot, A. I. and Kérisel, J. L. (1948). *Tables for the calculation of passive pressure, active pressure and bearing capacity of foundations*. Gautier-Villars.

Carder, D. (1995). Ground movements caused by different embedded retaining wall construction techniques. *Trl Report*, (172).

Chambers, P., Augarde, C., Reed, S., and Dobbins, A. (2016). Temporary propping at crossrail paddington station. *Geotechnical research*, 3(1):3–16.

Chan, T. H., Yu, L., Tam, H.-Y., Ni, Y.-Q., Liu, S., Chung, W., and Cheng, L. (2006). Fiber bragg grating sensors for structural health monitoring of tsing ma bridge: Background and experimental observation. *Engineering structures*, 28(5):648–659.

Chapman, K., Cording, E., and Schnabel, H. (1972). Performance of a braced excavation in granular and cohesive soils. In *Performance of Earth and Earth-Supported Structures*, page 271. ASCE.

Cho, S. E. (2007). Effects of spatial variability of soil properties on slope stability. *Engineering Geology*, 92(3-4):97–109.

Clarke, B. and Wroth, C. (1984). Analysis of dunton green retaining wall based on results of pressuremeter tests. *Géotechnique*, 34(4):549–561.

Clough, G. W. (1990). Construction induced movements of insitu wall, design and performance of earth retaining structure. In *ASCE*, pages 439–479.

Clough, G. W., Smith, E. M., and Sweeney, B. P. (1989). Movement control of excavation support systems by iterative design. In *Foundation engineering: Current principles and practices*, pages 869–884. ASCE.

Coulomb, C. A. (1773). Essai sur une application des regles de maximis et minimis a quelques problemes de statique relatifs a 1'architecture. *Mem. Div. Sav. Acad.*

Darcy, H. (1856). *Les fontaines publiques de la ville de Dijon: exposition et application des principes à suivre et des formules à employer dans les questions de distribution d'eau*, volume 1. Victor dalmont.

De Battista, N., Elshafie, M., Soga, K., Williamson, M., Hazelden, G., and Hsu, Y. (2015). Strain monitoring using embedded distributed fibre optic sensors in a sprayed concrete tunnel lining during the excavation of cross-passages. In *Proceedings of the 7th International Conference on Structural Health Monitoring of Intelligent Infrastructure, Torino, Italy*, pages 1–3.

Deliveris, A. V., Theocharis, A. I., Koukouzas, N. C., and Zevgolis, I. E. (2022). Numerical slope stability analysis of deep excavations under rainfall infiltration. *Geotechnical and Geological Engineering*, 40(8):4023–4039.

Donegan Civil Engineering (2019). Segmental shaft sinking. URL: https://www.donegan.co.uk/services/segmental-shaft-sinking/[Online; accessed August 8, 2022].

Dong, Y. (2014). *Advanced finite element analysis of deep excavation case histories*. PhD thesis, University of Oxford.

Dong, Y., Burd, H., and Houlsby, G. (2016). Finite-element analysis of a deep excavation case history. *Géotechnique*, 66(1):1–15.

Drucker, D. C., Prager, W., and Greenberg, H. J. (1952). Extended limit design theorems for continuous media. *Quarterly of applied mathematics*, 9(4):381–389.

Duncan, J. M. and Chang, C.-Y. (1970). Nonlinear analysis of stress and strain in soils. *Journal of the soil mechanics and foundations division*, 96(5):1629–1653.

EC7 (2004). Geotechnical design–part 1: General rules.

FBGS (2019). Fbgs instruction manual. *FBGS*.

Fernie, R. and Sucking, T. (1996). Simplified approach for estimating lateral wall movement of embedded walls in uk ground. In *Geotechnical aspects of underground construction in soft ground*, pages 131–136.

Finno, R., Atmatzidis, D., and Nerby, S. (1988). Ground response to sheet-pile installation in clay," proceedings, second international conference on case histories in geotechnical engineering, st. louis, mo.

Finno, R. J., Arboleda-Monsalve, L. G., and Sarabia, F. (2015). Observed performance of the one museum park west excavation. *Journal of Geotechnical and Geoenvironmental Engineering*, 141(1):04014078.

Finno, R. J., Atmatzidis, D. K., and Perkins, S. B. (1989). Observed performance of a deep excavation in clay. *Journal of Geotechnical Engineering*, 115(8):1045–1064.

Finno, R. J., Blackburn, J. T., and Roboski, J. F. (2007). Three-dimensional effects for supported excavations in clay. *Journal of Geotechnical and Geoenvironmental Engineering*, 133(1):30–36.

Finno, R. J., Bryson, S., and Calvello, M. (2002). Performance of a stiff support system in soft clay. *Journal of Geotechnical and Geoenvironmental Engineering*, 128(8):660–671.

Finno, R. J. and Calvello, M. (2005). Supported excavations: observational method and inverse modeling. *Journal of geotechnical and geoenvironmental engineering*, 131(7):826–836.

Finno, R. J., Kim, S., Lewis, J., and Van Winkle, N. (2019). Observed performance of a sheetpile-supported excavation in chicago clays. *Journal of Geotechnical and Geoenvironmental Engineering*, 145(2):05018005.

Finno, R. J. and Roboski, J. F. (2005). Three-dimensional responses of a tied-back excavation through clay. *Journal of Geotechnical and Geoenvironmental Engineering*, 131(3):273–282.

Franzius, J., Potts, D., and Burland, J. (2005). The influence of soil anisotropy and k 0 on ground surface movements resulting from tunnel excavation. *Géotechnique*, 55(3):189–199.

Gaba, A., Hardy, S., Doughty, L., Powrie, W., and Selemetas, D. (2017). *Guidance on embedded retaining wall design*. Ciria London, UK.

Geotechnical Consulting Group (2011). Witanhurst top-down construction. URL: https://gcg.co.uk/projects/deep-excavations-retaining-structures/witanhurst/ [Online; accessed July 12, 2023].

Goh, A., Kulhawy, F., and Wong, K. (2008). Reliability assessment of basal-heave stability for braced excavations in clay. *Journal of geotechnical and geoenvironmental engineering*, 134(2):145–153.

Grammatikopoulou, A. (2004). *Development, implementation and application of kinematic hardening models for overconsolidated clays*. PhD thesis, Imperial College London.

Hardin, B. O. and Drnevich, V. P. (1972). Shear modulus and damping in soils: measurement and parameter effects (terzaghi leture). *Journal of the soil mechanics and foundations division*, 98(6):603–624.

Harlén, M. and Poplasen, G. (2019). *Excavation in Soft Clay-Class A prediction of excavation in central Gothenburg*. PhD thesis, Chalmers University of Technology.

Harr, M. E. (1987). Reliability-based design in civil engineering. *(No Title)*.

Hashash, Y. M., Marulanda, C., Kershaw, K. A., Cording, E. J., Druss, D. L., Bobrow, D. J., and Das, P. K. (2003). Temperature correction and strut loads in central artery excavations. *Journal of geotechnical and geoenvironmental engineering*, 129(6):495–505.

Hashash, Y. M. and Whittle, A. J. (1996). Ground movement prediction for deep excavations in soft clay. *Journal of geotechnical engineering*, 122(6):474–486.

Hashash, Y. M. and Whittle, A. J. (2002). Mechanisms of load transfer and arching for braced excavations in clay. *Journal of Geotechnical and Geoenvironmental Engineering*, 128(3):187–197.

Hensman, P. J., Orazalin, Z. Y., and Sheil, B. B. (2023). Monitoring the construction of a deep energy-from-waste bunker in soft clay and peat. *Géotechnique*, pages 1–15.

Hensman, P. J. and Sheil, B. B. (2023). Monitoring strains and temperatures in a deep excavation base slab using fibre-optic bragg gratings. In *International Conference on Geotechnics for Sustainable Infrastructure Development*, pages 1967–1981. Springer.

Hewitt, R., Haley, M., and Kinner, E. (2003). Case history of deep excavation on an urban campus. In *Proc., 12th Panamerican Conf. on Soil Mechanics and Geotechnical Engineering*, pages 1997–2004.

Hou, Y., Wang, J., and Zhang, L. (2009). Finite-element modeling of a complex deep excavation in shanghai. *Acta Geotechnica*, 4:7–16.

Houlsby, G. (1999). A model for the variable stiffness of undrained clay. In *Proc. Int. Symp. on Pre-Failure Deformation Characteristics of Soils, Turin, 26*, volume 1, pages 443–450. Citeseer.

Hubbard, H., Potts, D., Miller, D., and Burland, J. (1984). Design of the retaining walls for the m25 cut and cover tunnel at bell common. *Géotechnique*, 34(4):495–512.

Janmonta, K., Uchimura, T., Amatya, B., Soga, K., Bennett, P., Lung, R., and Robertson, I. (2008). Fibre optics monitoring of clay cuttings and embankments along london's ring motorway. In *GeoCongress 2008: Characterization, Monitoring, and Modeling of GeoSystems*, pages 509–516.

Jardine, R., Potts, D., Fourie, A., and Burland, J. (1986). Studies of the influence of non-linear stress–strain characteristics in soil–structure interaction. *Géotechnique*, 36(3):377–396.

Jardine, R., Symes, M., and Burland, J. (1984). The measurement of soil stiffness in the triaxial apparatus. *Géotechnique*, 34(3):323–340.

Jen, L. C. (1997). *The design and performance of deep excavations in clay*. PhD thesis, Massachusetts Institute of Technology.

Jiang, S.-H., Li, D.-Q., Cao, Z.-J., Zhou, C.-B., and Phoon, K.-K. (2015). Efficient system reliability analysis of slope stability in spatially variable soils using monte carlo simulation. *Journal of Geotechnical and Geoenvironmental Engineering*, 141(2):04014096.

Johansson, E. and Sandeman, E. (2014). *Modelling of a deep excavation in soft clay a comparison of different calculation methods to in-situ measurements*. PhD thesis, Chalmers University of Technology.

Karlsrud, K., ENGELSTAD, O., Wunsch, R., and SVARD, D. (2006). Diaphragm walls with cross-walls used to prevent bottom heave in soft clay for lot 2 of lilla bommen tunnel in gothenburg. In *Geotechnical aspects of underground construction in soft ground. Proceedings of the 5th international conference of TC 28 of the ISSMGE, the Netherlands, 15-17 june 2005*, pages 835–844.

Kennedy, T. (1979). Practical use of the indirect tensile test for the characterisation of pavement materials. In *Australian road research board conference proc*, volume 9.

Kondner, R. L. (1963). Hyperbolic stress-strain response: cohesive soils. *Journal of the Soil Mechanics and Foundations Division*, 89(1):115–143.

Kulhawy, F. H. (1993). On the evaluation of static soil properties. In *Stability and performance of slopes and embankments II*, pages 95–115. ASCE.

Kulhawy, F. H. and Mayne, P. W. (1990). Manual on estimating soil properties for foundation design. Technical report, Electric Power Research Inst., Palo Alto, CA (USA); Cornell Univ., Ithaca ....

Langford, J., Karlsrud, K., Bengtsson, E., Hof, C., and Oscarsson, R. (2021). Comparison between predicted and measured performance of a deep excavation in soft clay in gothenburg, sweden. In *Geotechnical Aspects of Underground Construction in Soft Ground*, pages 83–90. CRC Press.

Lee, F.-H., Hong, S.-H., Gu, Q., and Zhao, P. (2011). Application of large three-dimensional finite-element analyses to practical problems. *International Journal of Geomechanics*, 11(6):529–539.

Lim, A., Ou, C.-Y., and Hsieh, P.-G. (2010). Evaluation of clay constitutive models for analysis of deep excavation under undrained conditions. *Journal of GeoEngineering*, 5(1):9–20.

Liu, G., Ng, C. W., and Wang, Z. (2005). Observed performance of a deep multistrutted excavation in shanghai soft clays. *Journal of Geotechnical and Geoenvironmental Engineering*, 131(8):1004–1013.

Liu, G. B., Jiang, R. J., Ng, C. W., and Hong, Y. (2011). Deformation characteristics of a 38 m deep excavation in soft clay. *Canadian Geotechnical Journal*, 48(12):1817–1828.

Long, M. (2001). Database for retaining wall and ground movements due to deep excavations. *Journal of Geotechnical and Geoenvironmental Engineering*, 127(3):203–224.

Lumb, P. (1974). Application of statistics in soil mechanics. *Soil Mechanics-new horizons*, pages 44–111.

Magne, S., Rougeault, S., Vilela, M., and Ferdinand, P. (1997). State-of-strain evaluation with fiber bragg grating rosettes: application to discrimination between strain and temperature effects in fiber sensors. *Applied optics*, 36(36):9437–9447.

Malcolm Drilling (2018). Oceanwide centre. URL: https://www.malcolmdrilling.com/projects/oceanwide-center [Online; accessed July 5, 2023].

Mana, A. I. and Clough, G. W. (1981). Prediction of movements for braced cuts in clay. *Journal of the Geotechnical Engineering Division*, 107(6):759–777.

Martello Piling (2022). Contiguous pile wall. URL: https://www.martellopiling.com/en/techniques/retaining-walls/pile-walls/contiguous-pile-wall [Online; accessed August 10, 2022].

Masini, L., Gaudio, D., Rampello, S., and Romani, E. (2021). Observed performance of a deep excavation in the historical center of rome. *Journal of Geotechnical and Geoenvironmental Engineering*, 147(2):05020015.

Mayne, P. and Campanella, R. (2005). Versatile site characterization by seismic piezocone. In *Proceedings of the 16th International Conference on Soil Mechanics and Geotechnical Engineering*, pages 721–724. IOS Press.

McKone, T. E. (1999). Trim. fate technical support document, volume i: Description of module.

Mieloszyk, M., Majewska, K., and Ostachowicz, W. (2021). Application of embedded fibre bragg grating sensors for structural health monitoring of complex composite structures for marine applications. *Marine Structures*, 76:102903.

Mohamad, H., Bennett, P., Soga, K., Mair, R., and Bowers, K. (2010). Behaviour of an old masonry tunnel due to tunnelling-induced ground settlement. *Géotechnique*, 60(12):927–938.

Mohamad, H., Soga, K., Pellew, A., and Bennett, P. J. (2011). Performance monitoring of a secant-piled wall using distributed fiber optic strain sensing. *Journal of Geotechnical and Geoenvironmental Engineering*, 137(12):1236–1243.

Momeni, E., Poormoosavian, M., Mahdiyar, A., and Fakher, A. (2018). Evaluating random set technique for reliability analysis of deep urban excavation using monte carlo simulation. *computers and Geotechnics*, 100:203–215.

Moormann, C. (2004). Analysis of wall and ground movements due to deep excavations in soft soil based on a new worldwide database. *Soils and foundations*, 44(1):87–98.

Nejjar, K., Dias, D., Cuira, F., Chapron, G., and Lebissonnais, H. (2021). Experimental study of the performance of a 32 m deep excavation in the suburbs of paris. *Géotechnique*, 73(6):469–479.

Ng, C. W. W., Hong, Y., Liu, G., and Liu, T. (2012). Ground deformations and soil–structure interaction of a multi-propped excavation in shanghai soft clays. *Géotechnique*, 62(10):907–921.

NGI (1962). Measurements at a strutted excavation. *Oslo Subway, Vaterland 1. Technical Report 7*.

Nguyen, T. S. and Likitlersuang, S. (2021). Influence of the spatial variability of soil shear strength on deep excavation: A case study of a bangkok underground mrt station. *International Journal of Geomechanics*, 21(2):04020248.

nscc International (2022). Diaphragm walls. URL: https://nsccme.com/solutions/foundation-engineering/earth-retaining-structures/diaphragm-walls/ [Online; accessed August 8, 2022].

O'Brien, A. (1991). Discussion of "use of sheet pile retaining walls for deep excavations in stiff clay. potts, d. and day, r. (1990). *Proceedings of the Institute of Civil Engineers*, Volume 88 Issue 6(PART 1):pp. 899–927.

Obrzud, R. (2010). *The hardening soil model: A practical guidebook*. Zace Services.

Ohde, J. (1939). *Zur theorie der druckverteilung im baugrund*.

Olsen, M. B. (2001). *Measured performance of a large excavation on the MIT campus*. PhD thesis, Massachusetts Institute of Technology.

Ooi, P. and Ramsey, T. (2003). Curvature and bending moments from inclinometer data. *International Journal of Geomechanics*, 3(1):64–74.

Orazalin, Z. Y., Whittle, A. J., and Olsen, M. B. (2015). Three-dimensional analyses of excavation support system for the stata center basement on the mit campus. *Journal of Geotechnical and Geoenvironmental Engineering*, 141(7):05015001.

O'Rourke, T. (1993). Base stability and ground movement prediction for excavations in soft clay. In *Retaining structures*, pages 657–686. Thomas Telford Publishing.

Orr, T. L. and Farrell, E. R. (2012). *Geotechnical design to Eurocode 7*. Springer Science & Business Media.

Ou, C.-Y., Chiou, D.-C., and Wu, T.-S. (1996). Three-dimensional finite element analysis of deep excavations. *Journal of Geotechnical Engineering*, 122(5):337–345.

Ou, C.-Y., Hsieh, P.-G., and Chiou, D.-C. (1993). Characteristics of ground surface settlement during excavation. *Canadian geotechnical journal*, 30(5):758–767.

Ou, C.-Y., Liao, J.-T., and Lin, H.-D. (1998). Performance of diaphragm wall constructed using top-down method. *Journal of geotechnical and geoenvironmental engineering*, 124(9):798–808.

Ou, C.-Y., Shiau, B.-Y., and Wang, I.-W. (2000). Three-dimensional deformation behavior of the taipei national enterprise center (tnec) excavation case history. *Canadian Geotechnical Journal*, 37(2):438–448.

Park, S., Park, T., and Han, K. (2011). Real-time monitoring of composite wind turbine blades using fiber bragg grating sensors. *Advanced Composite Materials*, 20(1):39–51.

Peck, B. (1969). Deep excavation and tunnelling in soft ground, state of the art volume. In *7th ICSMFE*, volume 4, pages 225–290.

Pelecanos, L. and Soga, K. (2018). Development of load-transfer curves for axially-loaded piles using fiber-optic strain data, finite element analysis and optimization. In *the 9th European Conference on Numerical Methods in Geotechnical Engineering, Portugal*, pages 1025–1030.

Pelecanos, L., Soga, K., Chunge, M. P., Ouyang, Y., Kwan, V., Kechavarzi, C., and Nicholson, D. (2017). Distributed fibre-optic monitoring of an osterberg-cell pile test in london. *Géotechnique Letters*, 7(2):152–160.

Phoon, K.-K. (1995). *Reliability-based design of foundations for transmission line structures*. Cornell University.

Poh, T., Wong, I., and Chandrasekaran, B. (1997). Performance of two propped diaphragm walls in stiff residual soils. *Journal of performance of constructed facilities*, 11(4):190–199.

Potts, D. and Fourie, A. (1984). The behaviour of a propped retaining wall: results of a numerical experiment. *Géotechnique*, 34(3):383–404.

Potts, D. M., Zdravković, L., Addenbrooke, T. I., Higgins, K. G., and Kovačević, N. (2001). *Finite element analysis in geotechnical engineering: application*, volume 2. Thomas Telford London.

Powrie, W. (2018). Soil mechanics: concepts and applications.

Powrie, W. and Batten, M. (2000). Comparison of measured and calculated temporary-prop loads at canada water station. *Géotechnique*, 50(2):127–140.

Powrie, W. and Li, E. (1991). Finite element analyses of an in situ wall propped at formation level. *Géotechnique*, 41(4):499–514.

Price, G. and Wardle, I. (1984). Recent developments in pile/soil instrumentation systems. In *Field measurements in geomechanics. International symposium*, pages 533–542.

Rankine, W. J. M. (1857). Ii. on the stability of loose earth. *Philosophical transactions of the Royal Society of London*, (147):9–27.

Richards, D., Holmes, G., and Beadman, D. (1999). Measurement of temporary prop loads at mayfair car park. *Proceedings of the Institution of Civil Engineers-Geotechnical Engineering*, 137(3):165–174.

Robertson, P. K. (2009). Interpretation of cone penetration tests—a unified approach. *Canadian geotechnical journal*, 46(11):1337–1355.

Robertson, P. K. (2010). Soil behaviour type from the cpt: an update. In *2nd International symposium on cone penetration testing*, volume 2, page 8. Cone Penetration Testing Organizing Committee Huntington Beach.

Roboski, J. F. (2004). *Three-dimensional performance and analyses of deep excavations*. Northwestern University.

Roscoe, K. and Burland, J. B. (1968). On the generalized stress-strain behaviour of wet clay.

Roscoe, K., Schofield, A., and Thurairajah, A. (1963). Yielding of clays in states wetter than critical. *Géotechnique*, 13(3):211–240.

Roscoe, K. H., Schofield, A., and Wroth, a. P. (1958). On the yielding of soils. *Géotechnique*, 8(1):22–53.

Royston, R. (2018). *Investigation of soil-structure interaction for large diameter caissons*. PhD thesis, University of Oxford.

Royston, R., B. Sheil, B., and W. Byrne, B. (2022). Monitoring the construction of a large-diameter caisson in sand. *Proceedings of the Institution of Civil Engineers-Geotechnical Engineering*, 175(3):323–339.

Schanz, T., Vermeer, P., and Bonnier, P. G. (1999). The hardening soil model: formulation and verification. *Beyond 2000 in computational geotechnics*, 1:281–296.

Schofield, A. N. (1980). Cambridge geotechnical centrifuge operations. *Géotechnique*, 30(3):227–268.

Schwamb, T. (2014). *Performance monitoring and numerical modelling of a deep circular excavation*. PhD thesis, University of Cambridge.

Schwamb, T., Soga, K., Mair, R. J., Elshafie, M. Z., Sutherden, R., Boquet, C., and Greenwood, J. (2014). Fibre optic monitoring of a deep circular excavation. *Proceedings of the Institution of Civil Engineers-Geotechnical Engineering*, 167(2):144–154.

Schweiger, H. and Peschl, G. (2005). Reliability analysis in geotechnics with the random set finite element method. *Computers and Geotechnics*, 32(6):422–435.

Schweiger, H., Peschl, G., and Pöttler, R. (2007). Application of the random set finite element method for analysing tunnel excavation. *Georisk*, 1(1):43–56.

Sekhavatian, A. (2018). Reliability analysis of deep excavations by rs and mcs methods: case study. *Innovative Infrastructure Solutions*, 3:1–15.

Sheil, B. B., Suryasentana, S. K., Templeman, J. O., Phillips, B. M., Cheng, W.-C., and Zhang, L. (2022). Prediction of pipe-jacking forces using a bayesian updating approach. *Journal of Geotechnical and Geoenvironmental Engineering*, 148(1):04021173.

Simpson, B. (1992). Retaining structures: displacement and design. *Géotechnique*, 42(4):541–576.

Simpson, B. and Powrie, W. (2002). Embedded retatining walls: theory, practice and understanding. In *Proceedings of the International Conference On Soil Mechanics and Geotechnical Engineering*, volume 4, pages 2505–2526. AA BALKEMA PUBLISHERS.

Soares, M. (1984). The instrumentation of a diaphragm wall for the excavation for the rio de janeiro underground. In *Field measurements in geomechanics. International symposium*, pages 553–563.

Sokolovskii, V. V. (2016). *Statics of granular media*. Elsevier.

St John, H., Higgins, K., Potts, D., and Jardine, R. (1992). Prediction and performance of ground response due to construction of a deep basement at 60 victoria embankment. In *Predictive soil mechanics: Proceedings of the Wroth Memorial Symposium held at St Catherine's College, Oxford, 27-29 July 1992*, pages 581–608. Thomas Telford Publishing.

Stallebrass, S. and Taylor, R. (1997). The development and evaluation of a constitutive model for the prediction of ground movements in overconsolidated clay. *Géotechnique*, 47(2):235–253.

Swatek, E., Asrow, S. P., and Seitz, A. M. (1972). Performance of bracing for deep chicago excavation. In *Performance of Earth and Earth-Supported Structures*, page 1303. ASCE.

Tan, Y. and Wei, B. (2012). Observed behaviors of a long and deep excavation constructed by cut-and-cover technique in shanghai soft clay. *Journal of Geotechnical and Geoenvironmental Engineering*, 138(1):69–88.

Terzaghi, K. (1925). *Erdbaumechanik auf bodenphysikalischer Grundlage*. F. Deuticke.

Terzaghi, K. (1943). Theoretical soil mechanics.

Terzaghi, K., Peck, R. B., and Mesri, G. (1967). *Soil mechanics in engineering practice*. John wiley & sons.

Tiwari, B., Ajmera, B., and Kaya, G. (2010). Shear strength reduction at soil structure interface. In *GeoFlorida 2010: Advances in Analysis, Modeling & Design*, pages 1747–1756.

Tjie-Liong, G. (2014). Common mistakes on the application of plaxis 2d in analyzing excavation problems. *International Journal of Applied Engineering Research*, 9(21):8291–8311.

Tornborg, J., Karlsson, M., Kullingsjö, A., and Karstunen, M. (2021). Experience from short-and long-term performance of deep excavations in soft sensitive clays. In *IOP Conference Series: Earth and Environmental Science*, volume 710, page 012053. IOP Publishing.

Tschebotarioff, G. P. (1973). Foundations: retaining and earth structures: the art of design and construction and its scientific basis in soil mechanics. *(No Title)*.

Twine, D. and Roscoe, H. (1997). Prop loads: guidance on design. *Funders Report CP/48. Construction Industry Research and Information Association, London*.

Valley, B., Kaiser, P. K., and Duff, D. (2010). Consideration of uncertainty in modelling the behaviour of underground excavations. In *Proceedings Fifth International Seminar on Deep and High Stress Mining (Deep Mining 2010), M. Van Sint Jan and Y. Potvin (eds)*, pages 6–8.

Viggiani, G. and Atkinson, J. (1995). Stiffness of fine-grained soil at very small strains. *Géotechnique*, 45(2):249–265.

von Soos, P. (1991). Grundbataschenbuch. *Part 4. Ernst and Sohn, Berlin*.

Vorster, T., Soga, K., Mair, R., Bennett, P., Klar, A., and Choy, C. (2006). The use of fibre optic sensors to monitor pipeline response to tunnelling. In *GeoCongress 2006: Geotechnical Engineering in the Information Technology Age*, pages 1–6.

Wang, J., Xu, Z., and Wang, W. (2010). Wall and ground movements due to deep excavations in shanghai soft soils. *Journal of Geotechnical and Geoenvironmental Engineering*, 136(7):985–994.

Whittle, A., Hashash, Y. M., and Whitman, R. (1994a). Analysis of deep excavation in boston. *Journal of Geotechnical Engineering*, 120(10):1911–1912.

Whittle, A. J., Corral, G., Jen, L. C., and Rawnsley, R. P. (2015). Prediction and performance of deep excavations for courthouse station, boston. *Journal of Geotechnical and Geoenvironmental Engineering*, 141(4):04014123.

Whittle, A. J., Degroot, D. J., Ladd, C. C., and Seah, T.-H. (1994b). Model prediction of anisotropic behavior of boston blue clay. *Journal of geotechnical Engineering*, 120(1):199–224.

Whittle, A. J. and Kavvadas, M. J. (1994). Formulation of mit-e3 constitutive model for overconsolidated clays. *Journal of Geotechnical engineering*, 120(1):173–198.

Wisser, C., Augarde, C., and Burd, H. (2005). Numerical modelling of compensation grouting above shallow tunnels. *International Journal for numerical and analytical methods in Geomechanics*, 29(5):443–471.

Wong, I. H., Poh, T. Y., and Chuah, H. L. (1997). Performance of excavations for depressed expressway in singapore. *Journal of geotechnical and geoenvironmental engineering*, 123(7):617–625.

Wood, D. M. (1990). *Soil behaviour and critical state soil mechanics*. Cambridge university press.

Wood, L. and Perrin, A. (1984). Observations of a strutted diaphragm wall in london clay: A preliminary assessment. *Géotechnique*, 34(4):563–579.

Wu, M., Du, C., Yang, K., Geng, X., Liu, X., and Xia, T. (2019). A new empirical approach to estimate temperature effects on strut loads in braced excavation. *Tunnelling and Underground Space Technology*, 94:103115.

Wu, S.-H., Ching, J., and Ou, C.-Y. (2013). Predicting wall displacements for excavations with cross walls in soft clay. *Journal of geotechnical and Geoenvironmental engineering*, 139(6):914–927.

Zakladani Staveb (2022). Secant pile wall. URL: https://www.zakladani.cz/cs/ [Online; accessed August 12, 2022].

Zdravkovic, L., Potts, D., and St John, H. (2005). Modelling of a 3d excavation in finite element analysis. *Géotechnique*, 55(7):497–513.

Zhang, W., Han, L., Gu, X., Wang, L., Chen, F., and Liu, H. (2022). Tunneling and deep excavations in spatially variable soil and rock masses: A short review. *Underground Space*, 7(3):380–407.

Zhang, Z. and Yao, X. (2005). *Accident analysis and technology dispose of certain deep foundation pit*. Constr. Technol. 34, 72–73 (in Chinese).